Hydrodynamics of Vertical Surface-Piercing Cylinders

by

Douglas Andrew Potts, B.Eng. (Civil)

National Centre for Maritime Engineering and Hydrodynamics

Australian Maritime College

Submitted in fulfilment of the requirements for the Master of Philosophy

(Maritime Engineering)

University of Tasmania

July 2019

TABLE OF CONTENTS

LIST OF FIGURES

LIST OF TABLES

SUMMARY

The fluid flow around a long, slender circular cylinder, either in air or water, is a practical circumstance that has been long-studied in the field of fluid dynamics (both aerodynamics and hydrodynamics). The advent of the offshore oil and gas industry after World War II, employed platforms, risers and pipelines formed from steel tubular sections. These were subject to hydrodynamic loading under waves and currents where the need to reliably characterise the fluid loading conditions provided significant impetus to this field of investigation on the fully submerged and vertical surface-piercing cylinders under uniform and oscillatory flow conditions.

This thesis sets out a detailed investigation of the hydrodynamics of vertical surface-piercing cylinders. The aims of this thesis were to experimentally investigate: the effect of the end conditions on the Vortex-Induced Vibrations (VIV), the near field wake and the drag coefficient; the relationship between the depth of the ventilated pocket behind the cylinder with respect to the velocity and the Froude number; the typical hydrodynamic wake topology of a cylinder; and the finite aspect ratio at which the drag coefficient equals that of a typical fully submerged infinite cylinder.

The findings derived within this thesis may be summarised as follows:

1. The submerged free end-tip condition does not influence the hydrodynamic wake properties of the bow wave nor the ventilated pocket depth.
2. The difference in results from the alternate end conditions affect the VIV by an approximate 25%, which may then be further influenced by the occurrence of VIV lock-in.
3. Although there is some disparity between the end conditions with respect to the drag coefficient, the overall difference may be deemed negligible.
4. A relationship may be developed between the ventilated pocket depth with respect to the velocity squared and the diameter.
5. A relationship between the non-dimensional bow wave height with respect to the velocity squared and the diameter may also be developed.

6. A finite vertical surface-piercing cylinder may be deemed to be infinite in length when the aspect ratio ≥ 47.

DECLARATION

The material contained in this thesis is the original work of the author, except where due reference is made in the text. It has not been previously presented to any other institution for any other award.

This thesis may be made available for loan and limited copying and communication in accordance with the Copyright Act 1968.

DEDICATION

This thesis is dedicated to my father

Andrew

Nullius in verba

On the word of no one

ACKNOWLEDGMENTS

I would like to express my sincere appreciation to my supervisors Prof. Jonathan Binns, Assoc. Prof. Hayden Marcollo and Assoc. Prof. Alex Skvortsov. Their support, guidance and intellectual contributions were invaluable.

I would like to thank AMOG Consulting for their support throughout the writing of this thesis and for sharing their knowledge, resources and expertise in the fields of VIV and hydrodynamics.

I thank Professor Jon Hinwood for his thoughts and insights into my work, particularly during thesis writing.

I would like to express my gratitude to Saeed Mohajernasab, without whom I would not have been able to complete my testing programme on time. Thank you for helping during the long days, nights and weekends spent in the towing tank.

Special thanks to the towing tank staff: Dr Gregor Macfarlane, Tim Lilienthal and Liam Honeychurch.

I would like to thank all my friends who helped support me through this thesis and provided me respite when times were tough.

I would like to express thanks to my family, in particular to all my sisters; Kathy, Lizzie and Maggie, for their endless and unwavering support.

Lastly, I would like to express my profound gratitude and admiration to my late father, Professor Andrew E. Potts, for moulding me into the engineer that I am today.

NOMENCLATURE

Symbol	Definition	Units
A	Projected Surface Area	m^2
A/D or A*	Amplitude/Diameter Ratio	
A_x/D	Inline Amplitude/Diameter Ratio	
A_y/D	Crossflow Amplitude/Diameter Ratio	
B	Towing Tank Width	m
c	Speed of Sound	m/s
C	Coefficient Magnitude	
C_D	Drag Coefficient	
C_D'	Fluctuating Fluid Dynamic Drag Coefficient	
$C_{D\infty}$	Drag Coefficient of a Fully Submerged Cylinder	
C_{Df} or C_f	Skin Friction Drag Coefficient	
C_{Dp} or C_p	Pressure Distribution Drag Coefficient	
C_L	Lift Coefficient	
C_L'	Fluctuating Fluid Dynamic Lift Coefficient	
C_{pb}	Base Pressure Coefficient	
D	Cylinder Diameter	m
D_1	Bow Wave Height	m
D_2	Trailing Wake Height	m
D_3	Trailing Wave Height	m
D_{EP}	End-plate Diameter	m
f_n	Natural Frequency	Hz
F_D	Drag Force	N
F_{Dp}	Net Pressure Drag Force	N
Fr	Froude Number	
Fr_D	Froude Number determined from D	
Fr_L	Froude Number determined from L	
g	Gravity	m/s^2
k	Explicit Roughness	μm
k_s	Explicit Roughness of Steel	μm
k_v	Explicit Roughness of Vinyl	μm
L	Submerged Length	m
L/D	Length/Diameter Ratio	
L_0	Depth of Ventilated Flow	m
L_2	Trailing Wake Location	m
L_3	Trailing Wave Length	m
LWL	Length of Waterline	√m/s
M	Mach Number	
p	Gauge Pressure	Pa
P_b	Base Pressure	Pa
P_s	Freestream Static Pressure	Pa
Re	Reynolds Number	
Re_D	Reynolds Number determined from D	
Re_L	Reynolds Number determined from L	
St	Strouhal Number	
V	Velocity	m/s
Vr or V*	Reduced Velocity	
y	Segmental Length along Cylinder from the Free end	m

Greek Symbol	Definition	Units
δ	Elevation of Boundary Layer of Incident Flow action on Model	
θ	Angle between Drag direction and Surface normal	^{o}
κ	Drag Reduction Factor	
μ	Dynamic Viscosity of the Fluid	kg/ms
ν	Kinematic Viscosity of the Fluid	m^2/s
ρ	Fluid Density	kg/m^3

Acronym	Definition
AMC	Australian Maritime College
CF	Crossflow
DoF	Degrees of Freedom
IL	Inline
ITTC	International Towing Tank Committee
LoBF	Line-of-Best-Fit
PSD	Power Spectral Density
TAV	Tip Associated Vortex
AUV	Automated Underwater Vehicle
VIV	Vortex-Induced Vibration

For ease of use, foldout legends for the plots presented in Chapter 3, Chapter 5 and Chapter 6 can be found in Appendix F.

Chapter 1 INTRODUCTION

1.1 BACKGROUND

The fluid flow around a long, slender circular cylinder, either in air or water, is a practical circumstance that has been long-studied in the field of fluid dynamics (both aerodynamics and hydrodynamics). The advent of the offshore oil and gas industry after World War II, employed platforms, risers and pipelines formed from steel tubular sections. These were subject to hydrodynamic loading under waves and currents where the need to reliably characterise the fluid loading conditions provided significant impetus to this field of investigation of the fluid loading on fully submerged and vertical surface-piercing cylinders under uniform and oscillatory flow conditions.

The primary area of focus in this field has been on fully submerged cylinders (e.g. subsea risers, offshore pipelines). There is a substantial body of knowledge and published guidance for determining the hydrodynamic loading of tubulars in currents, waves, in free spans, on or adjacent to the seabed and in arrays (Sumer and Fredsoe (2006); Zdravkovich (1997), (1981)). Whilst offshore structures have surface-piercing cylinders subject to hydrodynamic loading (e.g. drilling risers, platform legs, piers), the hydrodynamics at this interface are usually of a second order significance with respect to the overall fluid loading on the entire platform or riser system, such that it is rarely separated from the overall fluid loading on the structure.

Other applications such as circular bridge piers (Hogben (1974); Hsieh (1964)) in restricted waterways (e.g. river channels) have looked at the near field flow and wake conditions of the cylinder within the restricted flow field, with respect to increase in water level and blockage effects. In these circumstances the piers are typically finite in length, effectively fixed at the top and bottom, and restrained against any significant free end-tip effects and vibration.

In the offshore sector, it is common for seawater intake caissons to be vertical surface-piercing cylinders of a finite length that are typically secured above the water surface with a cantilevered free end below the maximum wave trough depth (Craig (2016)). However, for most fixed offshore structures there are intermediate bracing supports of the cylinder at the various bay elevations of the platform, such that only the lower most free end acts as a cantilever. On floating offshore platforms, seawater uptakes are in some instances suspended beneath or alongside the hull to a depth, where they can be considered to be cantilevered for their entire length through the sea-air interface to the free bottom end.

Applications involving surface-piercing cylinders of a finite length which are fixed below the water line with the free end in-air include masts and aerials on submersible crafts or submerged near-surface buoys (e.g. oceanographic buoys). In most instances the designers adopt a conservative approach assuming that the fluid loading is that of a fully submerged cylinder, as this aspect is not critical and there is no interest in the surface wave effects associated with the cylinder passing through the sea-air interface.

Submersible vehicles typically contain a communications mast which is projected up through the water surface when the vehicle is fully submerged. In this instance the mast can be considered as a slender cantilevered cylinder of finite length subjected to hydrodynamic loading from the forward speed of the hull and any near-surface wave action. The submersible will typically be still or moving at a low speed near the surface where the periscope and/or other masts may also be deployed so as to reduce the detectable wake generated by a single vertical surface-piercing mast. From a stealth perspective it is desirable for a submerged vehicle to be at as great a depth as possible when operating masts, whereby fluid loading on the mast is a significant factor in determining the practical maximum length of mast and thus periscope depth. As such, the mast application is largely unique in that it is concerned with both the near-field surface wake generated by fluid loading as well as the overall hydrodynamic loading on the entire length of the surface-piercing cylinder.

Surface-piercing cantilevered cylinders are also subject to excitation by Vortex-Induced Vibration (VIV). VIV is dependent upon the diameter and stiffness of the mast and the associated natural frequency of oscillation, with regard to the fluid velocity (speed of the hull through water). The longer and more slender the cylinder, the greater the propensity for exciting VIV. The crossflow vibration motions of the mast undergoing VIV excitation will impair the optical performance of periscopes, amplify the near-field wake from the increased apparent drag diameter, generate increased drag loading on the cantilevered mast and give rise to increased cyclic fatigue loading on the mast and the associated mechanical systems. It is therefore critical to calculate and compensate for VIV in the design of slender cantilevered structures such as Automated Underwater Vehicle (AUV) masts.

Studies to investigate and quantify VIV and to test possible solutions have been performed, chiefly in controlled laboratory settings.

Laboratory testing of vertical surface-piercing cylinders of finite length has predominantly been conducted in a top-down arrangement, as this is the easiest configuration to setup using conventional tow tank facilities. These tests can be limited in their scope due to the tow tank capabilities, including:

- The submerged length of the cylinder can be limited by the depth of the tow tank.
- The maximum diameter of the cylinder is limited by the width of the flume and associated blockage effects.
- The maximum diameter of the cylinder is limited by the drive capacity of the tow carriage.
- The maximum speed of the tow carriage is limited by the length of the tank.

Smaller diameter, slender cylinders are typically used in such investigations so as to increase the submerged length and avoid blockage effects. The same approach is employed to alter the flow regime characteristics of Reynolds number and Froude number Sumer and Fredsoe (2006) [p. 360]. However, in doing so these cylinders are more susceptible to VIV excitation, and will therefore be unrepresentative of larger diameter and more rigid masts.

The addition of the multi-fluid air and water interface provides an additional level of complexity, which is not experienced by fully submerged cylinders. When subject to the fluid flow velocity, the near-field surface wake conditions exhibit different characteristics:

- A bow wave, which is generated under all flow conditions, occurs where there is a rise in water surface level and the reflection of water from the upstream projected area of the cylinder. The bow wave height increases with velocity.
- A trailing depression follows immediately behind the cylinder at low velocities, with no apparent ventilation.
- With increasing velocity:
    - Formation of a trailing wake of sheet flow from the edges of the cylinder formed from the bow wave separation, whose height and length increases with increasing velocity.
    - Formation of a ventilated pocket behind the submerged length of the cylinder, whose depth increases with increasing velocity.
- Once the ventilated pocket reaches the free end-tip of the cylinder with increasing velocity, a trailing wave (also called a rooster tail) is formed where the ventilated pocket emerges through the water surface.

Hoerner (1965) discusses the ventilated flow condition, where a natural ventilation channel is formed by the separated space at the rear side of the cylinder such that “dead” liquid is sucked down through the pocket and replaced by air. The negative pressure required for the formation of a ventilation pocket is a function of the cross-sectional profile as well as the velocity. The negative pressure caused by the ventilation pocket on the downstream surface of the cylinder effectively reduces the fluid drag loading on the cylinder, with respect to its fully submerged unventilated state.

The extent of the trailing wave formation has two distinct velocity dependant phases:

1. The ventilated pocket has not reached the end-tip (i.e. not fully ventilated).
2. The pocket is fully ventilated along the entire submerged length.

Whilst the end-tip conditions will likely impact on the drag behaviour of the cylinder in the partially ventilated state, it is evident that the pronounced rooster tail that is formed behind a surface-piercing cylinder of finite length under fully ventilated flow condition will be influenced by the end-tip conditions of the cylinder, with respect to tip vorticity effects.

From the perspective of the application where the cylinder is secured above the waterline and penetrates a finite depth into the water column, the issue of the formation of the ventilated pocket, end effects and associated near-field wake characteristics may well be relevant. However, for applications such as AUV masts, where the cylinder is fixed at a finite depth below the water surface with a cantilevered free end in-air, the effect of the free end-tip becomes irrelevant, but the propensity impact of ventilated flow on drag and wake is still of significance.

For a top-down cylinder of a finite submerged length, the formation of a ventilated pocket along its length will likely have significant impact on the formation of Von-Karman alternating vortex streets, such that the oscillating crossflow lift force will likely be disrupted by the extent of ventilated flow. However, this aspect is not well understood. The relative impact of end-tip effects as a function of the submerged length and the proportion of the submerged length that is ventilated is not well understood.

1.2 AIMS AND OBJECTIVES

From the background it is evident that the determination of the near field wake and the hydrodynamic characteristics of a surface-piercing cylinder is a complex problem. The primary objective of this thesis is to experimentally investigate various aspect ratios and their influence on the hydrodynamic characteristics of a surface-piercing cylinder.

The objectives of the investigation were to determine the following:

1. How do the end conditions of a vertical surface-piercing cylinder effect the VIV, the near field wake, and the drag coefficient?
    - In order to test these, three different end conditions were implemented:
        - Open (i.e. the tube is open at both ends).
        - Closed (i.e. the submerged end is sealed).
        - End-plate disc (i.e. an end-plate is fixed to the submerged end).
2. What is the relationship of the depth and length of ventilated flow behind a vertical surface-piercing cylinder with respect to velocity and Froude number (*Fr*)?
3. What is the near field hydrodynamic wake topology for a vertical surface-piercing cylinder?
4. At what length/diameter (*L*/*D*) ratio does the drag coefficient (C_D) become equal to that of a typical fully submerged infinite cylinder (i.e. $C_{D\infty}$ = 1.2, at a Reynolds Range of 1E+4 – 2E+5) for a cylinder with an unventilated flow (i.e. when $L_0 < L$)?
    - This will define the *L*/*D* ratio at which a vertical surface-piercing cylinder may be considered to be infinite.

1.3 THESIS OUTLINE

The outline of this thesis is as follows:

Chapter 1: The introductory chapter outlines a brief background on the topic of surface-piercing cylinders and outlines the aims and objectives that will be addressed in this thesis.

Chapter 2: Presents and discusses the literature regarding the important parameters when describing cylinders in a fluid, such as; hydrodynamic drag, aspect ratio, vortex-induced vibration, hydrodynamic wake, and compressible flow.

Chapter 3: Presents a detailed reanalysis of the Hay (1947) data along with some of the previous analyses regarding the Princeton test results.

Chapter 4: Discusses the reasoning behind conducting a physical model test programme, and the necessary experimental equipment and procedures undertaken to fully capture and process all of the data collected.

Chapter 5: Presents the results in terms of the key identified parameters; drag coefficient, Froude number, Reynolds number, bow wave height, and ventilated pocket depth. The data will include single velocity steady state results, and ramps where the model was accelerated to a maximum allowable velocity.

Chapter 6: Is a discussion and analysis of the key results as presented in Chapter 5.

Chapter 7: Concludes the key findings with reference to the objectives. In addition to the key findings, further findings and recommendations have been presented.

Chapter 8: Provides a list of all the literature sources referenced throughout the thesis.

A summary of the findings is presented at the end of each chapter.

Chapter 2 LITERATURE REVIEW

The scope of this investigation encompasses many topics of the hydrodynamic literature. Accordingly, the literature review will address the following separate streams: non-dimensional numbers, hydrodynamic drag, the phenomenon of VIV, the effect of the aspect ratio on the hydrodynamic drag, the hydrodynamic wake, and the drag on surface-piercing cylinders.

Section 2.1 discusses the non-dimensional numbers which are typical in the presentation of results relating to the hydrodynamics of partially and fully submerged cylinders.

Section 2.2 examines hydrodynamic drag and the parameters which are used to describe this phenomenon.

Section 2.3 reviews the literature on VIV of fully submerged cylinders and surface-piercing cylinders.

Section 2.4 investigates the effect of the aspect ratio on the hydrodynamic drag. The aspect ratio along with the boundary layer and the end-plate conditions all affect the magnitude of the hydrodynamic drag.

Section 2.5 defines the hydrodynamic wake parameters and presents the data from several key sources regarding wake.

Section 2.6 presents the effects of both compressible flow and high Mach number on the drag coefficient.

Section 2.7 summarises the key findings, insights and deficiencies presented in the literature.

2.1 NON-DIMENSIONAL NUMBERS

Non-dimensional numbers are used in hydrodynamics as well as fluid mechanics, aerodynamics and many other fields of engineering. The purpose of using a non-dimensional number is to reduce the number of dimensional variables which may describe a system. In addition to the minimisation of dimensional values, non-dimensional values are used for comparing geometrically similar systems of various scales.

This section will present and discuss the typical non-dimensional numbers used in hydrodynamics.

2.1.1 Reynolds Number

Reynolds number (*Re*) is a dimensionless number that is used in the prediction of fluid flow patterns. It was named after Osbourne Reynolds, who popularised its use in Reynolds (1883). Reynolds number is the ratio of the inertial forces to the viscous forces as defined in Equation 1. The Reynolds number shown below has been presented in terms of diameter resulting in Re_D. The diameter variable is interchangeable with length to define Re_L. Throughout this thesis, Reynolds number has been calculated with respect to the model diameter, except where indicated.

$$Re = \frac{\rho V D}{\mu} = \frac{V D}{\nu} \qquad \text{Equation 1}$$

Where;

ρ = Fluid density

V = Velocity

μ = Dynamic viscosity of the fluid

ν = Kinematic viscosity of the fluid

D = Cylinder diameter

L = Submerged length

Figure 2-1 shows the relationship of non-dimensional drag coefficient (C_D) vs Reynolds number, overlaid, with the Reynolds flow regimes from Barltrop and Adams (1991); sub-critical (teal), sub-critical plateau (blue), critical (red), post-critical (green) and post super-critical (purple). For the purpose of this investigation the sub-critical plateau (blue) from *Re* = 1E+4 – 2E+5 is of interest as it is the Reynolds range in which most practical surface-piercing cylinders will operate.

Table 2-1 depicts the von Kármán street eddy formations for the Reynolds flow regimes shown in Figure 2-1.

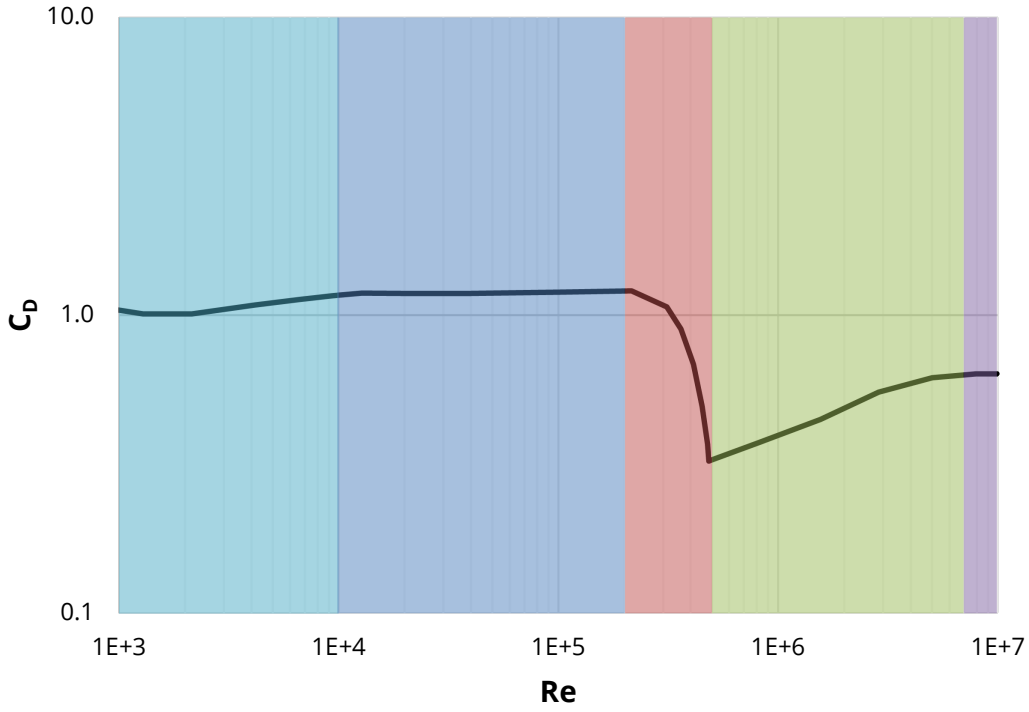

Figure 2-1: Drag coefficient (C_D) vs Reynolds number (Re > 1E+3) with Reynolds flow regimes, adapted from Barltrop and Adams (1991)

Table 2-1: Regimes of fluid flow across a fully submerged circular cylinder, from Lienhard (1966)

Fluid Flow Regime	Reynolds Range	Flow Description
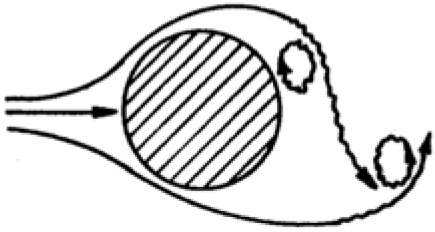	Sub-critical 150 – 2E+5 (teal/blue)	Vortex street is fully turbulent
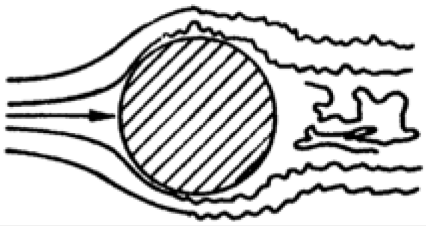	Post-critical 5E+5 – 7E+5 (green)	Laminar boundary layer has undergone turbulent transition. The wake is narrower and disorganised. No vortex street is apparent
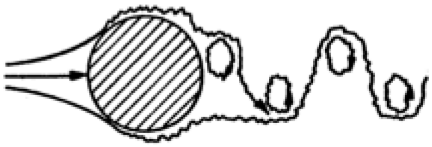	Post super-critical 7E+5 – ∞ (purple)	Re-establishment of the turbulent vortex street. The boundary layer is turbulent, and the wake is thinner

2.1.2 Froude Number

Froude number (*Fr*) was developed by William Froude, a naval architect, hydrodynamicist and engineer in the 1800s (Institution of Naval Architects (1955)). Froude initially developed a speed-length ratio formula shown here as Equation 2. This formula was originally a dimensioned value with the units $\frac{\sqrt{m}}{s}$.

$$Speed/Length\ Ratio = \frac{V}{\sqrt{LWL}} \qquad \text{Equation 2}$$

Where;

LWL = Length of waterline

The speed-length ratio was converted into the current dimensionless Froude number, which is defined as the ratio of the flow inertia to the external field (typically gravity), where the number is based on the speed-length ratio as defined in Equation 3.

$$Fr = \frac{V}{\sqrt{gD}}$$ Equation 3

Where;

g = Gravity

Froude number can be calculated for either the cylinder diameter or the submerged length, where a resultant *L*/*D* ratio is the translational factor between Froude diameter (Fr_D) and Froude length (Fr_L).

Froude number is used when discussing and conducting experimental test programmes due to its scalability and non-dimensionality. Typically wind tinnels and atmospheric chambers tend to contain a structure within a single fluid, where Reynolds scaling may be implemented. However, testing in a towing tank typically contains a multi-fluid structural interaction. Where Froude scaling is more appropriate and applicable.

2.1.3 Reynolds Number and Froude Number

A literature search in the field of the fluid flow past a cylinder reveals that, not all authors present Froude number or Reynolds number. However due to the similarity of the variables in the formulae for *Fr* and *Re*, a direct relationship between the two dimensionless numbers may be developed, as shown below in Equation 4.

$$Fr = \frac{Re}{\left(\frac{\sqrt{D^3 g}}{\nu}\right)}$$ Equation 4

$$Re = Fr\left(\frac{\sqrt{D^3 g}}{\nu}\right)$$

Application of the above formulae facilitated an expanded literature search and a more direct comparison between papers, which was previously incompatible due to the absence of either Froude number or Reynolds number.

2.1.4 Strouhal Number

Named after the Czech physicist, Vincenc Strouhal (Strouhal (1878)), the Strouhal number (*St*) represents the frequency of eddy shedding for a static/fixed cylinder, where the eddy shedding aligns with the natural frequency of the cylinder as defined in Equation 5.

$$St = \frac{f_n D}{V} \qquad \text{Equation 5}$$

Where;

f_n = Natural frequency

A recent review of the Strouhal number of long slender structures – constrained to 1DoF and 2DoF (degree(s) of freedom), Potts et al. (2018), presented and discussed the origin of Strouhal number and the associated relationship with the Reynolds number. Strouhal number is typically defined in terms of the lock-in range which in turn is described by the term Reduced Velocity (V_r).

2.1.5 Reduced Velocity

As the Strouhal number represents the frequency of eddy shedding for a cylinder, VIV occurs across a range of lock-in frequencies, where the eddy shedding aligns with the natural frequency of the cylinder. This is typically represented by the lock-in range, which is described by the term Reduced Velocity (V_r), as per Equation 6.

$$V_r = \frac{1}{St} = \frac{V}{f_n D} \qquad \text{Equation 6}$$

2.2 HYDRODYNAMIC DRAG

Hydrodynamic drag force (F_D) is determined by the sum of the viscous friction force (skin friction) along the surface of a body (C_{Df}) and an asymmetrical pressure distribution on the upstream and downstream side of a cylinder (C_{Dp}), as shown in Equation 7 from Zdravkovich (1997).

$$C_D = C_{Df} + C_{Dp} \qquad \text{Equation 7}$$

Figure 2-2 presents the variation of all six force coefficients – fluctuating drag and lift, C_D' and C_L', time averaged drag and lift, C_D and C_L – exerted on a 2D cylinder, across a whole Reynolds range for a disturbance-free flow around a nominal 2D cylinder. The skin friction (C_{Df}) is quite significant in the laminar state but becomes negligible beyond the shear layer transitional state.

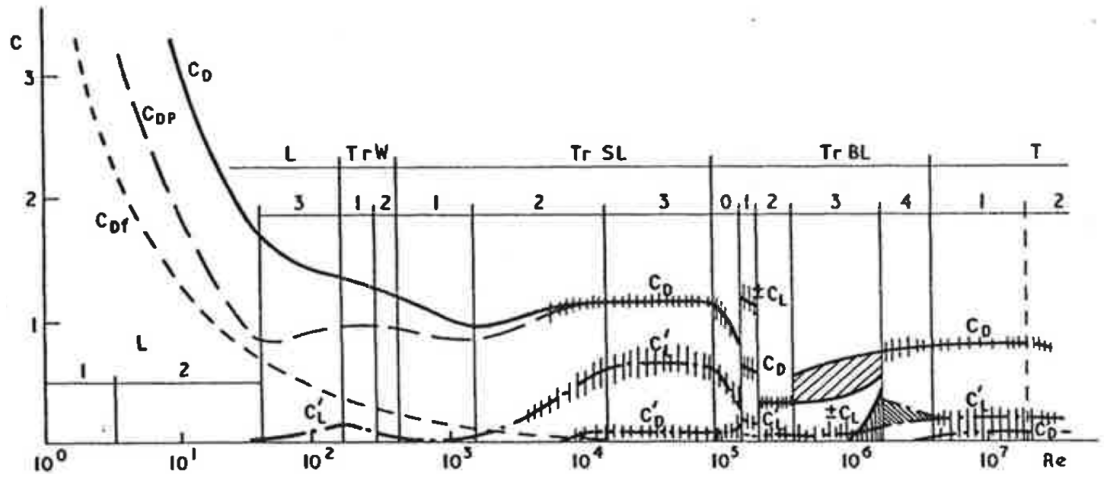

Figure 2-2: Variation of force coefficients for disturbance free flow, from Zdravkovich (1997)

Where;

L = Laminar state of flow

TrW = Transition-in-wake state of flow

TrSL = Transition-in-shear-layers (or Subcritical state)

TrBL = Transition-in-boundary-layers (or Critical state)

T = Fully turbulent state of flow

NB: Vertical axis is the coefficient magnitude (*C*), horizontal is Reynolds number (*Re*).

2.2.1 Drag Force

Drag force (F_D) is the force acting in the opposing direction to the relative motion of an objects movement relative to the surrounding fluid (Zdravkovich (1997)). The F_D relationship typically exists between a solid and a fluid. The force magnitude depends upon the dynamic pressure and the projected surface area which is exposed to the free stream, and the classic representation is expressed in Equation 8 as presented by Hoerner (1965).

$$F_D = C_D\left(\frac{1}{2}\rho V^2 A\right) \qquad \text{Equation 8}$$

Where;

A = Projected surface area

When a vertical surface-piercing cylinder is towed through a fluid (air or water), the drag force is susceptible to a change in the projected surface area as a bow wave forms on the upstream side. This includes a lower drag coefficient due to the then increased area subjected to force. Inclusion of the bow wave in calculations is limited in the literature, and is not applicable to fully submerged cylinders, as a bow wave will never form.

2.2.2 Drag Coefficient

The drag coefficient (C_D) is a dimensionless constant which varies with the shape of the object under drag force. The drag coefficient consists of the skin friction and form drag components as in Equation 7 and is dependent on the Reynolds number. The standard drag force formula is shown as Equation 8 as presented by Hoerner (1965).

Equation 9 presents Equation 8 modified in terms of the drag coefficient.

$$C_D = \frac{F_D}{\frac{1}{2}\rho V^2 DL} \qquad \text{Equation 9}$$

The current standard drag coefficient curve for an infinitely long smooth cylinder was compiled in Hoerner (1965) (Figure 2-3). Several reputable source papers were highly concordant on this topic. The author has retrieved all of the source data that Hoerner used to derive the standard C_D curve, including Lamb (1895); Relf (1914); Wieselsberger (1921); Eisner (1929); Schiller and Linke (1933); Pechstein (1942); White (1946); Finn (1953); Welsh (1953); Roshko (1955), (1961). Of note, several of the sources analyse the same raw data sets, but cite the previous data analysis (i.e. later year papers/references cite the data analysis from earlier sources, e.g. Finn (1953) cites Lamb (1895); Relf (1914); Schiller and Linke (1933); White (1946); Wieselsberger (1921)).

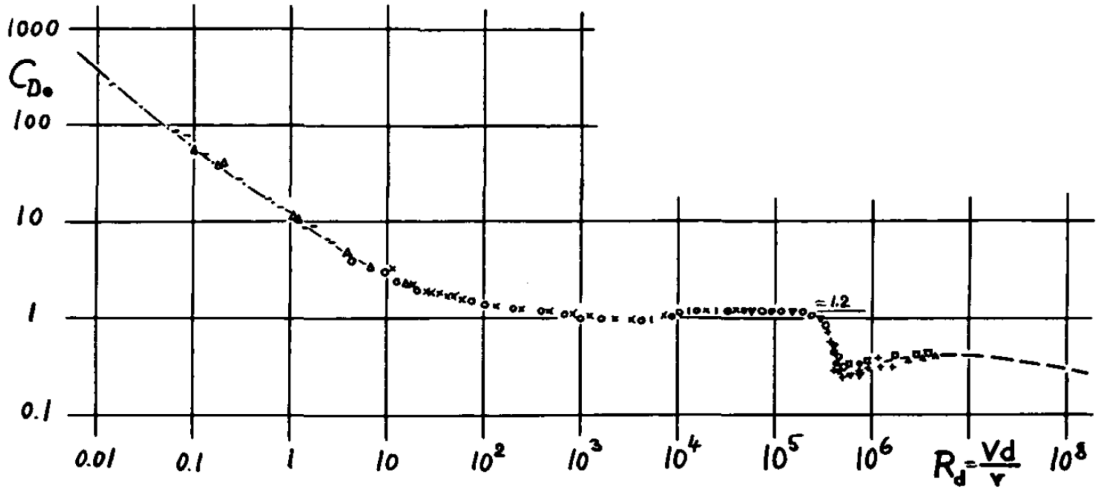

Figure 2-3: Drag coefficient versus Reynolds number for an infinitely long smooth rigid cylinder from Hoerner (1965)

Although the 1965 Hoerner plot is most recognisable, it is derived from the work of Wieselsberger (1921) (Figure 2-4), which was translated from German to English in Wieselsberger (1922).

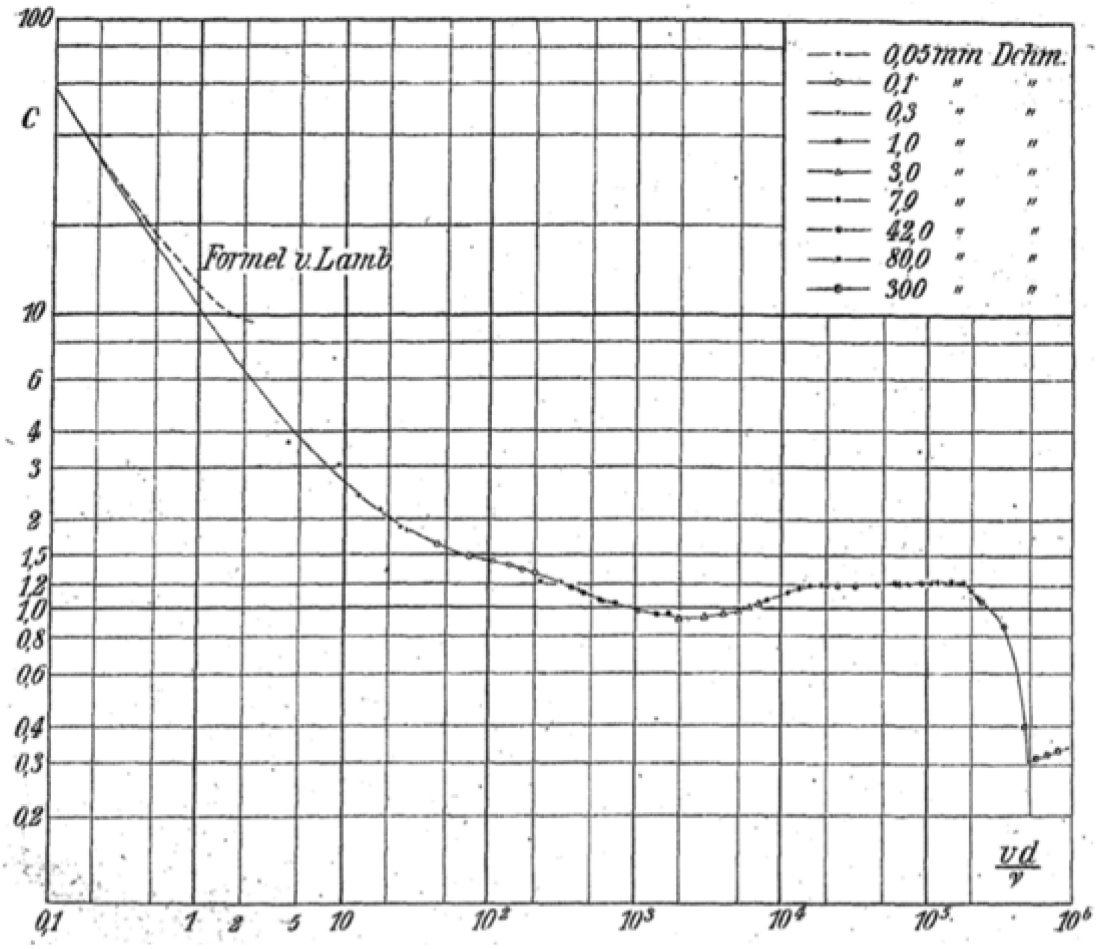

Figure 2-4: Drag coefficient vs Reynolds number for all tests from Wieselsberger (1921). The dashed line represents the formula from Lamb (1895)

Huang (2006), (2010), (2011) conducted several investigations to further quantify the effect of VIV on a cylindrical bluff body, with an interest in the drag characteristics. The 2006 specimen was surface-piercing, rigidly connected and elastically supported at one end from the tow carriage, and the elastic support allowed a crossflow motion (i.e. 1DoF) of the cylinder. The 2010 and 2011 specimens were fully submerged and elastically supported, allowing for both crossflow and inline motions (i.e. 2DoF). From these investigations, Huang reported a drag coefficient of 1.04 at a Reynolds number of 4.1E+4. The drag coefficient here was determined from a single free vibration test using the drag relationship derived by Vandiver (1983). This differs from the broader literature, in which a drag coefficient of 1.2 is widely reported within the same Reynolds number range.

Huang tested the cylinders across a Reynolds number range including regimes from sub-critical to critical, thereby allowing the drag crisis and subsequent reduction in the drag coefficient to occur and be measured. Huang tested cylinders with a varnished surface, where the absolute roughness of the cylinder was considered to be smooth.

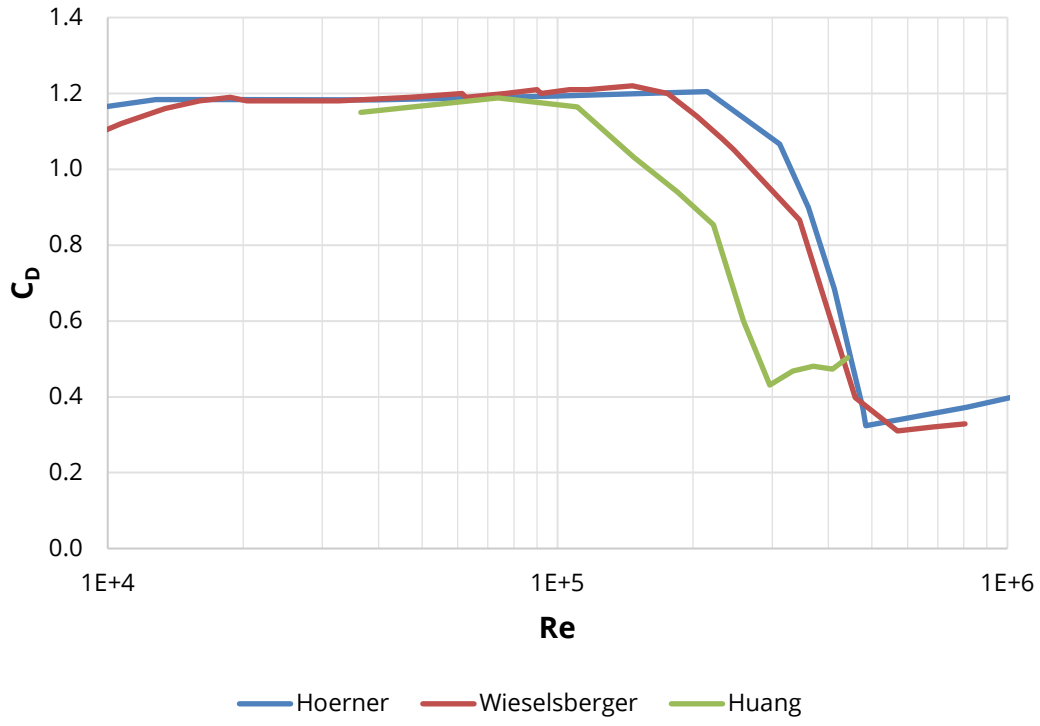

Figure 2-5: Drag coefficient vs Reynolds number, replotted from Hoerner (1965); Huang (2011); Wieselsberger (1922)

The drag coefficient data measured by Huang is plotted in Figure 2-5 along with the original Wieselsberger data and the more widely recognised Hoerner line. When compared to the Huang line, it is evident that the surface roughness may be the cause of the cylinder entering the drag crisis at a lower Reynolds number than the Hoerner and Wieselsberger lines (Kilner et al. (2018)).

Tanida et al. (1973) towed a cylinder in oil and water and measured the drag and lift forces and the Strouhal number. They presented their results in comparison to published findings for fixed in-air cylinders across the subcritical Reynolds regime (refer to Figure 2-6). Tanida conducted the testing with two different mediums, oil and water, and as such two different Reynolds ranges were 'available'. The drag force coefficient for the testing in oil highly correlates with Tritton (1959), but when testing in water there was only a correlation in the shape of the curve, with an approximate 5-10% lower drag coefficient than that measured by Relf and Simmons (1925).

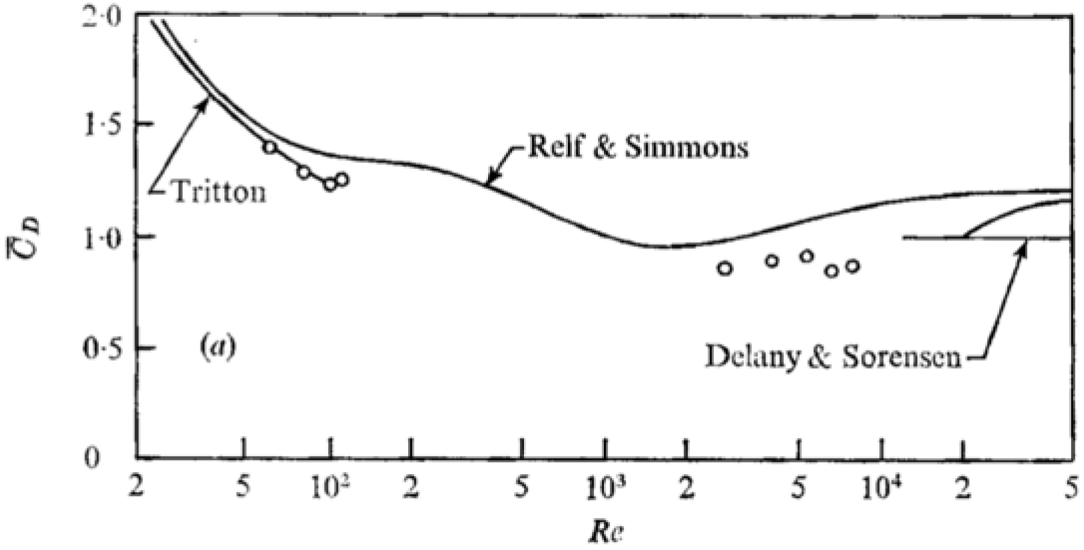

Figure 2-6: Mean drag characteristic of a single stationary cylinder, from Tanida et al. (1973)

2.2.3 Pressure around a Cylinder

Changes in C_D are closely related to changes in the pressure coefficient (C_{Dp} or C_p) on the back of the cylinder. Bruschi et al. (2003) presents a formula to determine the net pressure drag force (F_{Dp}), as per Equation 10.

$$C_{Dp} = \iint_s p(\theta) \cos\theta \, d\theta \qquad \text{Equation 10}$$

Where;

p = the gauge pressure

θ = the angle between the drag direction and the surface normal

Figure 2-7 represents the *x* and *y* directions in conjunction with the standard definition of *θ*.

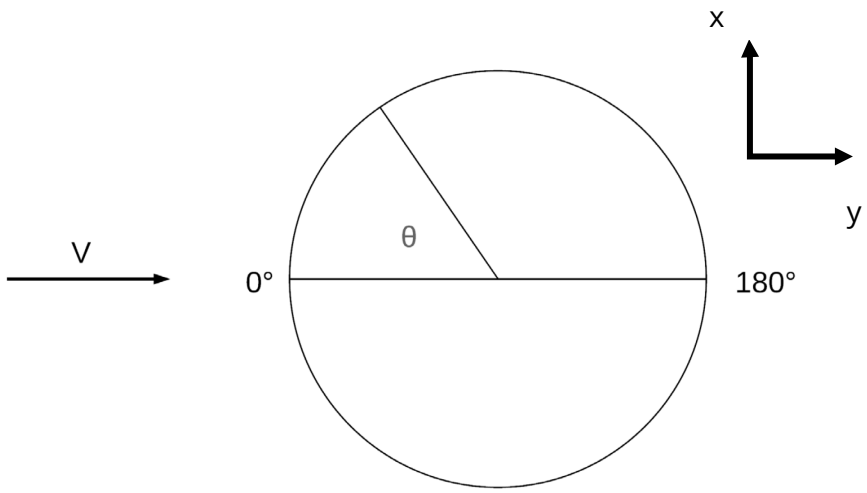

Figure 2-7: Flow, crossflow (x) and inline (y) directions with the sectional mean pressure coefficient angle definition.

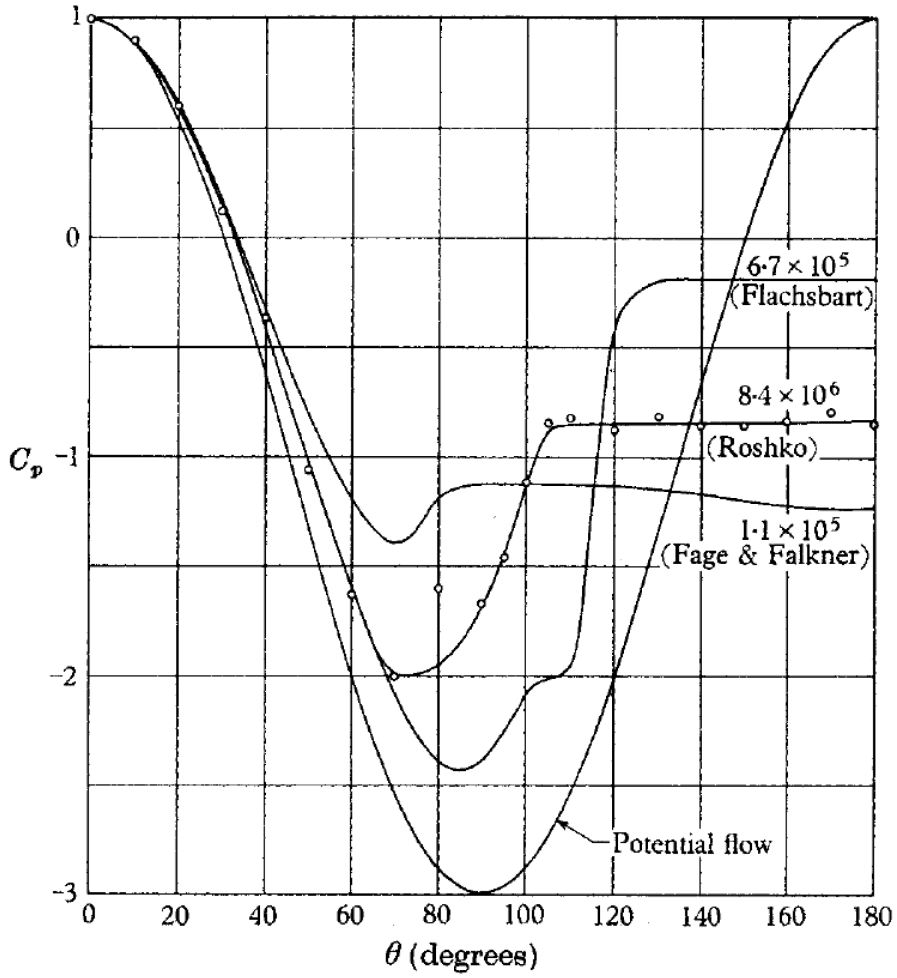

Figure 2-8: Pressure distributions around one half of a cylinder for various Reynolds numbers, from Roshko (1961)

Figure 2-8 presents the pressure distributions around one half of a cylinder.

Jones Jr et al. (1969) was able to capture the laminar separation bubble as shown in Figure 2-9 Jones highlights the laminar bubble and the turbulent separation point on the downstream side of the tested cylinder.

Wind tunnels are commonly used to measure the pressure at various points around the circumference of the cylinder at multiple elevations. The pressure readings are then used to derive a local circumferential pressure coefficient. A commonly reported pressure drag parameter is the base pressure coefficient (C_{pb}), which is the pressure on the rear of the cylinder and may be calculated using Equation 11.

$$C_{pb} = \left(\frac{P_b - P_s}{\frac{1}{2}\rho V^2} \right) \qquad \text{Equation 11}$$

Where;

P_b = Base pressure

P_s = Freestream static pressure

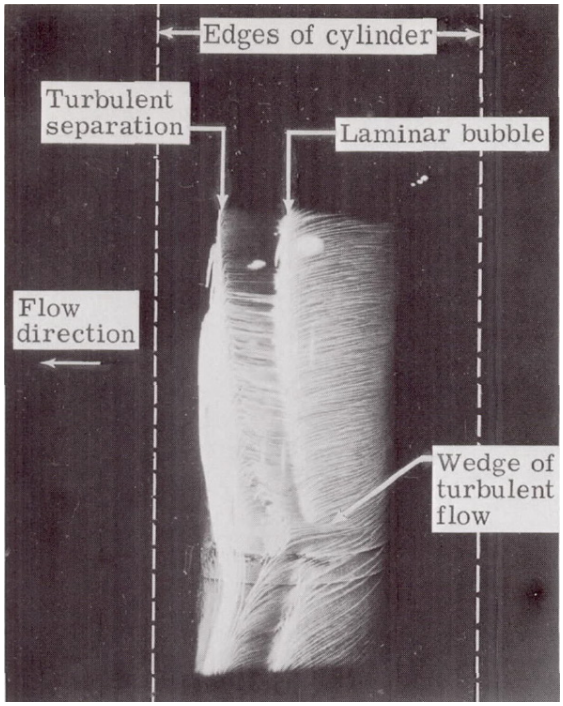

Figure 2-9: Oil flow photograph depicting the laminar bubble separation at a Reynolds number of 1.73E+6 from Jones Jr et al. (1969)

Norberg (1994) investigated a fully submerged cylinder and presents the *L*/*D* effects as a function of the negative of the base pressure coefficient (C_{pb}) denoted by base suction coefficient ($-C_{pb}$), and the Reynolds number. Figure 2-10 shows the effect of the *L*/*D* and D_{EP}/D (end-plate diameter/cylinder diameter) ratios for three different cylinder diameters (2, 6 and 20 mm). From the figure, note that the data falls onto a small spread from Re ≥ 5E+3. This shows that the *L*/*D* ratio has an effect on both C_{pb} and C_D (C_{pb} is an analogue of C_D), as seen when applying the result from Equation 11 to Equation 12. Equation 12 presents the derivation of the drag coefficient, where the skin friction drag coefficient has not been accounted for. As per Figure 2-2 the pressure drag coefficient is the primary drag coefficient within the target Reynolds range (1E+4 – 1E+5).

$$C_D = \int_0^{2\pi} C_p cos(\theta)\, d\theta \qquad \text{Equation 12}$$

Figure 2-11 presents the theoretical Reynolds flow regimes for several practical sized cylinders.

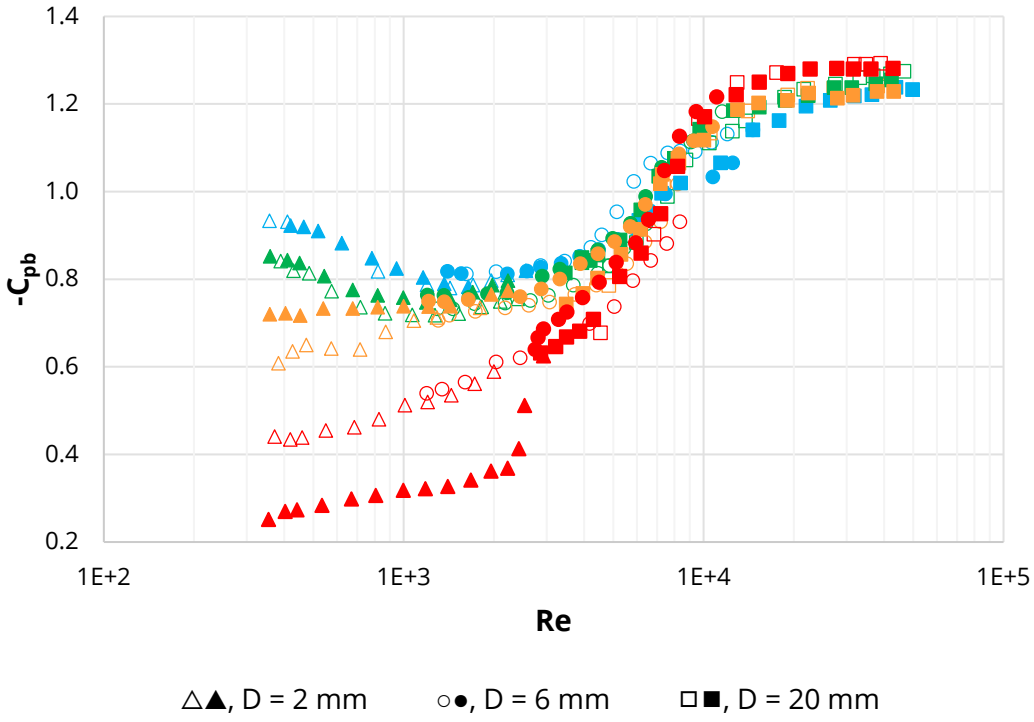

Figure 2-10: Base suction coefficient vs Reynolds number with respect to L/D ratios and D_{EP}/D ratios, replotted from Norberg (1994). Colours (L/D) – Blue = 50, Green = 20, Orange = 10, Red = 5. Symbols (D_{EP}/D) Filled = 10, Open = 15

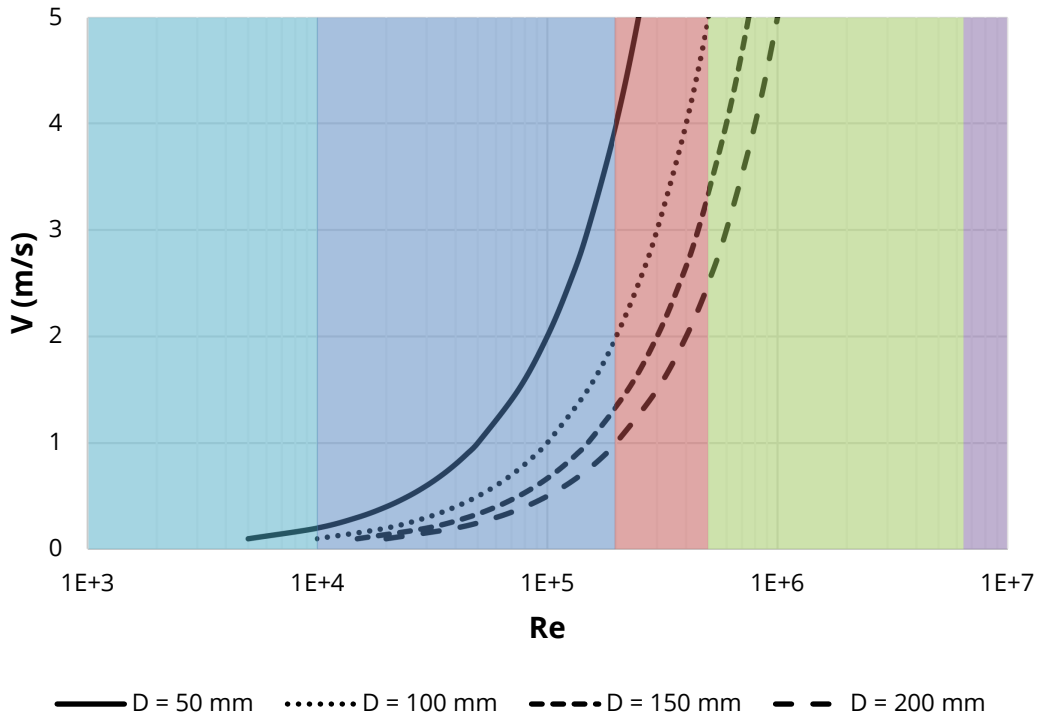

Figure 2-11: Flow velocity vs Reynolds for a variety of practical sized cylinders for water at 20℃, with associated Reynolds flow regimes adapted from Barltrop and Adams (1991)

2.3 PHENOMENON OF VIV

2.3.1 Vortex Induced Vibration (VIV)

The phenomenon of VIV occurs as a result of the frequency of the alternating eddy shedding of a fluid around a bluff body, typically a cylindrical structure (e.g. flexible riser, overhead transmission line, guy wires). The Reynolds number dictates the formation of vortices as previously shown in Table 2-1. VIV is important to consider for long slender structures due to unacceptable fatigue damage from unwanted oscillations.

2.3.2 Drag Amplification Associated with VIV

The maximum crossflow (CF) vibration amplitude (A_y/D_{max}) of VIV motion is limited by the lift coefficient (C_L) to at most A_y/D = 1.0 – 1.1. For an oscillating cylinder, the lift force reaches its maximum value well before the cylinder reaches its point of maximum oscillation displacement amplitude. At this point the lift is zero and reverses, becoming negative at the extreme point of the oscillatory motion cycle, thereby limiting motion amplitude, as shown in Figure 2-12.

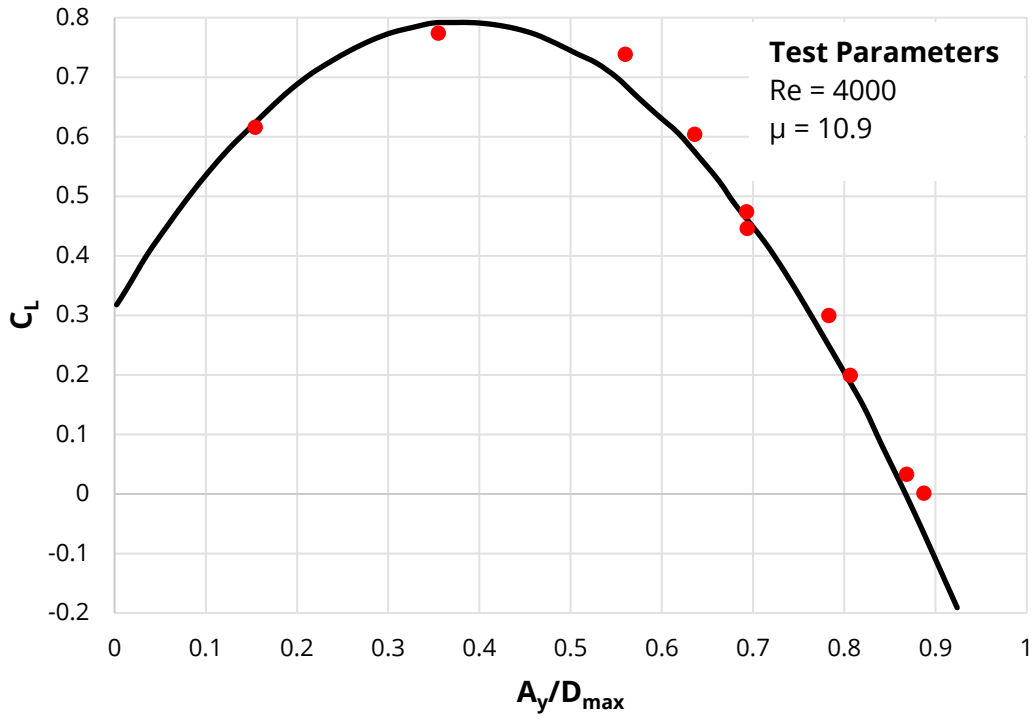

Figure 2-12: Lift coefficient variation as a function of crossflow VIV oscillation amplitude, replotted from Vandiver (2012)

This transverse vibration motion results in an increase in the "apparent" drag cross-sectional area of the cylinder within the flow, whereby with increasing *A*/*D* there is an amplification of total dynamic drag resistance experienced by the structure. Equation 13 from Vandiver (2012) presents the drag amplification from the static drag, as an empirical function of vibration *A*/*D* for bare cylinders.

$$C_{D,Total} = C_{D,Static}(1 + 1.043)\left(2\left(\frac{A}{D}\right)_{rms}^{0.65}\right) \quad \text{Equation 13}$$

Where;

A = Amplitude of oscillation

A/*D* = Non-dimensional amplitude of oscillation with respect to the diameter

Subject to the slenderness and flexural stiffness of the structure, the drag amplification may result in an increased deflection, and may increase fatigue damage due to the steady high frequency vibrations of the structure.

2.3.3 Lock-In Range

Lock-in occurs when the vortex shedding frequency is close to that of the natural frequency (a harmonic mode) of the cylinder and is associated with a significant increase in the vibration amplitude of the cylinder. Lock-in may occur in crossflow, in-line (IL), or both, but typically in crossflow as it is subject to the highest amplitude motions.

Figure 2-13 presents the crossflow displacement amplitude versus the reduced velocity for cylinders in both air and water in what is classically referred to as the typical lock-in for a cylinder in water. It has a range of V_r = 5.5 – 9.0, with the maximum crossflow amplitudes occurring at V_r = 6.0 – 7.5. Potts (2018) states that the broader lock-in range reflects the hydrodynamic added mass effect of the cylinder's acceleration through the fluid.

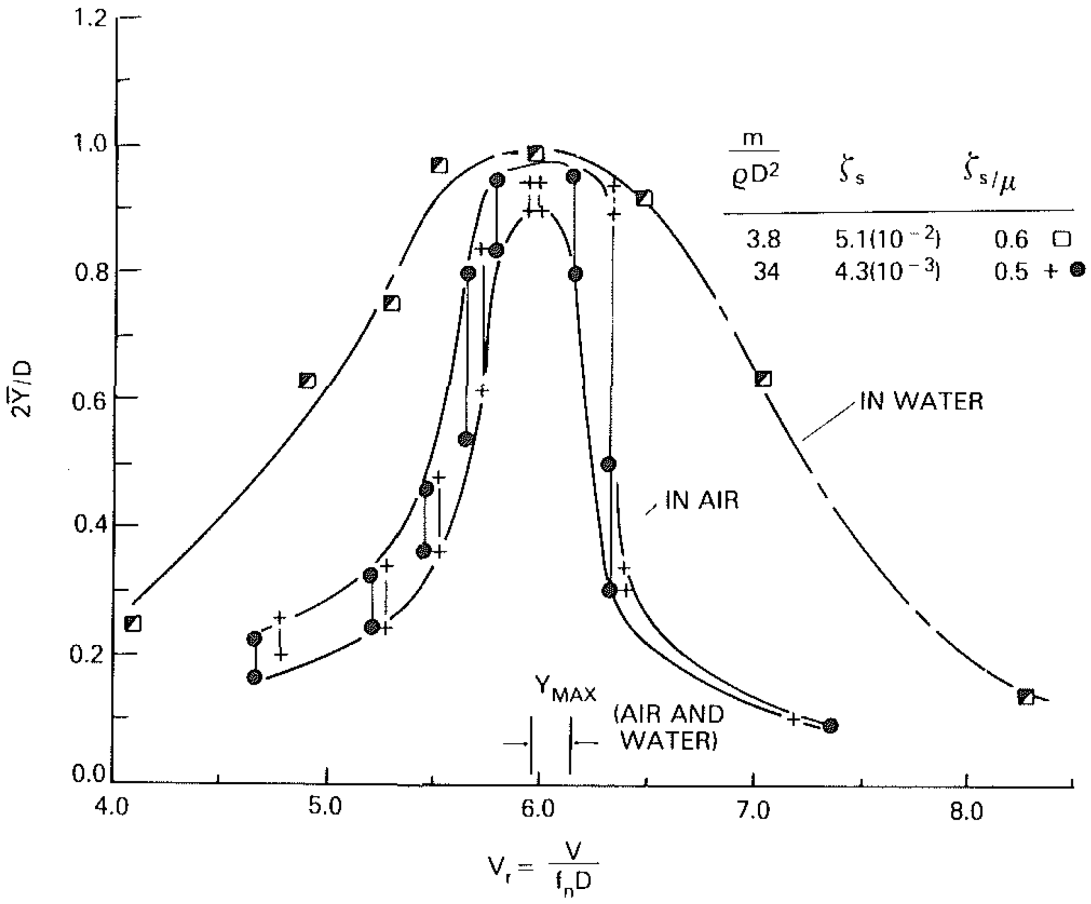

Figure 2-13: VIV cross flow displacement amplitude as a function of reduced velocity for cylinder in both air and water from Griffin and Ramberg (1982)

Figure 2-14 presents bounding curves for both crossflow and in-line oscillation amplitudes as defined by DNV GL (2017a), (2017b) (Det Norske Veritas Germanischer Lloyd). These bounding curves show the vast difference between crossflow and in-line oscillations not only in the amplitude magnitude, but also the reduced velocity range in which lock-in typically occurs.

Figure 2-15 presents a comparison of the peak maximum crossflow VIV oscillations of flexible and rigid cantilevered cylinders for the first eigenmode, from Fujarra et al. (2001). In addition to the test results, the DNV GL CF bounding curve from Figure 2-14 has been plotted. The flexible cantilever has a higher peak oscillation amplitude than the rigid cylinder. There is some disparity between the rigid cylinder data and the bounding curve, primarily in the reduced velocity, which could be due to the data not being completely rigid, but instead having some flexibility or elasticity.

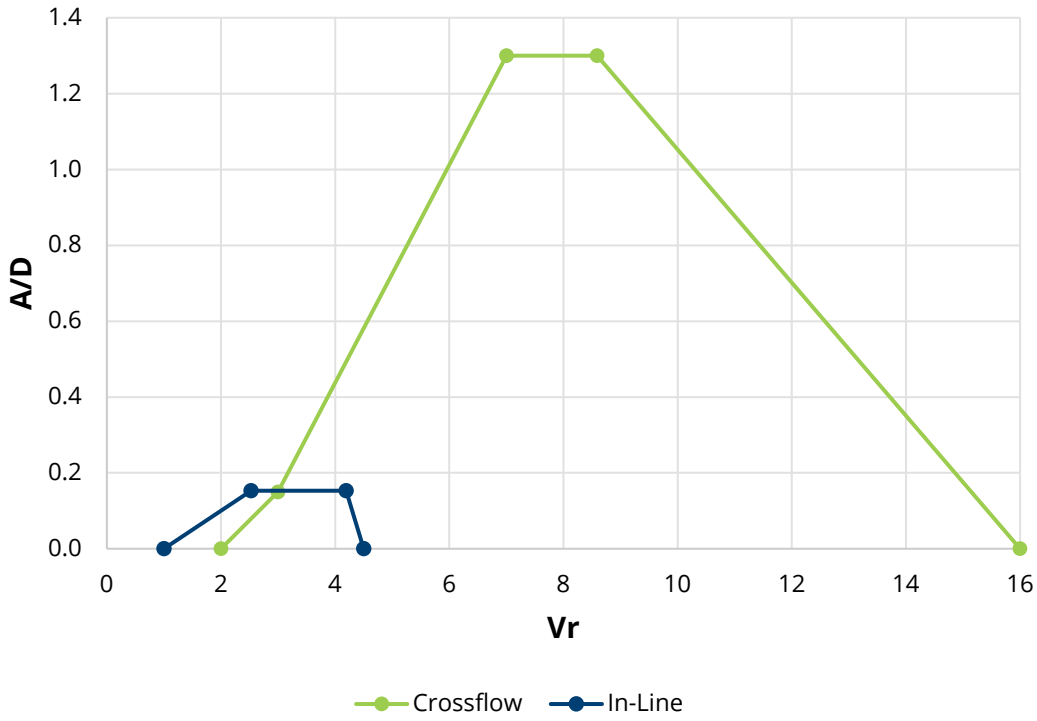

Figure 2-14: Bounding curves for both crossflow and in-line vibration amplitudes, replotted from DNV GL (2017a), (2017b)

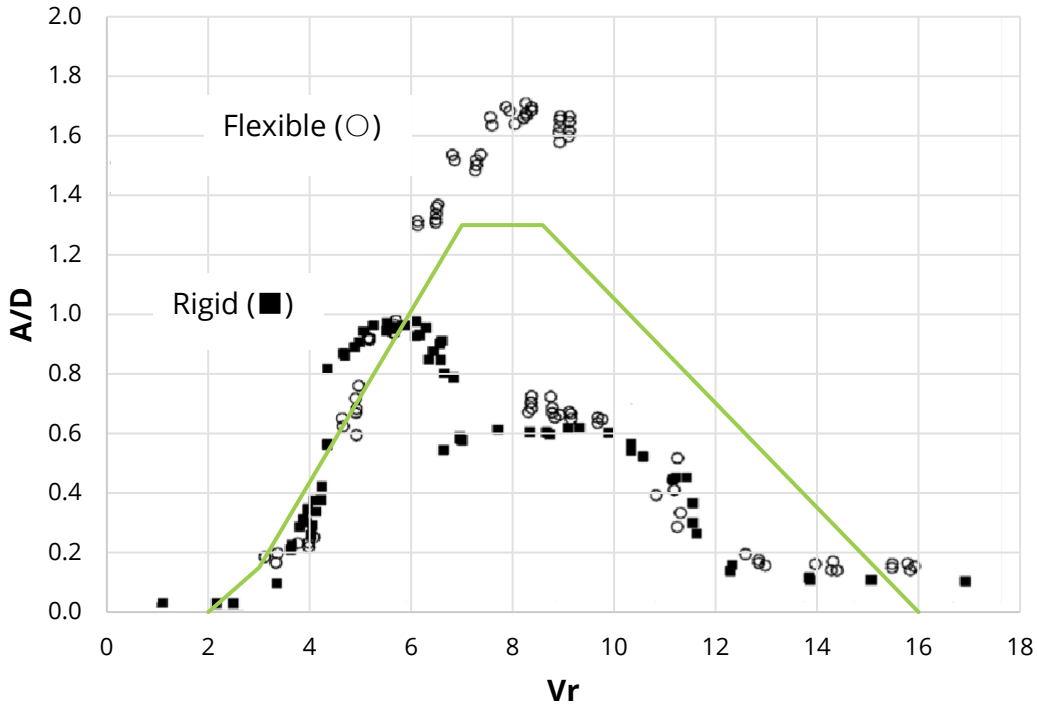

Figure 2-15: Amplitudes vs reduced velocity with the DNV GL bounding curve, after Fujarra et al. (2001)

2.4 Effect of Aspect Ratio (L/D) on Hydrodynamic Drag

2.4.1 Length/Diameter Ratio

The length/diameter or aspect ratio (*L/D*) is a non-dimensional presentation of the finiteness of a surface-piercing cylinder. The *L/D* ratio has an effect on the drag, the wake and the ventilated flow depth; each of these parameters is affected in a different manner dependent on the magnitude of the *L/D* ratio.

The current finiteness of a surface-piercing cylinder can be compared to that of a fully submerged cylinder where the comparison can be made by doubling the infinite *L/D* ratio as per the DNV GL-RP-C205 (2017) stated requirement:

> *For members with one end abuting on to another member or a wall in such a way that free flow around that end of the member is prevented, the ratio l/d should be doubled for the purpose of determining κ. When both ends are abuted as mentioned, the drag coefficient C_D should be taken equal to that for an infinitely long member. — DNV GL (2017b)*

As such, for a cantilevered cylinder with one end abutted to be comparable to a cylinder with both ends abutted, the aspect ratio is to be doubled (i.e. 50 → 100, 100 → 200).

Unfortunately there has yet to be a consistent definition for the *L/D* ratio for an infinite cylinder; the only study to actually define the ratio was DNV GL (2017b), which presents an infinite *L/D* of approximately 200.

The drag coefficient of a cylinder with respect to the *L/D* ratio is the most appropriate method for determining the infiniteness of vertical surface-piercing and fully submerged cylinders. Historically, investigations regarding the determination of an infinite aspect ratio are few and far between, with the most modern source being a revision of a British Standard (BSI (1972)).

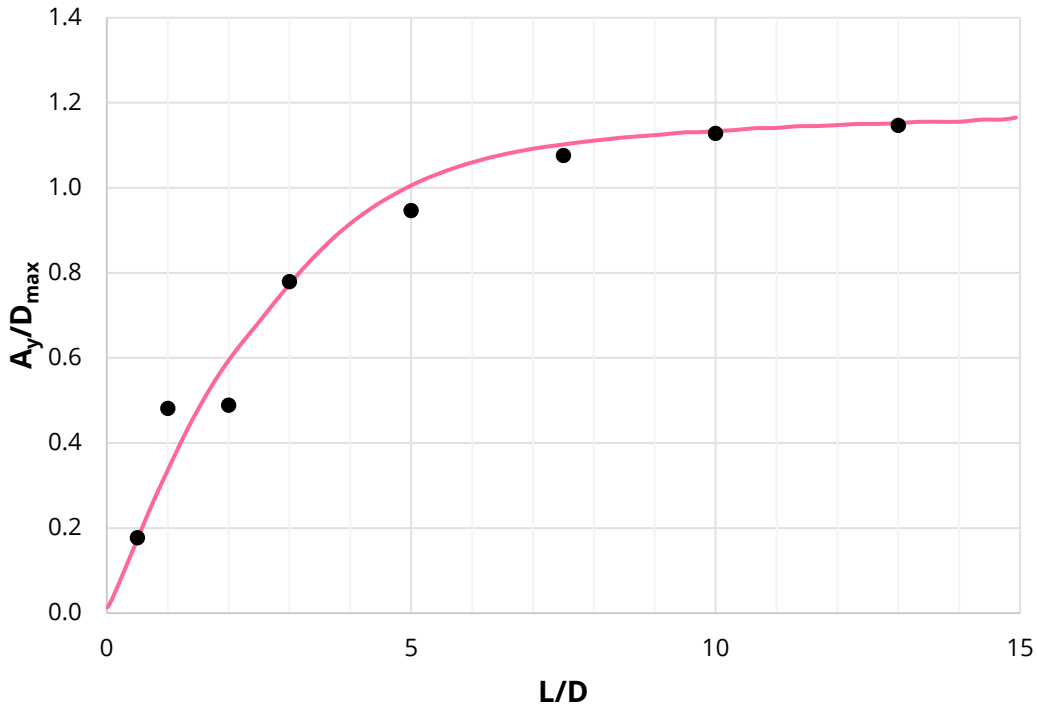

Figure 2-16: Maximum normalised oscillation amplitude against aspect ratio. Results from experimental work, replotted from A Rahman (2015)

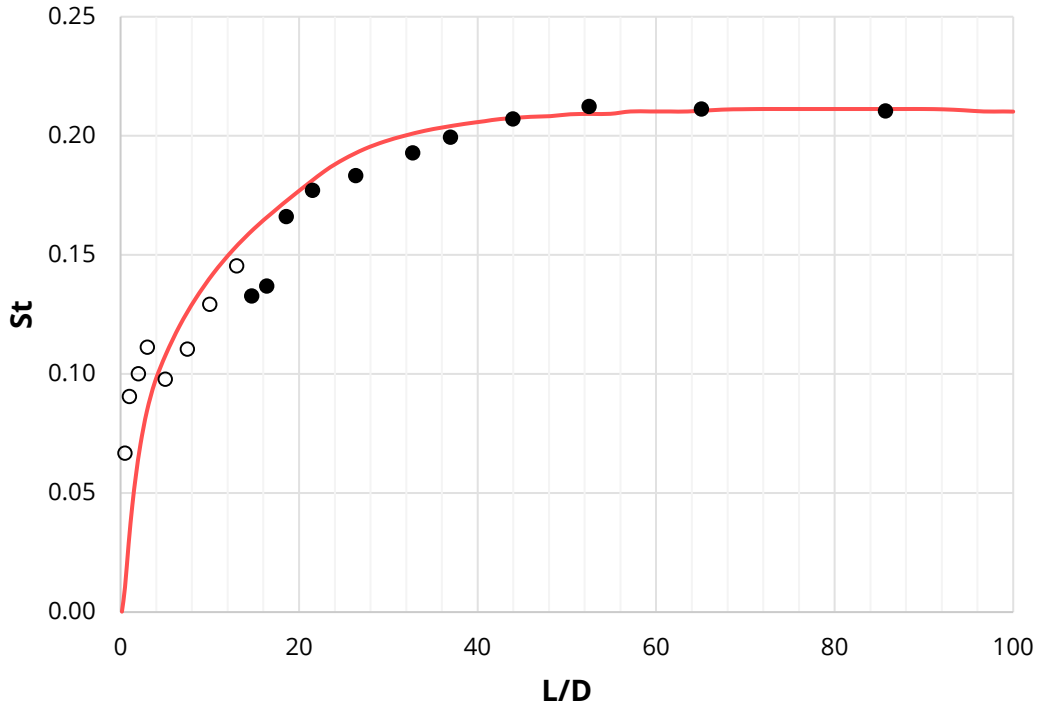

Figure 2-17: Strouhal number against cylinder aspect ratio. Compared with Gowda (1974). The red curve represents a line-of-best-fit relationship of the Strouhal number over the aspect ratio. The value of the Strouhal number proportionally increased and attains a value of the St = 0.2 for high aspect ratio cylinders, replotted from A Rahman (2015)

A Rahman (2015) conducted both experimental and numerical testing of a vertical surface-piercing cylinder across a range of *L/D* ratios. The experimental work consisted of an open-ended PVC pipe cantilevered down through the water free surface, where the cylinder had 1DoF allowing oscillations in the transverse direction.

Figure 2-16 displays the peak amplitude of oscillation as a function of aspect ratio for an elastically mounted cylinder as utilised by A Rahman (2015).

Figure 2-17 presents Strouhal number versus the aspect ratio in A Rahman (2015). The Strouhal number plateaus around an *L/D* of 40. Strouhal number is an analogue of C_D, which is a representation of the coherence of the eddy shedding flow structure and therefore the drag regime of flow around the cylinder. Gowda (1974) conducted a study in a sub *Re* = 1E+4 wind tunnel on cylinders ranging from 3 mm to 18 mm in diameter.

Gowen and Perkins (1953) investigated the drag of circular cylinders for a wide range of Reynolds numbers and Mach numbers using the NACA wind tunnel. Additionally, the effects of the finiteness ratio and the drag coefficient as a function of the distance from the free end of the cylinder were investigated.

The forces and ventilation depth of towed surface-piercing rods (struts) in water was experimentally examined by Perry (1954). Figure 2-18 presents Perry's results, which have been derived from small diameter rods (*D* = 0.25-0.5") at high towing speeds (*V* = 12-20 ft/s), and the results are plotted for the cases where the rod is fully ventilated (i.e. $L_0 = L$). For the 0.25" diameter rod the drag coefficient increases slightly as the aspect ratio increases; this is similarly observed for the 0.5" model, but the increase in the drag coefficient is more substantial.

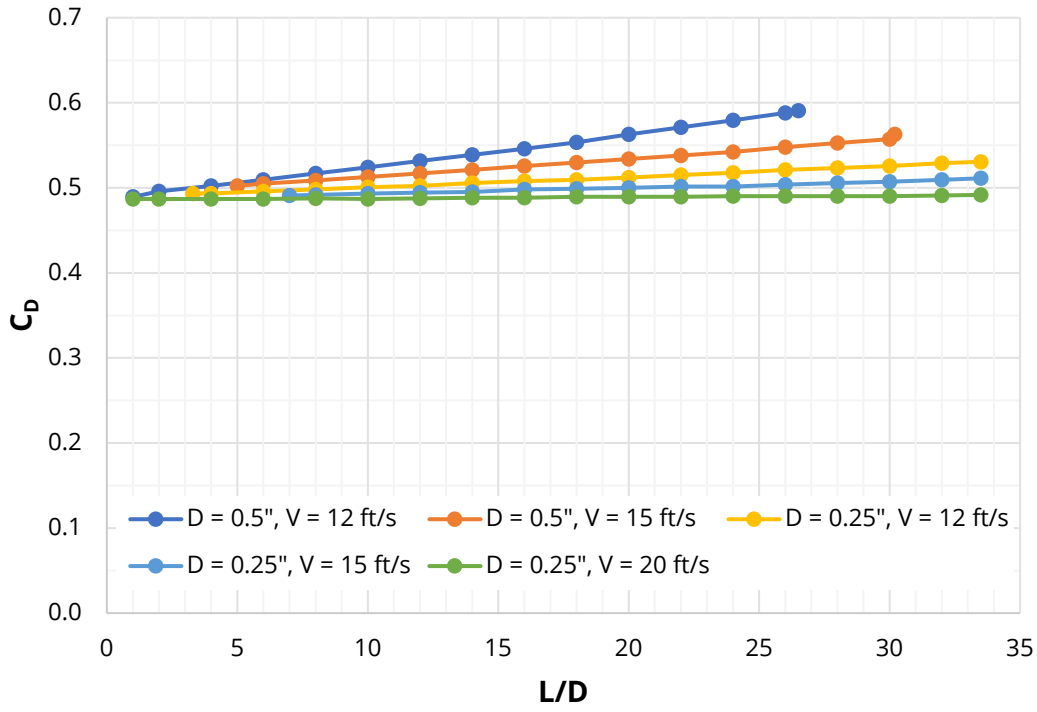

Figure 2-18: C_D vs aspect ratio for fully ventilated flow (L_0 = L), replotted from Perry (1954)

Perry does not discuss why there is an increase in the drag coefficient relative to the increase in aspect ratio, except for simply stating:

> *...as long as the end effects are kept in mind, one sees that the trends are reasonable. — Perry (1954) [p. 12]*

2.4.2 Boundary Layer Effect

For fluid motions, the measured pressure distribution almost agrees with the "perfect fluid" theory, such as the flow past a streamline body or an aerofoil. The influence of the fluid viscosity at high Reynolds numbers is confined to a very thin layer in the immediate neighbourhood of the solid wall. If the no-slip condition was not satisfied in the case of a real world fluid, then there would be no appreciable difference between the flow field of the real fluid as compared with that of a perfect fluid (Schlichting and Gersten (2017)).

Figure 2-19 presents the thickness of a boundary layer (δ) as a function of the flow velocity on a flat plate, where it may be taken to be the same when referring to the bottom of a tank or flume. Frictional forces retard the fluids motion in a thin layer near the wall. Within this thin layer, the fluid's velocity increases from zero at the wall to its full value, which corresponds to the external frictionless layer.

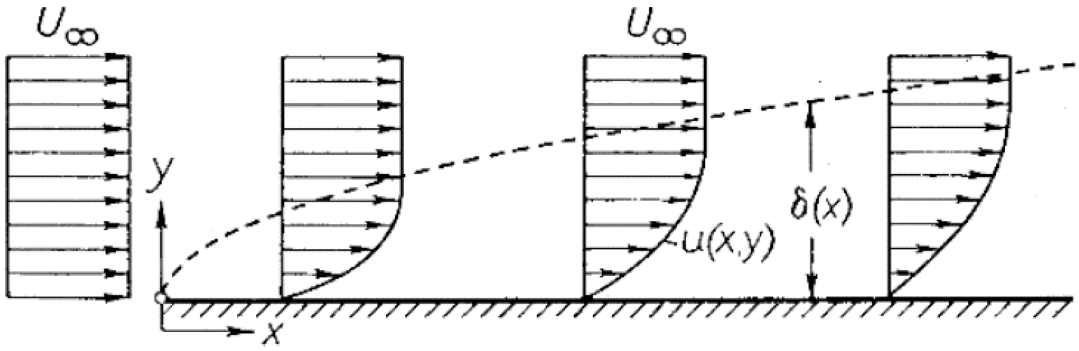

Figure 2-19: Sketch of the boundary layer on a flat plate in parallel flow at zero incidence, from Schlichting and Gersten (2017)

For the following plots Figure 2-20 visually represents the definition of the spanwise segmentation as a function of the length along the cylinder with respect to the free end-tip.

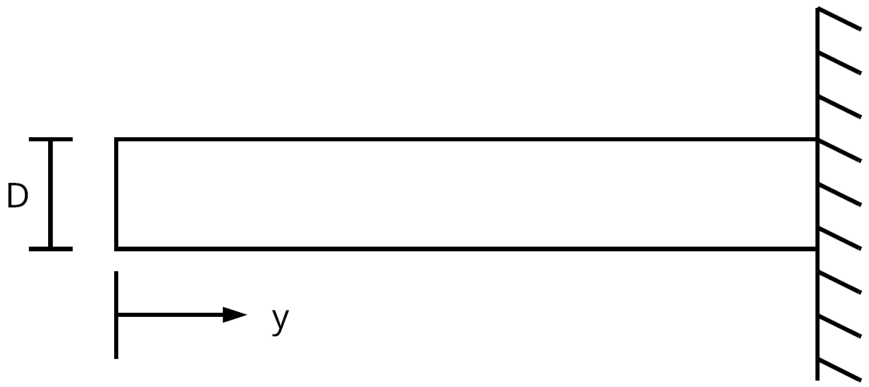

Figure 2-20: Spanwise segmentation of a cylinder with respect to the free end-tip

Figure 2-21 and Figure 2-22 present the segmental drag coefficient along the cylinder from their free end for differing aspect ratios, with data from Okamoto and Yagita (1973) for L/D = 1 – 12.5, and Fox and West (1993a) for L/D = 4 – 23. The resolution of the measurements of the Tip Associated Vortex (TAV) varies between investigators.

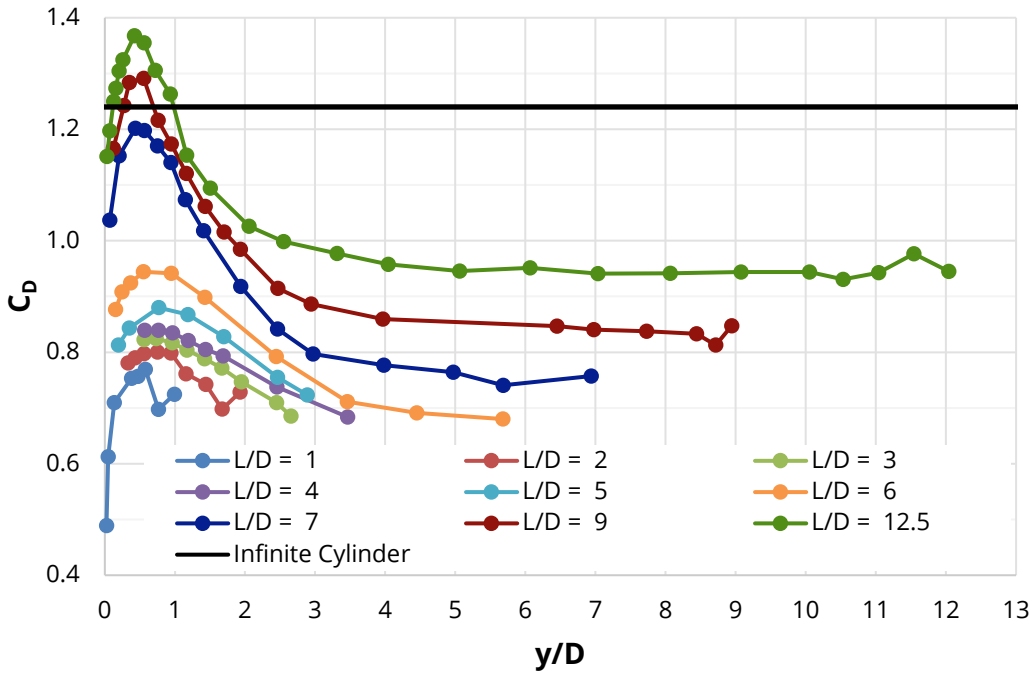

Figure 2-21: Drag coefficient along cylinders for aspect ratios L/D < 13, Re = 1.33E+4, after Okamoto and Yagita (1973)

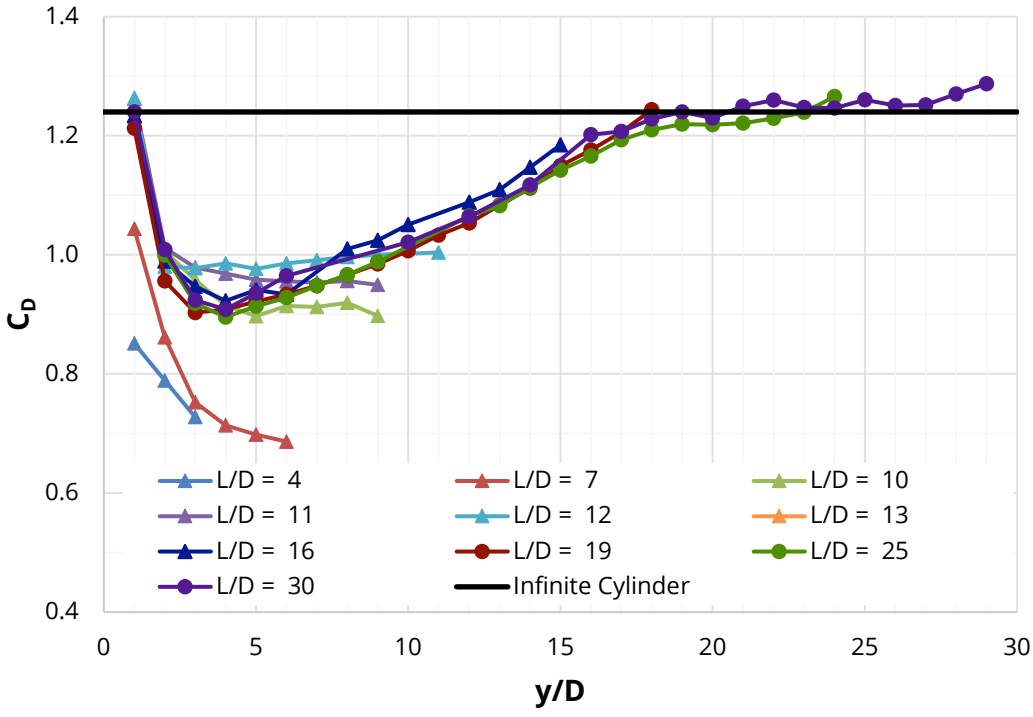

Figure 2-22: Drag coefficient along cylinders for aspect ratios L/D = 4 – 30, Re = 4.4E+4, after Fox and West (1993a)

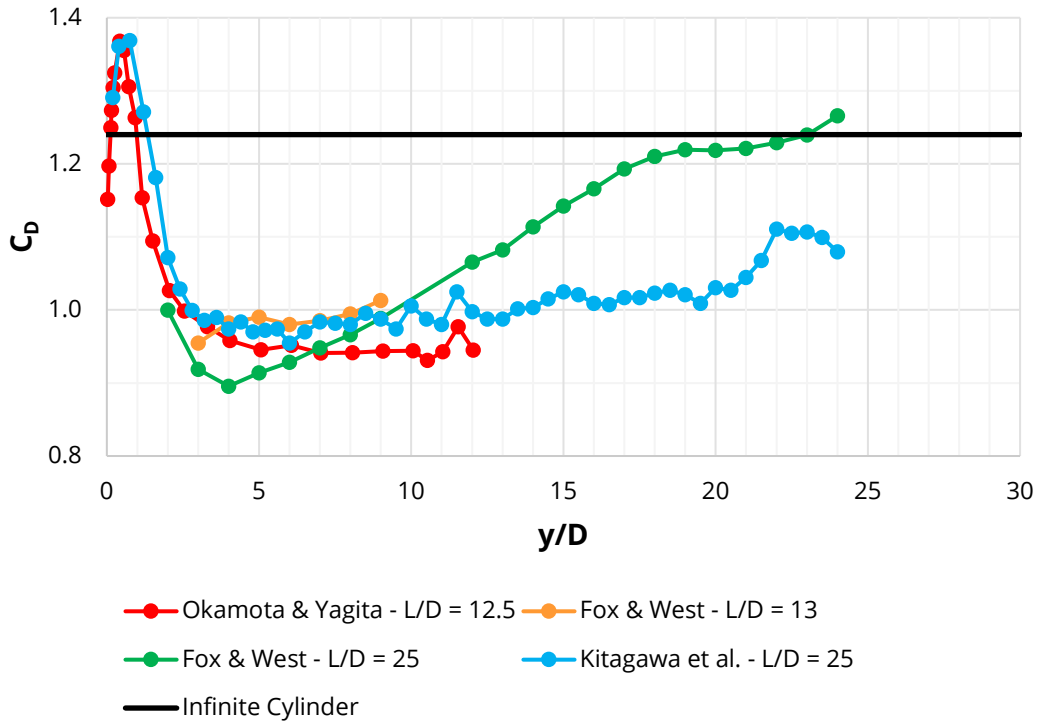

Figure 2-23: Comparison of drag coefficient along cylinder for long aspect ratios, replotted from: Fox and West (1993a) – Re= 4.4E+4; Okamoto and Yagita (1973) – Re = 1.33E+4; Kitagawa et al. (2001) – Re = 2.5E+4

Figure 2-23 compares the segmental C_D values for similar aspect ratios from Fox and West (1993a); Kitagawa et al. (2001); Okamoto and Yagita (1973). The magnitude of C_D is typically dependent upon the aspect ratio, where in this case the Reynolds number is the primary differential factor. The red and orange lines have similar aspect ratios, while the orange line has a higher Reynolds number. The difference in the C_D is approximately 5%, which may be deemed to be negligible. The green and blue lines are quite different, while the aspect ratios are the same. The results from the two authors show completely different drag phenomena. Kitagawa reaches a plateau within 5*D* from the free end at an approximate C_D = 1.0, in contrast the Fox & West data does not reach a plateau, but it does reach an approximate C_D = 1.2. These differences in similar aspect ratios may derive from, either the Reynolds number or a difference in the testing arrangement.

Various investigators have presented comparable plots of segmental (C_{pb}) cylinders from their free end for differing aspect ratios. Numerous infinite cylinder datasets suggest that the base pressure coefficient (C_{pb}) could be employed as a direct analogue for the drag coefficient where $C_D \approx -C_{pb}$. However, Uematsu et al. (1990) found that for cylinders with very short aspect ratios of L/D = 1, 2 & 4, $C_D = -1.4 \bullet C_{pb}$, which suggests that the relationship between these two drag parameters were indeed aspect ratio dependent.

The average spanwise drag coefficient for each aspect ratio may be derived by averaging the segmental (C_D) values over the entire length of the cylinder. The drag reduction factor (κ) is then calculated in accordance with Equation 14, using the infinite value presented by the investigator for that particular dataset, or in the absence of such a value, it was assumed that $C_{D\infty} = 1.2$. For datasets where the segmental drag parameter was not measured to the very tip of the cantilever, a tip value was estimated by extrapolating from the slope of the last two measured values. This latter extrapolation referred to the Fox and West (1993a) data, which largely impacted the shortest aspect ratio results. By way of comparison the drag reduction factor was similarly derived from the measured segmental C_{pb} data, where available.

$$C_{D\,finite} = \kappa * C_{D\infty}$$

$$\kappa = \frac{C_{D\,finite}}{C_{D\infty}} \qquad \text{Equation 14}$$

Figure 2-24 presents the drag reduction factor (κ) as a function of aspect ratio (L/D) derived using both segmental C_D and C_{pb}, and for reference the DNV GL recommended κ is set out in Table 2-2. It is apparent that for aspect ratios of L/D > 13 – 15, the C_D and C_{pb} derived κ values are relatively similar in magnitude and are greater than the design guidance, consistent with both cantilevers with a single free end and the Wieselsberger test data with two free ends.

Table 2-2: Drag reduction factor (κ) for cylinder aspect ratios, from DNV GL (2017b)

L/D	2	5	10	20	40	50	100
κ	0.58	0.62	0.68	0.74	0.82	0.87	0.98

What is most interesting about Table 2-2 is that DNV GL do not have any knowledge as to the location or author of the data from which the table has been derived, Nestegård (2018). The author here has found the first publicly available source of this table, BSI (1972). From investigating the origins of this table, the author found that DNV copied the table and its comments verbatim, from BSI (1972). The BSI does not specify the origins of the table. In the absence of the primary source data/material the application of the findings must be done in a cautious manner, due to the unknown origins.

The thickness of the boundary layer of the incident flow acting on a cylinder (δ) is important as it alters the C_D or C_{pb} measured within the boundary layer, as visible in Figure 2-25.

For aspect ratios of $L/D < 13$ there is a growing disparity between the κ values derived by C_D and C_{pb}. Figure 2-26 presents the ratio of the κ values derived by C_D and C_{pb} as a function of aspect ratio, indicating the strong L/D dependency for short aspect ratios and the ratio of boundary layer height to cylinder diameter (δ/D). For $L/D < 5$, the ratio of C_D/C_{pb} is not constant, but approximately the same order of $C_D = -1.4 \cdot C_{pb}$ as proposed by Uematsu et al. (1990).

The influence of δ/D on the average spanwise drag coefficient on smooth cantilevered cylinders was also investigated by Taniguchi et al. (1981), although their study focused on large boundary layers relative to the cylinder diameter (i.e. $\delta/D = 1 – 5$). Taniguchi found that when correlated with respect to the ratio of the cylinder height to the boundary layer height (L/δ), the drag coefficient conformed to a relatively narrow relationship. Figure 2-25 plots κ values derived by spanwise average C_D values from Kawamura et al. (1984); Taniguchi et al. (1981) for large boundary layers with $\delta/D = 1 – 5$, normalised to L/δ. Figure 2-27 recasts the data from Figure 2-25 normalised to L/D, indicating a high degree of scatter with respect to δ/D for $L/D < 6$.

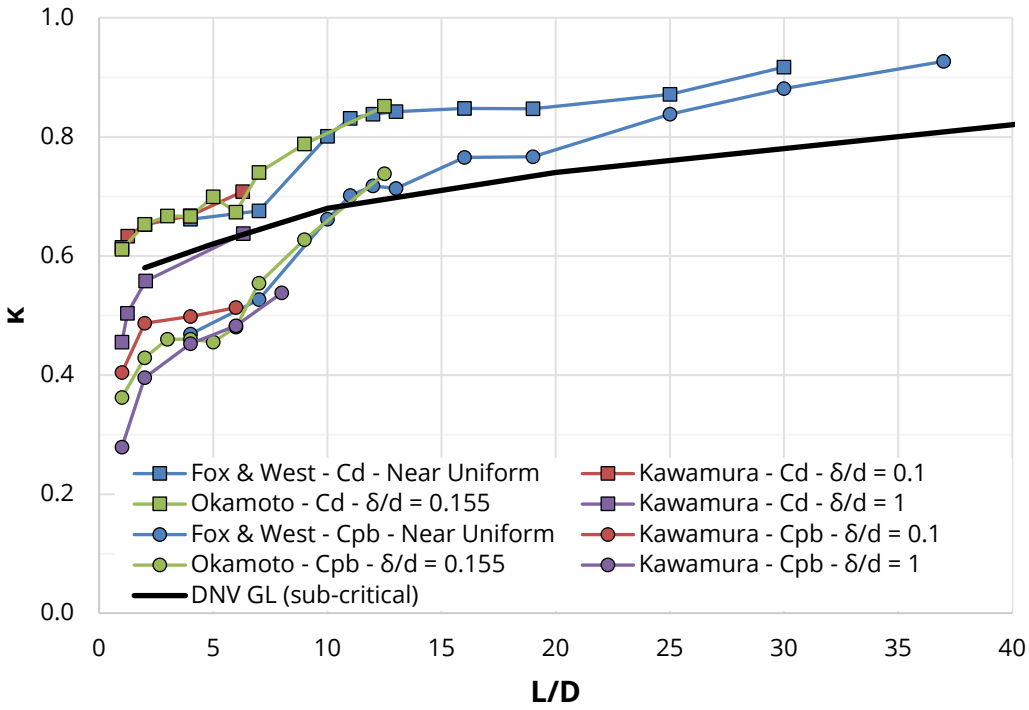

Figure 2-24: Drag reduction factor (κ) for various cylinder aspect ratios (L/D) derived by using measured C_D or C_{pb}, after Fox and West (1993a); Kawamura et al. (1984); Okamoto and Yagita (1973)

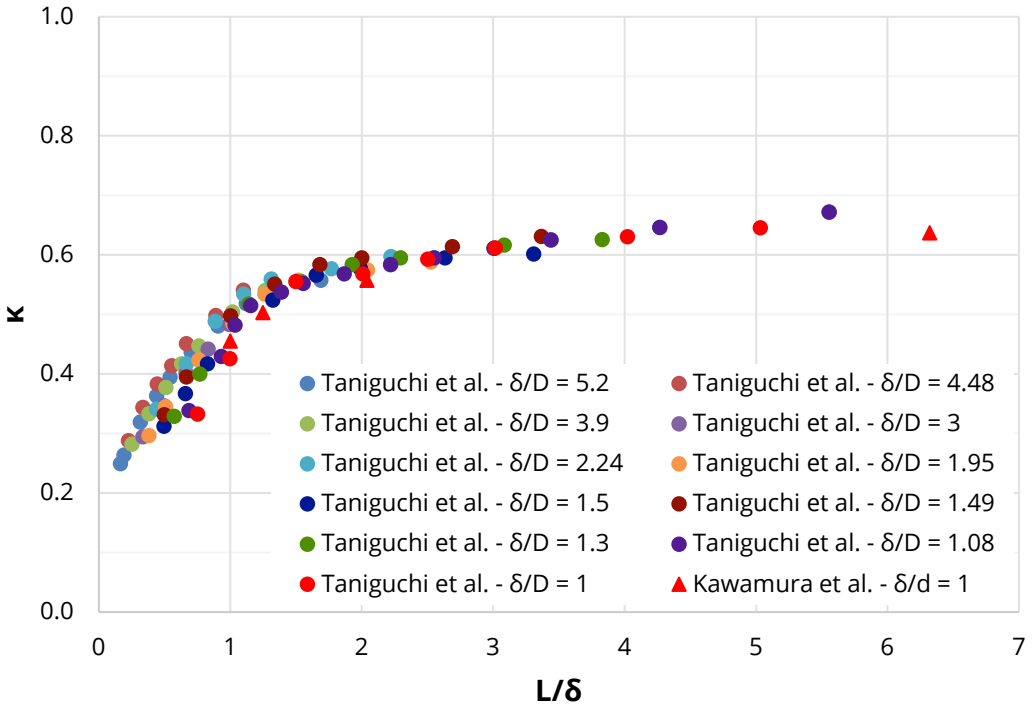

Figure 2-25: Boundary layer dependency of drag reduction factor (κ) with respect to L/δ for δ/D > 1, after Kawamura et al. (1984); Taniguchi et al. (1981)

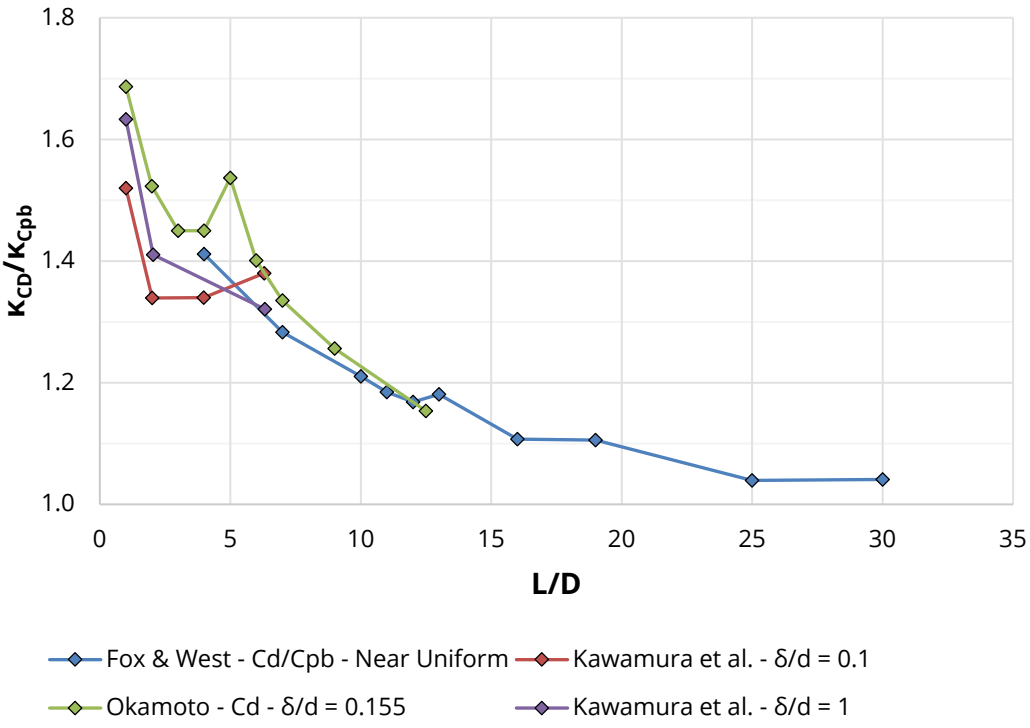

Figure 2-26: Ratio of drag reduction factors (κ_{CD}/κ_{Cpb}) for various cylinder aspect ratios, derived from Fox and West (1993a); Kawamura et al. (1984); Okamoto and Yagita (1973)

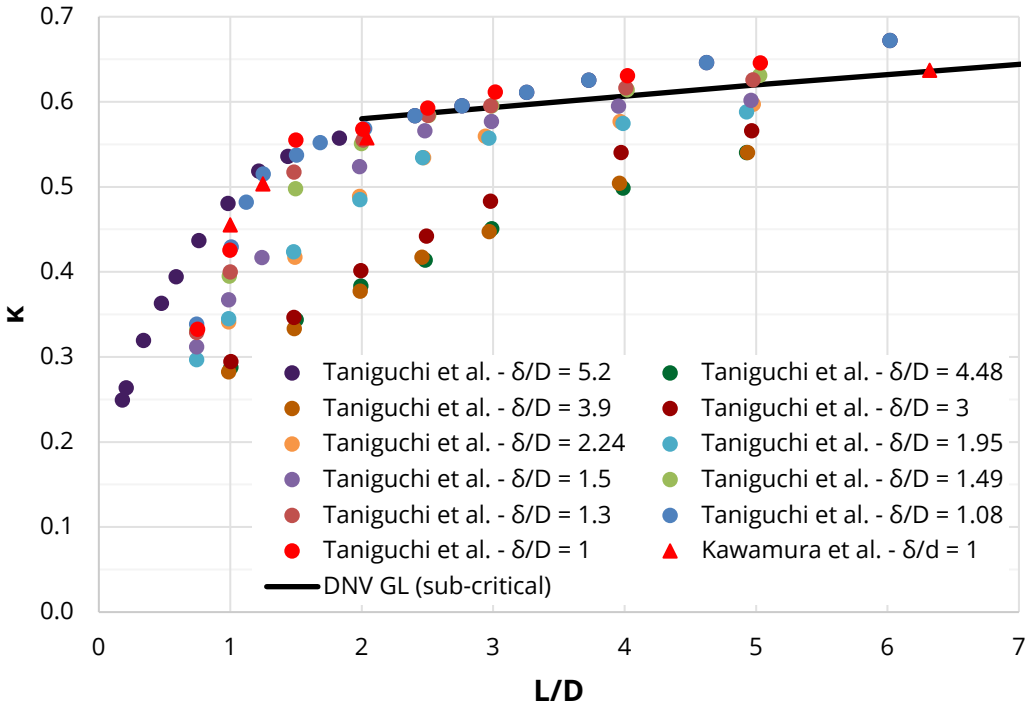

Figure 2-27: Boundary layer dependency of drag reduction factor with respect to the aspect ratio for $\delta/D > 1$, from Kawamura et al. (1984); Taniguchi et al. (1981)

2.4.3 End Condition Effect

The end conditions are significant both in terms of the practical designed circumstances, but also in evaluating and comparing test data from different sources, where the test configurations differ in a manner that will impact on the derived drag coefficient.

The end-tip vortices that are shed from the free end of a cylinder have been studied extensively, including but not limited to Kawamura et al. (1984); Kitagawa et al. (2002), (2001), (1999); Okamoto and Sunabashiri (1992); Rostamy et al. (2012); Sumner (2013); Tanaka and Murata (1999), with a comprehensive summary review paper by Sumner (2013).

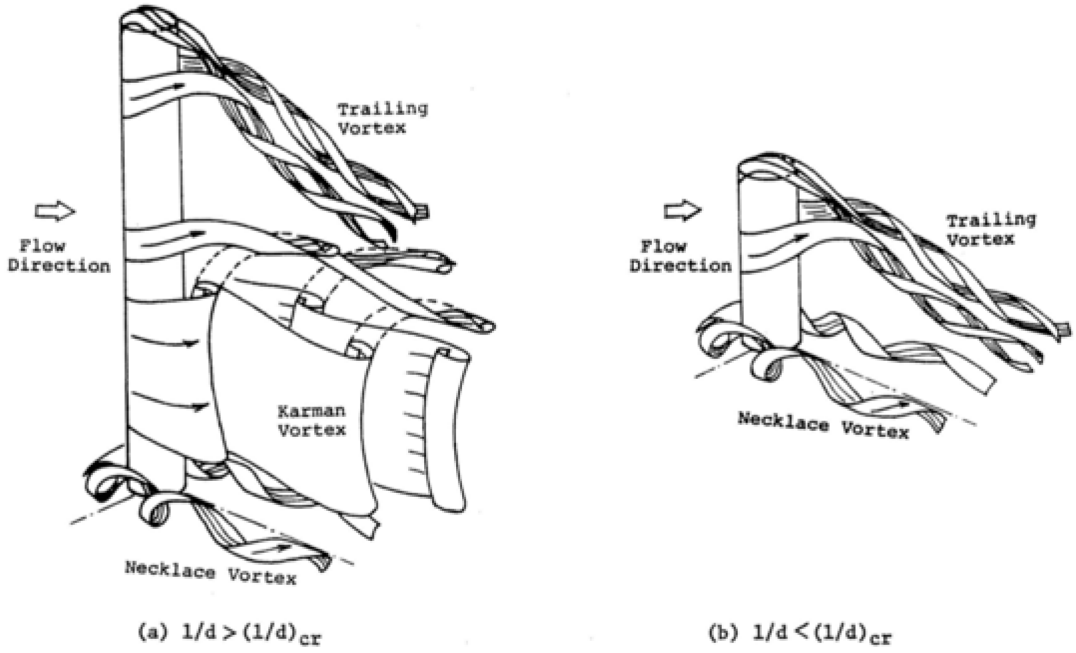

Figure 2-28: Schematic of vortex structures around a cantilever cylinder with a fixed base and free end form, from Kawamura et al. (1984)

Figure 2-28 from Kawamura et al. (1984) presents a schematic of the vortex structure on a cantilevered cylinder indicating two dominant regimes defined by the critical aspect ratio $(L/D)_{crit}$, where this ratio is a function of the height of the boundary layer relative to the diameter of the cylinder (δ/D). For very low values of (δ/D circa < 0.2), the boundary layer is largely inconsequential compared to uniform flow, whereby the $(L/D)_{crit}$ = 5 – 6. Once below the $(L/D)_{crit}$ threshold the entire length of the cantilever is dominated by the trailing wake of the end-tip vortex, and by the necklace (or horseshoe) vortex formed around the base of the cylinder.

For aspect ratios greater than the $(L/D)_{crit}$ threshold, an alternately shedding von Karman vortex street is formed along the body of the cylinder between the end-tip vortex structure at the free end and the necklace vortex at the base. The von Karman vortex street is consistent with the vortex structure along an infinite 2-D cylinder, for a rigid cylinder shedding at a Strouhal Number St = 0.2. A cylinder exhibiting von Karman vortex street formation increases in length with increasing aspect ratio, whereby at very large aspect ratios, the TAV has a relatively small impact on the average drag loading on the cylinder.

For a multi-fluid surface-piercing cylinder the above discussed horseshoe vortex forms at the surface boundary between the two fluids, which pushes the water up the cylinder as the free-stream velocity increases, thereby creating the bow wake.

The design guidance from BSI (1972) and DNV GL (2017b) advise that having both ends abutted is sufficient to remove the effects of the end-tip vortex, whereby the $C_{D\infty}$ is appropriate. However, the dimensions of the detail or end arrangement that sufficiently supress the end-tip vortex effect with a free end are not addressed in either guidance note.

For instance, a beam or column spanning a gap between walls has both ends abutted, but as is evident from wind tunnel test data for cantilevers (Apelt and Fox (1992); Etzold and Fiedler (1976); Fox and Apelt (1993); Fox and West (1993a), (1993b); Kitagawa et al. (2002); Okajima et al. (2004); Uematsu et al. (1990)), the turbulent boundary layer that may develop along those end walls will increase δ and thus impact on the C_D due to the relative influence of δ/D = 1 – 5 and L/δ (Figure 2-27).

Various investigations into the effect of end-plates on the drag loading of a cylinder (measured as C_D and/or C_{pb}) with respect to aspect ratio (L/D) have been reported by Fox and West (1990); Kitagawa et al. (2001); Norberg (1994); Szepessy and Bearman (1992). In these investigations the end-plate was typically defined with respect to the diameter of the test model (D_{EP}/D), where D_{EP} is the diameter of the end-plate. Szepessy & Bearman and Fox & West employed asymmetric rectangular end-plates as recommended by Stansby (1974) which has an effective $D_{EP}/D = 7$. Each study measured the effect on the lengthwise segmental drag, with Szepessy & Bearman measuring C_D and Fox & West C_{pb}. Norberg measured the midspan C_{pb} across a range of cylinders with aspect ratios from $L/D = 4 – 70$, with end-plates of two diameters, $D_{EP}/D = 10$ and 15. As such, Norberg was measuring the effect of the end-plates on interfering with the midspan drag regime and identifying the critical short aspect ratios.

By way of comparison, the tow tank tests by Eisner (1929) of a fully immersed horizontal smooth cylinder spanning between large end-plates with the largest cylinder had an $L/D = 3$ with an effective $D_{EP}/D = 3$.

Figure 2-29 from Norberg (1994) shows a fully submerged cylinder with end-plates some 10 times the cylinder diameter. The L/D ratio has been varied and it can be seen that the vortex shedding is different for the three L/D ratios. Thus, the L/D ratio does have an effect on the vortex shedding and therefore the VIV excitation.

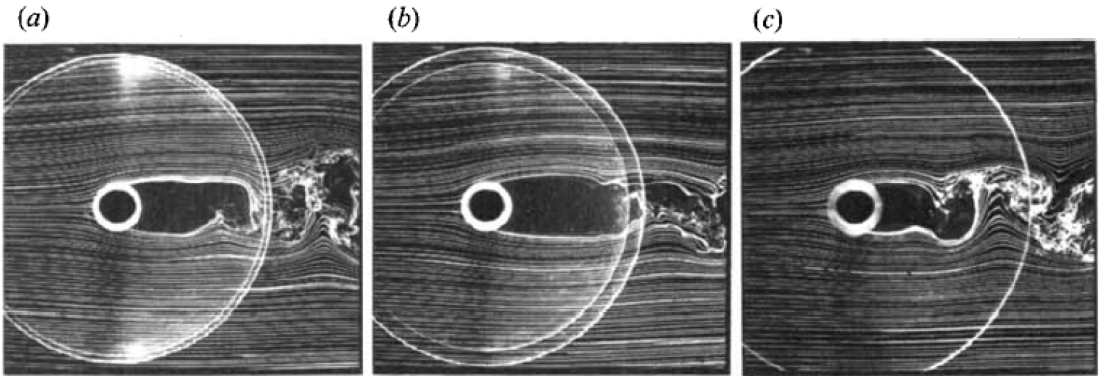

Figure 2-29: Smoke-wire visualisations for (a) L/D = 2, (b) L/D = 5, (c) L/D = 15. (Re = 3E+3, D = 20 mm, $D_{EP}/D = 10$), from Norberg (1994)

Figure 2-30 plots the spanwise drag reduction factor (κ) derived from the measured data in the referenced papers. It is presented with respect to the aspect ratio for 2-D cylinders between two end-plates of diameters varying from D_{EP}/D = 3 – 15D, for aspect ratio L/D < 15. Where κ = 1, this indicates that the TAVs have effectively been suppressed at this aspect ratio for the respective end-plate diameters, and it is evident that the aspect ratio at which this occurs is dependent upon the end-plate diameter ratio and ranging from L/D = 3 – 6.

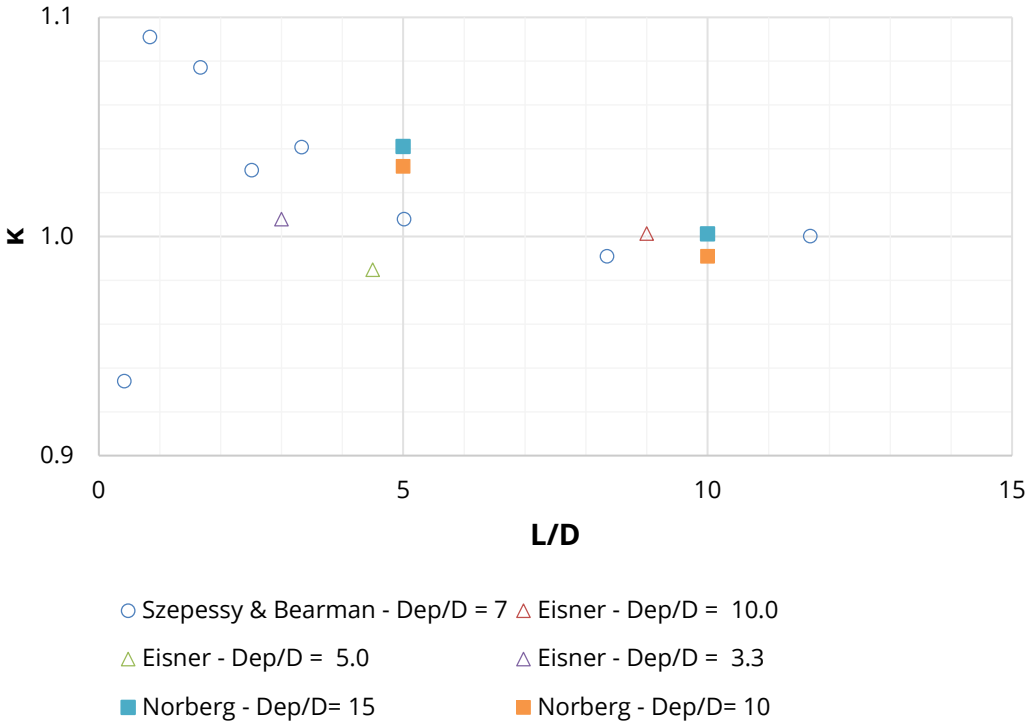

Figure 2-30: End-plate effects on drag reduction factor with respect to the aspect ratio, after Eisner (1929); Norberg (1994); Szepessy and Bearman (1992)

Kitagawa et al. (2001) fitted disc-like end-plates of various diameters (D_{EP}/D = 1.1, 1.2, 1.4, 1.6 and 1.8) to a cantilever of L/D = 25 (closed end data presented in Figure 2-23).

The segmental C_D values for the uppermost 5D of the cylinder for differing D_{EP}/D values have been plotted in Figure 2-31, which have been normalised with respect to the value at y/D = 5D. Also presented are the Fox & West segmental C_{pb} values for a D_{EP}/D for the 5D adjacent to the end-plates for 2-D spans of L/D = 7 – 35, which have been normalised to the value at y/D = 5D. These normalised values have then been averaged over the 5D end length, so as to derive an effective drag reduction factor (κ_{end}), which has been plotted as a function of the D_{EP}/D ratio in Figure 2-32. Also included in the plot are the data points from Figure 2-30 for κ = 1. The curve fitted to the data indicates that end-tip vortices can be suppressed with end-plates of diameter D_{EP}/D > 3, however larger end-plates induce a blockage effect between the end-plates, thereby requiring a larger aspect ratio to return to a κ = 1.

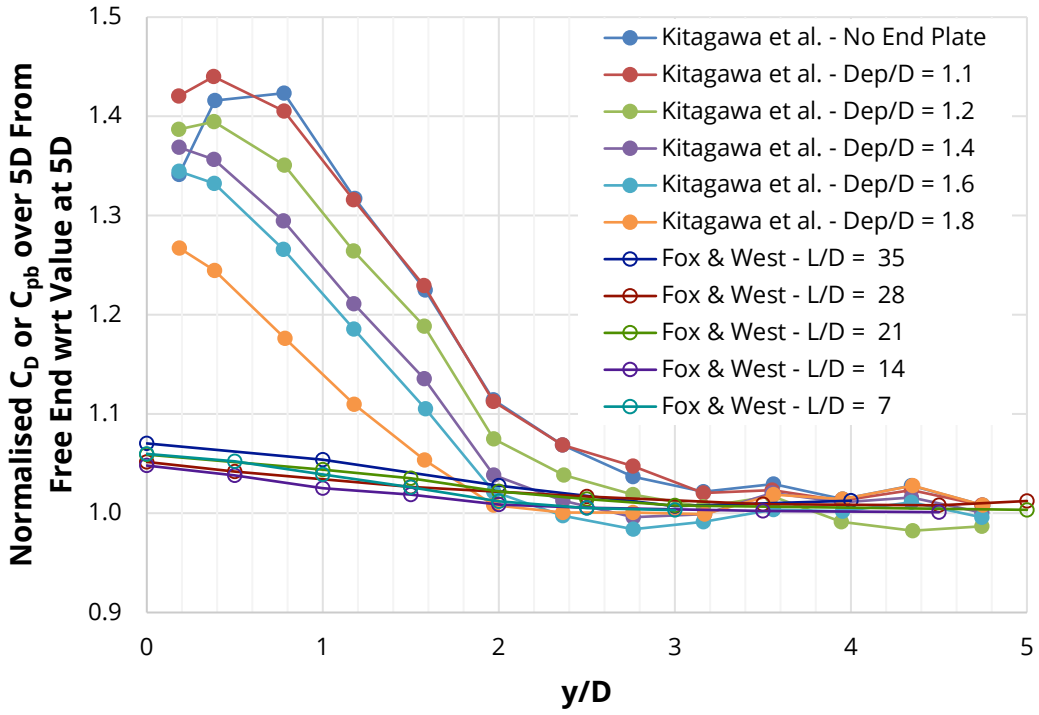

Figure 2-31: End-plate diameter effects on drag within 5D of the end-tip, after Fox and West (1990); Kitagawa et al. (2001)

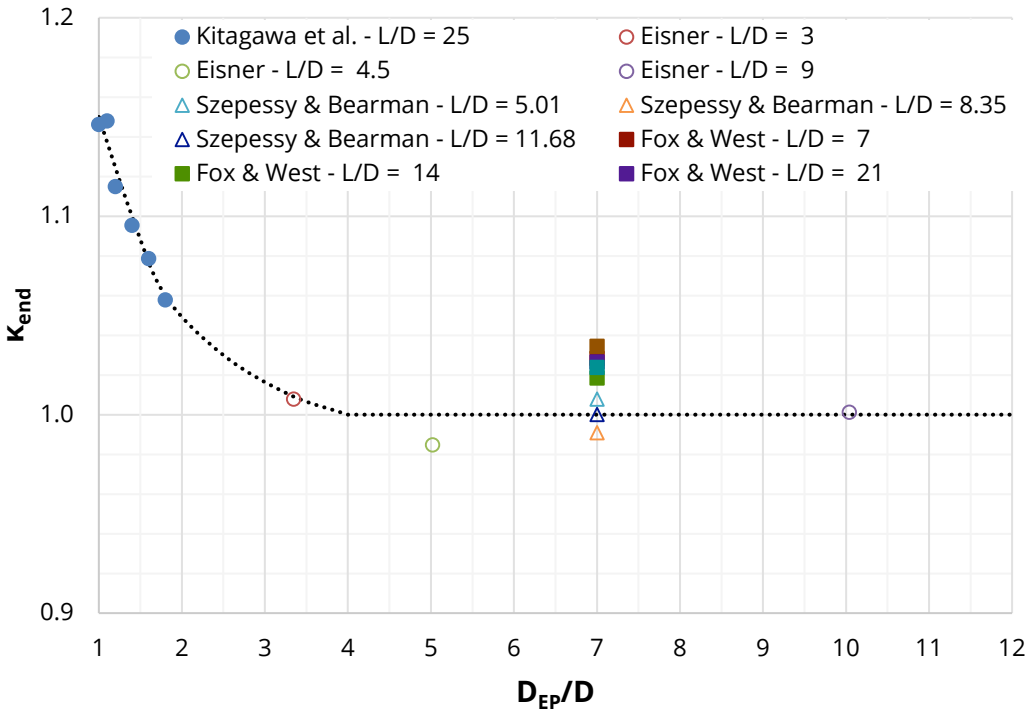

Figure 2-32: End-plate diameter effect on drag reduction factor within 5D of the end-tip, after Eisner (1929); Fox and West (1990); Kitagawa et al. (2001); Szepessy and Bearman (1992)

2.4.4 Drag Reduction Factor

Figure 2-33 from Gowen and Perkins (1953) is a representation of the drag proportionality factor, η (drag reduction factor, κ), as a function of the L/D ratio. When $\eta = 1$ a cylinder is considered to be infinite, where the $C_D = 1.2$. In this instance it seems only to be the case for the supersonic Mach number test series when $L/D = 8$. The results from the subsonic tests were much lower and reach a maximum drag proportionality factor of 0.92 at an L/D of 60.

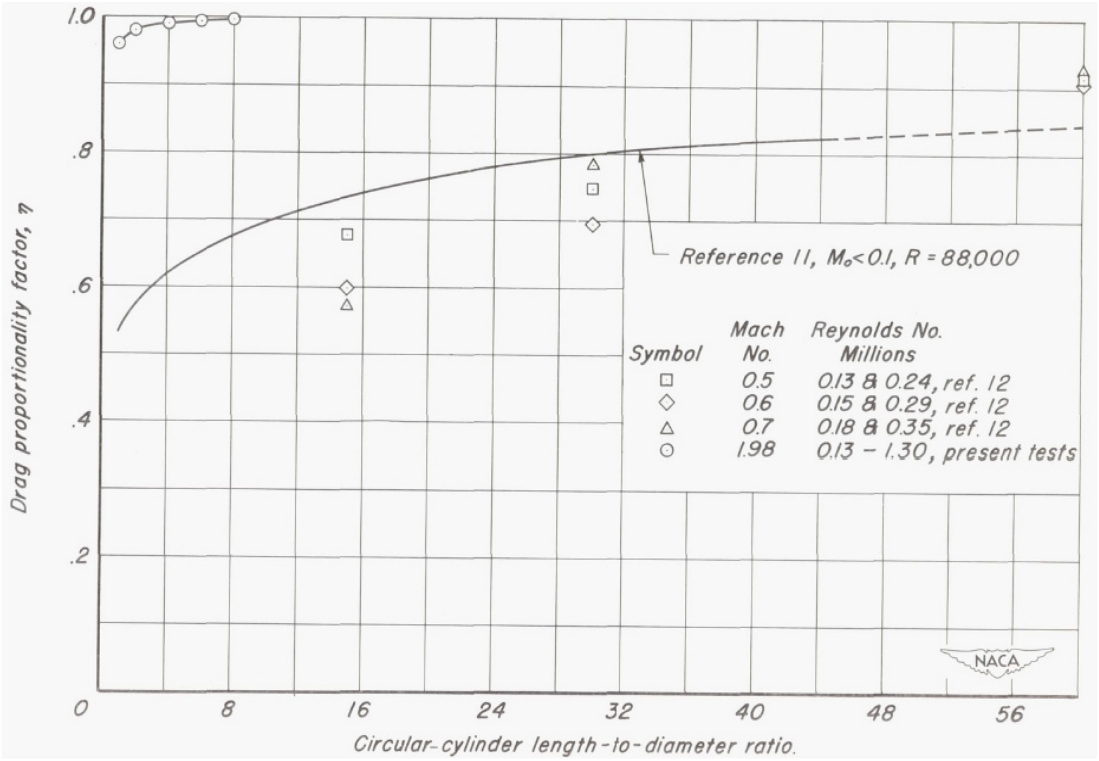

Figure 2-33: Ratio of the drag coefficient of a circular cylinder of finite length to that of a cylinder of infinite length (η) as a function of length-to-diameter ratio, from Gowen and Perkins (1953)

DNV GL (2017b) presents the reduction factor due to finite length, where the reduction factors have been determined for a circular cylinder in both sub-critical and super-critical flow, and for a flat plate perpendicular to the flow. Referring back to Table 2-2, which presented the reduction factors to be applied to the drag coefficient for certain *L*/*D* ratios. The aspect ratio values presented relate to fully submerged cylinders.

The drag reduction factors from DNV GL for both the sub-critical and super-critical flow conditions for a cylinder of infinite length as a function of the *L*/*D* ratio are presented in Figure 2-34, where each date series has been plotted with a power law LoBF. DNV GL does not cite any reference material which supports the origins of the data presented.

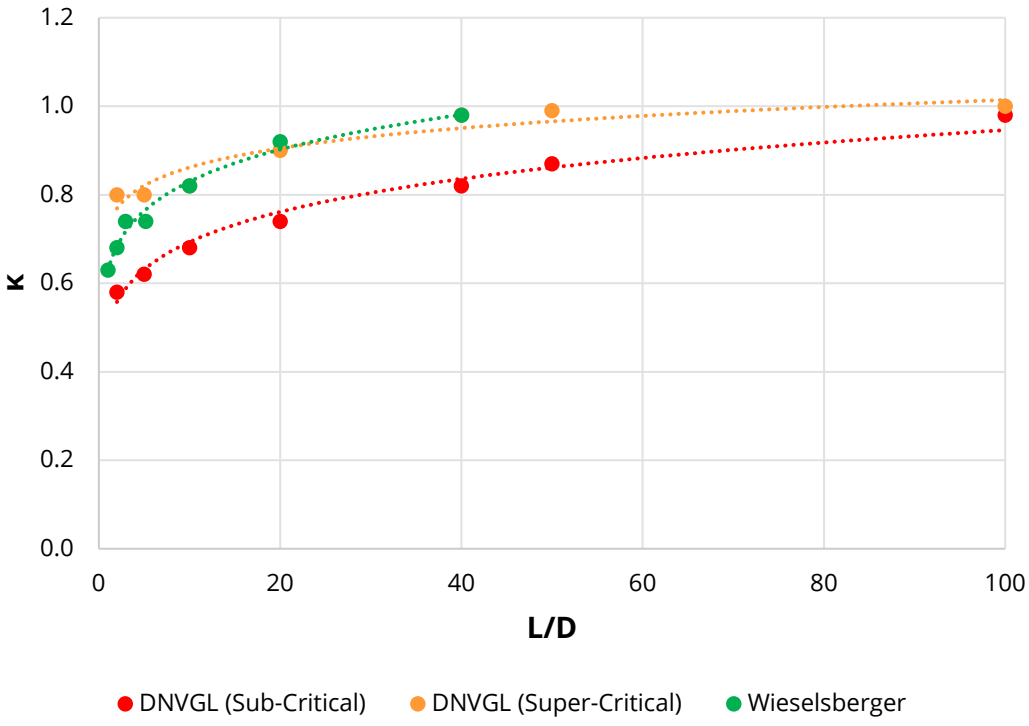

Figure 2-34: Drag reduction factor after DNV GL (2017b) and Wieselsberger (1921)

Figure 2-34 presents the reduction factor versus the *L*/*D* ratio from DNV GL (2017b); Wieselsberger (1921). The Wieselsberger data presented here is the same as the solid line presented in Figure 2-33. (**NB:** To convert from C_D to κ, a factor $C_{D\infty}$ of a fully submerged cylinder (1.2) must be applied, as per Equation 14).

Figure 2-35 is the graphical representation of the data in Table 2-3 with the addition of the Wieselsberger curve. This plot depicts the old and new formulations regarding the aspect ratio at which a fully submerged cylinder may be considered infinite in length for the conditions of two free ends and cantilevered.

The blue line in Figure 2-35 derives a curve for a cylinder with two free ends (Equation 15), whereby for the same κ the $(L/D)_{\text{free ends}} = 2 \cdot (L/D)_{\text{cantilever}}$. This is also shown in comparison with the Wieselsberger data points and demonstrates poor correlation to the proposed DNV GL curve.

$$\kappa_{cantilever} = 0.583 \left(\frac{L}{D}\right)^{0.14} \qquad \text{Equation 15}$$

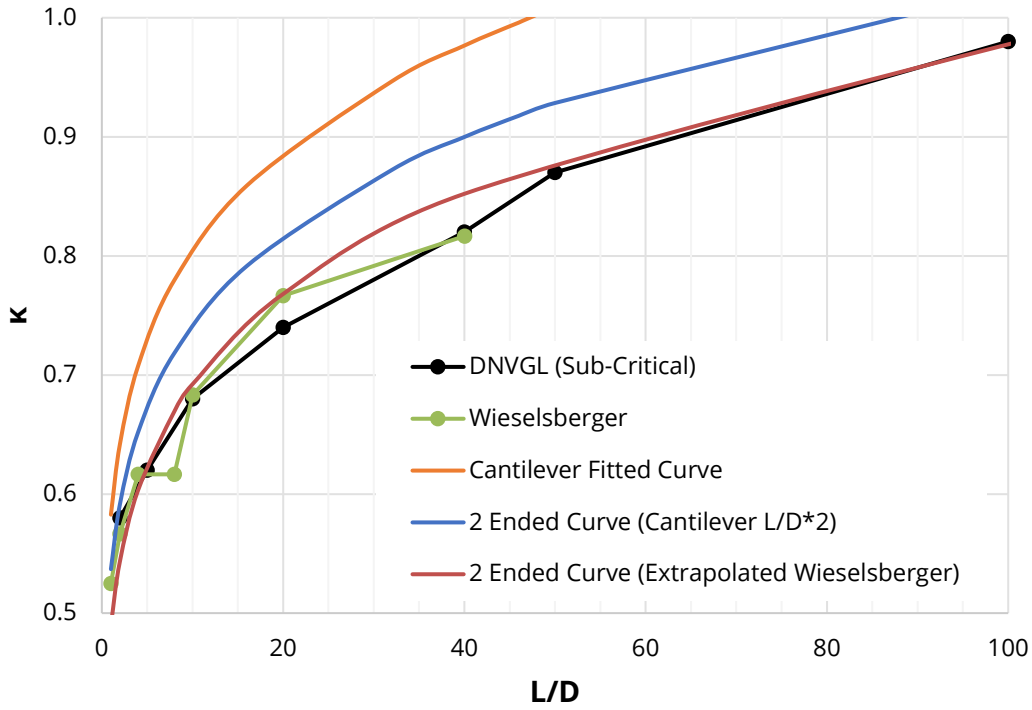

Figure 2-35: Drag reduction factor (κ) with respect to aspect ratio (L/D) fitted to cantilever cylinders in near uniform flow

The red curve is a log-log regression fit extrapolated through the Wieselsberger data, as described by Equation 16. This results in a slight departure from the $DNVGL_{(sub\text{-}critical)}$ values, which is presented as the black line in Figure 2-35.

$$\kappa_{2_{ended}} = 0.49\left(\frac{L}{D}\right)^{0.15} \qquad \text{Equation 16}$$

The above original analysis of the literature covers wind tunnel test results on the drag on cantilevers of varying aspect ratios in uniform flow, or near uniform flow in the sub-critical Reynolds flow regime. Table 2-3 summarises these findings for cylinder with one free end and two free ends and suggests an alternate relationship for the drag reduction factor for cantilevered cylinders.

Table 2-3: The drag reduction factor (κ) for cylinders with one or two free ends, including the recommended design values from DNV GL (2017b)

L/D		2	5	10	20	40	50	100
κ	**Cantilever 1 Free End**	0.64	0.73	0.80	0.89	0.98	1.00	1.00
	2 Free Ends	0.54	0.62	0.69	0.77	0.85	0.88	0.98
	Current Code 2 Free Ends	0.58	0.62	0.68	0.74	0.82	0.87	0.98

2.5 HYDRODYNAMIC WAKE

2.5.1 General Properties and Definitions

Wake is typically defined as:

- The water surface or pattern downstream of an object subject to fluid flow or created by an object moving through/on the water (e.g. a ship, ducks). Surface wake is caused by the difference in fluid density both above and below the free surface and gravity (Thomson (1880)).
- The relative motion of an obstacle in the flow and is the region of retarded fluid behind the obstacle, including any vortices, shear layers, and regions of separated flow.

Hay (1947) is the seminal source paper on the subject of hydrodynamic wake of a vertical surface-piercing cylinder. Hay conducted a series of tow tank tests to quantify the resistance applied to an open-ended cylinder when towed through a still water surface. The testing conducted by Hay comprised several different cylinder diameters (D) ranging from 1/8" to 8", and different submerged lengths (L), with set L/D ratios varying from 1 to 32. Both the cylinder diameters and L/D ratios were incrementally increased in stepped ratios of 2.

The hydrodynamic wake is dependent on several cylinder parameters: velocity, diameter, and submerged depth. When investigating the hydrodynamic wake for surface-piercing cylinders, the author has chosen to adopt the terminology as described in Hay (1947), with the Hay definition of hydrodynamic wakes differing from the Kelvin (gravity) wave definition above.

Figure 2-36 presents the Hay hydrodynamic wake definitions, in which he captured and analysed extensive photographic images of the wake effects generated by the submerged cylinder at different tow speeds, including: bow wave height (D_1); height and location of the peak of trailing wake (D_2 & L_2); and height and length of trailing wave (D_3 & L_3) generated by the ventilated pocket shedding from the bottom of the cylinder.

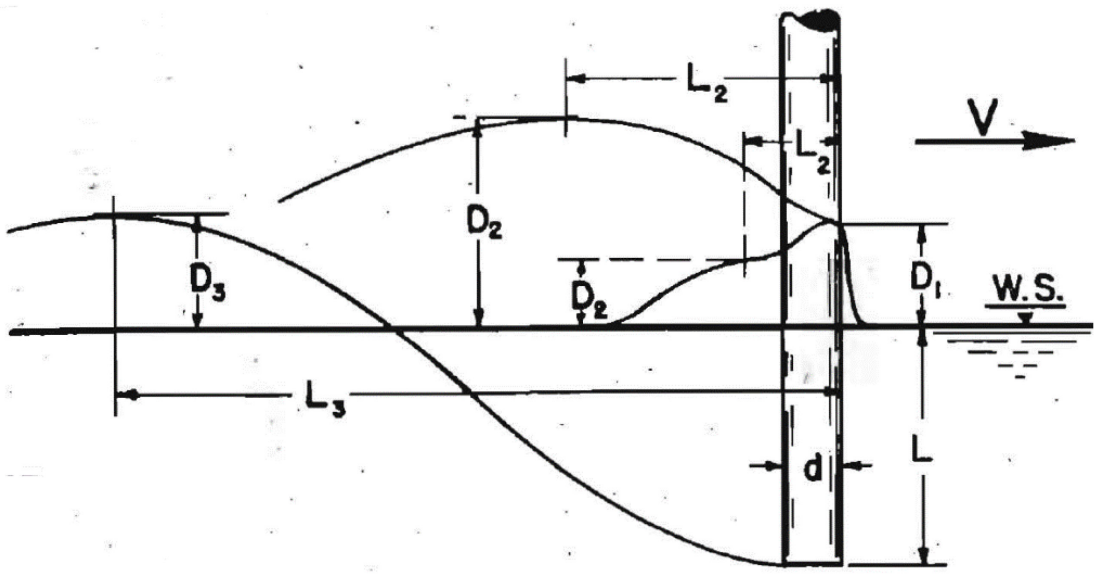

Figure 2-36: Depiction of the hydrodynamic wake from Hay (1947)

Where;

D_1 = Bow wave height

D_2 = Main wake peak height

D_3 = Peak rooster tail height

L_2 = Main wake peak distance downstream

L_3 = Peak rooster tail height distance downstream

Figure 2-37 from Hay (1947) presents the major changes in the hydrodynamic wake characteristics both above and below the water surface relative to an increase in towing velocity. The findings of Hay (1947) will be discussed in greater detail in Chapter 3.

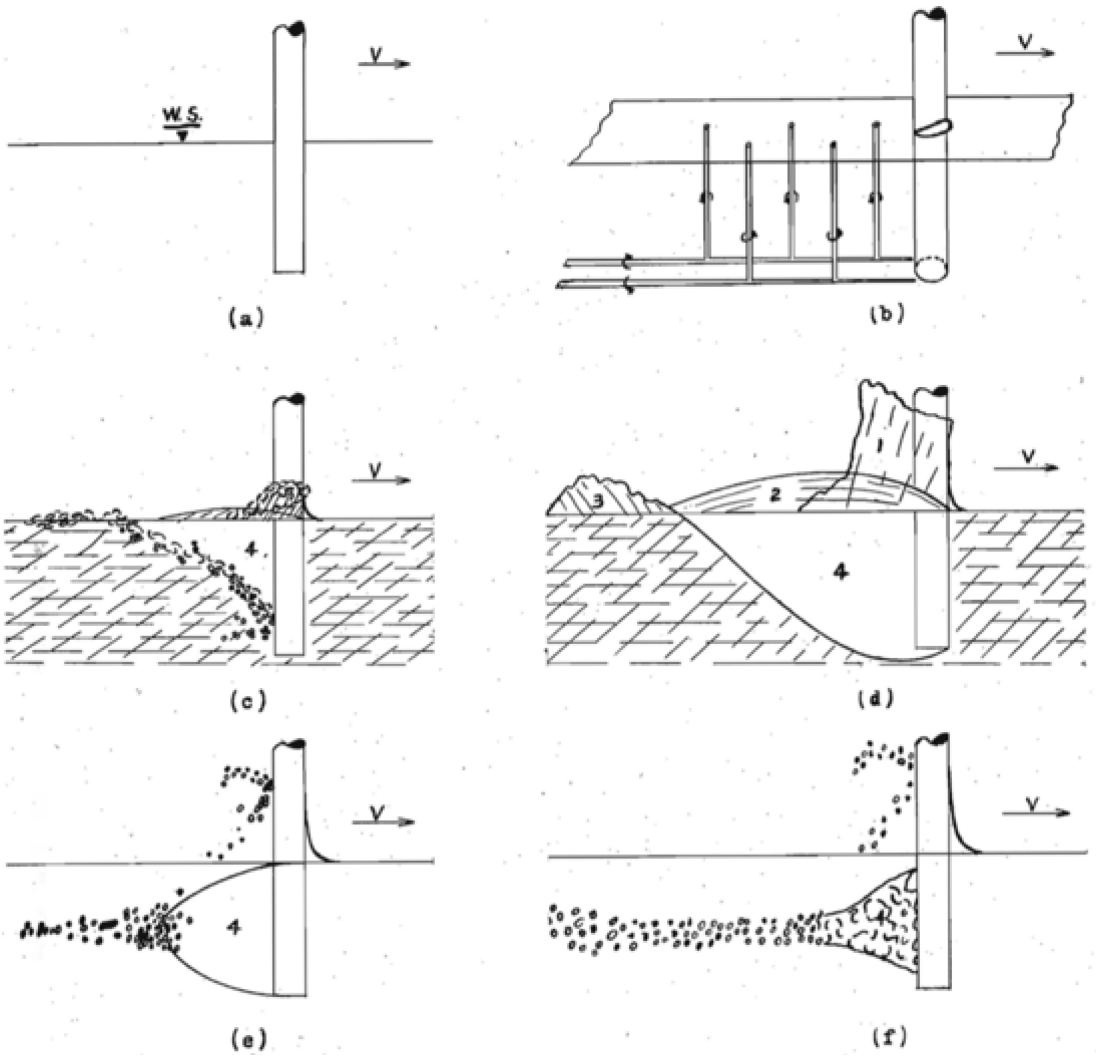

Figure 2-37: Major changes in the flow pattern about a semi-submerged cylinder of finite length with velocity increasing in each frame, from Hay (1947)

2.5.2 Bow Wake

Keough et al. (2016) undertook tow tank experiments to measure the bow wave height for two different diameter cylinders (100 and 216 mm). The bow wave height was measured using an automatic tracking algorithm for the full run time of each test. This represents a vast improvement on the established technique implemented by Chaplin and Teigen (2003); Conway et al. (2015); Hay (1947), in which measurements were derived from static snapshots within the test. Keough concluded that:

- When the $Fr < 0.5$, the bow wave height was steady and unchanging. When $0.5 < Fr < 1.5$ the bow wave height increased in size due to an unsteady chaotic flow. When $Fr > 1.5$ the bow wave began to break due to the dominant unsteady flow.

- The bow wave height can be numerically determined using the Bernoulli equation for inviscid flow (Equation 17). The Bernoulli equation, in theory, clearly shows that the bow wave height is independent of cylinder diameter.

$$D_1 = \frac{V^2}{2g} \qquad \text{Equation 17}$$

However, as the Bernoulli equation does not consider energy dissipation, a modified equation was developed by Keough in order to more accurately determine the bow wave height (Equation 18).

$$D_1 = \frac{V^2}{2g} - C_{dissp}V^2 \qquad \text{Equation 18}$$

Keough et al. (2016) developed C_{dissp}, a constant less than $0.5g$ with a value of 0.005. The C_{dissp} value was empirically derived from his data. The modified Bernoulli equation (Equation 18) more closely represents the test results presented in Chaplin and Teigen (2003); Conway et al. (2015); Keough et al. (2016).

2.5.3 Phenomenon of Ventilated Flow

Ventilation occurs when a bluff body moves through a fluid, and an air pocket forms behind the body. As the velocity of the bluff body increases, so too does the depth of the air pocket. In the case of a surface-piercing cylinder, the depth of ventilation increases with the velocity until it reaches the tip, where the flow is now considered to be fully ventilated.

Hoerner (1965) discusses the ventilated flow condition, where a natural ventilation channel is formed by the separated space at the rear side of the cylinder such that “dead” liquid is sucked down through the pocket and replaced by air. The negative pressure required for the formation of a ventilation pocket is a function of the cross-sectional profile as well as velocity. The smaller negative pressure on the downstream surface of the cylinder effectively reduces the fluid drag loading on the cylinder, with respect to its fully submerged unventilated state.

Figure 2-38 presents the ventilated flow characteristic as defined by Hay (1947), where with increasing tow speed, the ventilated pocket formed on the downstream side of the cylinder as it increased its penetration depth (L_0), where eventually L_0 reached the end of the submerged length (i.e. $L_0 = L$).

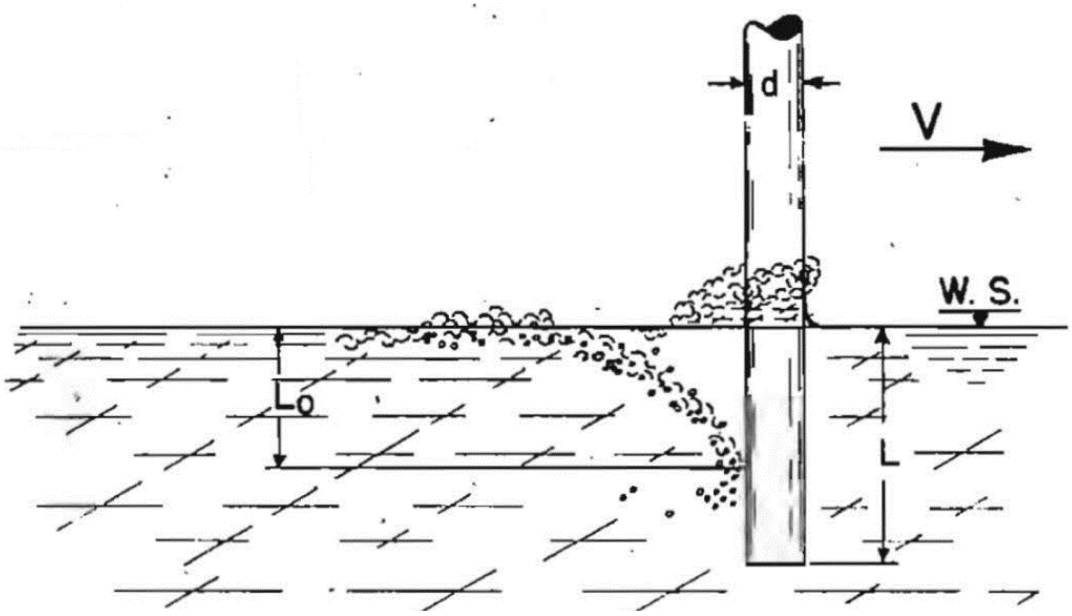

Figure 2-38: Depiction of the ventilated flow pocket depth from Hay (1947)

The ventilated flow pocket effectively halves the hydrodynamic drag force over the length L_0. The effective drag coefficient over the entire submerged length incorporates conventional drag of the fully submerged section, reduced drag from ventilated flow, bow wave pressure drag, and vortex tip drag on the end of the submerged cylinder.

Hoerner (1965) presents the Hay data and discusses the ventilated flow condition and its applicability to circular cylinders as follows:

- In case of bluff surface piercing bodies (rods or cylinders), a natural ventilation channel is provided by the separated space at the rear side of such shapes. “Dead” liquid is sucked down through the channel and replaced by air. The negative pressure required for the formation of a ventilation pocket is a function of shape as well as velocity. This neglects the dynamic pressure acting on the front half of the cylinder.

- In the fully-ventilated condition (i.e. ventilation pocket extends to the fully submerged length), the average pressure differential between pocket and ambient liquid corresponds to half the submerged length (*L*) (h as used by Hoerner).
- The rear side drag component is constant for a cylinder with a constant submerged length (*L*). For test results on various vertical cylinders at subcritical Reynolds numbers, the constant residual drag coefficient is $C_D = 0.49 \approx 0.5$.
- The total drag coefficient of a surface piercing cylinder at high Froude numbers is given by Equation 19. (Note that Fr_L is the Froude number with respect to the submerged length of the cylinder, whereas Fr_D is the Froude number with respect to the diameter of the cylinder).

$$C_D \approx \frac{1}{2} + \frac{1}{Fr_L^2} \qquad \text{Equation 19}$$

Thomsen (1963) proposed the notion that there are three states of ventilation, which are shown here in Figure 2-39:

1. Inception and pre-base ventilation state:
    - The ventilated cavity builds up behind the member as speed increases, reaching down to a depth approximately 1*D* above the free end-tip.
2. Base ventilation state:
    - The ventilated cavity springs from the free end-tip.
3. Post-base ventilation state:
    - The cavity is sealed off at the free surface by the flow.
    - The change in the depth of ventilation is directly proportional to the velocity of either the fluid or the test model.

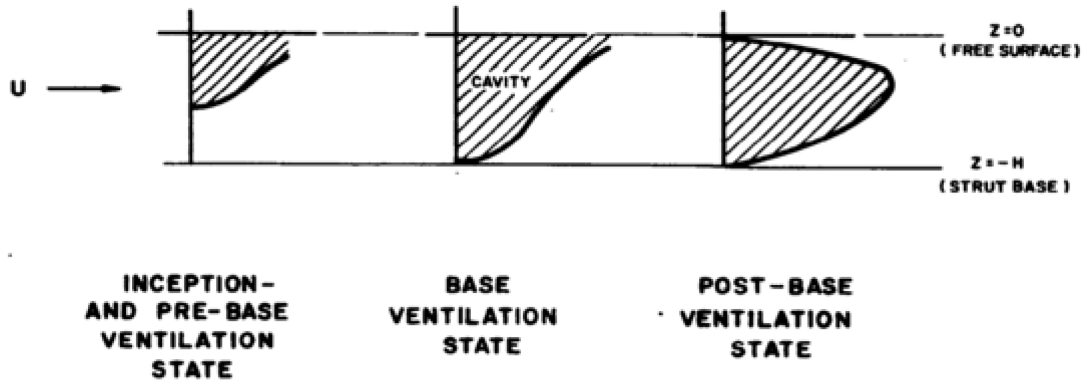

Figure 2-39: Flow states as flow velocity increases, from Thomsen (1963)

Figure 2-40 from Hoerner, purports to present test data from Hay, of drag coefficient C_D versus Fr_L for cylinder diameters 1/4" to 4" and L/D ratios 1 to 32. Hay produced a far greater body of data than this and did not present a comparable plot to Hoerner.

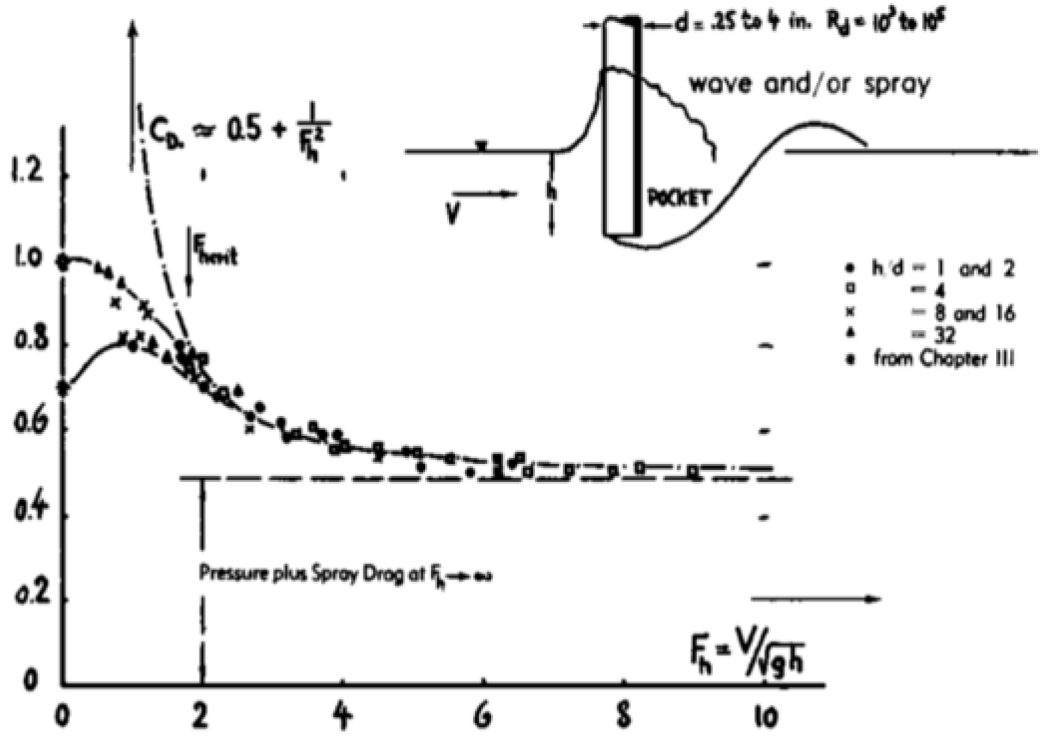

Figure 2-40: Drag coefficient of a surface piercing semi-submerged cylinder as a function of Froude with respect to submerged length from Hoerner (1965)

Figure 2-41 from Hay (1947) presents a log-log plot of all the measured drag 'resistance' coefficients as a function of Fr_L^2. Alone, this plot shows no apparent trend occurring as a function of diameter, except that after $Fr_L^2 \geq 1$ the scatter of the drag coefficients for all diameters initially reduces and has a similar negative trend.

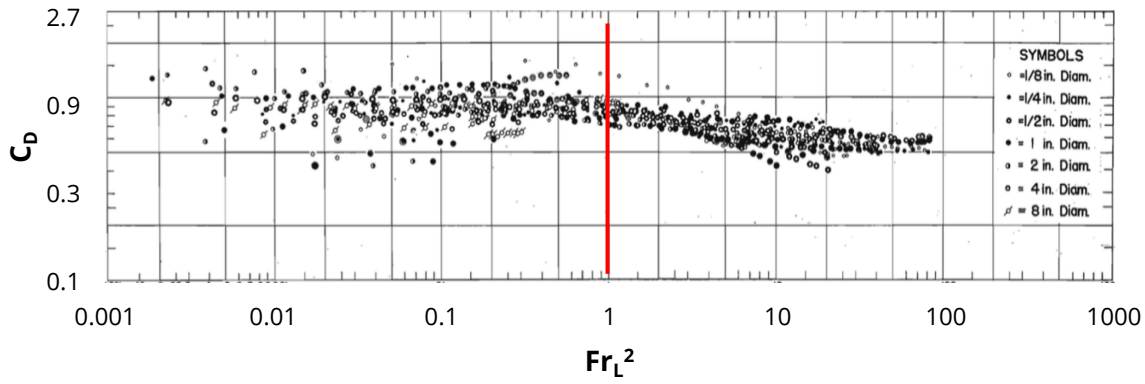

Figure 2-41: Drag coefficient of a surface piercing semi-submerged cylinder as a function of Froude squared with respect to submerged length from Hay (1947)

Figure 2-42 is a compilation plot of Figure 2-40 and Figure 2-41 (Fr_L^2 has been converted to Fr_L), where the 1/8" and 8" diameter data has been excluded in order to properly compare the two figures. It is quite apparent that Hoerner sub-sampled the data: he only incorporated some 48 points out of a possible 718 points. It is unknown how Hoerner selected those specific 48 points, but it may have been from the removal of cylinders subjected to VIV, or poor force measurement resolution. With that said, the data does asymptote to a lower $C_D \approx 0.5$, which is consistent with the ventilated pocket drag reduction, resulting in the pressure acting only on the front half of the cylinder.

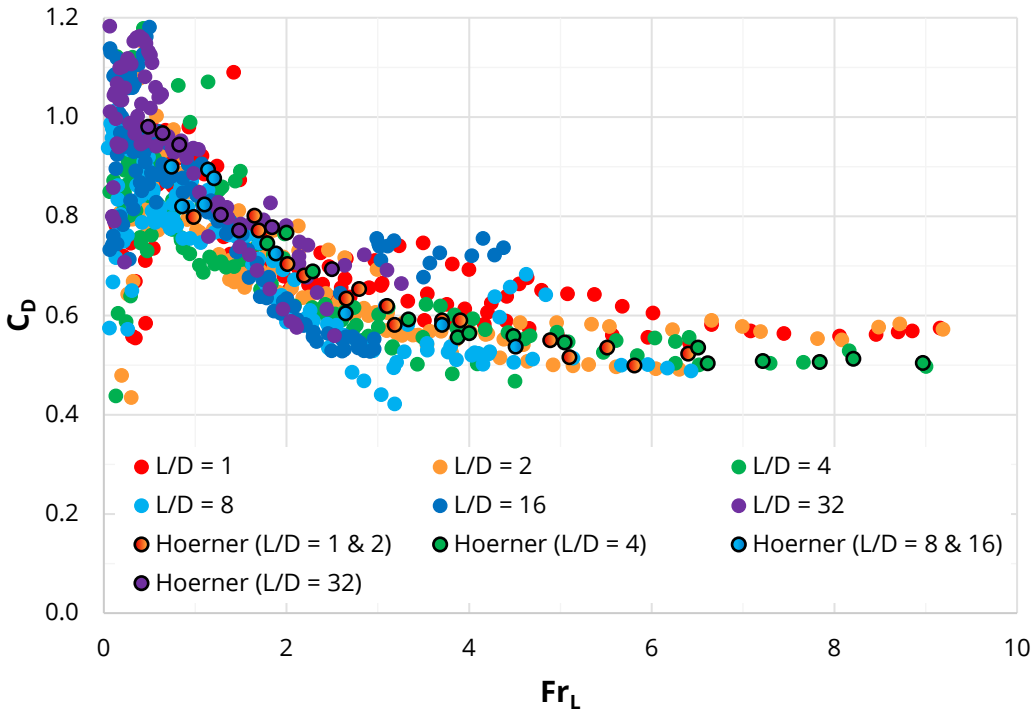

Figure 2-42: Drag coefficient vs Froude as a function of length for both results from Figure 2-40 and Figure 2-41

Chaplin and Teigen (2003) re-analysed the data from Hay (1947) and non-dimensionalised the ventilated depth with respect to the diameter of the cylinder as a function of Fr_D as shown in Figure 2-43. As the towing velocity increased, so too did the ventilated pocket depth until it reached the bottom of the cylinder (i.e. $L_0 = L$). At this stage the cylinder is considered to be fully ventilated, and as such the ventilation depth can no longer increase. This relationship was determined empirically and is shown here in Equation 20 and as the solid line presented in Figure 2-43. The horizontal trend lines represent this fully ventilated state.

$$\frac{L_0}{D} = 0.286 Fr_D^2 \qquad \text{Equation 20}$$

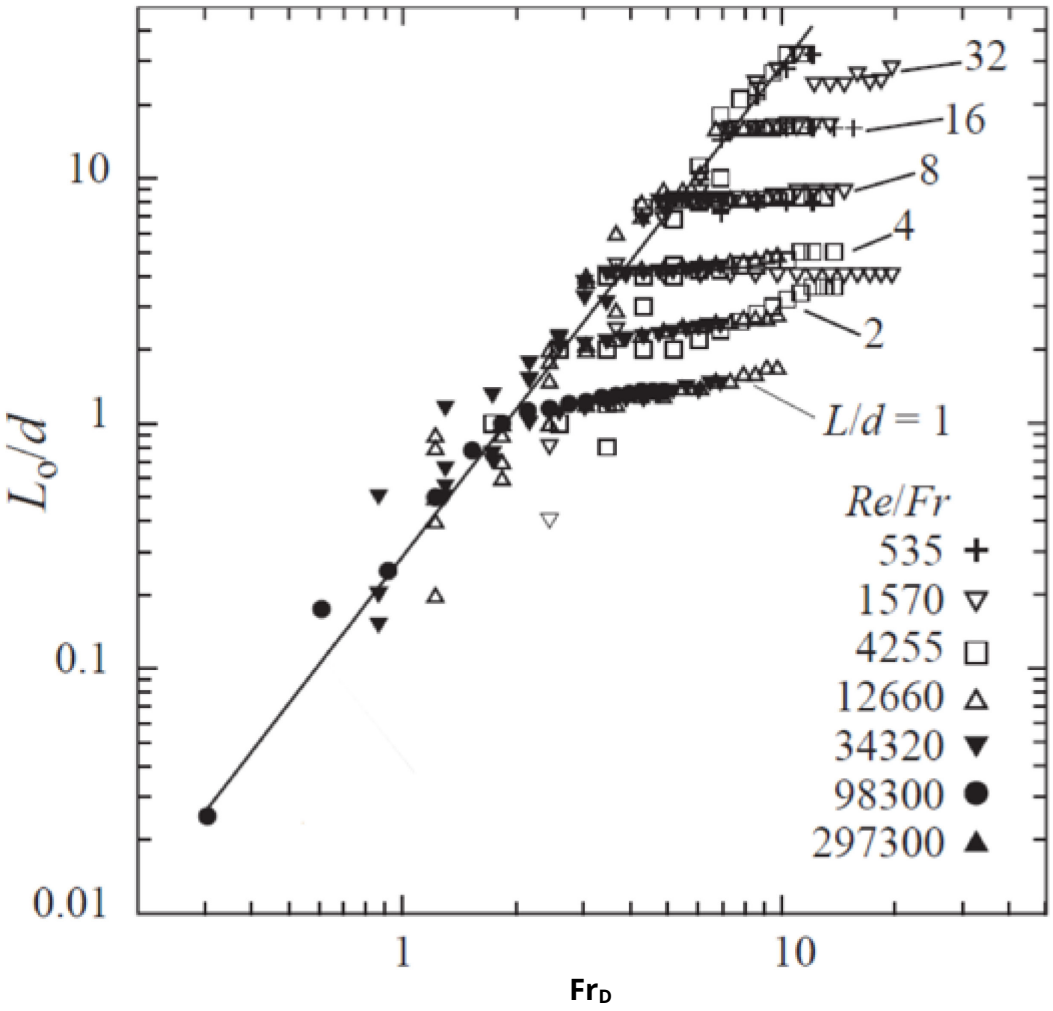

Figure 2-43: Hay's (1947) measurement of the depth L_0 of the depression on the centre-line behind the cylinder, normalised with respect to the cylinder's diameter d, plotted as a function of the Froude number. The line is a best-fit quadratic to the data for cases where $L_0 < L$, from Chaplin and Teigen (2003)

2.6 COMPRESSIBLE FLOW

Although compressible flow is not representative of the practicality and scope of this investigation, it is nonetheless important. This section outlines some of the effects of compressed flow, which are typically derived from wind tunnel testing, resulting in high Reynolds numbers and supersonic Mach numbers.

2.6.1 Mach Number

The Mach number (*M*) represents the ratio of the fluid flow velocity (*V*) to the speed of sound (*c*) in the fluid. Equation 21 presents the standard formula for determining the Mach number.

$$M = \frac{V}{c} \qquad \text{Equation 21}$$

The Mach number is presented in papers in which the testing was conducted in a wind tunnel as these facilities can achieve far higher velocities than standard towing tanks.

2.6.2 Boundary Layer Effect

Gowen and Perkins (1953) investigated the effect of the boundary layer on the drag coefficient for a cylinder with and without an end-plate. The results of this investigation are clearly presented in Figure 2-44. It must be mentioned that the model was well within the post-critical Reynolds regime as well as having a supersonic Mach number of 1.98, which is far beyond what is reasonably practical for a surface-piercing cylinder (within the subsonic Mach number range (0 – 0.3)).

In light of this it was determined that the end-plate begins to have an effect when within 1*D* from the free end, with complete separation between the two end conditions occurring within 0.5*D* of the cylinder end tip. The end-plate has a higher drag coefficient than the cylinder with no end-plate by approximately 20%.

This splitting phenomenon is not observed when looking at the other end of the cylinder when within 2.55*D* of the boundary layer plate. The two different end conditions rise to a drag coefficient of approximately 1.7 at 1*D* from the boundary layer, which then resolves to an approximate C_D = 1.45-1.5 at the boundary layer plate.

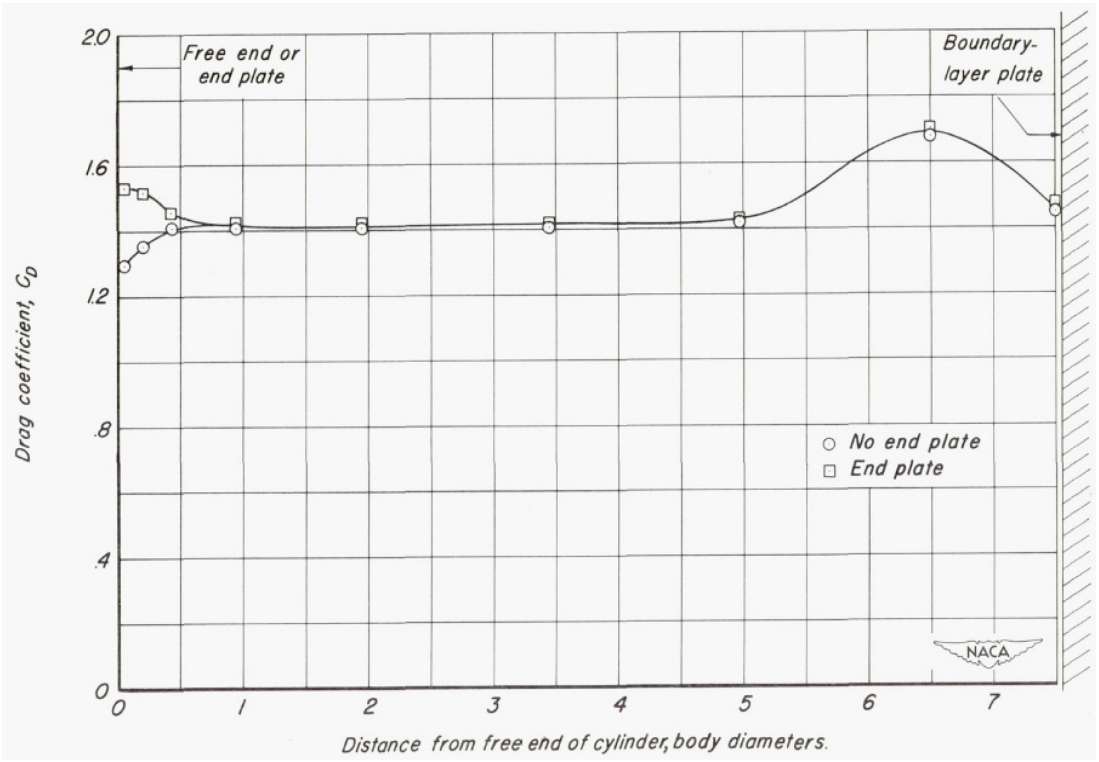

Figure 2-44: Comparison of longitudinal distributions of drag coefficient for a circular cylinder with and without an end-plate for a Reynolds number of 7.4E+5 and a Mach number of 1.98, from Gowen and Perkins (1953)

2.7 SUMMARY OF FINDINGS

The following insights and conclusions were derived from the critical review and analyses of the literature as set out above:

1. The use of non-dimensional numbers, such as Reynolds and Froude are optimal for comparison and correlation of data presented in the literature.
2. When investigating the infiniteness of a surface-piercing cylinder by interpreting the drag coefficient, the fluid flow regime must be sub-critical as in this regime the drag coefficient has a constant value of 1.2 (refer to sections 2.1.1 and 2.2.2).
3. The hydrodynamics analysis of surface piercing cylinders to date has largely relied upon the seminal work of Hay (1947), which will be further presented in Chapter 3
    - Despite the comprehensive scope and detail of Hay's study, it has numerous shortcomings. These limitations give rise to uncertainty in the determination of drag and wake characteristics.
    - Recent work has been of a more limited scope and has not analysed data across a sufficiently large range of L/D ratios, Froude numbers, or Reynolds numbers.
4. While there is an abundance of literature regarding the VIV of a fully submerged cylinder, there is a distinct lack of studies regarding the VIV oscillations of a vertical surface-piercing cylinder. Additionally, the design guides do not accommodate for VIV of surface-piercing cylinders.
5. Aspect ratio has a significant influence on the drag coefficient as is described in Table 2-2, where there is no justification or evidence as to how the table was developed. Figure 2-25 shows clearly that the aspect ratio has a distinct effect on the reduction factor and thus the drag coefficient.
6. The condition of the free end-tip has been shown to affect the measured drag force and subsequently the drag coefficient. Figure 2-32 demonstrates that the end-tip vortex shedding can be suppressed when an end-plate of $D_{EP}/D > 3$ is attached to the free end-tip of the cylinder.

- While there is an abundance of literature on cylinders with an open end, a closed end, or with an end-plate attached, there is a deficiency of analyses comparing these end conditions.

7. The influence of the tank or flume floor boundary layer thickness (δ) has a significant effect on the average spanwise drag coefficient. A reanalysis of Taniguchi et al. (1981) has shown that the boundary layer (when presented in terms of δ/D and L/δ as in Figure 2-25) has a narrow banding of the various boundary layer thicknesses.
    - Depending on the experimental test setup, the boundary layer effect may be removed by adding a splitter plate close to the base of the model or the free end-tip, or by adding an end-plate to the free end-tip.
8. The current codified design guidance for the drag reduction factor (κ) with respect to cylinder aspect ratio (L/D) for cylinders of a finite length is not adequate, due to the unknown directives surrounding the "abutment" of a cylinder. A more appropriate derivation of the drag reduction factor as a function of the aspect ratio has been presented in Table 2-3.
9. Although there is some uncertainty in the exact analytical derivation of the bow wave height, the proposed relationships have shown that it is dependent on both the diameter of the cylinder and the velocity.
10. There is a distinct inverse relationship between the drag coefficient and the ventilated pocket depth, whereby the drag decreases as the ventilation increases.
11. It is evident that compressible flow influences the drag coefficient as a function of the aspect ratio.

Chapter 3 HAY ANALYSIS

As previously noted, Hay (1947) is the seminal paper regarding vertical surface-piercing cylinder testing. This chapter will present and discuss the results of a reanalysis of Hay's data in comparison to comments and analyses by Cathcart (2014); Chaplin and Teigen (2003).

Section 3.1 provides the testing setup, models, equipment, the measurement resolution, and the methodology implemented by Hay. These were derived from the original testing report by Hay, and from the Princeton University Library, where the testing was conducted.

Section 3.2 presents some of the analyses and interpretations previously conducted regarding Hay's experiments and results.

Section 3.3 conducts an original and thorough reanalysis of the results measured by Hay. The reanalysis includes the ventilated flow, the drag coefficient, bow wave and the drag modification factor in comparison to the literature.

Section 3.4 summarises the findings and insights from the analyses presented within this chapter.

3.1 HAY TESTING SETUP

Hay measured drag resistance force, from which he derived an effective drag coefficient acting over the wetted submerged length of the cylinder. The cylinders employed were predominantly open-ended brass or steel tubes, and one was a solid timber rod (4”).

Hay (1947) conducted a thorough test programme on the hydrodynamics of surface-piercing cylinders, with a comprehensive scope of test conditions and parameters measured, however his investigation was limited by the state-of-the-art of instrumentation technology of the times. Furthermore, as he did not measure cylinder vibration (as can be done with modern accelerometers), he was unable to determine the onset and magnitude of hydrodynamic VIV that was excited under a range of test conditions.

Such VIV excitation would have corrupted direct comparison between test conditions, but was not characterised other than in Hay’s sole comment as follows:

> *…the cylinder was permitted to vibrate laterally…Permitting the cylinder to vibrate in this manner raises the water resistance up to twice the non-vibrating resistance. —Hay (1947) [p. 95]*

This observation is offered in conjunction with discussion of the 1/8” cylinder with an L/D = 32 at a tow speed of 6 ft/sec, which confirms that at least this test cylinder was subject to VIV, but it is not known which, if any, other cylinders were similarly affected, nor under what test conditions and at what tow speeds.

3.1.1 Equipment

The towing carriage was mounted above the towing tank on rails; the tank was 4.5 feet (1.37 m) wide, 5 feet (1.52 m) deep, and 133 feet (40.54 m) long. Hay tested a range on cylinder varying from 1/8” up to 8” (3.175 - 203.2 mm).

Hay measured drag resistance using a sensitive spring dynamometer, in conjunction with counterbalanced dead-weight to accommodate the major drag component, whereby he made spring extension measurements to a resolution of a thousandth of an inch (0.001”, 0.0254 mm). Using this arrangement Hay reported the smallest drag resistance to two ten-thousandths of a pound (0.0002 lb, 9.07E-5 kg), but also raises the uncertainty of such measurements as follows:

> *…though these are definite and repeated scale readings, it is not claimed that any reading in ten thousandths of a pound is not to be challenged. With this one exception, all resistance measurements were obtained accurately to three significant figures by choosing the proper dynamometer with the proper springs or dead-weights. —Hay (1947) [pp. 8–9]*

This measurement of uncertainty calls into question the quality of results for a large proportion of the low tow speed tests with small diameter cylinders. These include tests with the greatest *L*/*D* ratios, which have particular interest and relevance to practical AUV mast applications. A thorough error analysis was unable to be conducted due to the exact dimensions of the models being unknown.

Hay also took extensive photographic images of the wake effects generated by the submerged cylinder at different tow speeds, including: bow wave height (D_1); depth of ventilated pocket (L_0); height and location of the peak of trailing wake (D_2 & L_2); and height and length of trailing wave (D_3 & L_3) generated by the ventilated pocket shedding from the bottom of the cylinder. L_0 was measured using a camera through a side window in the tow tank. However, the resolution of all the measurements taken from the photographs was 0.1”, which was quite coarse with respect to the small cylinder diameters, particularly the 1/8”, 1/4” and 1/2” cylinders, making correlation unreliable for normalisation to cylinder diameter.

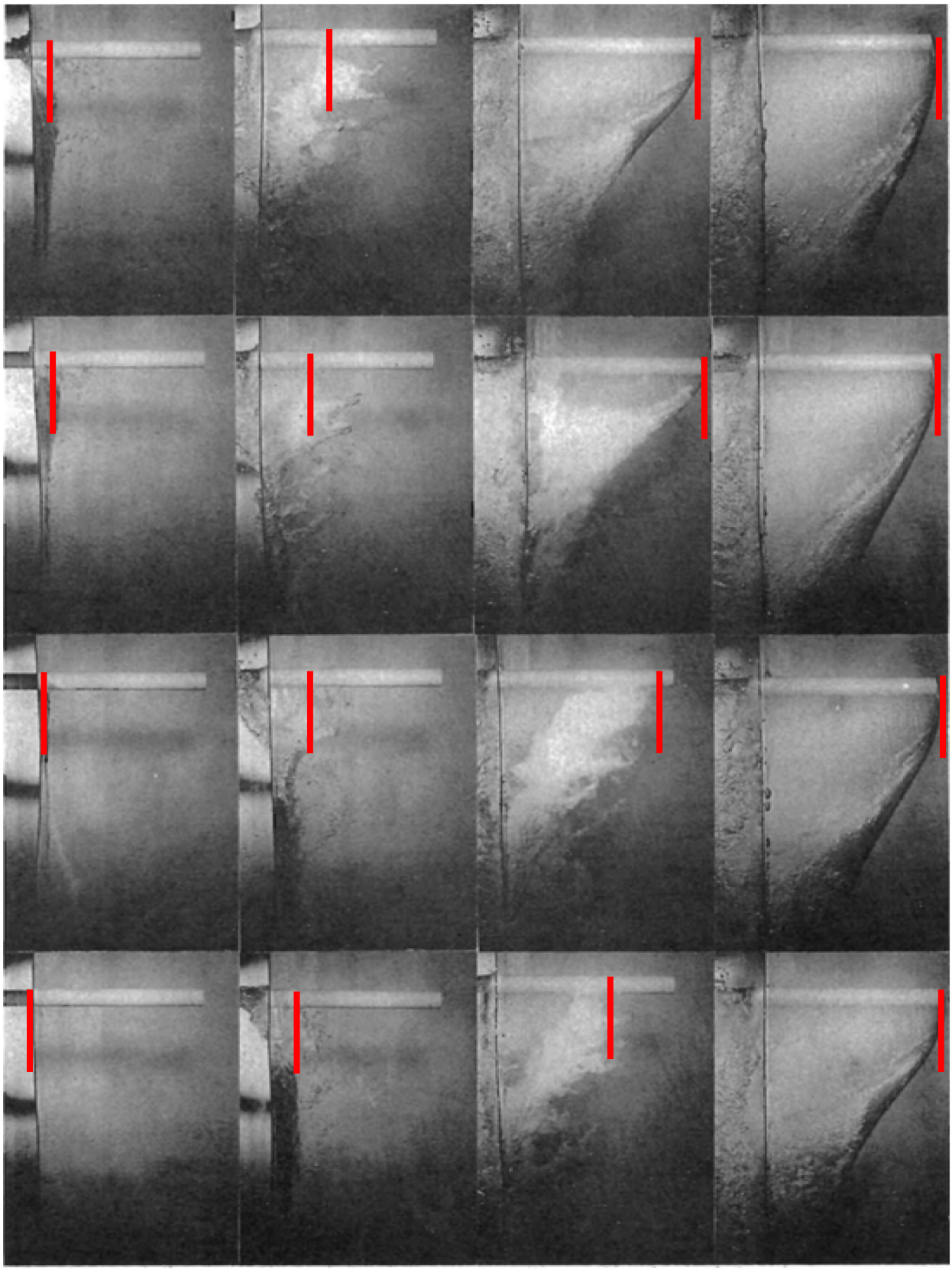

Figure 3-1: Plate 77 – D = 2", L = 16", V = 1-16 ft/s, from Hay (1947)

Figure 3-1 presents the underwater ventilated photos taken by Hay for D = 2″, L = 16″, V = 1-16 ft/s. The red lines indicate the approximate location of Hays measurements of the ventilated flow. For the conditions where $L_0 > L$ (V = 11-16 ft/s), the maximum pocket depth occurred within one diameter downstream of the model, where this value was measured by Hay.

3.1.2 Models

Hay tested seven different diameter cylinders at several submerged depths as presented in Table 3-1.

Table 3-1: Model diameter and submerged depth matrix

	Diameter						
	1/8	1/4	1/2	1	2	4	8
Submerged Depth	1	1	1	1	2	4	8
	2	2	2	2	4	8	16
	4	4	4	4	8	16	32
		8	8	8	16	32	
			16	16	32		
				32			

Table 3-2 presents the same matrix as Table 3-1, however the submerged depth has been replaced with the L/D ratio.

Table 3-2: Model diameter and L/D ratio matrix

	Diameter						
	1/8	1/4	1/2	1	2	4	8
L/D Ratio	8	4	2	1	1	1	1
	16	8	4	2	2	2	2
	32	16	8	4	4	4	4
		32	16	8	8	8	
			32	16	16		
				32			

Unfortunately, within the Hay report, the cylinder specifics were not provided except in broad terms where it was described that the cylinders less than 2" were either drawn brass or cold rolled steel tubes, the 4" was a solid timber rod, and the 8" was a cold rolled steel tube. Unfortunately, the Princeton University Library, which houses the original documentation from Hay, did not possess further specifics from the testing either (i.e. dimensions of cylinders, method of restraint to test rig, etc), other than the direct communications between Hay and the clients at the David Taylor Model Basin (DTMB).

Without the cylinder material and dimensional specifics there is no way to confirm whether Hay's models were subject to VIV.

The following excerpts from the Hay-DTMB communications revealed some interesting observations made by Hay:

> *The 4-inch diameter cylinder at 16-inch depth vibrates so violently that the wheels at times leave the rails. — Hay (1941) [sec. Job Order No.1 NObs-34006]*

This further confirms the author's suspicion that some of Hay's test results were affected by VIV, which in turn questions the reliability of the Hay test rig in accomplishing the originally proposed test matrix.

Keeping the original test matrix in mind (Table 3-1), the following quote refers to the test velocities that Hay achieved:

> *The other models develop vibrations starting at about 5-1/2 feet per second which cannot be stopped. — Hay (1941) [sec. Job Order No.1 NObs-34006]]*

The high-speed test matrix presented in Table 3-3 shows that several of the conditions proposed originally were unachievable.

Table 3-3: Model diameter and submerged depth for testing velocities up to 15 ft/s

	Diameter					
	1/8	1/4	1/2	1	2	4
Submerged Depth	1	1	1	1		
	2	2	2	2	2	
	4	4	4	4	4	4
		8	8	8	8	8
			16	16	16	

With this new insight into Hay's testing, it is evident that the high-speed results for several test conditions should be dismissed due to the unmeasured VIV phenomenon. The cells in Table 3-4 highlighted in red present the differences between Table 3-1 and Table 3-3, where the red cells are only 'reliable' up to tow velocities of 5.5 ft/s.

Table 3-4: Proposed test matrix with highlighted cells vibrating after 5-1/2 ft/s

	Diameter						
	1/8	1/4	1/2	1	2	4	8
Submerged Depth	1	1	1	1	2	4	8
	2	2	2	2	4	8	16
	4	4	4	4	8	16	32
		8	8	8	16	32	
			16	16	32		
				32			

These highlighted vibrating data series have been excluded from the ensuing analysis of the Hay data.

3.2 PREVIOUS ANALYSES

More recent work by Chaplin and Teigen (2003) and Cathcart (2014) repeated some of the Hay tests using closed-end cylinders, which attribute some differences to the vortex tip drag contributions of open-ended vs closed-ended cylinders. This may be significant for short *L*/*D* ratios, but such end effects are more likely second order above certain thresholds of *L*/*D*.

Chaplin and Teigen (2003) also reanalysed the Hay data and found that the data more consistently conformed to Equation 22 (an altered Hoerner formula), which significantly differs from Hoerner (Equation 19). Also, they noted that the relationship between Fr_D and Fr_L is $Fr_D = \sqrt{(L/D)} \bullet Fr_L$, and re-expressed the equation in terms of Fr_D.

$$C_D = \frac{1}{2}\left(1 + \frac{1}{Fr_L^2}\right) \qquad \text{Equation 22}$$

Chaplin derived an equation for the drag coefficient for a surface piercing cylinder in partially ventilated flow (i.e. $L_0 < L$), which incorporates the bow wave contribution as presented in Equation 23, where $C_{D\infty}$ is the fully submerged drag coefficient for an infinite cylinder.

$$C_D = C_{D\infty} + \frac{Fr_D^2}{(L/D)}(0.618 - 0.286\, C_{D\infty}) \qquad \text{Equation 23}$$

Chaplin derived Equation 24 to describe the drag coefficient for the fully ventilated flow condition (i.e. $L_0 = L$).

$$C_D = 1 + \frac{(L/D)}{Fr_D^2} \qquad \text{Equation 24}$$

Figure 3-2 presents a plot of Equation 19, Equation 22, Equation 23 and Equation 24, which calculate the drag coefficient as a function of Froude number squared. The plot is in terms of C_D and Froude diameter, where the cylinder length and diameter were given the same arbitrary values to have them provide an aspect ratio of 1.

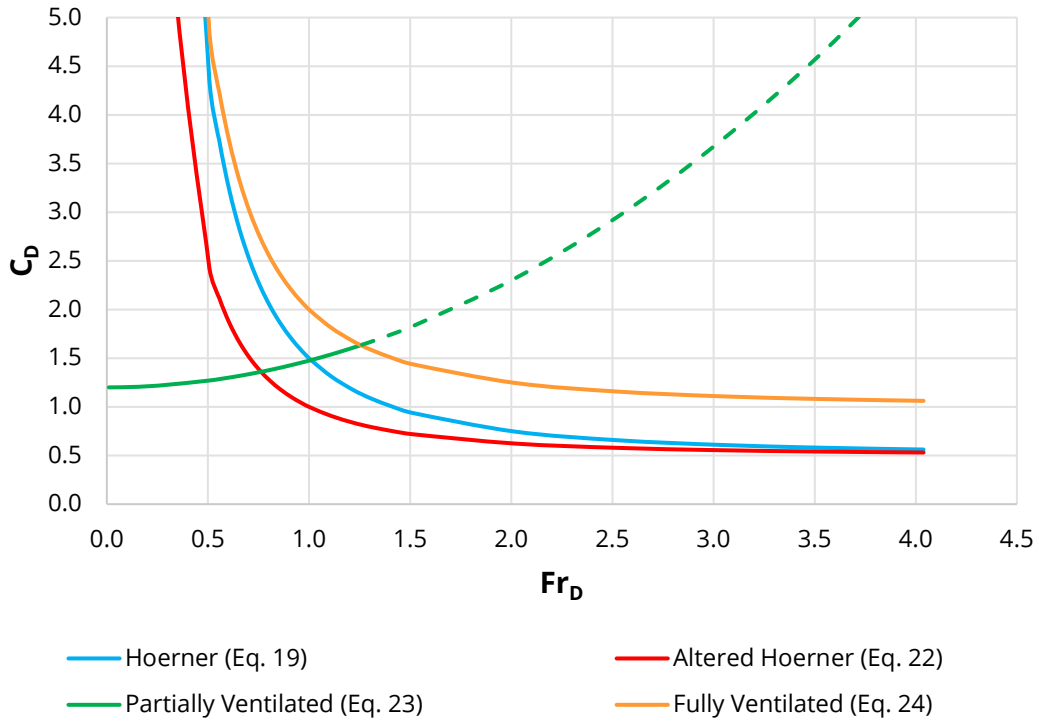

Figure 3-2: Derived drag coefficient formulae from previous analyses of Hay, L/D = 1

Three of the curves in Figure 3-2 present with the same form, whereby at a Froude number of approximately 3.5 they have almost reached the asymptote of 0.5. Yet, the '*Partially Ventilated*' formulation goes in the opposite direction with a continuous rise, which is due to the inclusion of the bow wave height in the derivation of the formula.

The '*Partially Ventilated*' line would theoretically stop rising when intersecting with one of the other lines, because the model would no longer be partially ventilated, but instead it would become fully ventilated.

More recent testing at AMC reported by Cathcart (2014) interrogated a 101.6 mm (4") diameter cylinder at *L*/*D* ratios of 2 and 10, for Froude numbers up to 4. The Cathcart data was then compared against Hay's 4" diameter cylinder with an *L*/*D* of 2. It should be noted that the Cathcart cylinders were made of steel and were closed ended and the Hay cylinder was a solid timber rod, and was therefore closed ended, providing comparable end-tip conditions. In general, the Cathcart and Hay *L*/*D* = 2 data are in good agreement for $Fr_L > 1$, with significant disparity when $Fr_L < 1$ (Figure 3-3). It is also apparent that the Cathcart *L*/*D* = 2 and *L*/*D* = 10 data are also in close agreement for $Fr_L > 1$, where one would have expected some degree of separation with respect to the submerged lengths, degree of ventilated length, and relative contribution of the tip vortex drag.

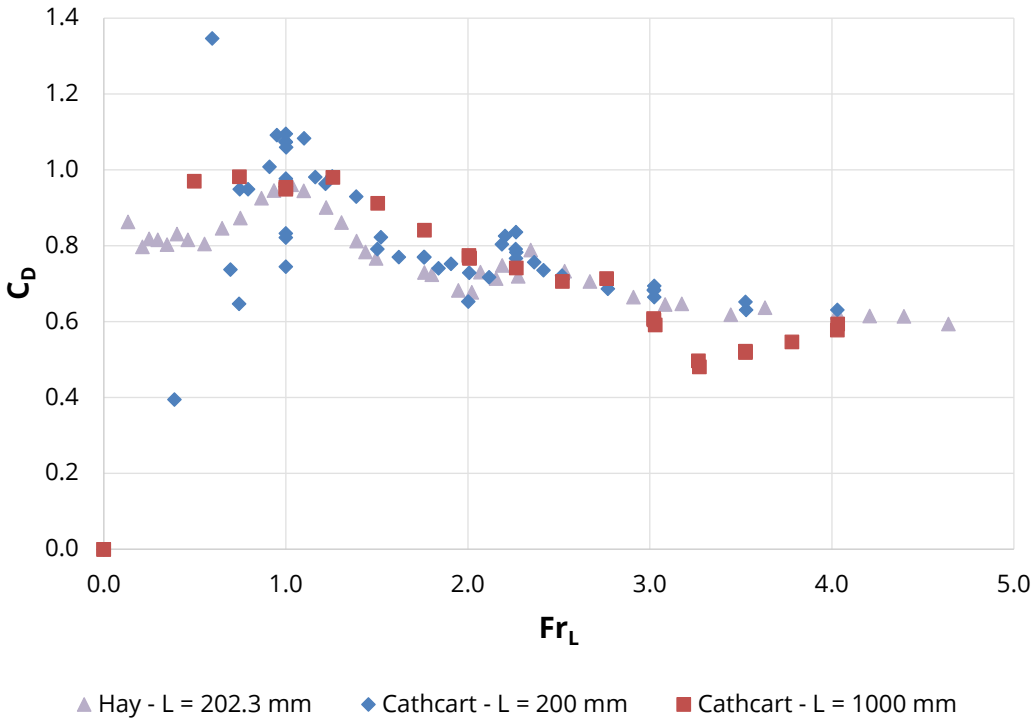

Figure 3-3: Drag coefficient versus Froude number for a surface piercing cylinder (101.6 mm) with L/Ds of 2 and 10 compared against Hay 4" and CFD, after Cathcart (2014)

The state of ventilated pocket depth for the Cathcart results was predicted using the relationship developed by Chaplin as per Equation 20.

For L/D = 2, the fully ventilated flow occurs at a Froude number of 0.6, whereas at an L/D of 10 ventilated flow occurs at a Fr_L = 2.6. The L/D = 2 results from Cathcart is entirely in the fully ventilated condition, unlike the L/D = 10 data set, where the full ventilation condition occurs at or around the plateau between Fr_L = 2 – 3. It is interesting to note that the Hay data is constant below Fr_L = 0.6, rising thereafter with what may be attributed to bow wave effects, and subsequently falls away.

From the perspective of AUV masts, the prospect of fully ventilated flow with a trailing wake generated from the bottom of the cylinder would seem impractical and irrelevant. Similarly, very short L/D ratios, with high impact of tip vortex drag effects, are also impractical for the AUV mast application, but are of interest for determining a reliable minimum finite length of submerged cylinder that should be employed to evaluate drag effects on long and slender surface piercing cylinders. One can hypothesise that drag effects are best represented by an "infinitely" long cylinder, but this would be impossible to accommodate in a tow tank of finite depth and is beyond the drive capacity of a practical tow carriage.

Similarly, there is a tow speed (or across a range of cylinder diameters a particular Froude Number) at which the depth of the ventilated pocket reaches a practical limit beyond which it cannot grow. The Hay tests on small diameter cylinders with the largest submerged length condition (L/D = 32) found $L_0 \geq L$ at $Fr_D \approx 9$ (**NB:** Hay actually reported $Fr_D^2 \approx 100$), thereafter the trailing wake generated from the bottom of the cylinder prevailed. It was noted that these tests were affected by VIV excitation. More recent tests by Chaplin and Teigen (2003) on a 210 mm diameter cylinder went up to Fr_D of 1.67 for varying L/D = 4.1 – 7.2, and those of Cathcart (2014) on a 101.6 mm diameter cylinder went up to Fr_D = 4.0 at an L/D = 10. These are far from the L/D = 32 and Fr_D = 9 limits of the Hay tests.

3.3 RESULTS

Hay presented a wide variety of results and discussion points, which have been further investigated herein.

When presenting Froude number, Hay was in fact presenting Froude number squared, thus the Froude numbers presented herein relates to that presented in Equation 3, except for where clearly stated otherwise.

When a figure herein refers to the '*target Reynolds range*', this is in reference to Table 3-6, which highlights the Reynolds regimes for each test case and velocity. The colour scheme shown refers to Figure 2-1, where sub-critical (teal), sub-critical plateau (blue), critical (red). The subcritical plateau (*Re* = 1E+4 – 1E+5) is the focus of the results as in this region the drag coefficient remains at the constant value of 1.2.

Table 3-5 provides a master legend for all figures containing raw Hay data presented in this chapter.

Table 3-5: Legend for the various Hay test series

Aspect Ratio	Colour
1	
2	
4	
8	
16	
32	

Model Cylinder	Symbol
1/8″	■
1/4"	◆
1/2″	▲
1″	●
2″	×
4″	✳
8″	+

Table 3-6: Reynolds number regimes for each diameter (inches), L/D and the associated velocities

Diameter		1/8			1/4				1/2					1						2					4				8		
Submerged Length		1	2	4	1	2	4	8	1	2	4	8	16	1	2	4	8	16	32	2	4	8	16	32	4	8	16	32	4	8	16
L/D		8	16	32	4	8	16	32	2	4	8	16	32	1	2	4	8	16	32	1	2	4	8	16	1	2	4	8	1	2	4
Velocity																															
ft/s	m/s																														
1	0.30																														
2	0.61																														
3	0.91																														
4	1.22																														
5	1.52																														
6	1.83																														
7	2.13																														
8	2.44																														
9	2.74																														
10	3.05																														
11	3.35																														
12	3.66																														
13	3.96																														
14	4.27																														
15	4.57																														
16	4.88																														

3.3.1 Ventilated Flow

The data presented in Figure 3-4 encompasses all the results from Hays testing for the ventilated flow depth normalised to the cylinder's diameter versus the Froude number as a function of the diameter. The black line-of-best-fit (LoBF) was determined as per Equation 20 (Chaplin and Teigen (2003)), but modified to be in terms of *Fr* rather than Fr^2. This applies for cases where the ventilated flow depth is less than the submerged depth ($L_0 < L$). The horizontal lines which form to the right of the LoBF represent measured values where the ventilated pocket depth is greater than the submerged depth ($L_0 > L$), which comes from the inclusion of the trailing tip vortices. These results should not be considered, as the cylinder has become fully ventilated and therefore $L_0 = L$.

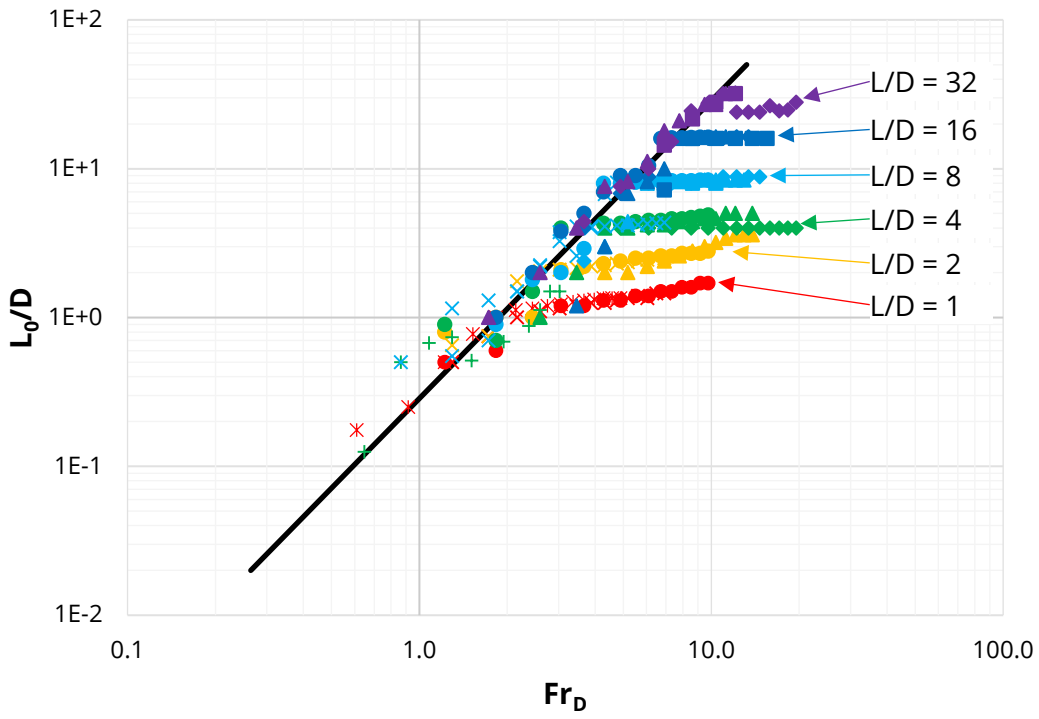

Figure 3-4: Ventilated flow depth normalised with diameter vs Froude number, with Chaplin LoBF

From the recorded results, the 1/4" cylinder at a submerged depth of 8” (indicated with purple diamonds) is the only data series where Hay continued to measure the ventilated flow depth once the air pocket had collapsed. For the purpose of this analysis, these results have been omitted as the air pocket had collapsed once the ventilated flow reached the bottom of the cylinder. This produced lower L_0 values when compared to the rest of Hay’s measured results, in which Hay did not record any further values after the pocket had collapsed.

Figure 3-5 presents the data restricted to results where the ventilated flow depth is less than the submerged depth for each of the cases wherein the data falls within the target Reynolds range. The majority of the data falls on or around the line of best fit (black line) as proposed by Chaplin and Teigen (2003).

As shown in Figure 3-6 over 80% of the fully ventilated, and Reynolds number range results from Hay, fall within one standard deviation of the LoBF from Chaplin and Teigen (2003). The standard deviation was calculated from partially ventilated results which lay within the sub-critical Reynolds regime as presented in Figure 3-5.

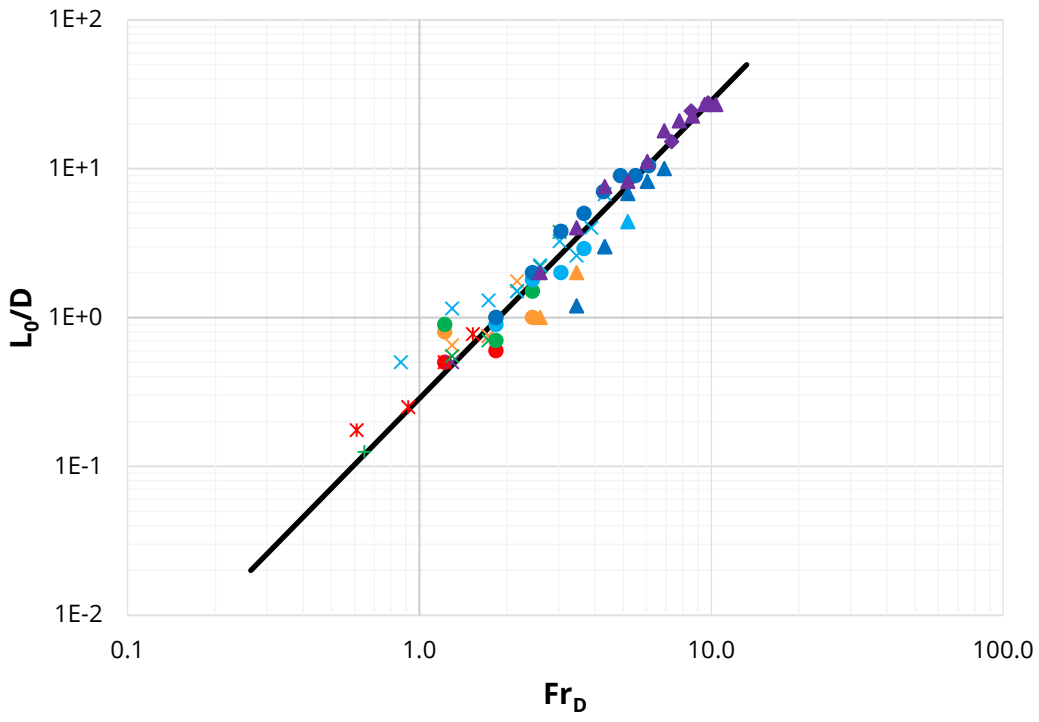

Figure 3-5: Ventilated flow depth normalised with diameter vs Froude number where $L_0 < L$ and within the target Reynolds range (1E+4 – 2E+5), with Chaplin LoBF

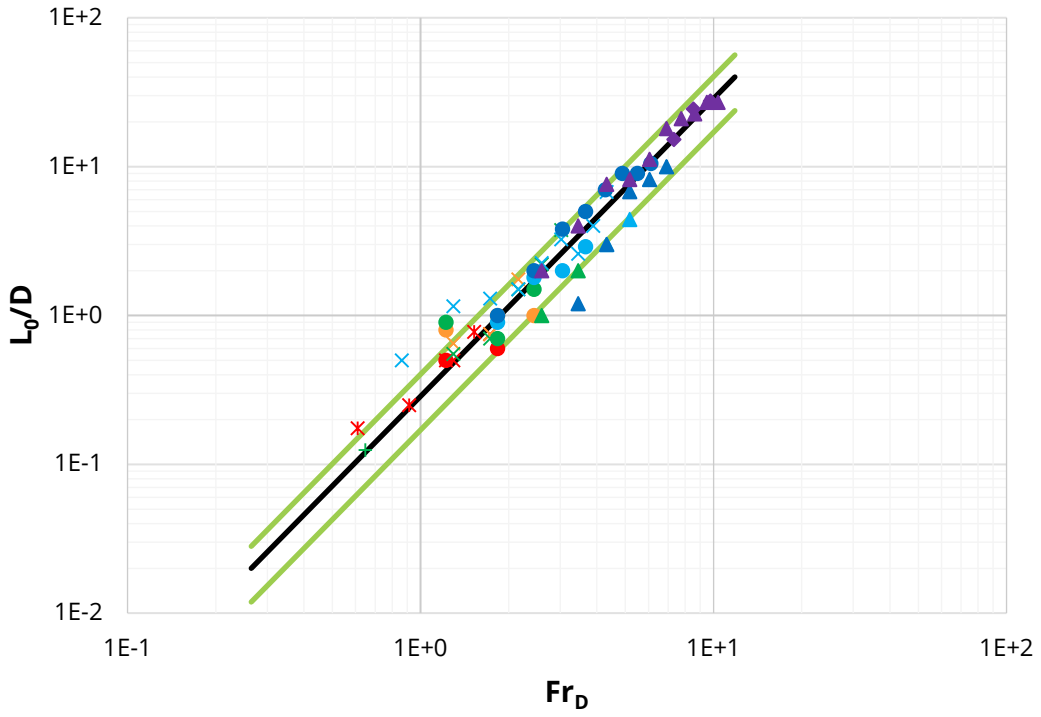

Figure 3-6: Ventilated flow depth normalised with diameter vs Froude number where $L_0 < L$ and within the target Reynolds range (1E+4 – 2E+5), along with green lines of one standard deviation, with Chaplin LoBF

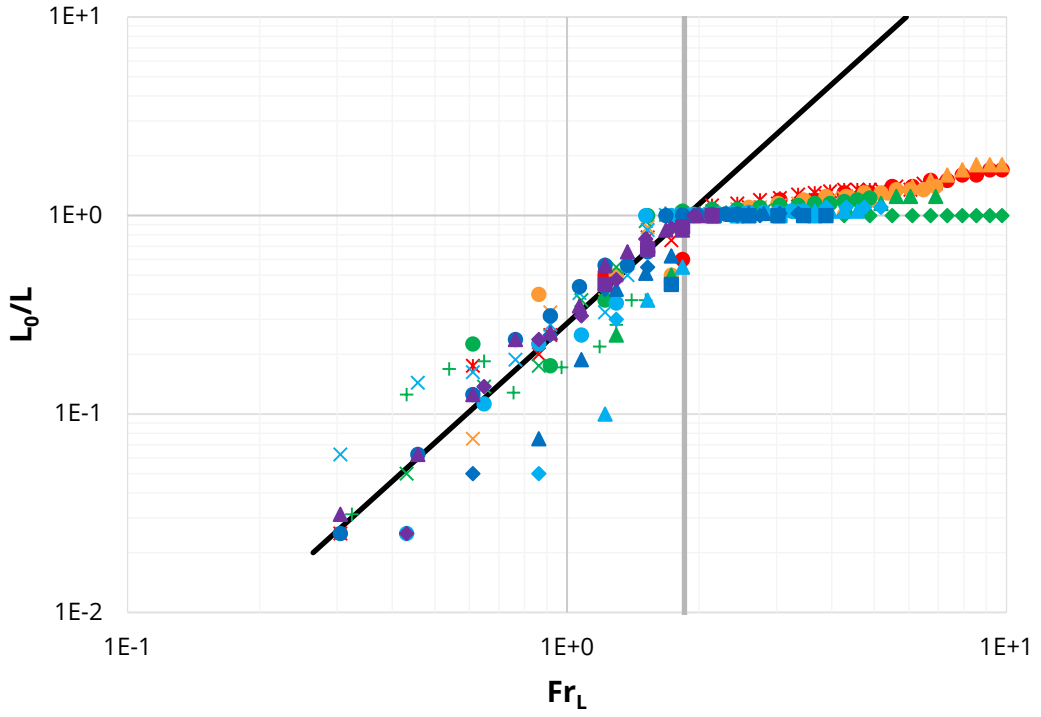

Figure 3-7: Ventilated flow depth normalised with submerged length vs Froude number, with Chaplin LoBF (black) and limiting Froude number line (grey)

Figure 3-7 presents the ventilated depth normalised to the submerged length as a function of Froude relative to the submerged length. It is quite evident that there is a limiting Fr_L for all L/D ratios at which the ventilated depth reaches the submerged length resulting in the flattening of the results when $L_0/L = 1$. At this point $Fr_L = 1.87$ and the vertical grey line represents the condition of full ventilation. Equation 25 defines the Chaplin LoBF (black line) plotted with substitution of alike variables as per Equation 20.

$$\frac{L_0}{L} = 0.286 Fr_L^2 \qquad \text{Equation 25}$$

3.3.2 Drag Coefficient

Hay presented two different drag coefficient values and associated formulae:

1. C_D – Drag coefficient based on static frontally projected wetted area:

$$C_R = C_D = \frac{2F}{\rho d L V^2} \qquad \text{Equation 26}$$

2. C_{TD} – Drag coefficient based on dynamic frontally projected wetted area:

$$C_{TD} = \frac{2F}{\rho d (L + D_1) V^2} \qquad \text{Equation 27}$$

Equation 26 presents the standard formula for drag coefficient acting on a cylinder. This formula is representative of a fully submerged cylinder (or a cylinder within a single fluid). Unlike Equation 26, Equation 27 incorporates the bow wave height, which is only possible in multi-fluid conditions.

NB: The drag coefficient formula may be altered to be in terms of a circular cross-section, where the above formulae are for rectangular cross-sections.

The Chaplin and Teigen-derived Equation 23 is an empirical fit to what Hay had previously described as Equation 27. This empirical fit was developed in order to define a relationship between C_D, Froude, and aspect ratio.

The drag coefficients presented and discussed below are C_D as defined in Equation 26.

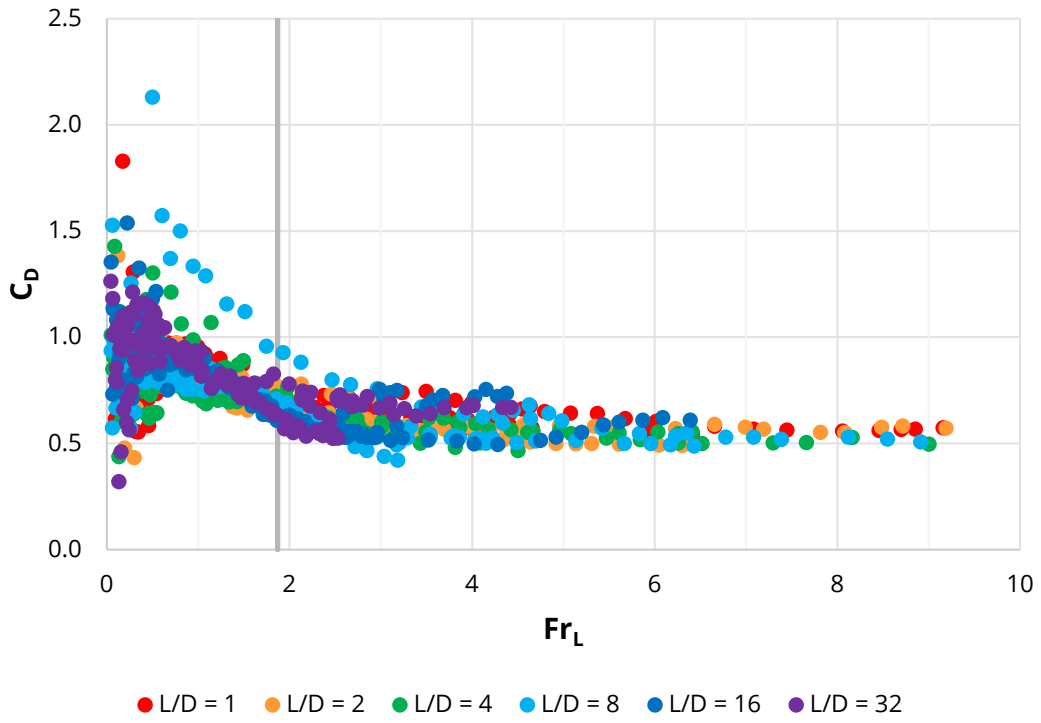

Figure 3-8: Drag coefficient vs Froude number for all cases with limiting Froude length line

Figure 3-8 presents the drag coefficient vs Froude number as a function of the submerged length, where the same grey line from Figure 3-7 has been plotted to show the limiting Froude number for fully ventilated flow. This limiting value is derived from calculating the Fr_L for the fully ventilated condition (L_0/L = 1), whereby Fr_L = 1.87.

Figure 3-9 presents the Hay data that falls within the target Reynolds number range. In comparison to Figure 3-8, it is visible that there are fewer data points below Fr_L = 2. This is due to the data being outside of the target Reynolds range.

The solid black line in Figure 3-9 comes from Equation 19, which was derived by Hoerner (1965) using the Hay data. The line has a poor correlative fit to Hays data below sub Fr_L = 2 which is the point at which Hoerner presented a critical Froude number (F_{crit}) (Figure 2-40).

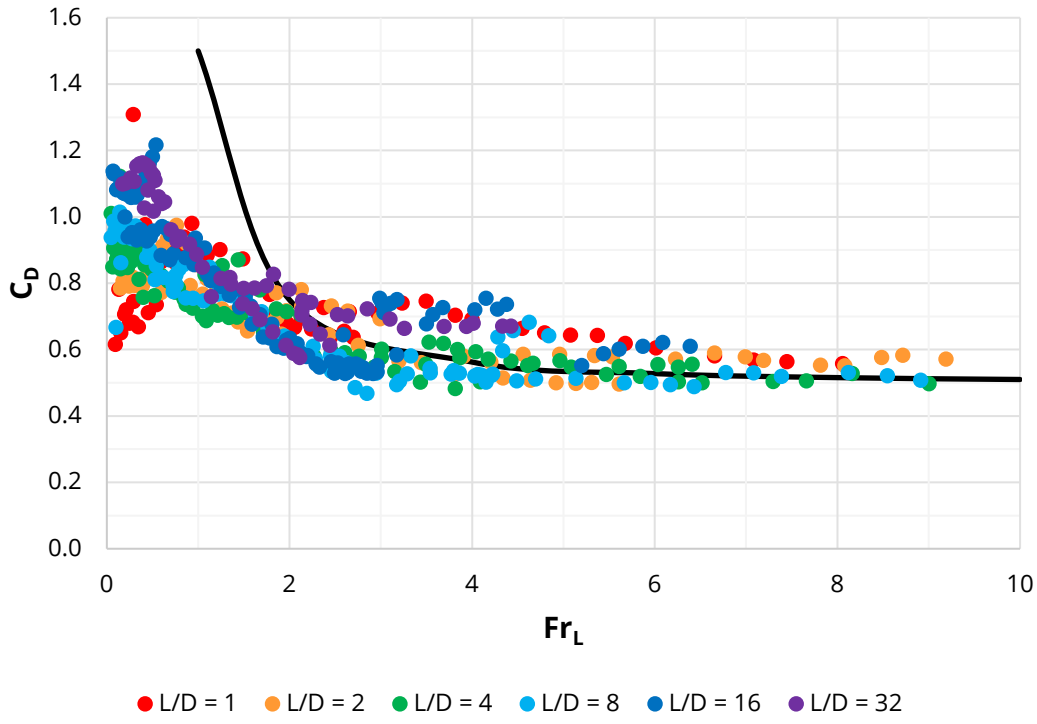

Figure 3-9: Drag coefficient vs Froude number within the target Reynolds range (1E+4 – 2E+5), with Hoerner fit line

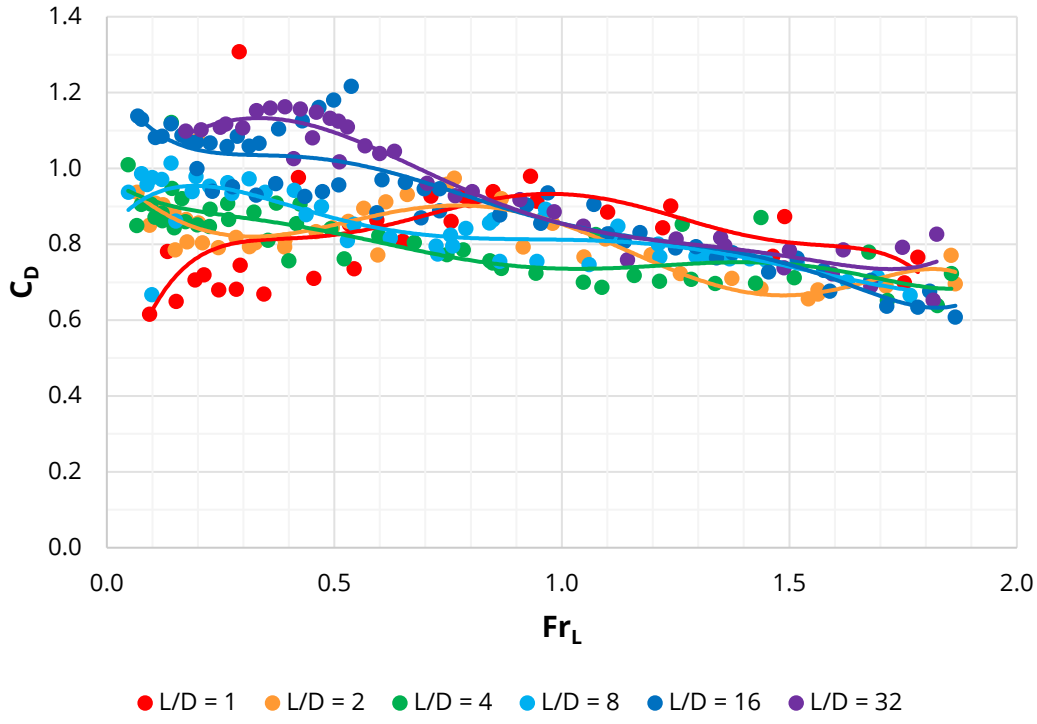

Figure 3-10: Drag coefficient vs Froude where L_0 < L and within the target Reynolds range (1E+4 – 2E+5)

Figure 3-10 presents the combined results from Figure 3-9 and the limiting fully ventilated Froude number as per Figure 3-8. A 6th order polynomial LoBF has been fitted to each of the data series in order to show at which convergence of the various aspect ratio results, these lines converge at approximately $Fr_L \approx 0.7$, after which all the aspect ratios have a similar trend.

Each aspect ratio is subject to its own unique LoBF, however the initial C_D spread as a function of Fr_L changes from the relatively flat plateau to an asymptotic exponential function at $Fr_L = 0.6$. At this Froude number the results fall into a somewhat narrow band with minimal spread.

There are several anomalous results when initially plotting the drag coefficient against the ventilated flow (Figure 3-11). The basis for the anomalies is unclear as Hay does not mention these awry points, nor is there a noticeable cause except that these points are well below the target Reynolds regime.

Figure 3-12 presents the drag coefficient versus the ventilated flow depth normalised to the submerged length when the ventilated flow depth is less than the submerged length ($L_0 < L = 1$) and within the target Reynolds range. The ventilated depth limit is implemented due to real-world practical considerations, where the L_0/L can far exceed 1.

An asymptotic relationship is evident for each of the data series. The asymptote appears to be in the range of $C_D \approx 0.6 – 0.65$.

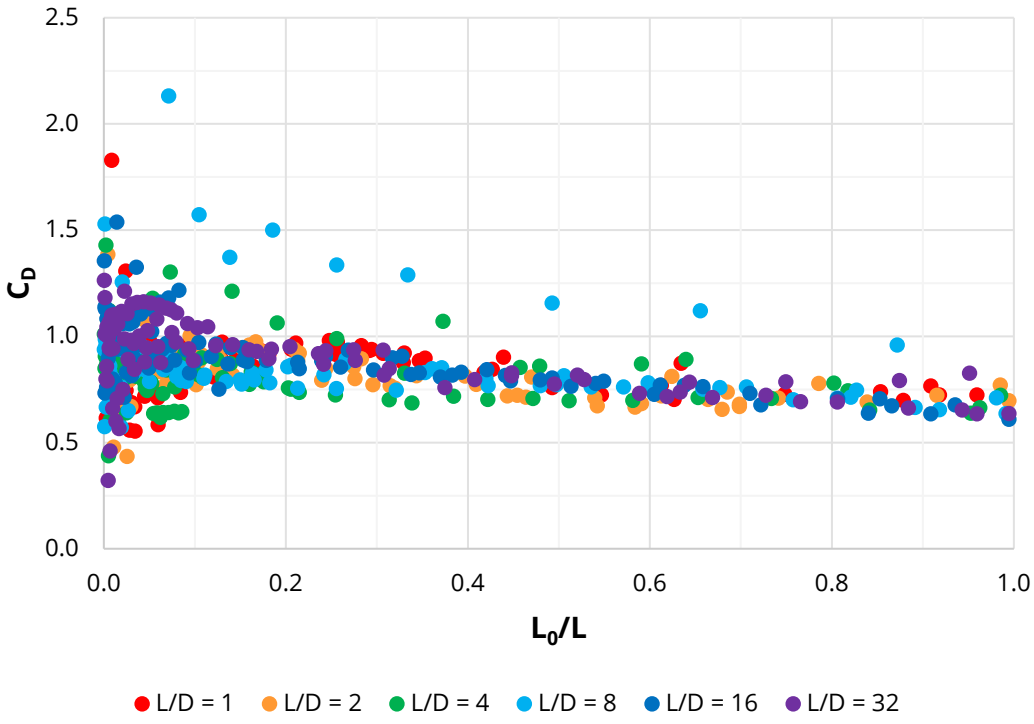

Figure 3-11: Drag coefficient vs L_0/L for fully ventilated flow

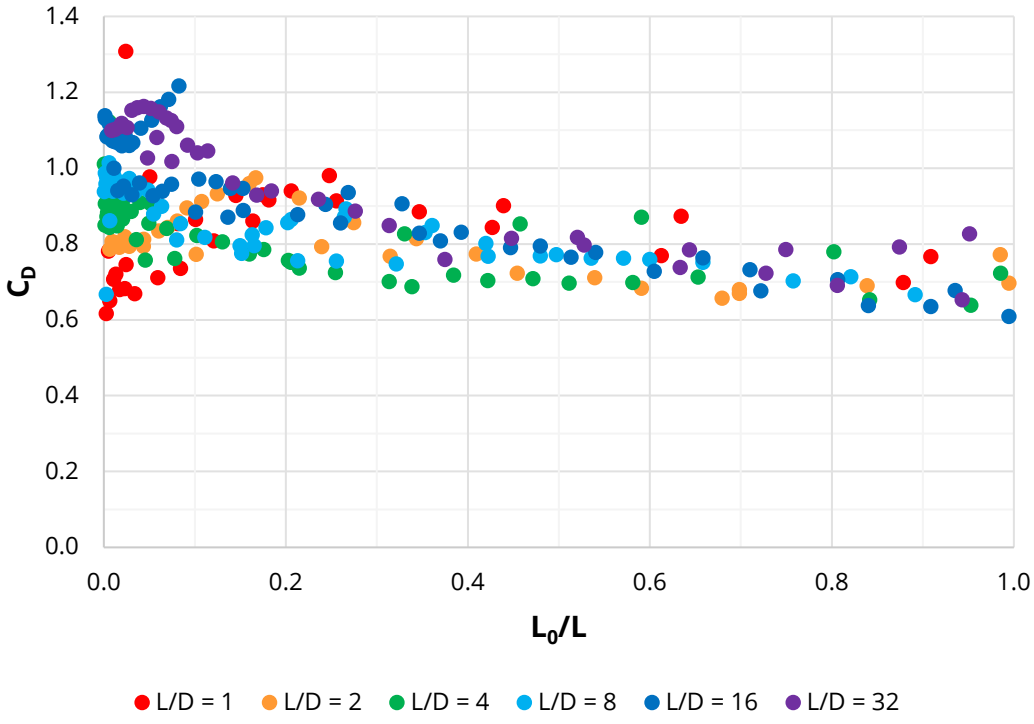

Figure 3-12: Drag coefficient vs L_0/L within the target Reynolds range (1E+4 – 2E+5)

3.3.3 Bow Wave

Keough et al. (2016) proposed an alternate form of the Bernoulli inviscid flow formula, shown here as Equation 28. In this formula a dissipation factor (C_{dissp}) has been considered, which aims to incorporate the bow wave eventually breaking at its maximum value.

$$D_1 = \frac{V^2}{2g} - C_{dissp}V^2 \qquad \text{Equation 28}$$

Equation 29 is a rearrangement of Bernoulli's inviscid flow formula as presented by Chaplin and Teigen (2003), and is plotted as the solid black line on Figure 3-13, Figure 3-14 and Figure 3-15.

$$\frac{D_1}{D} = 0.5Fr_D^2 \qquad \text{Equation 29}$$

When dividing the diameter through Equation 28 and substituting in the Froude number squared, the formula may be re-written as Equation 30, and is plotted as the red line on the ensuing plots.

$$\frac{D_1}{D} = 0.495Fr_D^2 \qquad \text{Equation 30}$$

It is apparent when comparing Equation 30 to Equation 29 that the Keough formulation of non-dimensional bow wave height results in a slight lateral shift of the log-log plot from the Bernoulli equation, with no reduction in the slope.

Figure 3-13 plots the bow wave height versus Fr_D for all conditions along with the calculated bow wave height from Keough as defined in Equation 28. It is further evident that the aspect ratio (L/D) has a negligible effect on the magnitude of the bow wave height with all of the different diameter symbols being grouped together regardless of the aspect ratio as shown in Figure 3-13.

It is apparent that the bow wave height is a function of the diameter as shown by the clustering of the symbols (thus agreeing with Bernoulli) shown in Figure 3-14.

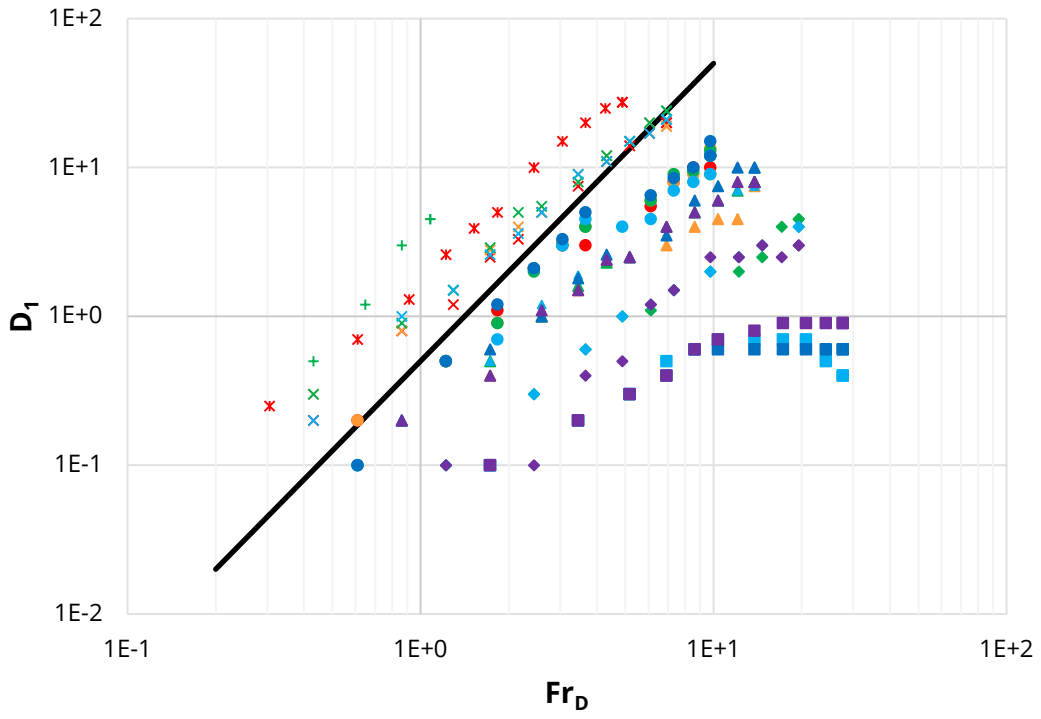

Figure 3-13: Bow wave vs Froude number for all cases, with the Bernoulli line (black)

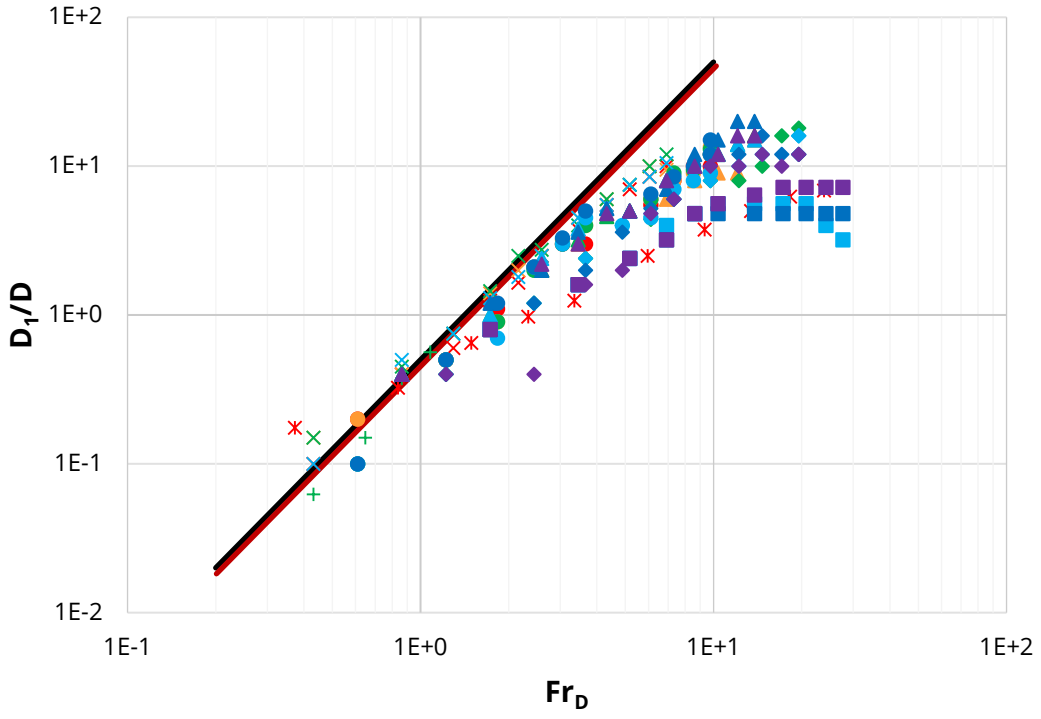

Figure 3-14: Bow wave normalised to diameter vs Froude number, with the Bernoulli (black) and Keough (red) lines

The Bernoulli equation closely resembles Hay's measurements of the bow wave up to a Froude squared of approximately 10, at which point the wave begins to asymptote to D_1/D = 20, as seen in Figure 3-14. Additionally, the Bernoulli equation presents what is effectively a limiting line, where the vast majority of the points fall below this line.

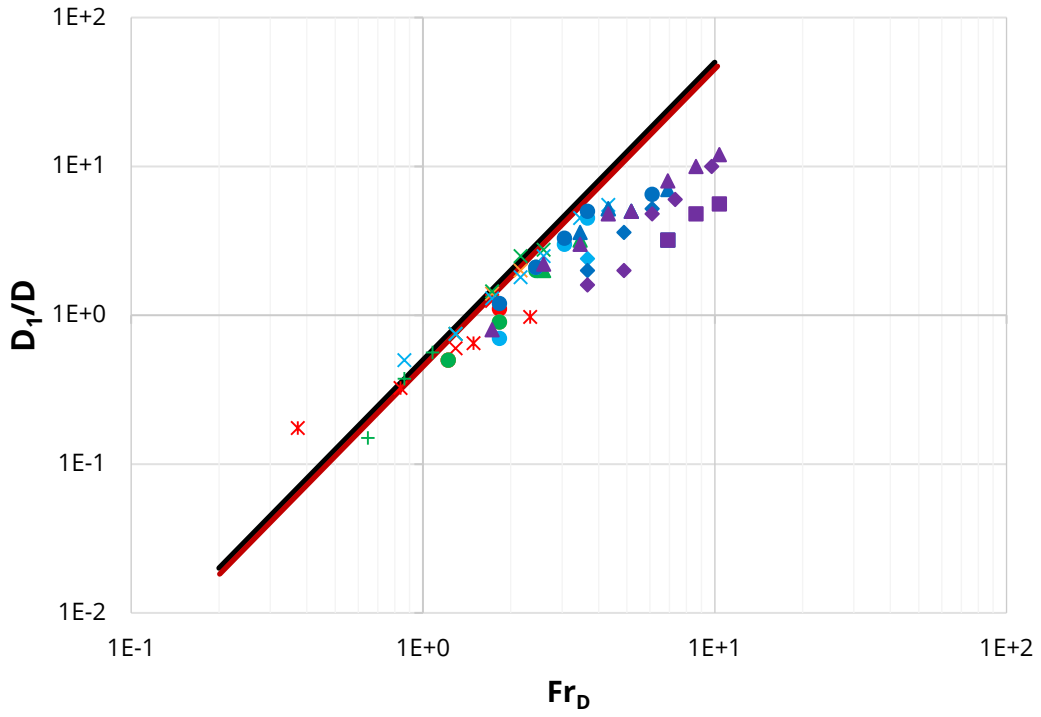

Figure 3-15: Bow wave normalised to diameter vs Froude number where L_0 < L, with the Bernoulli (black) and Keough (red) lines

Figure 3-15 confirms that there is a limiting Froude number in the determination in the relationship D_1/D: a hard Froude number limit occurs when Fr_D = 10. This limit occurs when the cylinder has become fully ventilated, which is opportune, as at this point the D_1/D data begins to plateau (see Figure 3-14).

3.3.4 Drag Modification Factor

The drag modification factor (κ) is a method of quantifying the drag coefficient as an additional multiplier applied to the base drag coefficient ($C_{D\infty} = 1.2$). When the modification factor is equal to 1 then the drag coefficient is equal to 1.2.

Figure 3-16 presents the modification factor from DNV GL (2017b); Wieselsberger (1921). It is evident that there is an error with the DNV GL data: the subcritical and supercritical data should be swapped. When referring to Figure 2-1, it is established that the drag coefficient in the super-critical regime is lower than that in the sub-critical regime. There is a high correlation between Weiselsberger and Hay showing that the modification factor reaches 1 at approximately $L/D \approx$ 32-40, which, when compared to the DNV GL data, the L/D value is far less than the stated L/D = 100. This level of correlation between Hay and Wieselsberger is unexpected as Wieselsberger's tests were performed fully on submerged cylinders and not surface-piercing cylinders as in Hay's study.

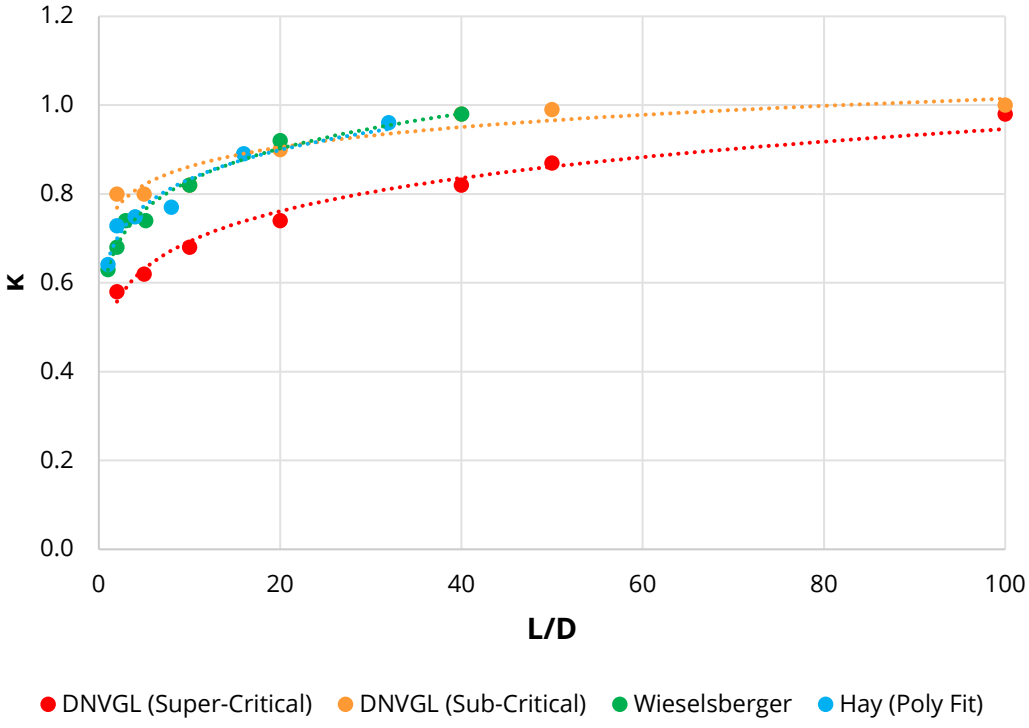

Figure 3-16: Drag modification factor vs L/D ratio for cylinders with one end abutted

3.4 SUMMARY OF FINDINGS

The following insights and findings were derived from the data analysis set out in this chapter:

1. The Chaplin and Teigen (2003) LoBF through the Hay results for L_0/D or L_0/L as a function of the Froude number has been found to correlate well with the Hay data. 80% of the partially ventilated results within the target Reynolds regime fall within one single standard deviation of the line. As such, it may be said that this line is representative of the Hay results.
2. In terms of the drag coefficient, the primary discernible outcome of the Hay data is that as the ventilated pocket depth increases, the drag coefficient decreases towards an asymptote of $C_D \approx 0.6 – 0.65$
3. A relationship between the bow wave height and Froude number derived from the Hay results is yet be elucidated, as the Bernoulli formula for inviscid flow and the altered formula by Keough et al. (2016) both appear to act as limiting lines, but are neither predictive nor representative lines.
4. The drag modification factor from Hay has a high correlation with Wieselsberger. This high correlation means that Hay's results resemble an infinitely long, fully submerged cylinder.

Therefore, there is a need to address each of the relationships discussed above in either a confirmatory manner or a new development manner.

Chapter 4 TESTING PROGRAMME

This chapter will discuss the model test programme undertaken in this investigation to measure the forces and accelerations of a series of circular cylinders. This test programme was performed using a modified test rig at AMC.

Section 4.1 explains the rationale for the model testing approach.

Section 4.2 describes the testing facility used, the natural frequency of the system, the selected models to be tested and the unique cylinder mounting system designed for this test programme.

Section 4.3 discusses the design of the models used in the test programme, including the anticipated dynamic frequencies for the prediction of VIV, the structural loading to ensure that the models chosen would not break at the desired testing criteria, the design of one of the end conditions and how the surface roughness of the models may alter the results.

Section 4.4 discusses the instrumentation used, the calibration of the instruments and the methodology of data acquisition.

Section 4.5 outlines the signal processing methodology, including a step-by-step acquisition process to generate the results.

Section 4.6 presents the methodology used to conduct photogrammetry of videos in order to capture and measure the bow wave height (D_1) and the ventilated pocket depth (L_0).

4.1 PURPOSE OF TESTING PROGRAMME

There is a significant gap in the body of knowledge regarding hydrodynamics of surface-piercing cylinders as shown in Chapter 2. To address this, the author has performed a thorough literature review and analysis of the seminal paper in the field and expanded the study to perform a model test programme.

This original test programme was designed to be directly comparable to published experimental results regarding cylinder properties including aspect ratio, velocity, and diameter.

In more recent times, Computational Fluid Dynamics (CFD) has solely been used by some researchers. However, this approach has limitations including:

- Inability to validate the simulation in the Hay test results. As discussed in Chapter 3, there are multiple issues with the Hay results, meaning that the CFD model would be validated against questionable data.
- Historically, CFD simulations were not capable of providing comprehensive results for super-critical flow and transitional flow conditions. Regardless of this point, physical model testing would be required in order to validate the model.

A physical model test programme was therefore undertaken to address these issues and to achieve the aims and objectives of the investigation.

4.2 FACILITY AND EQUIPMENT

This section describes the testing facility and equipment used in the testing programme to quantify the previously discussed parameters. Calibration of each of the instruments is briefly discussed.

4.2.1 Towing Tank

Figure 4-1 shows the AMC Towing Tank, which is 100 m long, 3.55 m wide, and has a 1.5 m nominal depth of water. The towing tank is filled with fresh water.

Figure 4-1: AMC Towing Tank including the towing carriage

The calculated blockage ratios (D/B) of the cylinder diameter (D) with respect to the tank width (B) equated to 0.01, 0.03 and 0.06 for the 24-, 48.3- and 101.6 mm diameter cylinders respectively. As per Allen and Vincenti (1944) and Zdravkovich (2003), blockage effects need to be accounted for when $D/B \geq 0.1$. As the blockage ratios were all < 0.1 blockage effects were determined to be negligible.

The temperature in the tank was measured on a daily basis during the testing programme and was found to be 18.5°C ± 0.5°C. Utilising the temperature and the fresh water parameters, several constants were calculated, including density (ρ) = 1000 kg/m^3, kinematic viscosity (ν) = 1.04E-6 m^2/s, and dynamic viscosity (μ) = 1.04E-3 Pa•s.

4.2.2 Tow Carriage

The speed of the tow carriage was measured using continuous recording from the rear motor controller. The carriage has the capability of a maximum speed of 4.6 m/s, where the constantly measured speed was close to the recommended tolerances as set out by the ITTC (Procedure 7.5-02-02-01), and the measured speed of the model should be within 3 mm/s or 0.1% of the maximum speed, whichever is greater (ITTC (2017)).

A laser range finder was mounted on the tow carriage with a receiving target at the end of the tow tank, which is critical to the control of the tow carriage. If the laser beam is deflected off the target, the carriage control system is shut down as a fail-safe and brought to an immediate halt. During the tests where excessive cylinder vibration occurred, these vibrations were transmitted into the laser whereby on occasions the excessive vibration caused the laser beam to be deflected off target and prematurely curtailed that test. In such instances this caused the author to redefine the maximum velocities from those as set out in the original test plan.

Figure 4-2 and Figure 4-3 present the results of a test run that aimed to determine the natural vibration frequency and the noise of the carriage, which was measured via both the accelerometer and the load cells. The cylinder was mounted in-air (not penetrating the free-surface) and the carriage was accelerated to the maximum testing velocity (4 m/s). The Power Spectral Density (PSD) shows two distinct peaks, with the first peak being the first natural frequency of the test rig.

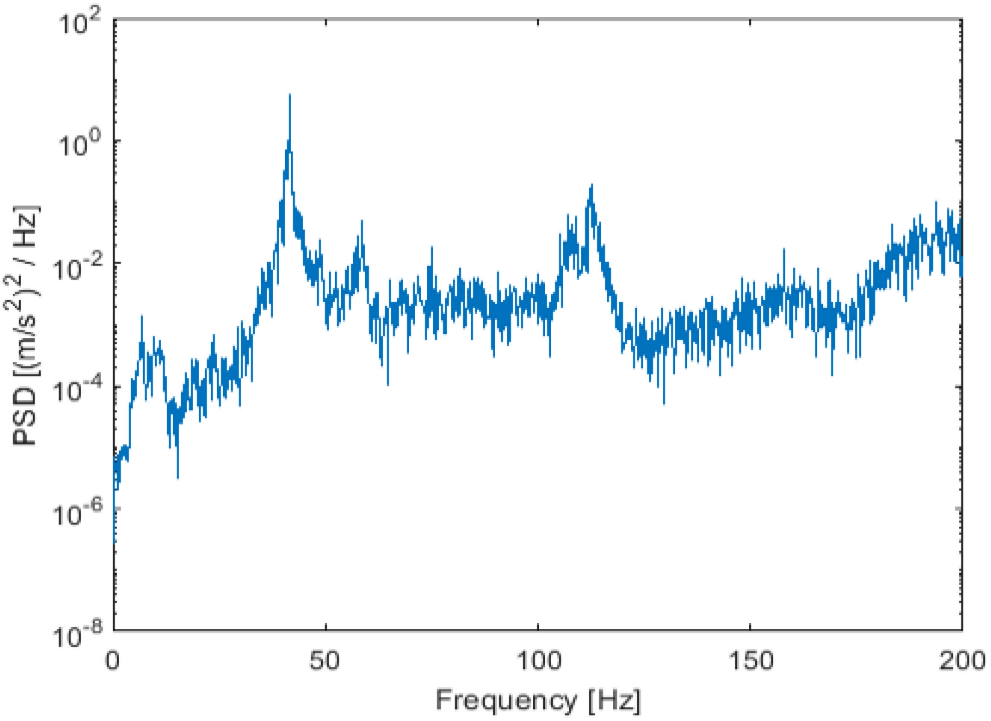

Figure 4-2: Run 195 – Accelerometer Power Spectral Density vs frequency of tow carriage

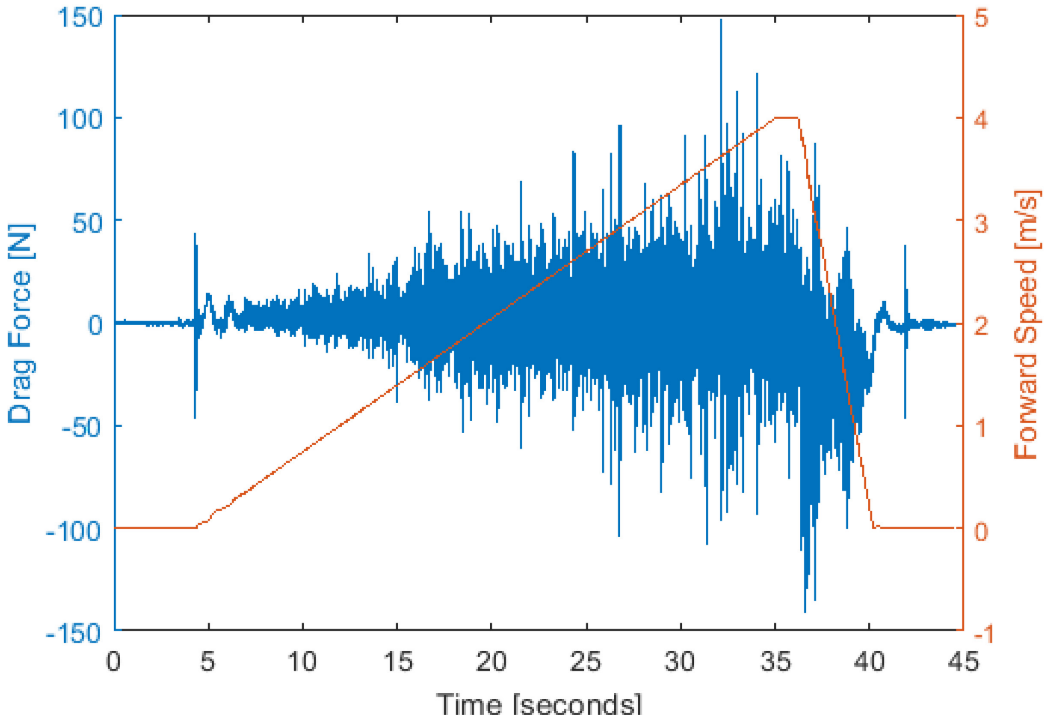

Figure 4-3: Run 195 – Drag force and towing speed time series

4.2.3 Test Models

The test models consisted of three different diameter cylinders/rods made of Black CHS steel in accordance with AS/NZS 1163:2016 (Standards Australia and Standards New Zealand (2016)): 24 mm (rod), 48.3 mm (cylinder), and 101.6 mm (cylinder). Table 4-1 presents the diameters and aspect ratios that were tested.

Table 4-1: Test model diameters and aspect ratios tested

	Diameter (mm)		
L/D	**24**	**48.3**	**101.6**
1	X	X	X
2	X	X	X
4	X	X	X
8	X	X	X
10	X	X	X
16	X	X	
20	X	X	
32	X		
40	X		

Figure 4-4 presents the Reynolds number regime as a function of the tow velocity for each of the selected cylinder models, where the selection was based primarily on the blue subcritical Reynolds range (as per Figure 2-1).

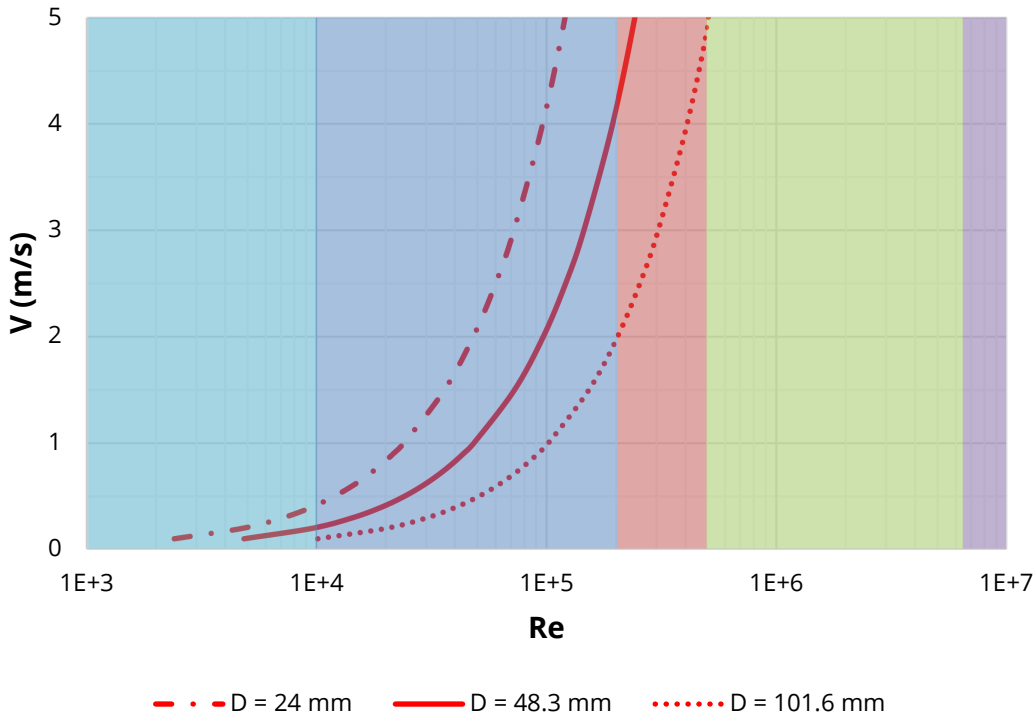

Figure 4-4: Flow velocity vs Reynolds number for test model cylinder diameters, with associated Reynolds flow regimes adapted from Barltrop and Adams (1991)

4.2.4 Model Cylinder Mounting System

The conventional testing arrangement for mounting surface-piercing cylinders on the AMC tow tank carriage was employed in the investigations by Cathcart (2014); Conway et al. (2015); Keough et al. (2016). They utilised a lower mounting point with a sliding pivot point, with load cells located at the uppermost reaction point and on the lower slide support. This arrangement did not readily enable adjustment to the length of the cylinder submerged in the tank. A new clamping mechanism for the cylinders was designed for this investigation enabling the submerged depth of the models to be easily changed. This also transformed the lower mounting point from a sliding pivot to a fixed clamp point with in-line and crossflow degrees of freedom, thereby better retaining rigidity of the cylinders in these degrees of freedom.

Figure 4-5 shows the cylinder mounting system on the towing carriage. The mount consists of four key components:

1. The ‘Strongback’ – this is the AMC vertical mount for use in the surface-piercing cylinder testing.
2. Load Cell Mounting Plate – this small plate attaches the load cell to the strong back.
3. Rigid Plate – a long plate which connected the two load cells. It provided rigidity to the load cell connections and alignment of the load cells, and it was the connection point for the cylinder clamps to the load cells.
4. Cylinder Clamps – these were specifically designed for each different cylinder diameter, facilitating easy un-clamping from the model in order to change the aspect ratio with minimal downtime between test series.

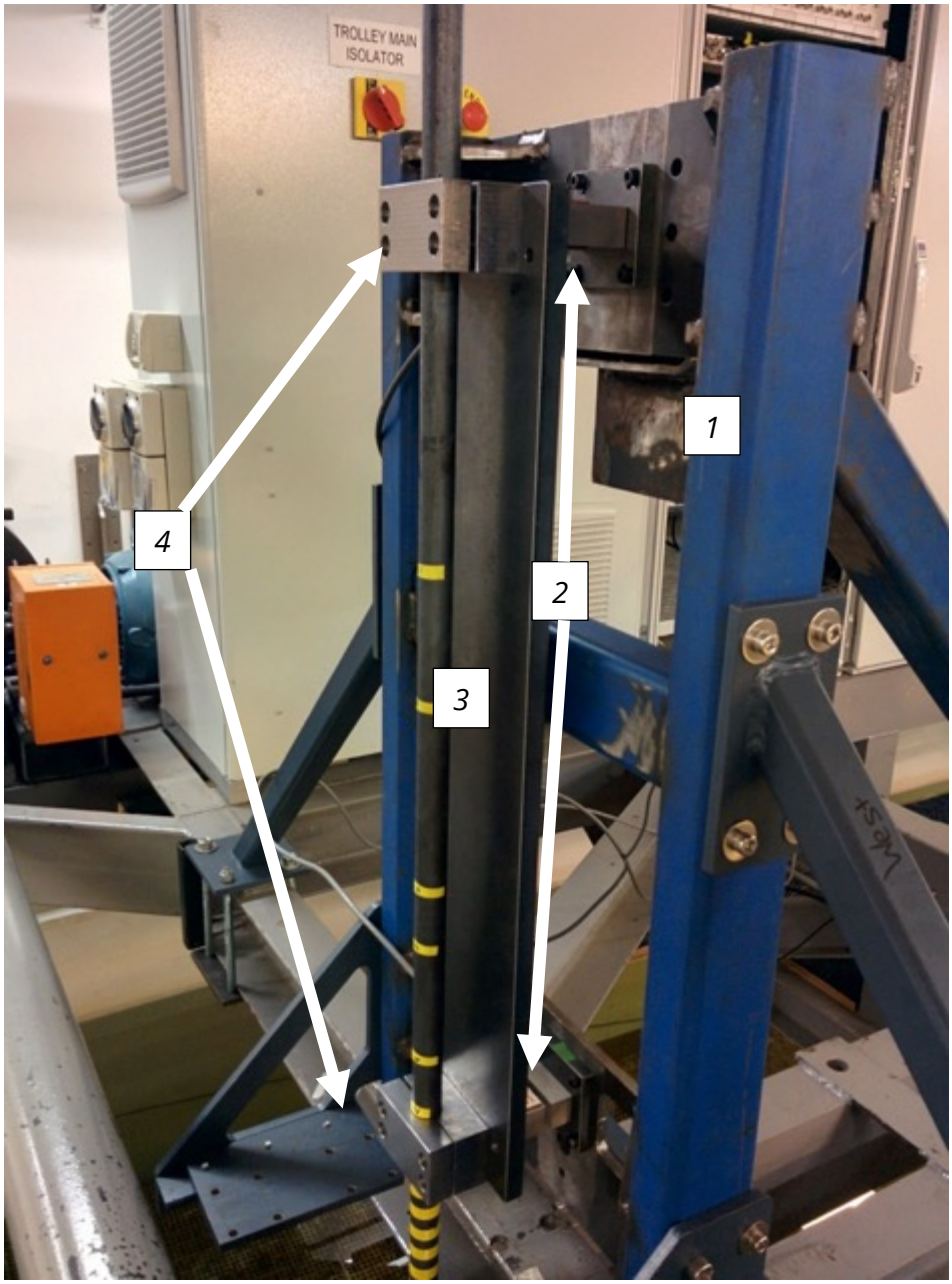

Figure 4-5: Cylinder mounting system on tow carriage

4.3 TEST MODEL DESIGN

4.3.1 Anticipated Dynamic Frequencies

Prior to test programme development, the anticipated vibration for the natural frequencies of the cylinders for each *L*/*D* ratio were calculated using propped cantilever theory (Blevins (1979)) to determine the appropriate Nyquist (critical sampling) rate to avoid aliasing distortion. Table 4-2 presents the calculated anticipated natural frequencies for all test model conditions, and Appendix A presents the frequencies in terms of the Reduced Velocity (*Vr*).

Preliminary calculations concluded that the 24 mm rod was to go through the lock-in nominal reduced velocity in the first natural mode for all aspect ratio conditions, and partially enter the lock-in range for the second natural mode for *L*/*D* = 40. The 48 mm was anticipated to begin entering lock-in at an *L*/*D* = 8, only for the first natural mode. The 101 mm cylinder was never expected to enter lock-in.

Table 4-2: Anticipated natural frequencies of the first two modes of vibration

Diameter (mm)	L/D	f_{n1} (Hz)	f_{n2} (Hz)
24	1	11	73
	2	10.4	72
	4	9.3	69
	8	7.5	64
	10	6.8	62
	16	5.1	54
	20	4.3	48
	32	2.8	34
	40	4	27
48.3	1	28.6	193
	2	25	184
	4	19.6	166
	8	12.8	133
	10	10.6	118
	16	6.5	80
	20	4.9	61
101.6	1	51.9	385
	2	39.5	339
	4	24.8	261
	8	12.1	148
	10	9	112

From the anticipated first natural frequencies the Nyquist (sampling) rate was required to be at least two times the highest expected first natural frequency. For the 101 mm cylinder, f_{n1} = 51.9 Hz, therefore the sampling rate required was at least 103.8 Hz.

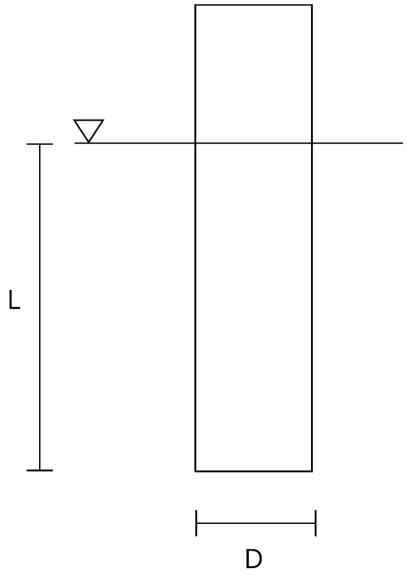

Figure 4-6: Diagram representing the parameters of submerged length (L) and diameter (D)

Figure 4-6 presents a simple diagram which defines both the variable submerged length (*L*), which is measured from the still water level down to the submerged free end-tip, and the model diameter (*D*).

4.3.2 Structural Loading

Structural load calculations were undertaken to determine the approximate loading on each cylinder for the *L*/*D* ratios and velocities and to develop the test programme. These calculations comprised three checks to determine whether the specific test case was viable:

1. The maximum load which can be applied to the load cells.
2. Stress checking the cylinder section capacity.
3. Checking the tip deflection.
    - If the model is deflected too much due to the structural loading, then the likelihood of VIV is reduced due to the added stiffness.

The 24 mm rod at L/D ratios of 32 and 40 failed the section capacity check at 4 m/s, as such the maximum speed was reduced to the point where the rod passed the section capacity check. Additionally, the expected forces acting on the 101 mm cylinder were greater than the load cell capacity, thus the maximum speed was reduced. During the testing, it was discovered that the expected forces were less than anticipated; the same may be said for the end-tip deflections. As such the test programme was altered to allow for higher speeds where possible. This however was not the case for some conditions, where the end-tip deflections were far greater than expected and the velocities had to be reduced. Only the 48 mm cylinder was affected by an increase in tip deflections, such that for aspect ratios of 16 and 32 the velocities were reduced to 2.5 m/s and 2 m/s respectively.

4.3.3 End Condition

Three end conditions were tested to determine the different end-tip effects. The three conditions were: Open, Closed, and End-plate. The open condition comprises a hollow cylinder, where air and water could flow freely through the pipe. The closed condition had an end cap on the submerged end which prevented air and water from entering the pipe. The end-plate, as shown in Figure 4-7, was a circular disk with the dimension D_{EP}/D = 3 (144.9 mm) and a thickness of 4 mm, which was determined by Potts et al. (2019b) to be the bare minimum end-plate to diameter ratio required to minimise the end-tip effects. All three end conditions were tested on the 48 mm cylinder, whereas the 24 mm and the 101 mm were both closed.

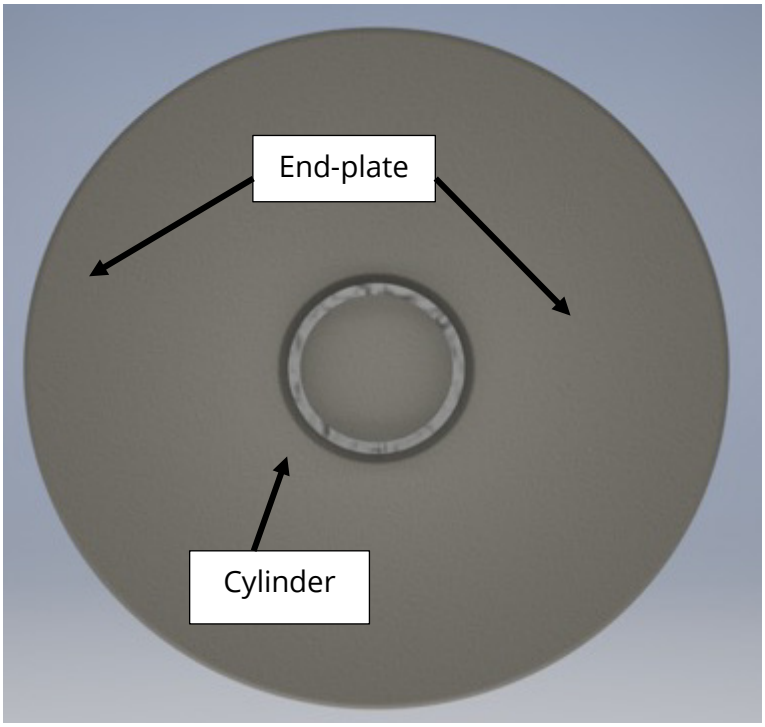

Figure 4-7: 48.3 mm cylinder with end-plate

4.3.4 Geometric Surface Roughness

The models were made of black steel covered incrementally with 10 mm wide vinyl strips to provide a contrasting scale for photogrammetry. The vinyl wrap was 64 microns (0.064 mm) thick with a surface roughness of k_v = 0.005 (Nayyar (2000)) compared with the black steel surface having a roughness of k_s = 0.025 (Nayyar (2000)). The overlay of the vinyl strip corresponded to an alternating step change in model test cylinder diameter of 0.13% – 0.53% from largest to smallest cylinders.

Table 4-3 presents a roughness categorisation for each of the test model diameters.

Table 4-3: Roughness categorisation of test models

Diameter (m)	k_s (μm)	k_s/D	k_v (μm)	k_v/D	Total Roughness
0.024	25	1.04E-03	5	2.08E-04	1.25E-03
0.0483	25	5.18E-04	5	1.04E-04	6.21E-04
0.1016	25	2.46E-04	5	4.92E-05	2.95E-04

Where:

k = explicit roughness

k/D = relative roughness

Achenbach (1971) discusses the effect that the surface roughness has on the drag coefficient. It was found that roughness does not have an effect on the flow pattern and the force parameters in the sub-critical regime due to the boundary layer thickness. When this logic is applied to the testing conducted, the 24 mm and low velocity tests of the 48.3 mm models were not affected.

For the 48 mm and the 101 mm models the surface roughness would only affect the drag crisis. However, since their respective roughness's are towards the 'smooth' end of the scale, the effect would be minimal and may therefore be considered inconsequential.

4.4 INSTRUMENTATION AND DATA ACQUISITION

4.4.1 Load Cells

Two X-Trans S1W load cells were used to measure the force acting at the cylinder connection points. These load cells had a maximum working load range of 3.5 kN.

To calibrate, the load cells were attached to a load bearing column attached to the roof, where known weights (subsequently converted to Newton) were continuously added until the desired maximum force as per structural load calculations was achieved.

The following calibration steps were performed:

1. Hang load cell from ceiling.
2. Measure the zero voltage with nothing attached to the load cell.
3. Begin to add weights and capture the voltage of the weight. (Note: the weights were converted to forces, as such the calibrations were in Newton).
4. Once at the desired maximum working load (Figure 4-8), a hysteretic unloading was conducted, where the weights were removed, and the associated calibration force was captured.
5. Once the weights were removed the load cell was then attached to the mounting rig, ready for testing.

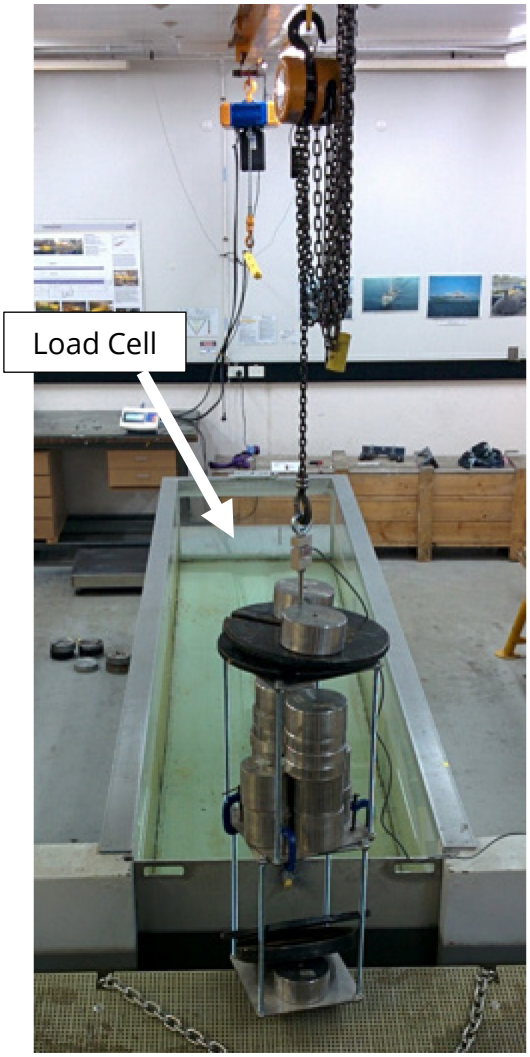

Figure 4-8: Load cell calibration set-up

Appendix B presents the calibration curves for both load cells for all three test cylinders.

This check was performed at the start of each cylinder diameter test series in order to establish the gain settings for the desired working range. A drift check was conducted at the end of each test series for each test cylinder diameter.

The load cell data was digitised using a Vishay Strain Gage Conditioner. The gain was altered during each of the calibration processes, and the difference between the two force transducers was minimal.

Table 4-4 presents the gain settings for each of the load cells on the Strain Gage Conditioner for each cylinder diameter.

For each diameter cylinder, different gain settings were required as each model had a different calculated maximum loading. As such, the amplification of the signal for each cylinder needed alteration, hence why different gains were required.

Table 4-4: Calibration gains for the load cells for each cylinder diameter

Diameter (mm)	Upper Load Cell	Lower Load Cell	Working Load Range (N)
101.6	2.13	2.06	2550
48.3	3.54	3.35	1550
24	7.00	6.98	869

The sampling frequency for the load cells was set to 2000 Hz, which was much greater than the required Nyquist rate, thereby allowing for decimation if necessary.

The test programme was conducted over a period of five days. During that time the load cells were in continuous use and were not removed from the tow carriage mounting, except for calibration. There was no change in the linearity or the Voltage vs Force slope, however there was a very slight drift in the recorded zero force voltage. The drift of 0.5% occurred with each of the model cylinder diameter test series and was attributed to the calibration measurement procedure where no adjustment was made.

A drift check was conducted before changing the cylinders between tests. It was found that the initial reference point had drifted 0.5% of the maximum load (i.e. max force ≈ 2550 N, drift ≈ 12 N). This drift had occurred over the duration of the testing programme for each model, which was 2-3 days depending on the model.

4.4.2 Accelerometer

An X-sens MTi-30-2A5G4 series accelerometer was used to measure the accelerations and subsequently calculate the displacements of the submerged end-tip. The accelerometer was positioned 300 mm below the centreline of the lower force transducer. A jig was designed, and 3D printed which allowed for the alignment of the accelerometer to be consistent between each test set-up as well as running along an axial centreline allowing for consistent capturing of the in-line and crossflow vibration motions. The accelerometer was bolted to a 3D printed mount which was then tightly cable-tied to the cylinder (the location of the accelerometer was checked at the start, end and during each test set-up to check for any movement).

The accelerometer was calibrated by the manufacturer prior to our application (i.e. no further calibrations were conducted). A sense check was conducted at the beginning to ensure that the vertical axis (the local x-axis) was measuring gravity (9.81 m/s^2).

The accelerometer was set to a sampling frequency of 400 Hz, which would allow for decimation if necessary, as this was much greater than the anticipated Nyquist rate.

4.4.3 Cameras

Two GoPro Hero 4 Black cameras were used for capturing the cylinder above and below the water surface. The cameras were run using the linear field of vision capture mode at a rate of 60 frames per second (60 Hz). The underwater camera was located 660 mm to the side from the centroid of the cylinders and was submerged 400 mm below the water surface inside a large slightly modified Gottingen GOE 775 hydrofoil (referred to as a borescope), similar to the one used by Ashworth Briggs et al. (2018). The above water camera was located 1100 mm in front of the cylinder and 445 mm from the water surface. Figure 4-9 presents a comparison of the borescope used to house the camera, alongside the GOE 775 hydrofoil.

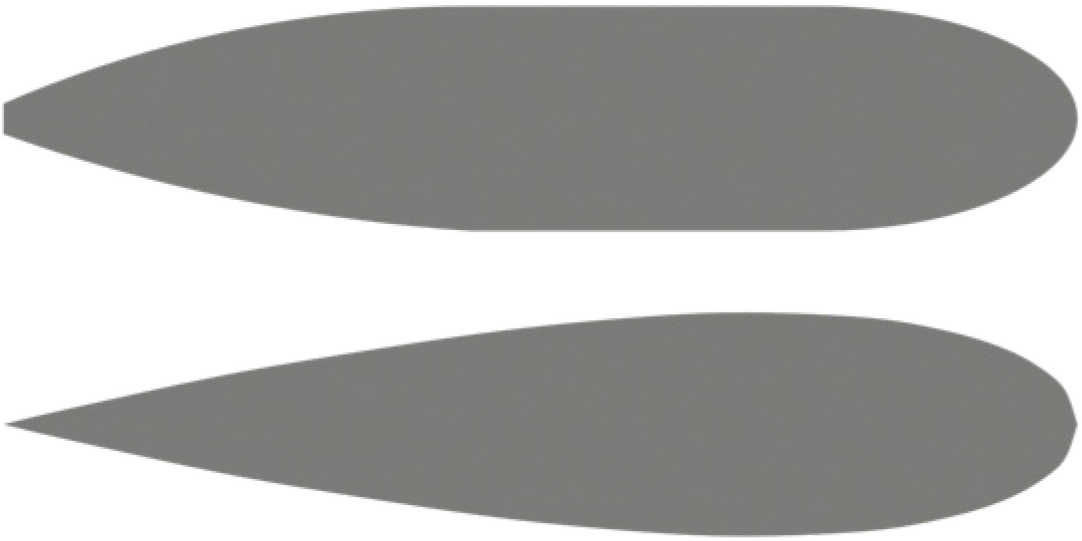

Figure 4-9: Profile comparison of borescope (top), and GOE 775 hydrofoil (bottom)

Figure 4-10 presents the profile view of the borescope and the 101.6 mm model cylinder. Here it can be seen that the spacing is large enough for the boundary layer developed from the borescope to not influence the cylinder model. Furthermore, it is noted that during the testing the borescope did produce a large bow wave both in height and spray width, but it did not affect the bow wave development of the test cylinder. The interference of the borescope was visually checked during the initial test run for each model diameter. In addition to the visual check, the blockage effect of the borescope was calculated, where the *D*/*B* value for each diameter was deemed to be negligible.

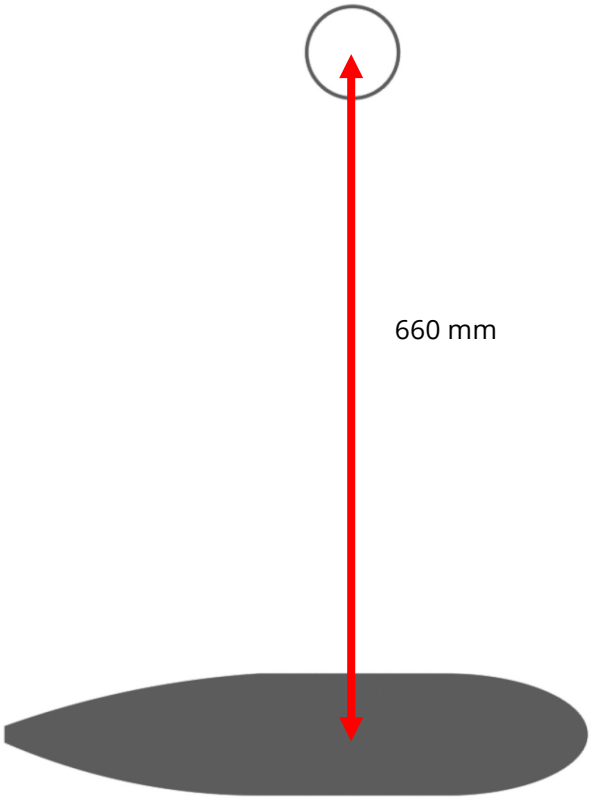

Figure 4-10: Profile separation of test model cylinder (101.6 mm) and the borescope

4.4.4 Data Acquisition System and File Format

The signals from each instrument, excluding the X-Sens accelerometer, were digitised using a National Instruments PCI-6254M Multifunction Data Acquisition Card and recorded on a Dell computer. The data acquisition process was controlled by a LabVIEW based software that was developed in-house.

The data acquisition for the X-Sens accelerometer was controlled by X-Sens MT Manager software on the same Dell computer. The general format of the raw data files remained constant throughout the test program. Each run file contains information about the instruments utilised at the head of the file, followed by columns of run time data.

Figure 4-11 shows a simple block diagram indicating the instruments and devices for data measurement, capture, processing, storage and analysis.

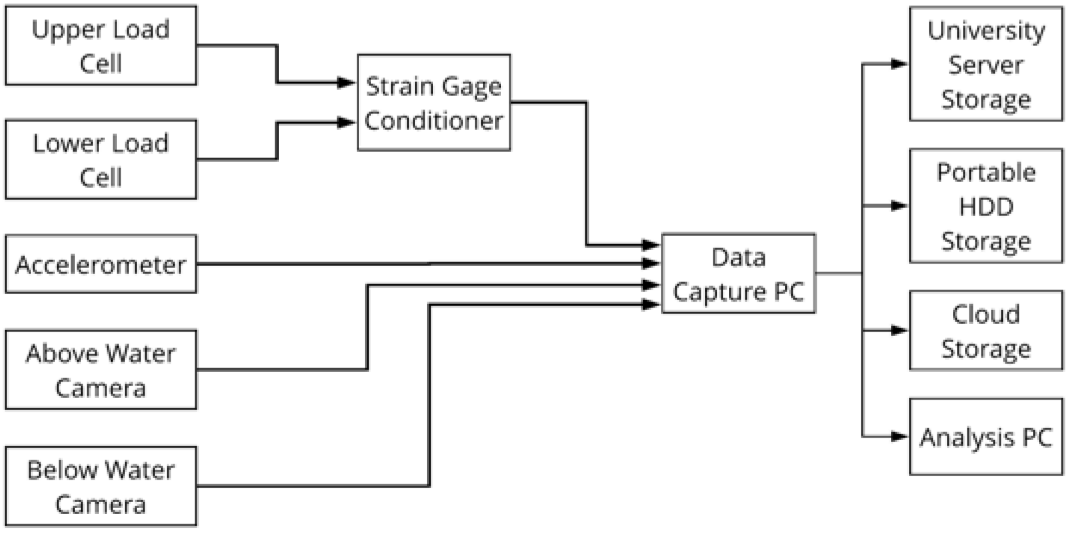

Figure 4-11: Block diagram of the instruments and devices utilised in the testing programme.

4.4.5 Data Zeroing at Test Commencement

Prior to each run being conducted, three seconds of data was collected while the carriage was static. This provided an initial ‘zero’ position for each of the instruments. Following the ‘zeroing’ of the data, the video recording was started. Recording continued until the carriage had come to a complete stop; thus, the duration of recording time varied with the various carriage speeds.

During the tests the instruments were monitored live, to ensure that there were no serious anomalies, and in the cases where there were, the test was re-run.

4.5 SIGNAL PROCESSING

Each time series was comprised of the data from the accelerometer and the load cells, where the signal processing was conducted consequentially for each test case.

The duration of the collected data was manually selected from each time series. For the steady state tests, each domain was selected based on the most uniform response, and for the ramp up tests, the domain was selected based on the start and end of the velocity range.

Hereafter the steps taken in processing the data gathered will be discussed. The signal processing was conducted in MATLAB 2018a, using the signal processing toolbox.

4.5.1 Accelerometer

The block diagram presented in Figure 4-12 presents the key steps taken in converting the raw accelerometer data into the accelerations and displacements at the fully submerged end-tip.

The numbered points describe details of the related step elements.

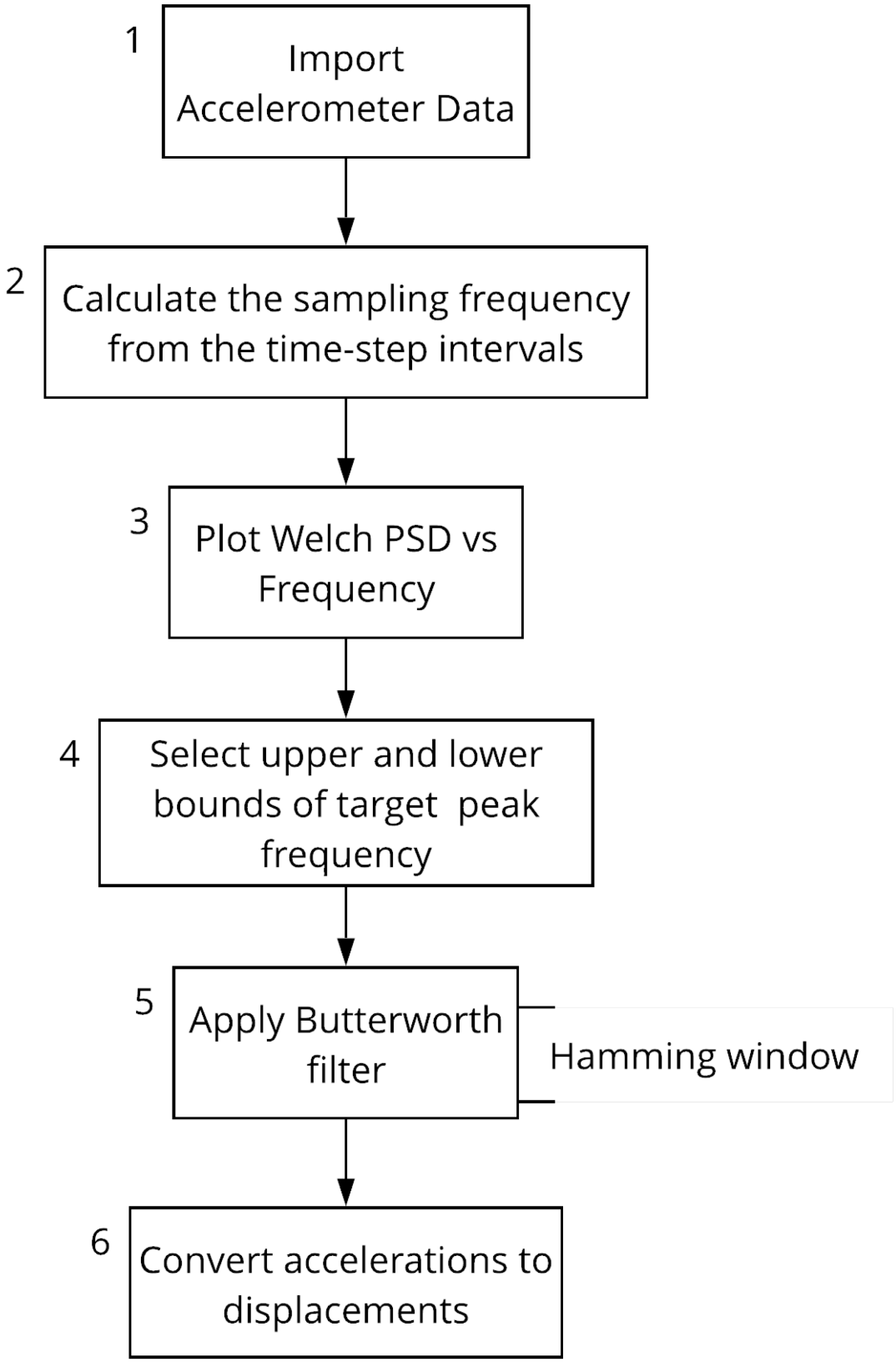

Figure 4-12: Block diagram of the accelerometer signal processing steps

1. The accelerometer data was imported, where the window width, overlapping window width and the number of frequency points were set as user inputs to provide high-resolution signal processing.
2. The sampling frequency, although already known to be 400 Hz by design, was confirmed via calculation from the time steps.
3. The Welch Power Spectral Density (PSD) versus the frequencies up to the Nyquist frequency (200 Hz, Figure 4-13) was plotted, and then the frequency range was cropped to a maximum of 50 Hz (Figure 4-14). This frequency is where the predicted first natural vibration mode should occur. It was determined empirically that the transverse natural frequency of the towing carriage is approximately 42 Hz.
4. On the PSD plot, the upper and lower bounding limits of the target peak frequency were selected (Figure 4-14). The limits act as a low and high pass filter, thereby removing all non-essential data.
5. Using the data within the bounding upper and lower limits, a Butterworth filter was applied with a Hamming window implemented to reduce the end effects of each window bin.
6. From the windowed and filtered data, double integration of the accelerations resulted in the displacements at the accelerometer location. To transfer the displacements from the accelerometer down to the fully submerged end-tip, Modal Amplification Factors from Blevins (1979) were implemented (see Figure 4-15 and Figure 4-16). Additionally, the peak frequency value can be used in calculating the Strouhal number.

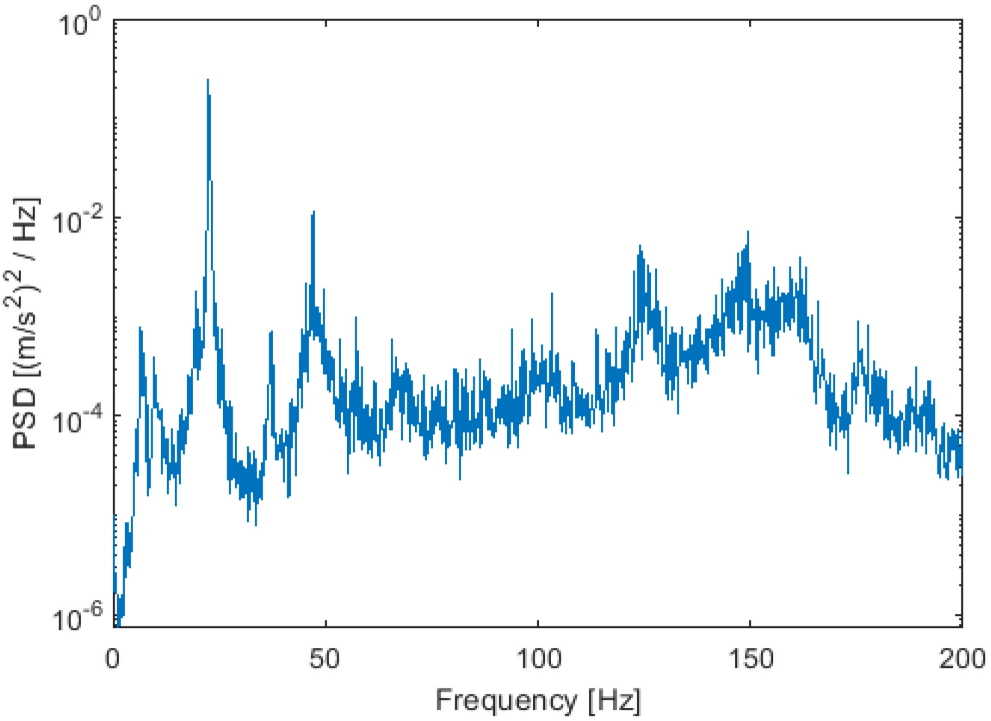

Figure 4-13: Run 106 – Crossflow PSD vs Nyquist frequency range

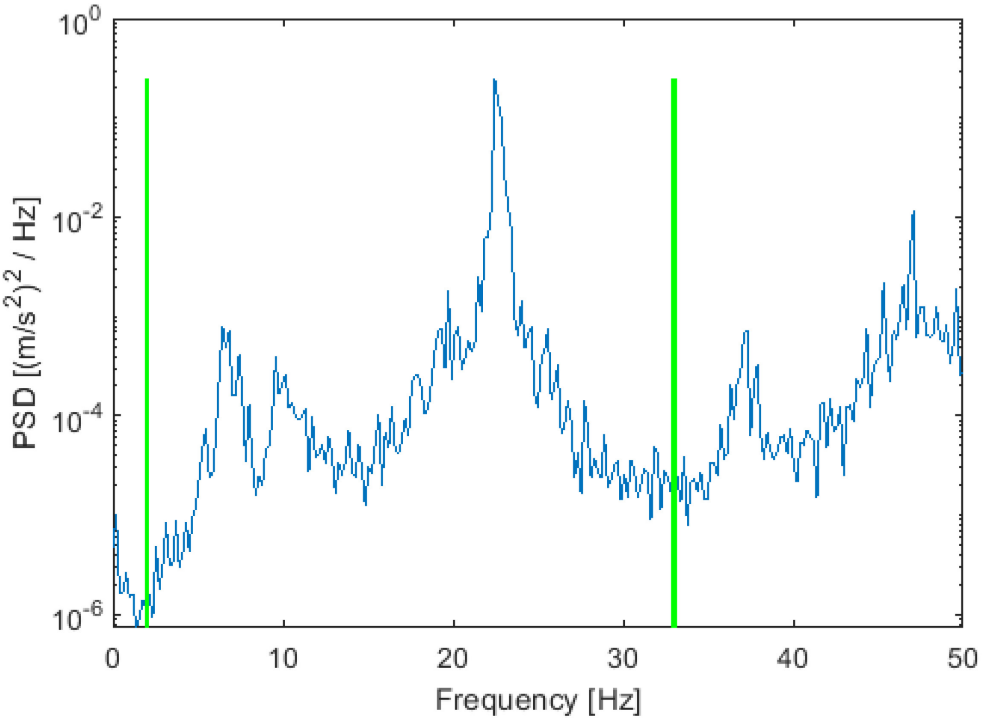

Figure 4-14: Run 106 – Upper and lower limits of target frequency

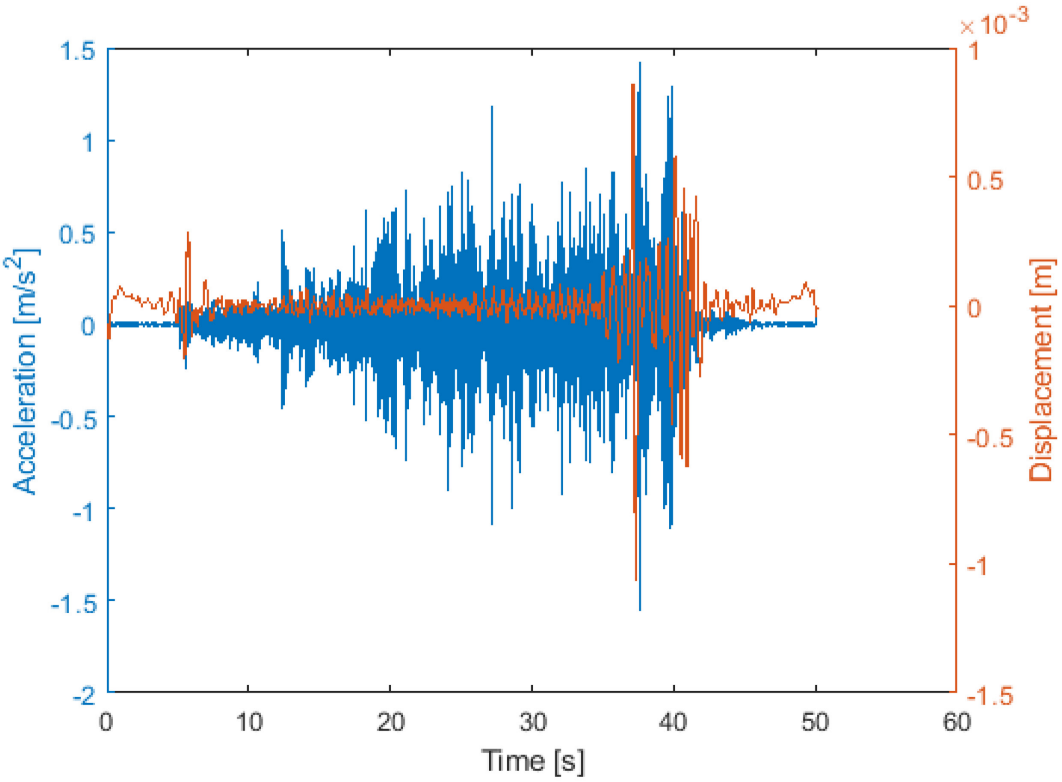

Figure 4-15: Run 105 – Filtered crossflow accelerations and displacements

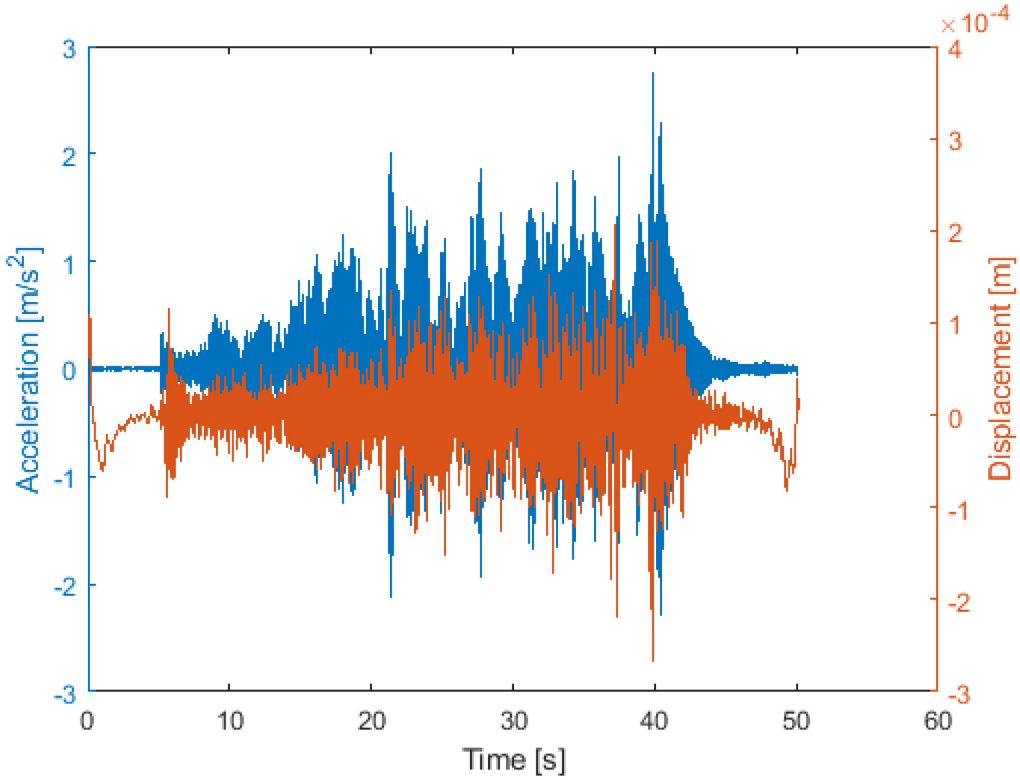

Figure 4-16: Run 105 – Filtered inline accelerations and displacements

4.5.2 Load Cell

Figure 4-17 presents a block diagram of the signal processing of the load cell data.

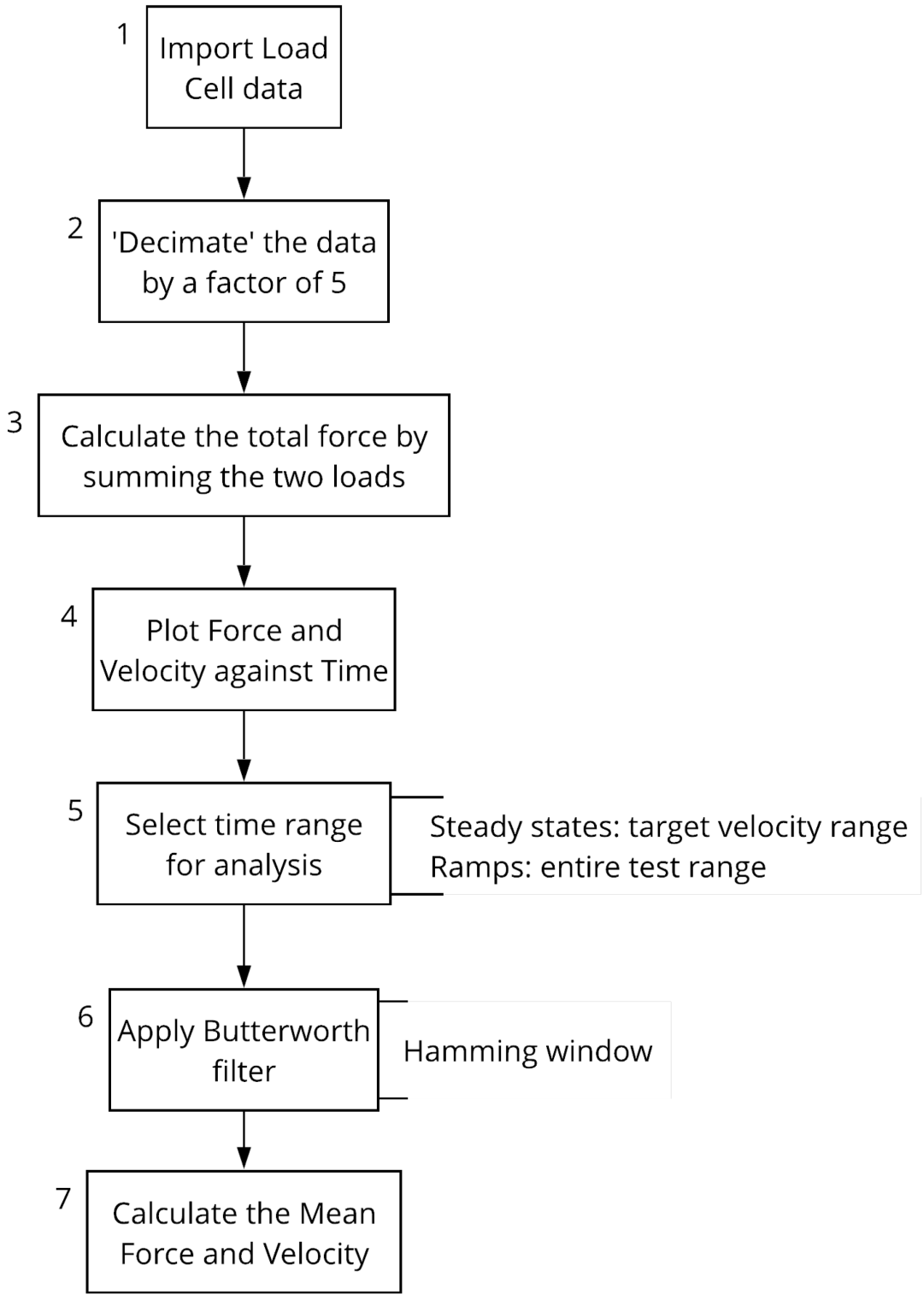

Figure 4-17: Block diagram of the load cell signal processing steps

1. The data from the load cells were imported, where the windowing width, overlap window width and the number of frequency points were set as user inputs to provide a high-resolution signal processing.
2. The data was then 'decimated' to match that of the accelerometer (i.e. from 2000 Hz to 400 Hz), as the load cell sampling frequency was five times larger than the accelerometer.
3. The measured forces from the load cells were summed together to determine the total force applied to the model. Figure 4-18 presents a simplified side-view diagram of the test cylinder model, the load cells, the towing direction and the drag force direction.
4. The time series of the total drag force and the towing velocity was plotted (Figure 4-19).
5. As for the accelerometer, the upper and lower bounds of the data were manually selected. For the steady state tests (Figure 4-19) the range was in respect to the uniformity of the towing velocity (i.e. when the velocity was stable). However, for the ramp up tests (Figure 4-20), the range was selected based on the full velocity spectrum, cutting out the initial zeroes and deceleration at the end of the runs.
6. Similarly, the drag force and towing velocity data were passed through a Butterworth filter with a Hamming window. The "Filtered" data in Figure 4-21 is derived from this step.
7. The filtered data was then used to calculate the mean force (yellow line from Figure 4-21), the mean velocity, the drag coefficient, Froude number, nominal Reduced Velocity, Strouhal number, and Reynolds number.

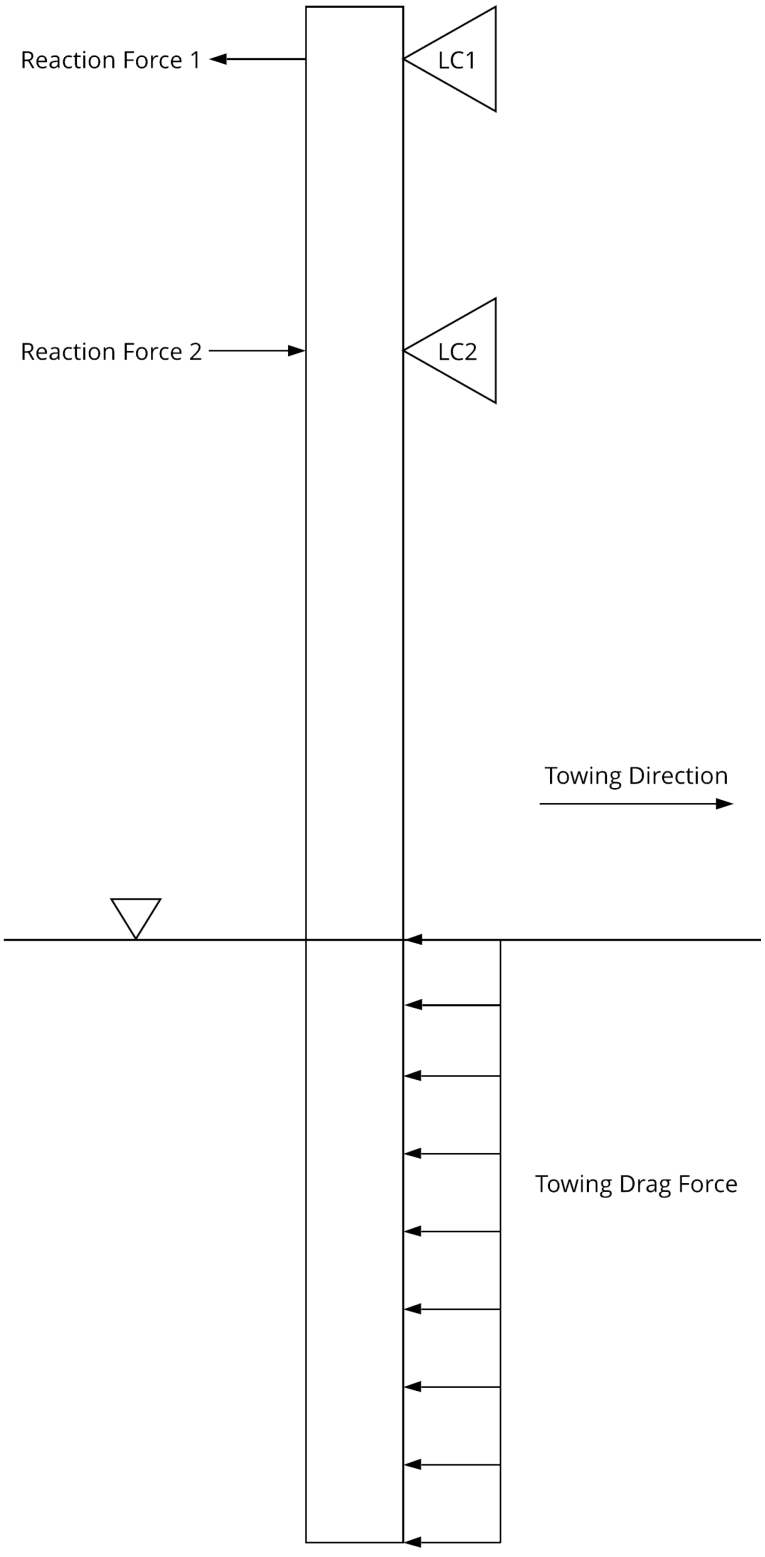

Figure 4-18: Diagram of the loading acting on the models

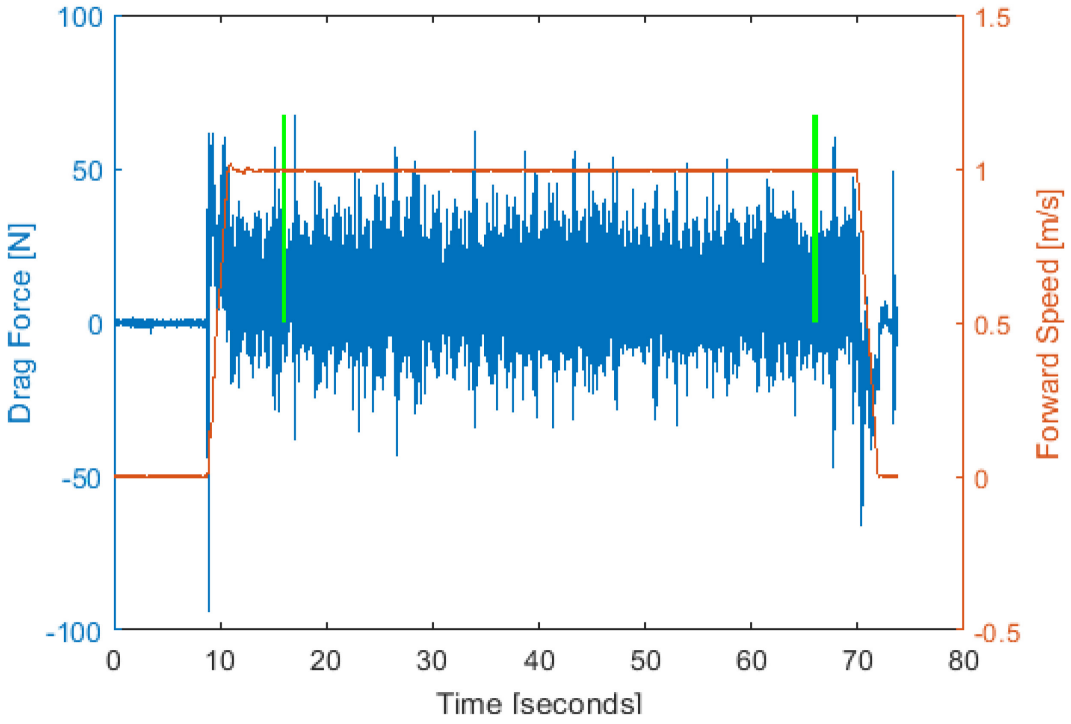

Figure 4-19: Run 106 – Upper and lower limits of target speed range. The green lines are the upper and lower bounds of the data of interest

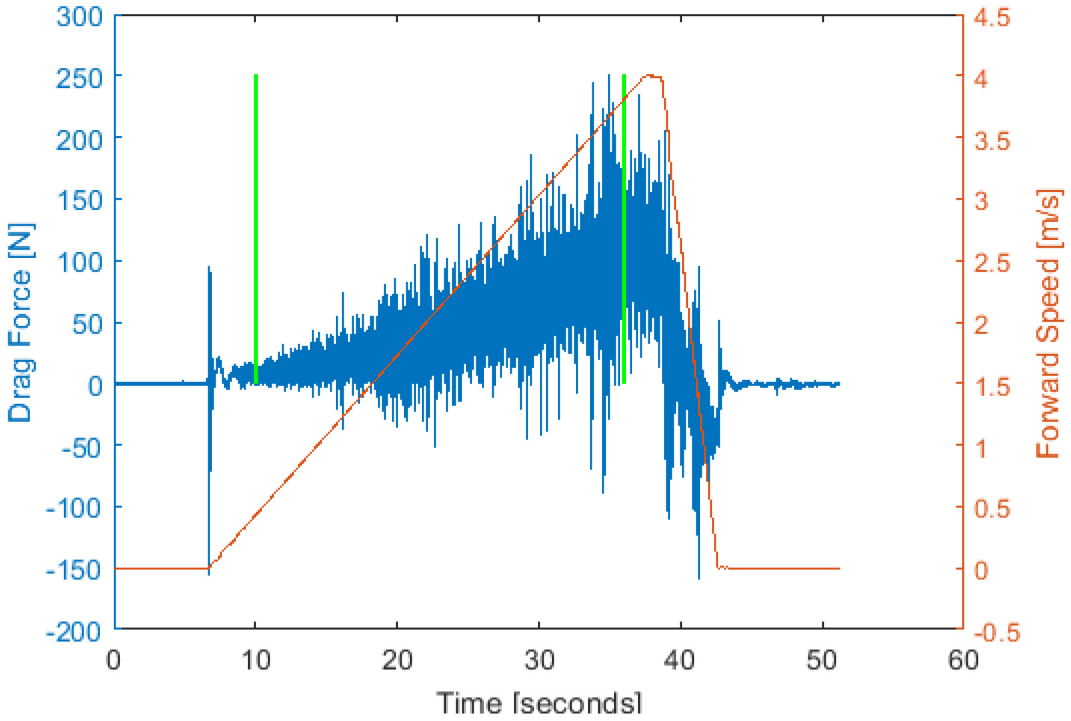

Figure 4-20: Run 110 – Upper and lower limits of target speed range. The green lines are the upper and lower bounds of the data of interest

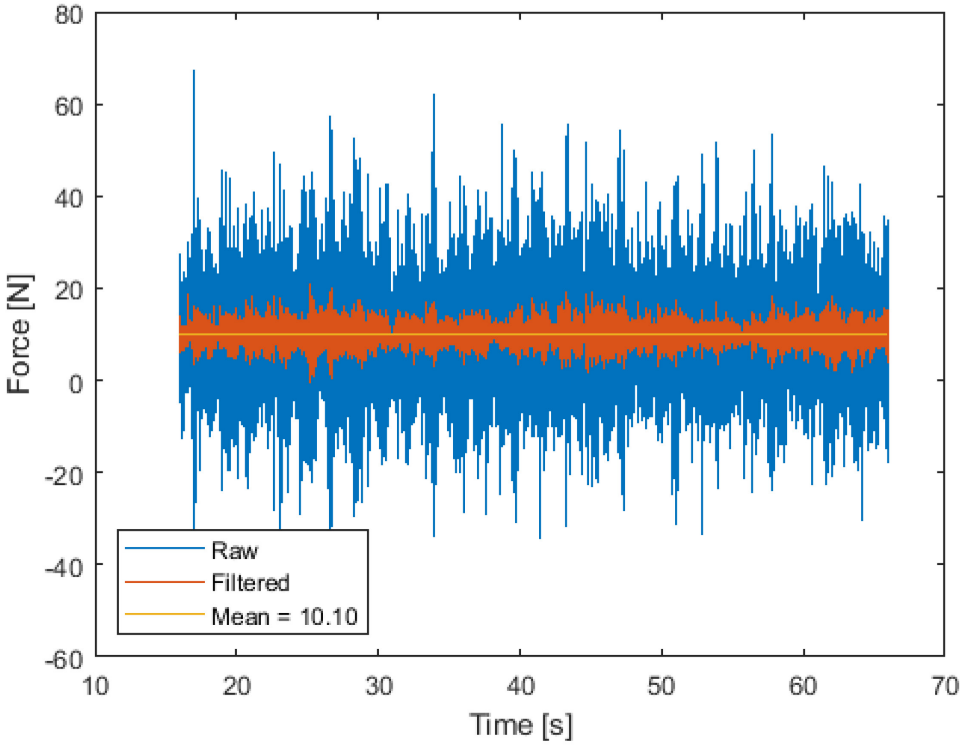

Figure 4-21: Run 106 – Raw, filtered and mean force

4.5.3 Uncertainty Analysis

To ensure that the measured results were not anomalous, a series of tests were conducted to determine the measurement variance and uncertainty. A total of 19 tests of the 101 mm cylinder at 1 m/s were undertaken generating the uncertainty results presented in Table 4-5.

Table 4-5: Uncertainty, variance and standard deviation for loads and accelerations

	Variance	Average	Standard Deviation	Std Dev as % of Average
V (m/s)	4.1E-09	9.9E-01	6.4E-05	0.01%
F_D (N)	6.2E-02	4.7E+01	2.5E-01	0.52%
C_D	2.4E-05	9.3E-01	4.9E-03	0.53%
A_y/D	3.9E-10	2.6E-04	2.0E-05	7.68%
A_x/D	2.0E-11	6.6E-05	4.4E-06	6.73%

The crossflow (A_y/D) and the inline (A_x/D) oscillations had the largest standard deviations as a percentage of the average, however as these values are less than 10% they are within the standard allowable engineering tolerance.

4.6 PHOTOGRAMMETRY

Figure 4-22 presents a block diagram of the steps taken to process the videos. The image processing toolbox in MATLAB 2018a was used to process the videos of the capture the bow wave height and the ventilated pocket depth.

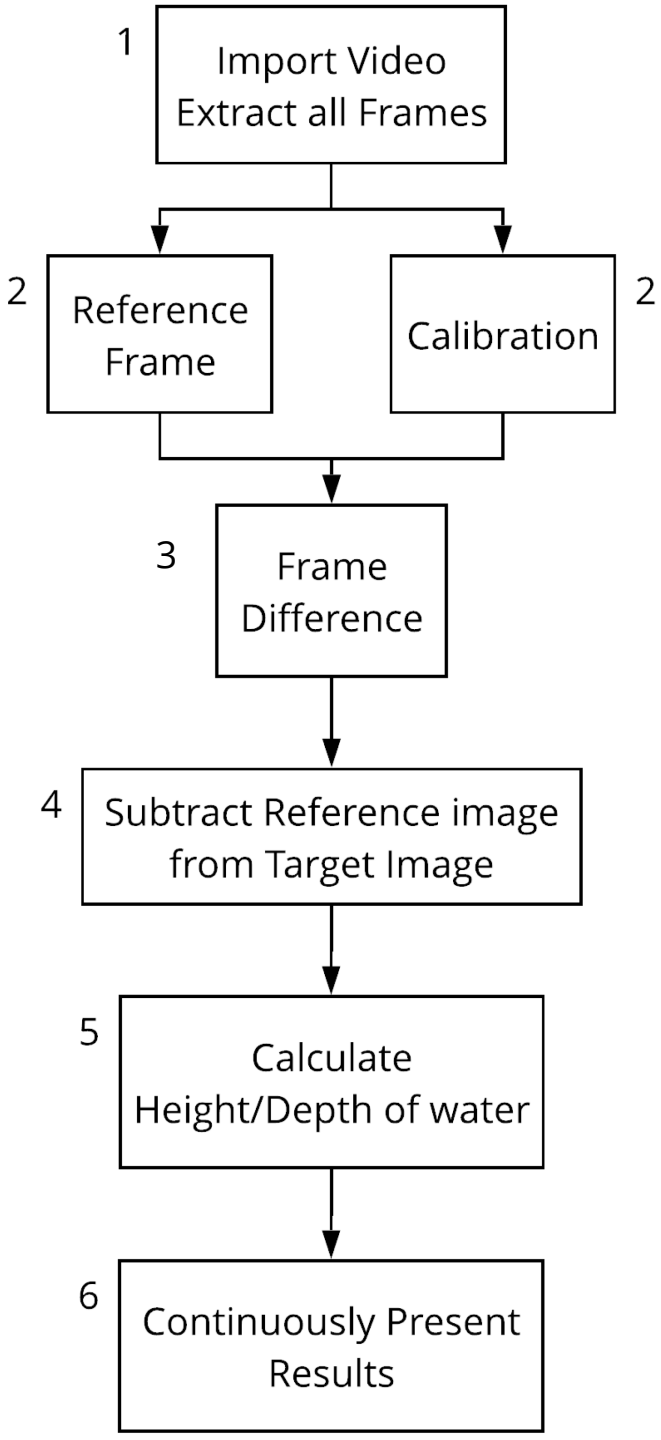

Figure 4-22: Block diagram of the photogrammetry and video processing

1. Each video is imported into MATLAB, where the frames are extracted and saved as a high-quality image (Figure 4-23).
2. From each test run, the first frame is converted into a 'Reference Frame', which is used as the zero-reference image. From the reference frame a manual calibration is conducted, where the zero-point (water level) is assigned a value of zero, and the conversion of the number of pixels per millimetre is determined from the stripes (i.e. each stripe is 10 mm wide).
3. Each frame is re-imported into MATLAB as the 'Original Colour Image' along with the 'Reference Frame'. The mask is then used to strip out the background of each image and leaving the cylinder on a black background.
4. The reference image is then subtracted from the target image, which presents a visualisation of the increase of the bow wave height/ventilated pocket depth.
5. Using the calibration factor, the height/depth of the water is found by multiplying the difference in the number of pixels between the red measurement line and the calibrated zero-point.
6. The results are continuously presented as per Figure 4-24.

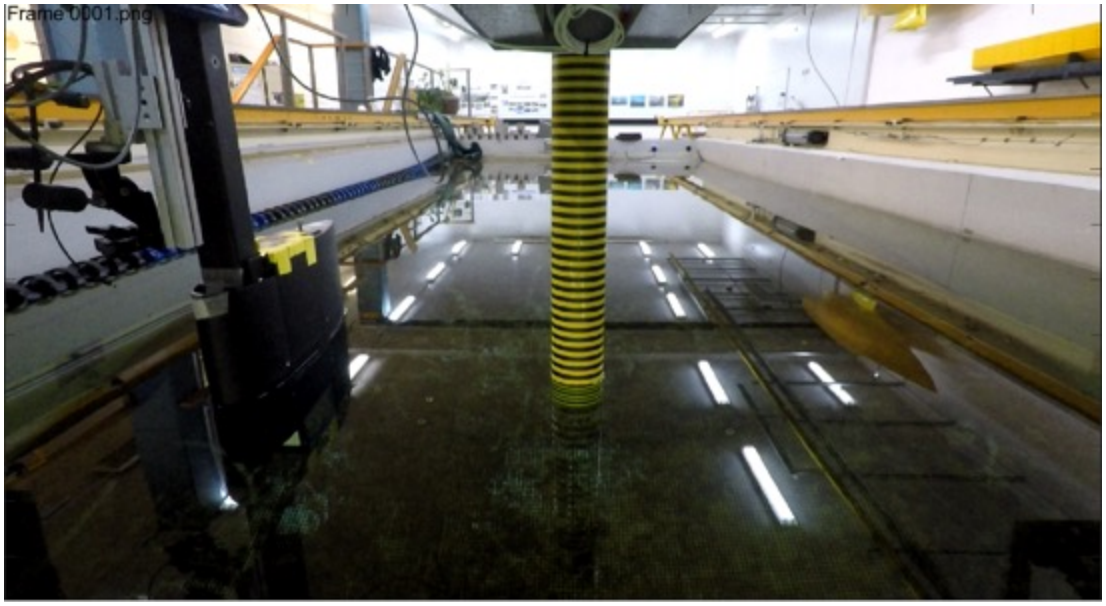

Figure 4-23: Frame 1 of 4540 from Run 100

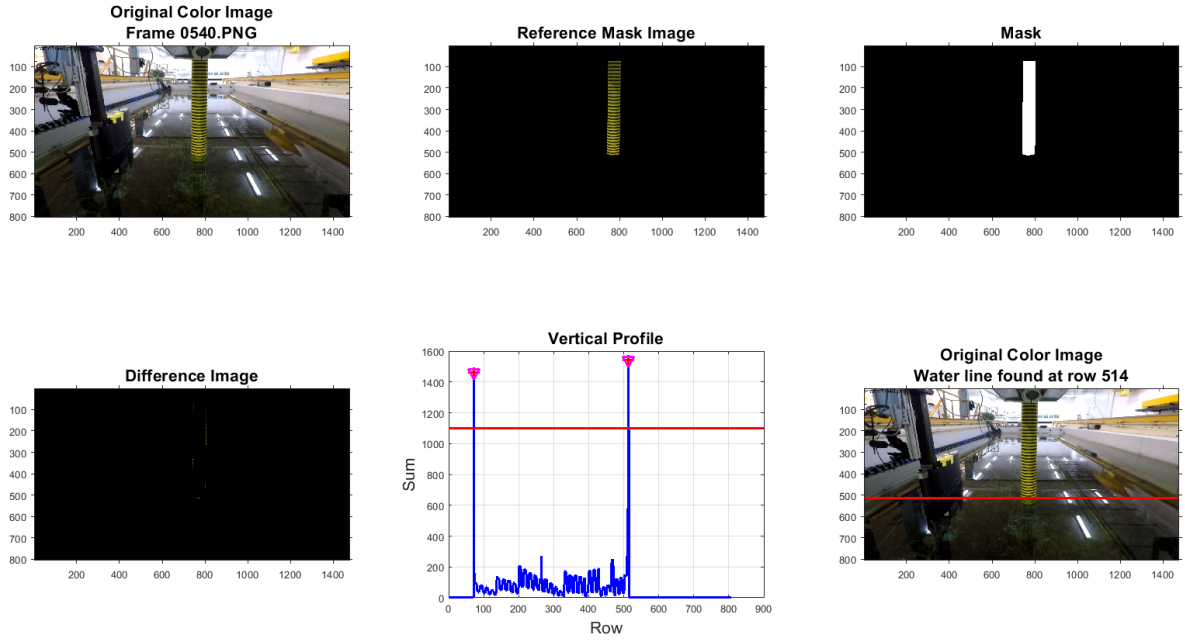

Figure 4-24: Frame-by-frame output from the photogrammetry processing

Figure 4-25 presents an example of the bow wave height.

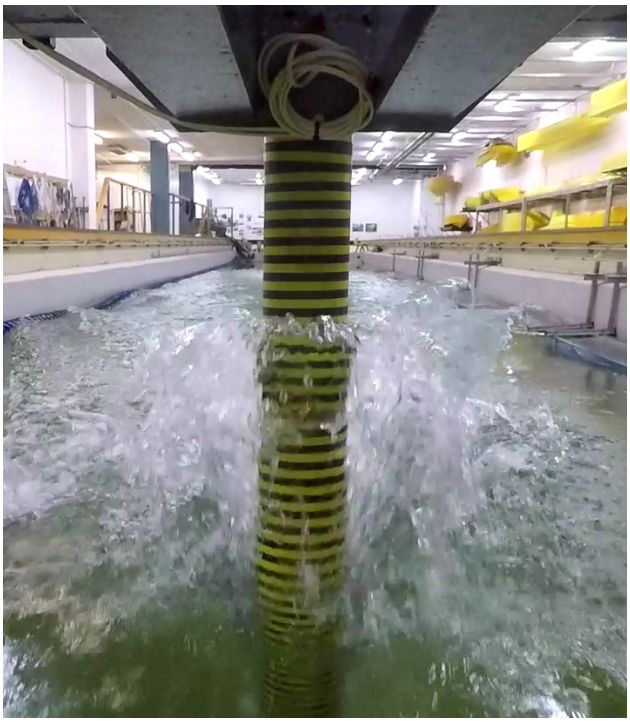

Figure 4-25: Run 122 – Bow wave height (D_1) example

The ventilated pocket depth has two distinct conditions; (1) the inception and pre-base ventilation state, as shown in Figure 4-26; and (2) the fully (base) ventilated state, as per Figure 4-27. For this investigation, once the cylinder was determined to be fully ventilated the results displayed $L_0 = L$, meaning that $L_0 > L$ was not presented as it was by Hay (1947).

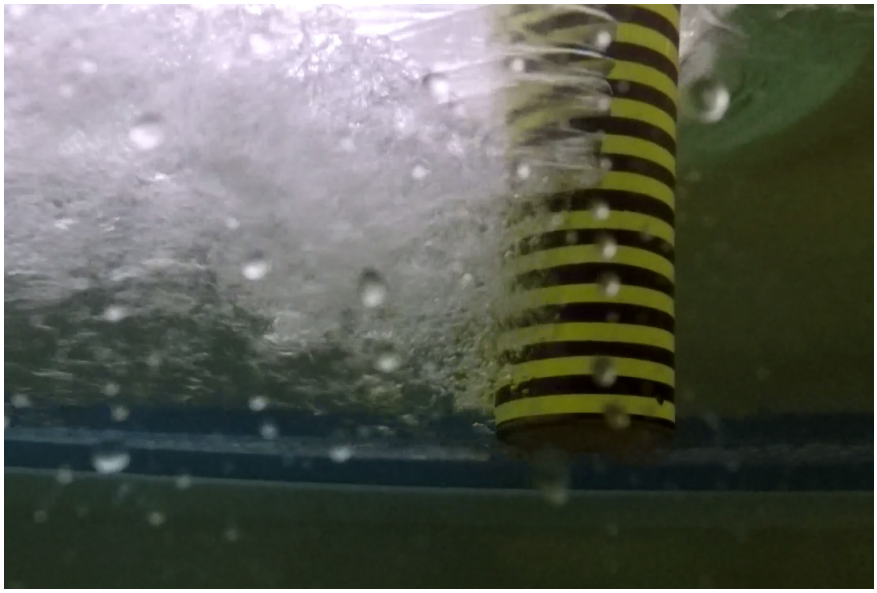

Figure 4-26: Run 107– Ventilated depth (L_0) example

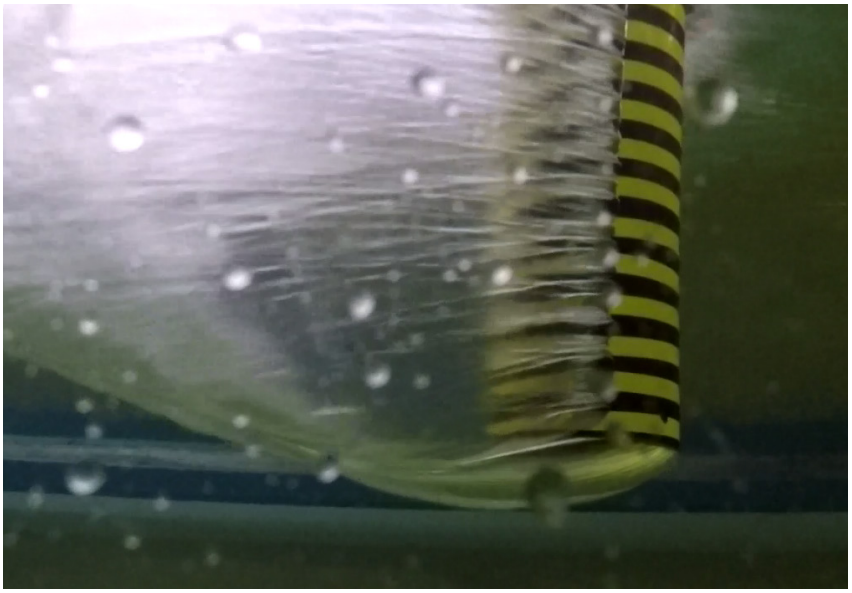

Figure 4-27: Run 108 – Full ventilation ($L_0 = L$) example

4.6.1 Sensitivity Analysis

A sensitivity analysis was conducted to assess the quality of the photogrammetry processing. To reduce the required processing time a single test run was selected, where the total number of frames varied from the full 60 FPS down to 10 FPS. The results of this analysis are shown in Table 4-6.

Table 4-6: Sensitivity analysis of photogrammetry – Run 100

	Average			
	60 FPS	**30 FPS**	**20 FPS**	**10 FPS**
D_1 (mm)	50.2	50.2	50.1	50.1

From the sensitivity analysis the difference between each of the frame rates was less than 5%, therefore the frame rate of 10 FPS was selected as it required less time to produce a near identical results when compared to 60 FPS.

4.6.2 Uncertainty Analysis

Using the same series of tests referenced in Section 4.5.3 an uncertainty analysis was conducted for the measurements from the photogrammetry processing.

Table 4-7: Uncertainty variance and standard deviation for photogrammetry

	Variance	**Average**	**Standard Deviation**	**Std Dev as % of Average**
D_1 (mm)	3.7E-8	50.1	4.2E-3	0.5%

The bow wave height (D_1) presents with a negligible standard deviation as a percentage of the average, where the use of the photogrammetry methodology has been demonstrated to provide accurate results.

4.7 SUMMARY

The following insights and findings were derived from the testing methodologies set out in this chapter:

1. A physical model testing programme was undertaken for this investigation due to the current limited capabilities of CFD along with the necessary requirement of a model test programme to validate the model.
2. Three model cylinder diameters (24, 48.3 and 101.6 mm) were selected for testing. In conjunction with the towing tank, use of three cylinder diameters facilitated the testing of a broad range of aspect ratios (Table 4-1) and velocities (Figure 4-4). The 101.6 mm cylinder was specifically chosen to allow direct comparison to the literature.
3. The blockage effects were found to be negligible for each of the cylinder diameters and were therefore unaccounted for.
4. The models were rigidly mounted to the towing carriage, thereby reducing the amount by which the models could vibrate.
5. A maximum estimated natural frequency of 51.9 Hz was calculated across all the diameters and aspect ratios. From the natural frequency the Nyquist rate was calculated to be 103.8 Hz.
6. For each condition the estimated structural loading was calculated, which included the load cell maximum, section capacity, and tip deflection. If a condition failed any of these calculations, the test matrix (Appendix D) was adapted to accommodate for the failure condition.
7. The black steel models were determined to be towards the ‘smooth’ end of the roughness scale. The roughness was calculated from the average roughness along the length of the cylinder, which included the vinyl strips used for the purpose of photogrammetry.

8. Both of the load cells were calibrated for each different cylinder diameter, where an additional drift check was conducted prior to the next cylinder diameter being tested. This drift check was found to be 0.5% of the maximum calibrated load, and therefore adjustments were not required. The load cells sampling frequency was set to 2000 Hz, which allowed for decimation if necessary.
9. The accelerometer was attached to the models in between the water surface and the lowest mounting clamp. The accelerometer did not require an explicit calibration, as this had been done by the manufacturer prior to shipping. However, a sense check of the accelerometers' vertical axis presented with a reading of approximately 9.81 m/s^2 (gravity). The sampling frequency of the accelerometer was set to 400 Hz.
10. Two GoPro cameras were set up above and below the water surface to capture the bow wave height and the ventilated pocket depth.
11. The data from the load cells and the accelerometer were processed using the MATLAB2018a Signal Processing Toolbox.
12. The visual photogrammetry analysis was conducted using the MATLAB2018a Image Processing Toolbox.

Chapter 5 RESULTS

This chapter presents original test data, which was collected from the test programme described in Chapter 4 to address the aims and objectives of this investigation.

Section 5.1 summarises the test programme which was undertaken to meet the aims and objectives to this investigation.

Section 5.2 discusses the measured bow wave height with a comparison to the Keough et al. (2016) proposed modified Bernoulli inviscid flow formula.

Section 5.3 examines the results in relation to the ventilated pocket depth, both steady state and ramp test.

Section 5.4 and 5.5 present the Crossflow (CF) and Inline (IL) VIV respectively. These sections present only ramp tests as they encompass the entire velocity range. The CF and IL results will be compared to the DNV GL curves for the respective response models. The results presented are the maximum free end-tip amplitudes.

Section 5.6 presents the drag coefficient results in terms of both the Reynolds number and the ventilated pocket depth. The Reynolds plots show the flow regime for each of the cylinders and the ventilated depth plots are presented to show the relationship between the drag coefficient and ventilation depth.

Section 5.7 summarises the general trends presented herein and provides insights into the results presented.

5.1 TEST SETUP

A test programme was developed in order to fully capture the anticipated dynamic vibration frequencies and the estimated structural loading of each model. The full test matrix is presented in Appendix D.

The loads were captured through two loads cells located at the rigid points of fixity. An accelerometer attached above the waterline recorded the motions of the model. An above water camera captured the bow wave height and an underwater camera captured the ventilated pocket depth. All the measured parameters were processed using the signal processing and image processing toolboxes in MATLAB 2018a.

Three different cylinder diameters were tested: 101.6 mm, 48.3 mm, and 24 mm. These cylinders were selected to test a broad range of aspect ratios varying from 1 – 40. In addition to the various diameters and aspect ratios, three distinctive end conditions were tested: Open, Closed, and End-plate (D_{EP}/D = 3).

A single universal legend is presented as Table 5-1, which is applicable to the ensuing plots, except where an explicit legend is provided. A fold-out version of Table 5-1 may be found on the very last page of this thesis.

Table 5-1: Legend for the various test series results

Aspect Ratio	Colour
1	
2	
4	
8	
10	
16	
20	
32	
40	

Model Cylinder	Symbol
24 mm Closed	◆
48.3 mm Closed	●
48.3 mm Open	○
48.3 mm End-plate	■
101.6 mm Closed	▲

NB: When plotting the ramp test results below the inertial force due to acceleration has been calculated and removed resulting in the true drag coefficient.

For the 48.3 mm cylinder, one plot has been presented herein due to the similarity in results between the three end conditions. In the caption of each plot there will be a reference to which end condition is shown, with the additional plots in Appendix E.

5.2 Bow Wave Height

The bow wave height, D_1, has the units mm.

5.2.1 Steady State

Figure 5-1 plots the dimensional values from the Bernoulli (Equation 17) and proposed Keough (Equation 18) equations for the purpose of visualising the difference between the two formulae.

$$D_1 = \frac{V^2}{2g} \qquad \text{Equation 17}$$

$$D_1 = \frac{V^2}{2g} - C_{dissp}V^2 \qquad \text{Equation 18}$$

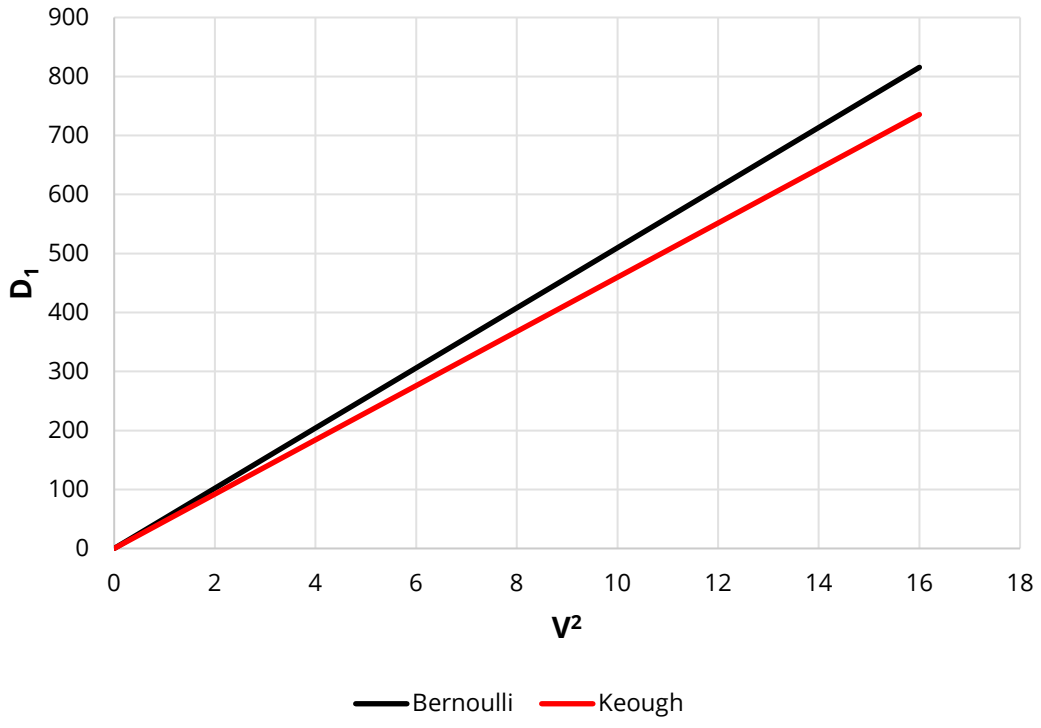

Figure 5-1: Dimensional comparison of the Bernoulli inviscid flow theory against Keough's modified Bernoulli equation

On each of the following plots the measured data has been presented alongside the Keough-modified Bernoulli equation, which has been plotted as a solid red line.

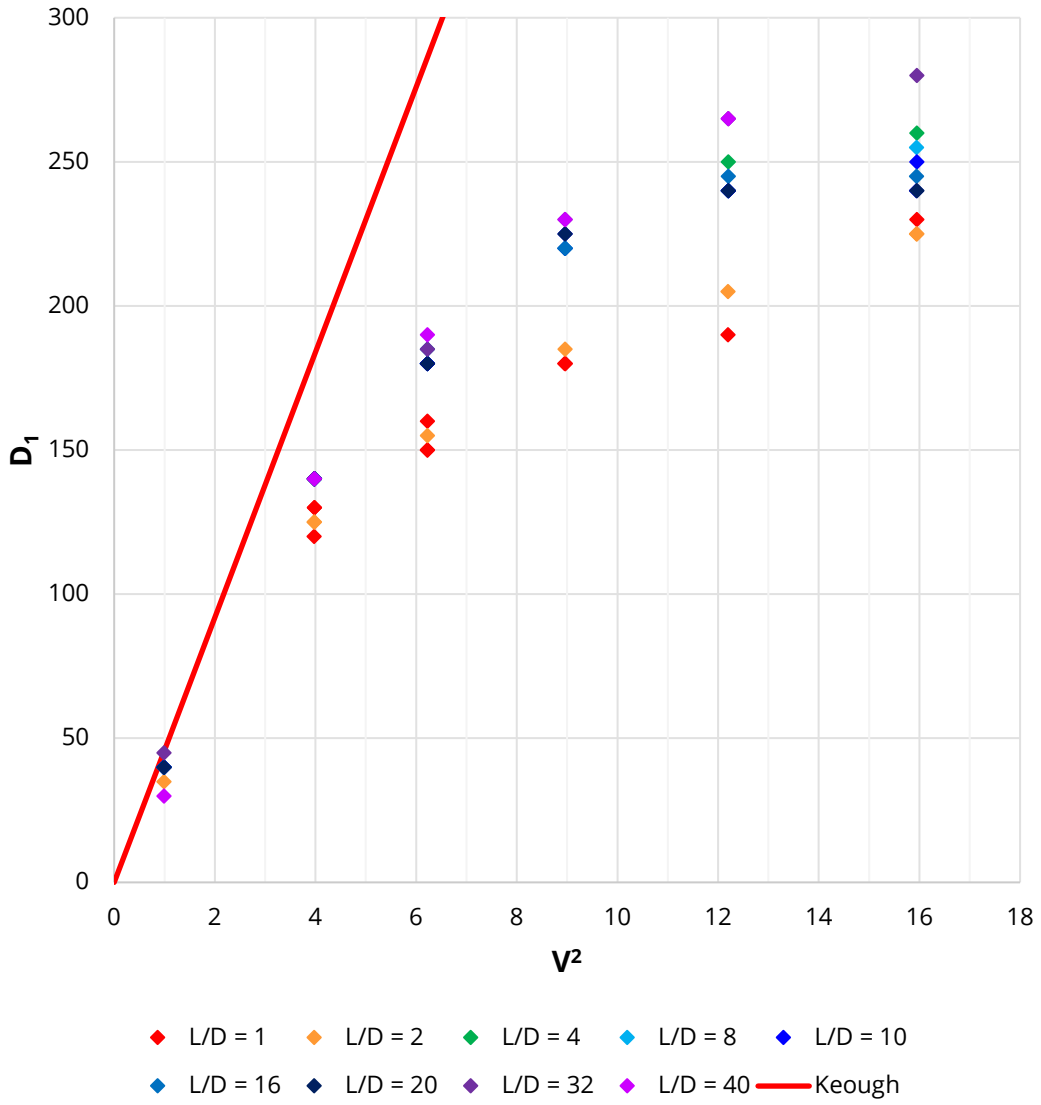

Figure 5-2: 24 mm – Bow wave height vs velocity squared

The results shown in Figure 5-2 present a distinct relationship between D_1 and V^2.

There is an obvious disparity between the current test data and the proposed Keough equation. The data diverges from the line almost immediately, where only the $V^2 = 1$ approximately concurs with the line.

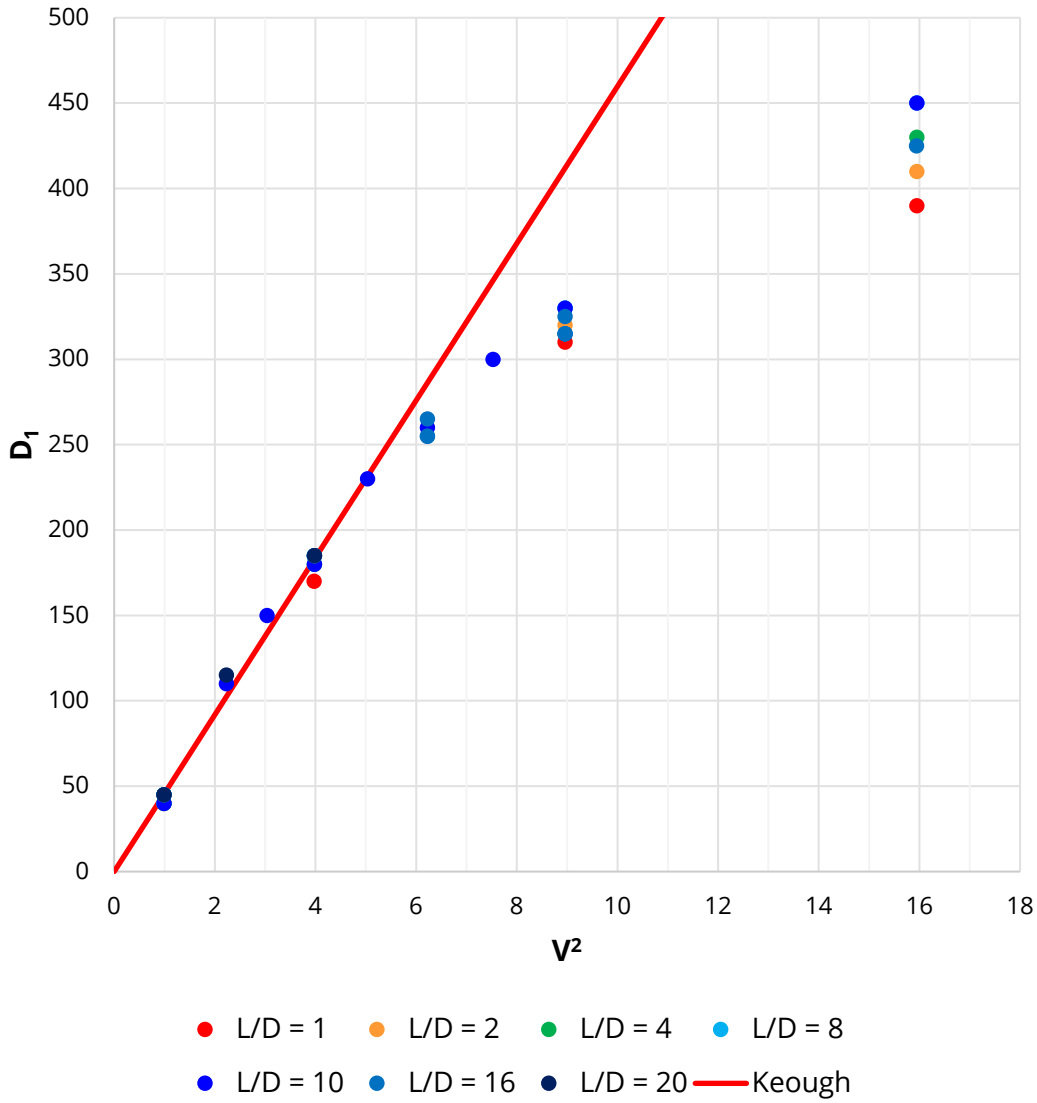

Figure 5-3: 48.3 mm – Closed – Bow wave height vs velocity squared

The 48.3 mm results presented in Figure 5-3, Figure E-1 and Figure E-2 all show the same phenomenon, in which the Keough line is initially comparable to the results. However, similar to the 24 mm rod, the proposed line diverges from the data, again resulting in disparity.

From the comparison of the 48.3 mm cylinder results, it can be concluded that the different end conditions do not have an effect on the height of the bow wave.

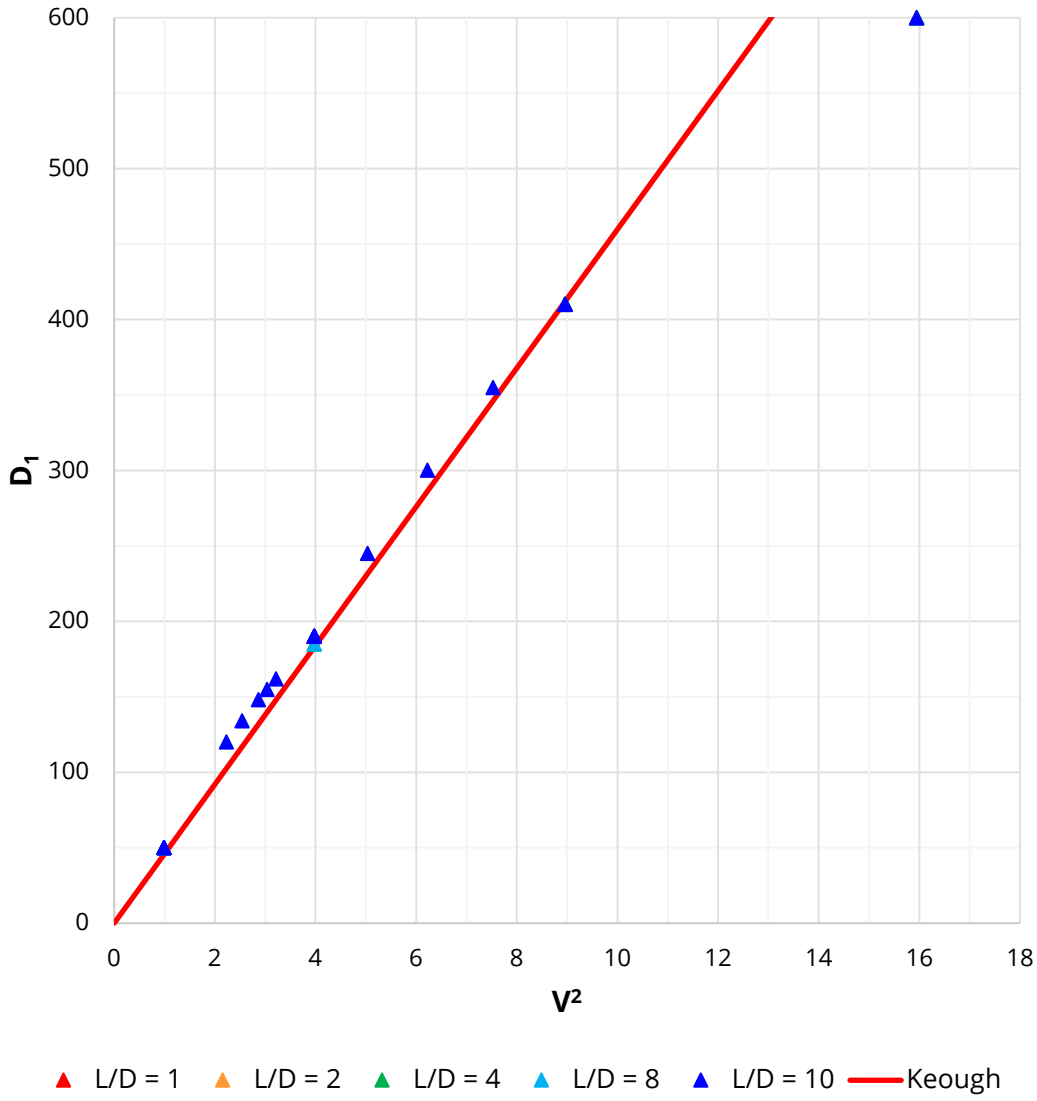

Figure 5-4: 101.6 mm – Bow wave height vs velocity squared

The 101.6 mm results shown in Figure 5-4 conform to the Keough line far more closely than the smaller diameter models, with close conformity when $V^2 < 10$.

5.3 VENTILATED POCKET DEPTH

All of the plots in this section contain the Chaplin and Teigen (2003) relationship between L_0/D and Fr_D^2, as previously described by Equation 19. This relationship is represented in the following section in the form of a solid orange line.

5.3.1 Steady State

The 24 mm data shown in Figure 5-5, although not directly sitting atop the proposed Chaplin and Teigen line, does exhibit a similar slope up to the fully ventilated state.

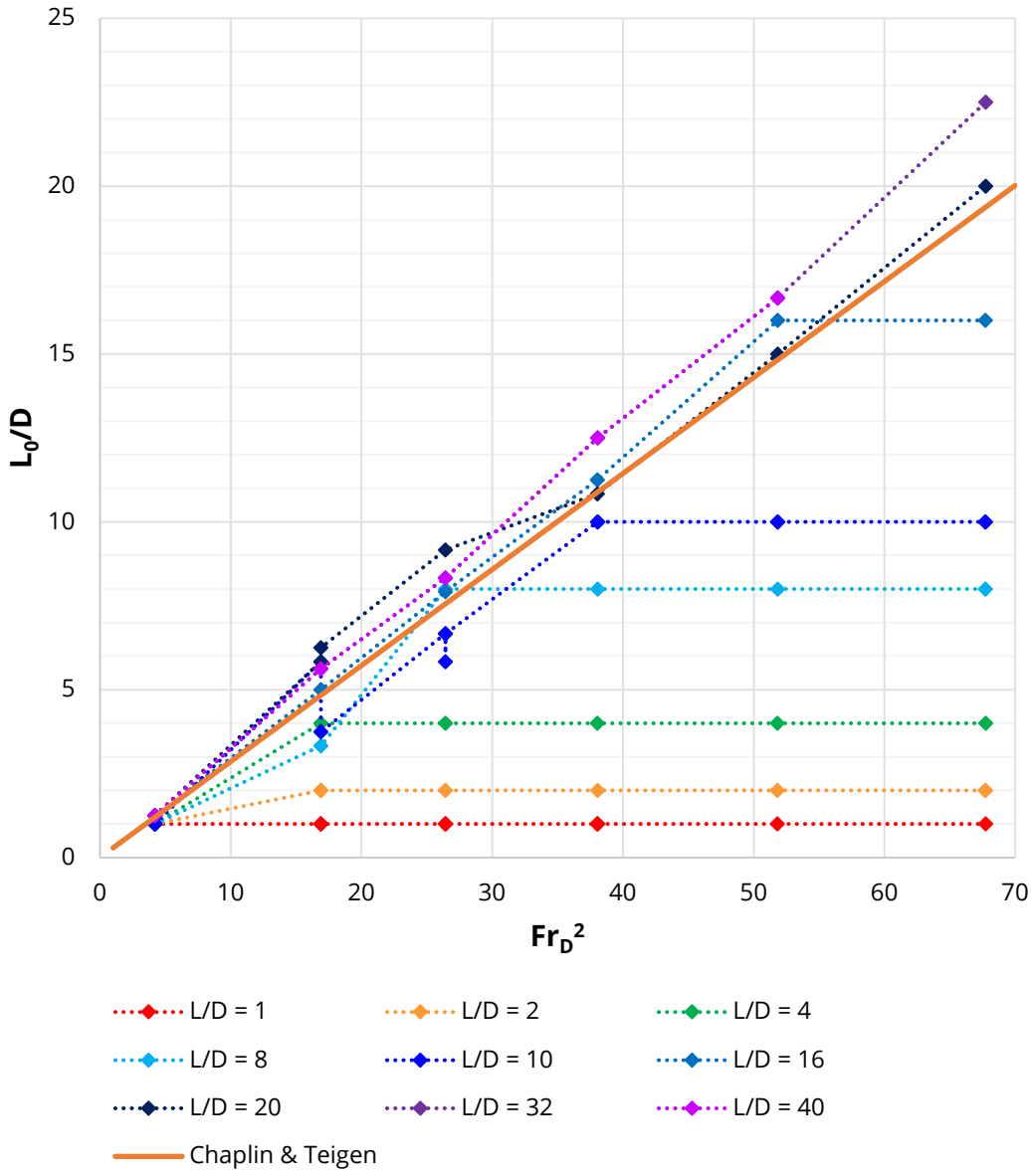

Figure 5-5: 24 mm – Ventilated pocket depth vs Froude squared

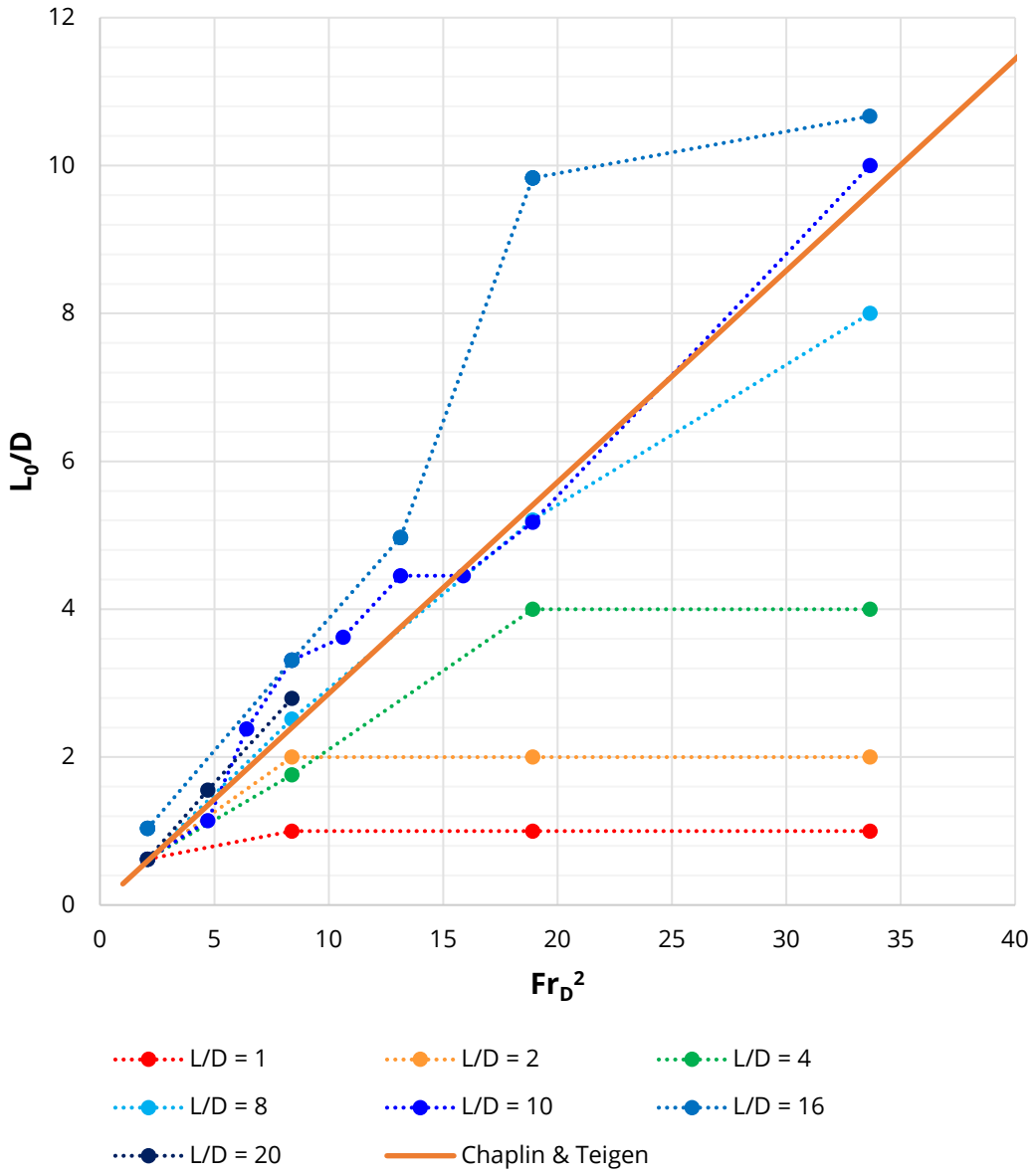

Figure 5-6: 48.3 mm – Closed – Ventilated pocket depth vs Froude squared

Regardless of the end condition, all of the 48.3 mm results (Figure 5-6, Figure E-3 and Figure E-4), show similar trends in the magnitude and slope of the ventilated pocket depth. The measured results for aspect ratios greater than eight are typically greater than the orange LoBF, a trend which is apparent throughout the three different end conditions.

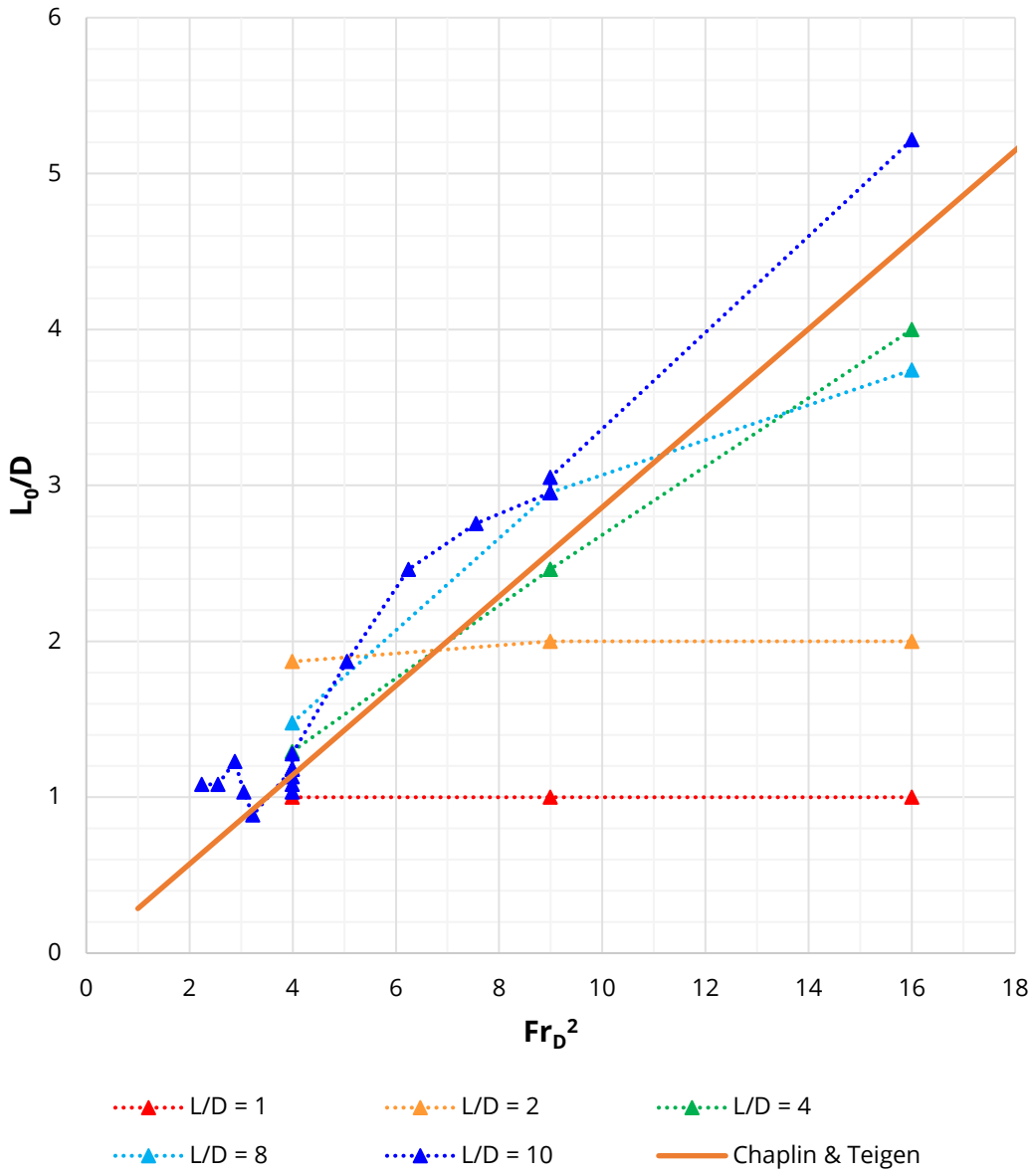

Figure 5-7: 101.6 mm – Ventilated pocket depth vs Froude squared

The 101.6 mm results (Figure 5-7) present with the same trends that the 24 mm and 48.3 mm models exhibited.

5.4 CROSSFLOW VIV

5.4.1 DNVGL-RP-C205

DNVGL-RP-C205 *Environmental Conditions and Environmental Loads* provides a guidance for the modelling, analysis and prediction of the environmental conditions as well as a guidance to calculate then environmental loads acting on structures. Section 9.6 from the code refers to *Current induced vortex shedding*, which describes the conditions relating to the reduced velocity in which crossflow VIV typically occurs. Furthermore, the formulae for the calculation of a maximum crossflow response model are presented in Section 9.6.4.3 of the code.

Due to the limited nature of the clamping conditions as presented by DNV GL, the author has conducted a comparison of the tested fully fixed models versus the elastically mounted cylinders from DNVGL-RP-C205 and DNVGL-RP-F105. The purpose of this comparison is primarily to show how the clamping conditions affect the end-tip amplitudes of oscillation.

In-line VIV is briefly discussed, where for more detailed predictions of the IL response amplitude, the code references DNVGL-RP-F105.

5.4.2 Crossflow Results

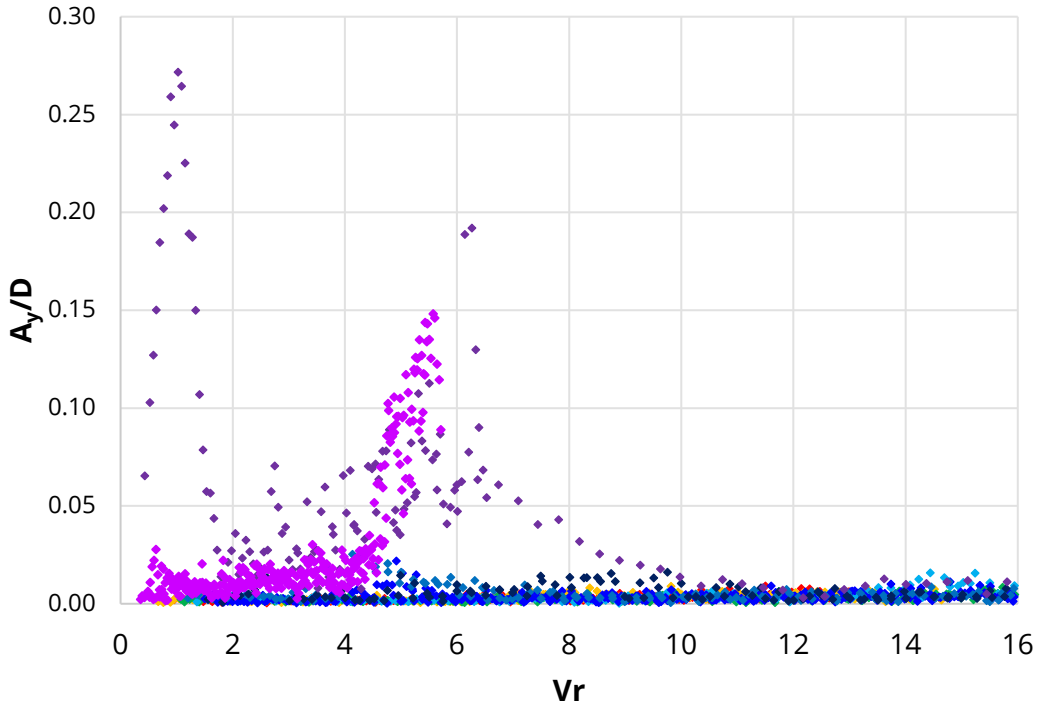

Figure 5-8: 24 mm – Ramp – Crossflow oscillation vs reduced velocity

The 24 mm rod shows significant peak amplitudes when the aspect ratio equals 32 and 40 (Figure 5-8). These peak values are insignificant when compared to the DNV GL crossflow VIV response model shown in Figure 5-9.

The peak amplitudes were expected to be small due to the design of the clamps in a fully fixed model. The flexural stiffness was the primary factor, which allowed for oscillations.

Peak amplitudes of small magnitude would be expected from the designed test setup due to the models being fully fixed, with only the flexural stiffness allowing for any movement.

Figure 5-9 presents the peak amplitudes from Figure 5-8 and the crossflow response model from DNV GL (2017b) (black line). It is clear that the observed crossflow amplitudes are less than the maximum estimated for the conditions by a factor of 3-4.

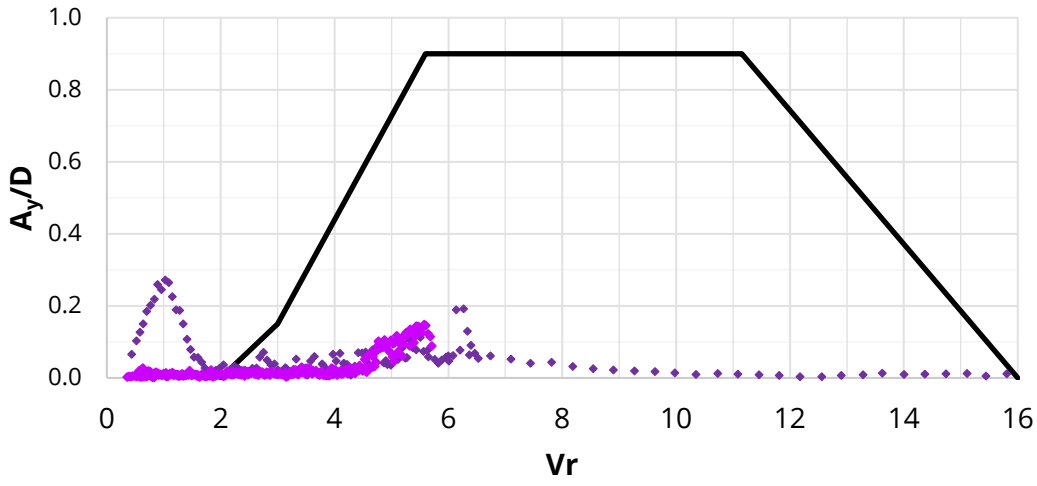

Figure 5-9: Peak 24 mm amplitudes of crossflow VIV with DNV GL CF VIV response model (black line)

The closed 48.3 mm cylinder has a distinct peak for the two largest aspect ratios tested for that diameter (Figure 5-10). These peaks, although of the same magnitude, are offset, indicating an aspect ratio effect on the measured oscillations, most likely due to the different frequencies of oscillation.

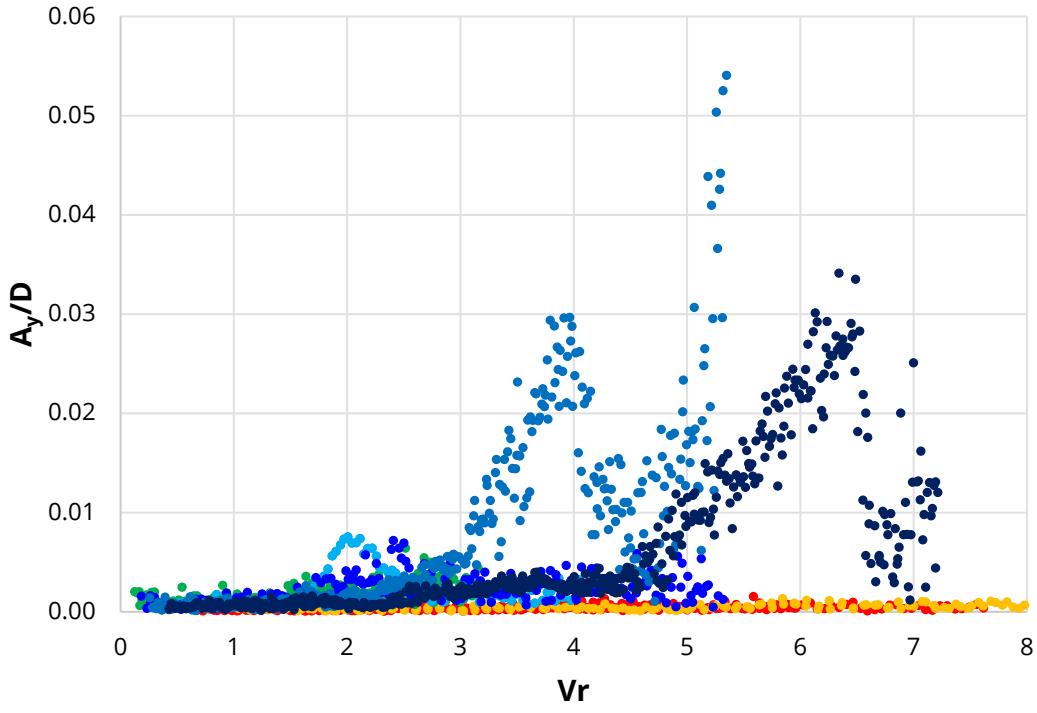

Figure 5-10: 48.3 mm – Ramp – Closed – Crossflow oscillation vs reduced velocity

For the 48.3 mm cylinder of the three different end conditions, the open cylinder had the lowest measured crossflow oscillations (Figure E-5). In contrast, the open cylinder gave aspect ratios of the two oscillation peaks that were reversed (i.e. *L*/*D* = 20 peaks before *L*/*D* = 16).

It is suspected that the tapered edges of the end disc produced a hydrofoil-like response, resulting in larger amplitudes of oscillation (Figure E-6). This aspect ratio factor directly relates to the first modal natural vibration frequency of the model, and with this suspected amplification of oscillations, the results roughly follow the same trend as the closed and open conditions.

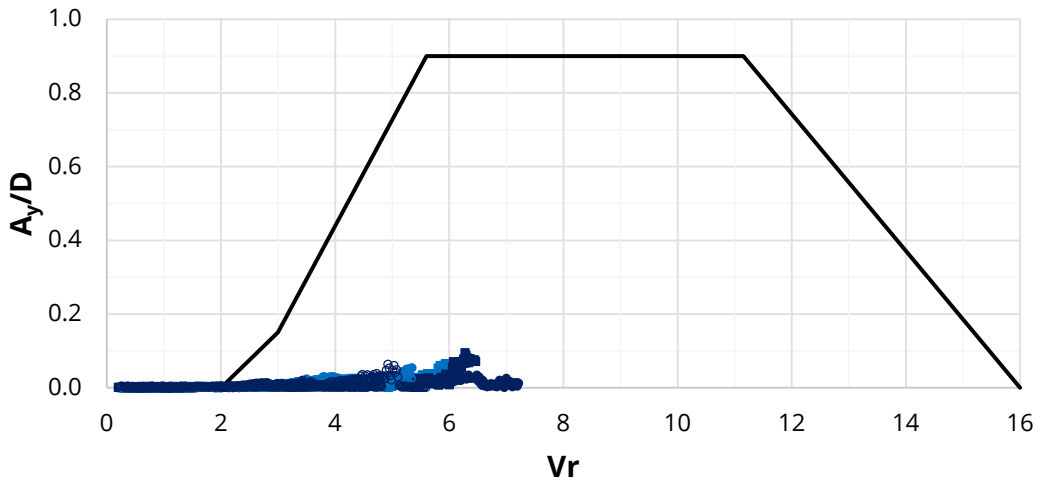

Figure 5-11: Peak 48.3 mm amplitudes of crossflow VIV with DNV GL CF VIV response model (black line)

As observed in Figure 5-9, plotting the two largest aspect ratio results of a single cylinder diameter along with the crossflow (CF) response model from DNV GL (2017b) (black line) reveals that the measured oscillations are <11% of the typical predicted maximum (Figure 5-11).

The measured oscillations from the 101.6 mm cylinder are very small in magnitude as shown in Figure 5-12, which is due to cylinder rigidity. It can be seen that for *L*/*D* = 10 the cylinder is entering the lock-in range. The *L*/*D* = 2 results are anomalous, as adjacent aspect ratios (1 and 4) do not exhibit the same peak. A simple comparison to the DNV GL response curve in Figure 5-13 indicates that VIV is infinitesimal.

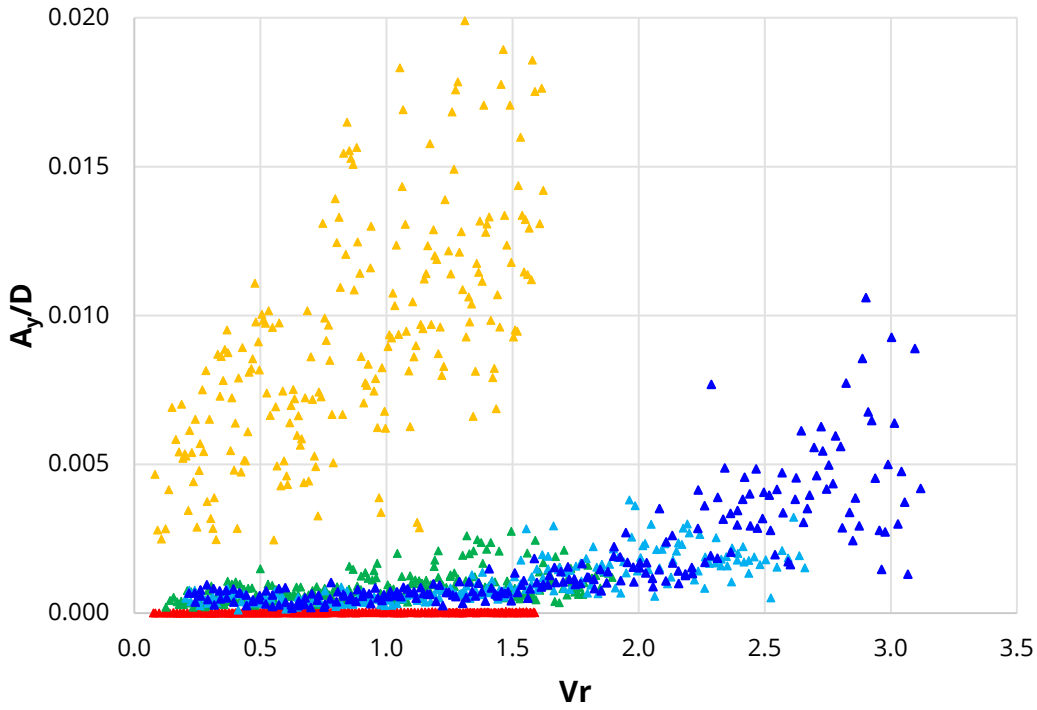

Figure 5-12: 101.6 mm – Ramp – Crossflow oscillation vs reduced velocity

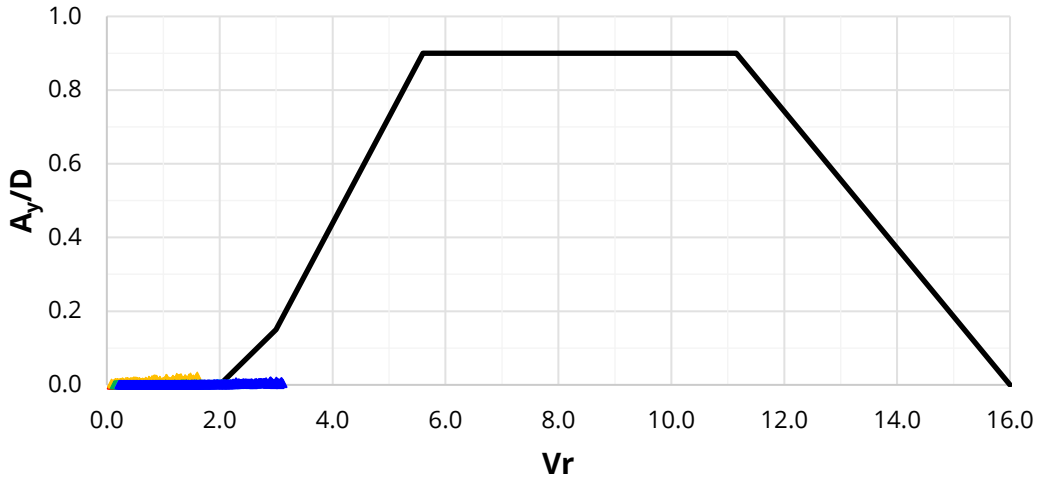

Figure 5-13: Peak 101.6 mm amplitudes of crossflow VIV with DNV GL CF VIV response model (black line)

5.5 INLINE VIV

5.5.1 DNVGL-RP-F105

DNVGL-RP-F105 *Free Spanning Pipelines* considers the combined wave and current loading on subsea pipelines. Section 4.6 *In-line response model* discusses the characteristics of IL VIV and the associated formulae in the calculation of the maximum in-line response model.

5.5.2 Inline Results

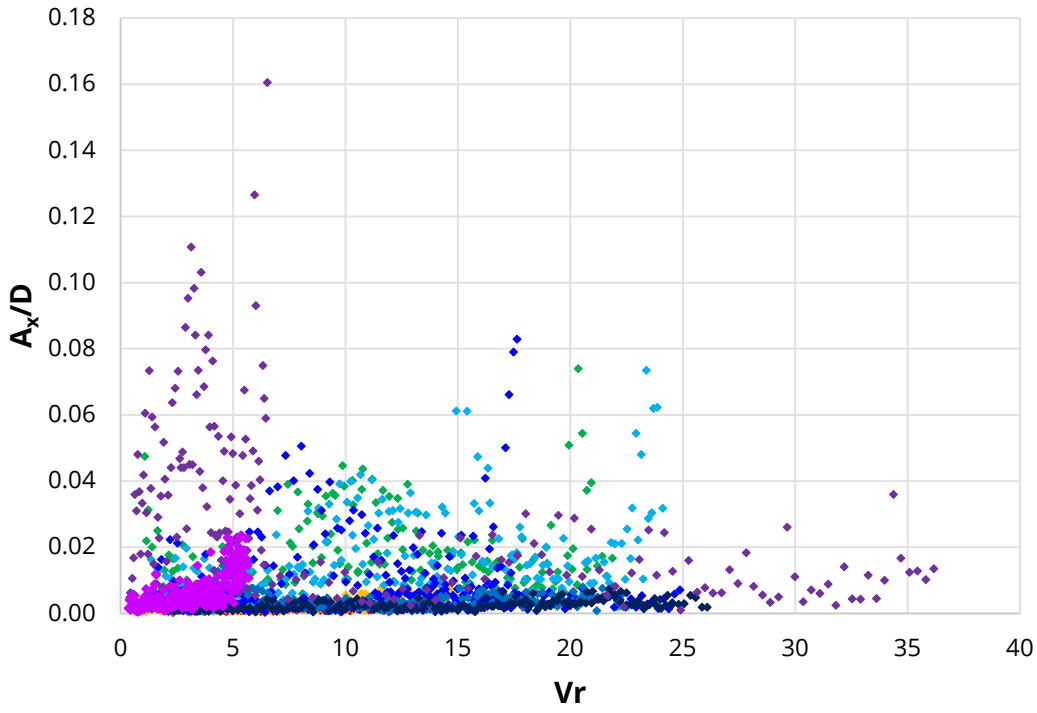

Figure 5-14: 24 mm – Ramp – In-line oscillation vs reduced velocity

The 24 mm rod generates an odd series of inline oscillation results, in which multiple aspect ratios reach peak value but all at different reduced velocities (Figure 5-14).

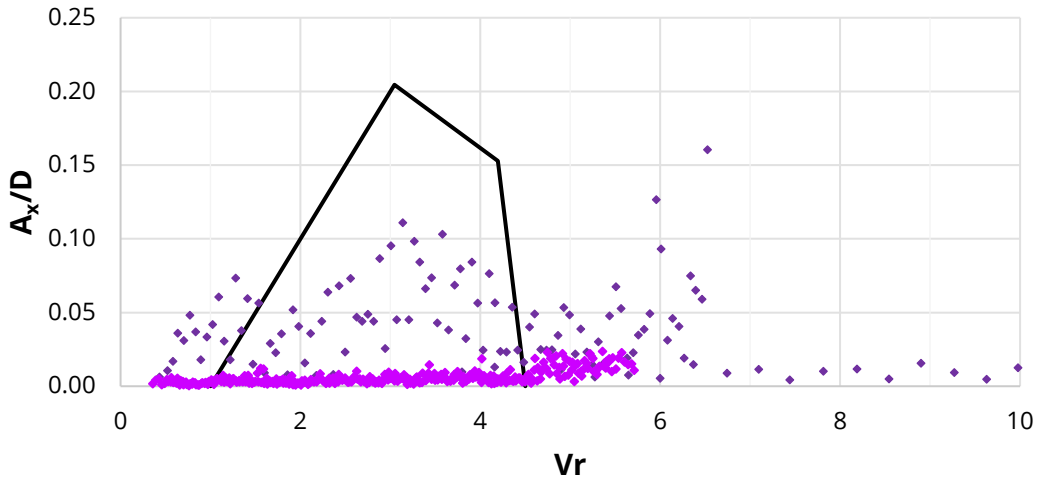

Figure 5-15: Peak 24 mm amplitudes of inline VIV with DNV GL IL VIV response model (black line)

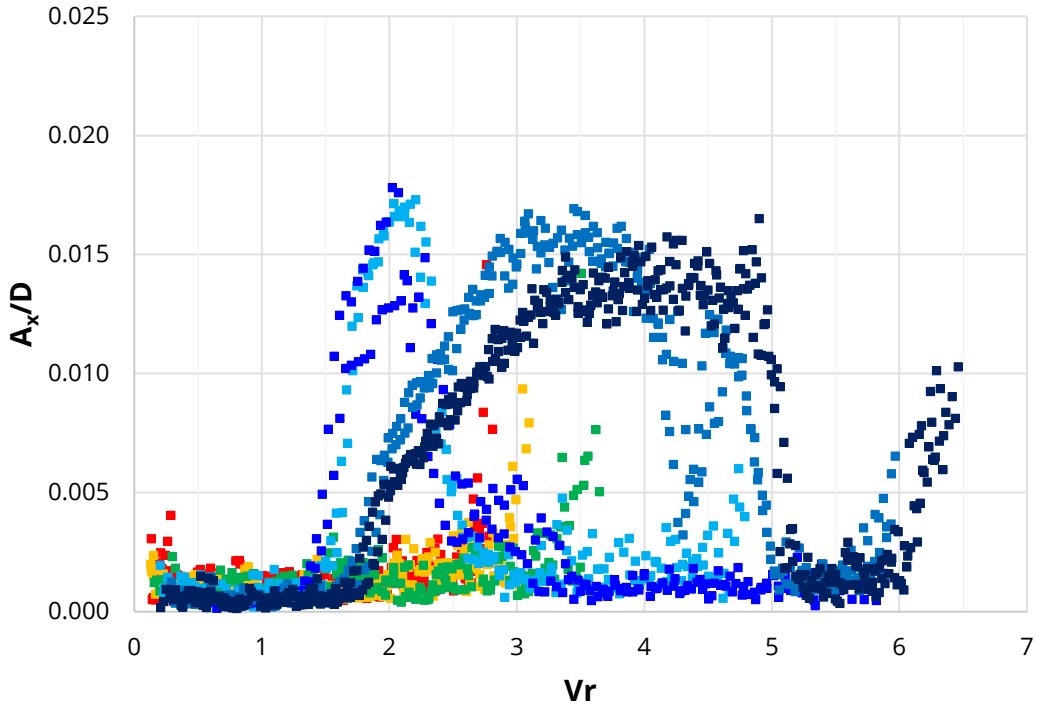

Figure 5-16: 48.3 mm – Ramp – End-plate – In-line oscillation vs reduced velocity

The 48.3 mm cylinder with the end-plate shown in Figure 5-16 illustrates an impeccable example of an inline vibration curve. The results for aspect ratios greater than eight go through the instability region for a cantilevered cylinder. This phenomenon is prevalent for the closed and open conditions shown in Figure E-7 and Figure E-8 respectively.

When the results from Figure 5-16 are compared to the DNV GL IL response curve as per Figure 5-17, it may be stated that the test results are minute in magnitude and are therefore inconsequential when related to the bounding curve.

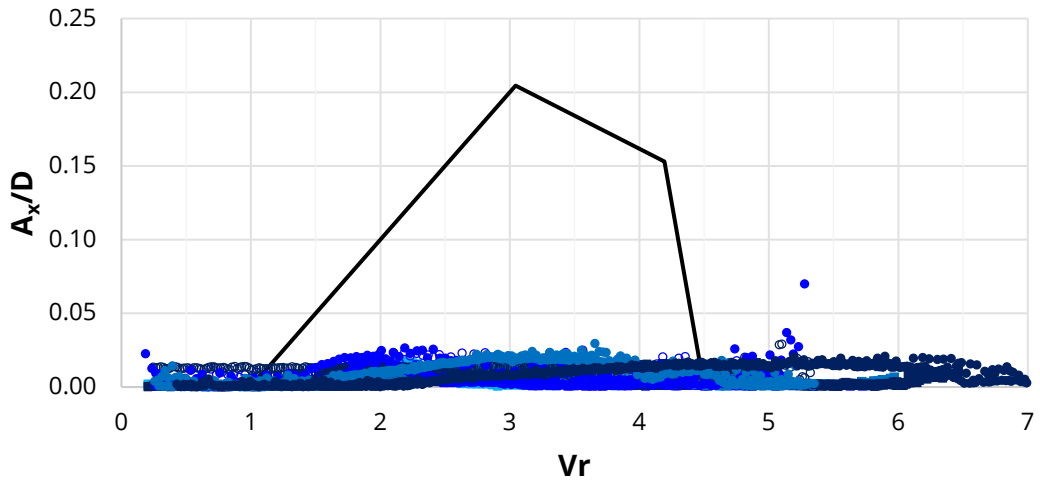

Figure 5-17: Peak 48.3 mm amplitudes of inline VIV with DNV GL IL VIV response model (black line)

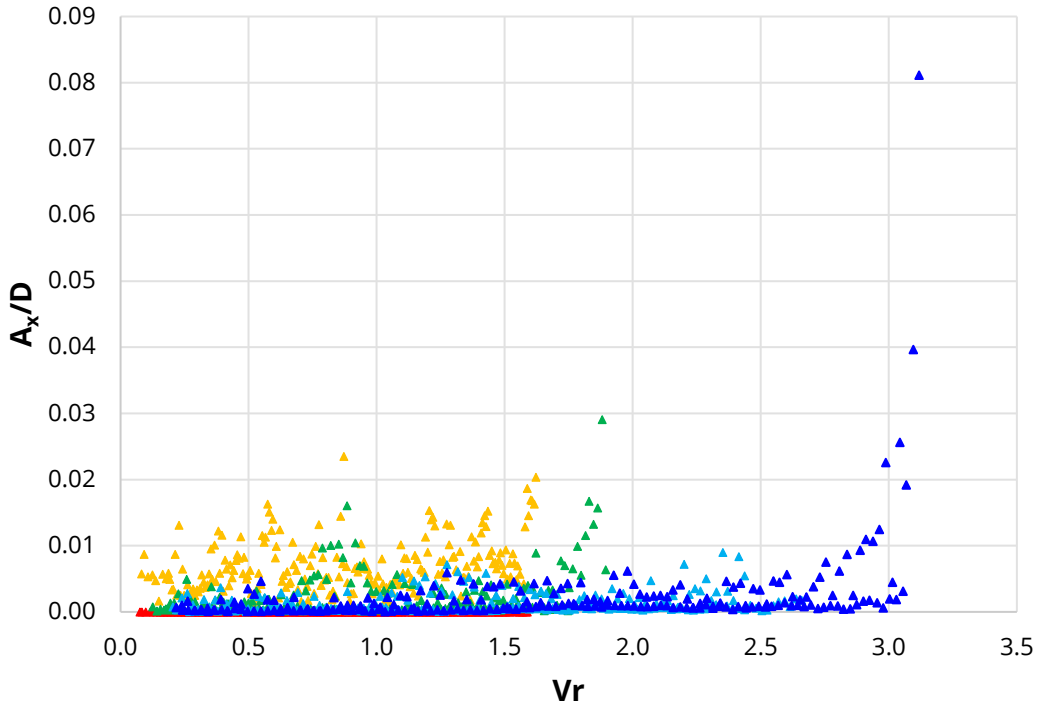

Figure 5-18: 101.6 mm – Ramp – In-line oscillation vs reduced velocity

The inline vibrations in Figure 5-18 show similar results to the crossflow oscillations of the 101.6 mm cylinder. It has been determined that the aspect ratios below $L/D = 10$ were not undergoing periodic VIV but were instead fluttering randomly. In particular the $L/D = 2$ results showed no correlation between crossflow and inline oscillations. The response curve is comparable to the test data, which is insignificant (Figure 5-19).

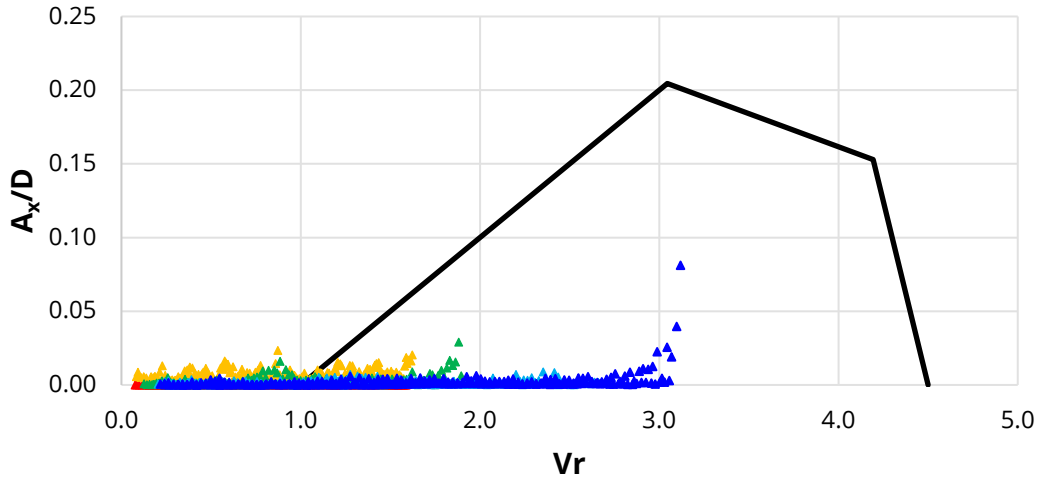

Figure 5-19: Peak 101.6 mm amplitudes of inline VIV with DNV GL IL VIV response model (black line)

5.6 Drag Coefficient

This section will present and discuss the drag coefficient relationships for each of the different diameter cylinders and respective end conditions, where applicable, between the Reynolds number (*Re*) and the Ventilated pocket depth (L_0/L).

5.6.1 Reynolds Number

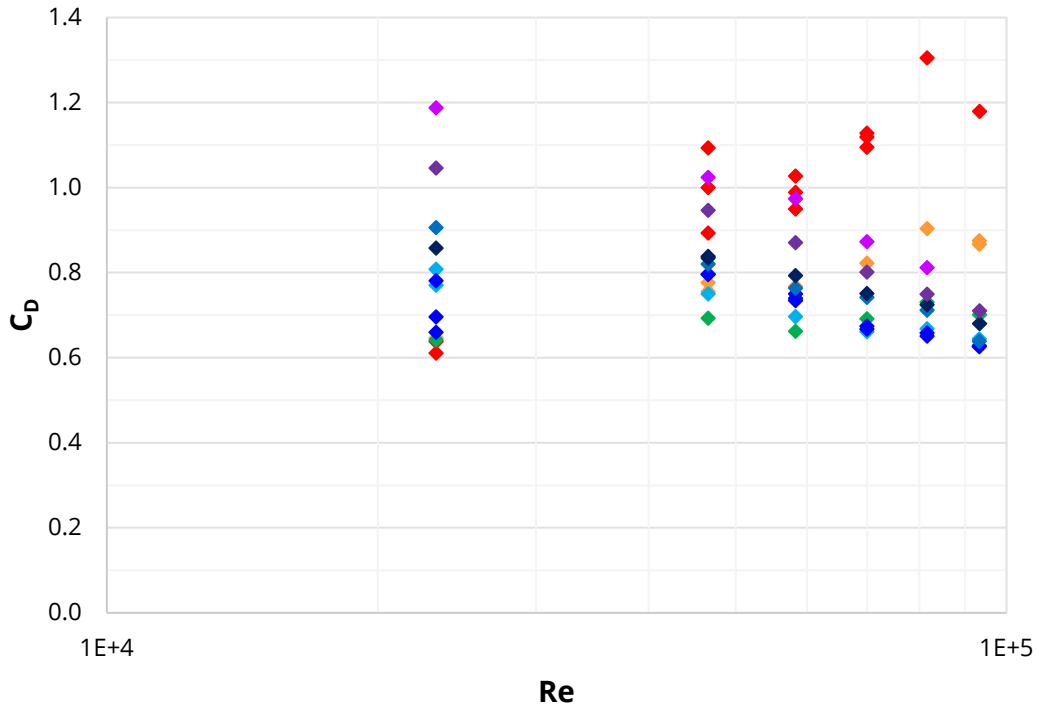

Figure 5-20: 24 mm – Drag coefficient vs Reynolds number

The 24 mm rod was entirely within the sub-critical Reynolds number regime as shown in Figure 5-20. There are visible trend lines within the results from each aspect ratio: where at L/D = 1 the trend is a positive power, and at L/D = 40 the trend is a negative power. All of the aspect ratios between these bounding values gradually transition from positive to negative, with an approximate plateau occurring when L/D = 4.

Where multiple points have been presented for each cylinder diameter and aspect ratio in Figure 5-20, an average of those values has been taken and plotted in Figure 5-21, where the trend for each aspect ratio becomes more apparent.

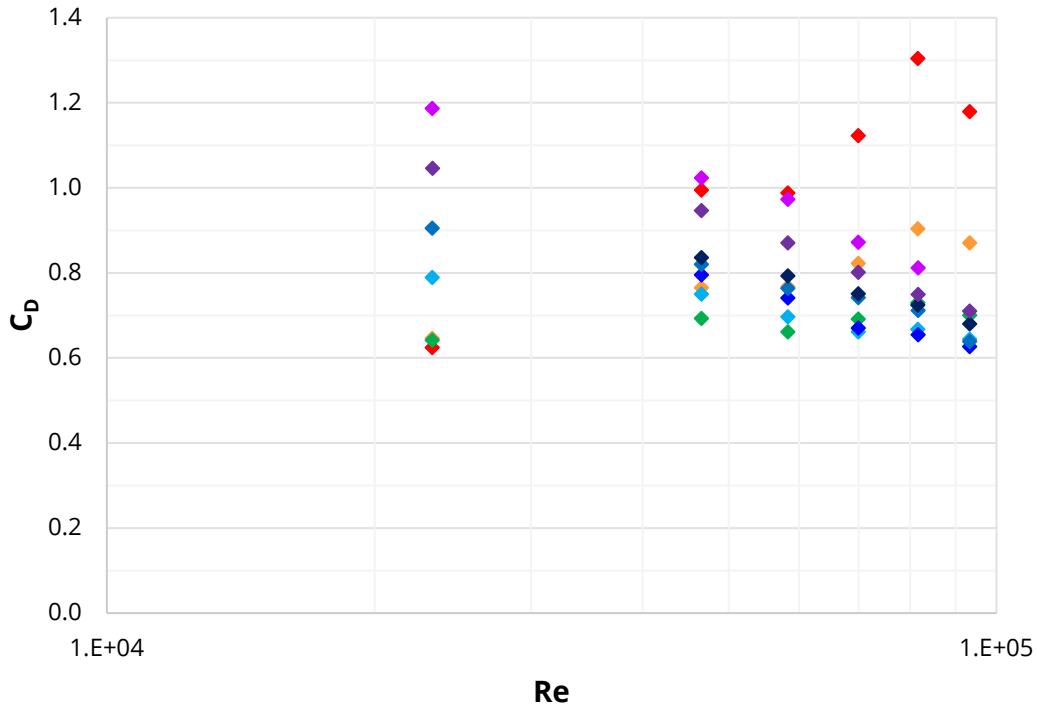

Figure 5-21: 24 mm – Drag coefficient vs Reynolds number with averaged results for each towing velocity

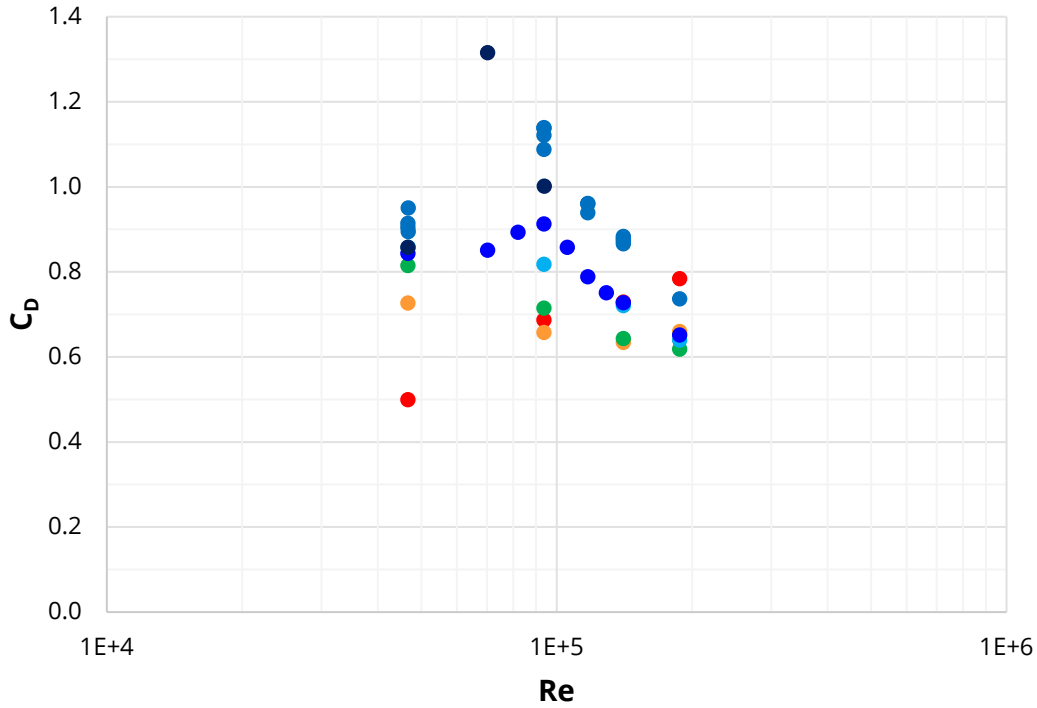

Figure 5-22: 48.3 mm – Closed – Drag coefficient vs Reynolds number

Figure 5-22, Figure E-9 and Figure E-10 all exhibit the same phenomena relating to the general shape for each of the different aspect ratios.

The closed and open cylinders gave almost identical results for each measured data point. The differences observed were infrequent and did not affect the overall result.

The end-plate data gave a higher drag coefficient result, which is most likely due to the previously discussed factors including skin friction on the plate or hydrofoil-like properties.

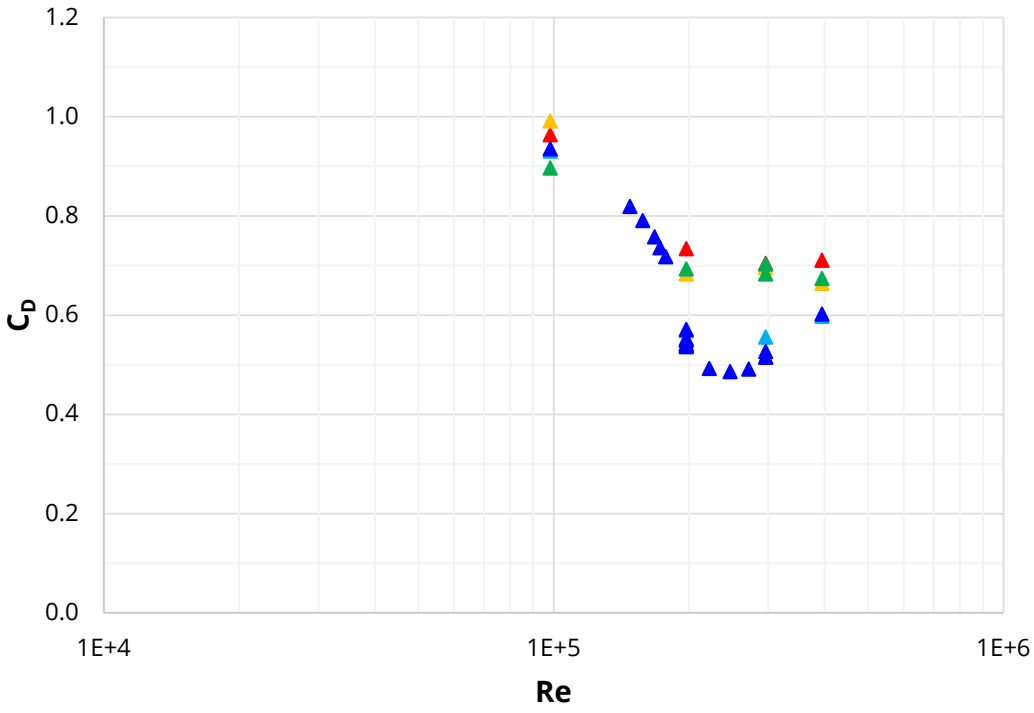

Figure 5-23: 101.6 mm – Drag coefficient vs Reynolds number

The results shown in Figure 5-23 from the 101.6 mm cylinder show that the model goes through the Reynolds drag crisis, with the beginning of the post-critical recovery of the drag coefficient.

5.6.2 Ventilated Pocket Depth

The aspect ratio tends to have an adverse effect on the magnitude of the ventilated pocket depth, splitting the results into two distinct sub-groups:

1. Full ventilation (L/D = 1, 2, and 4):
    - Full ventilation is reached almost immediately (i.e. when V = 1 m/s).
2. Minor ventilation (L/D = 8, 10, 16, 20, 32, and 40):
    - The lower velocity results are not fully ventilated.

The above groupings are clearly visible on the following plots, along with the apparent trend for $L/D \geq 8$.

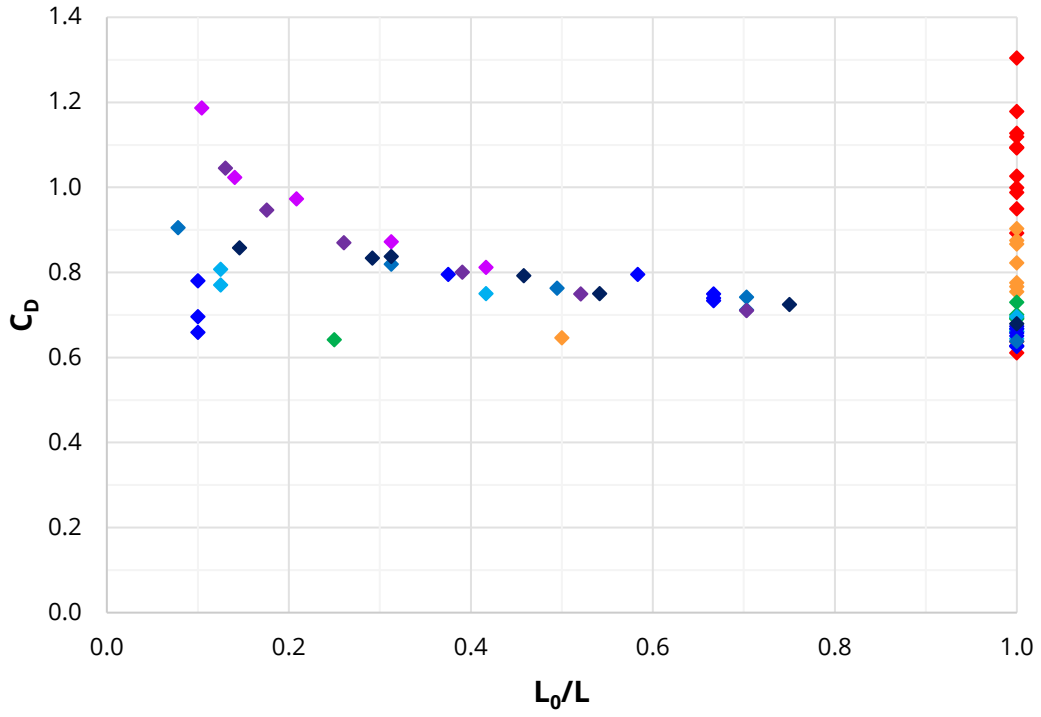

Figure 5-24: 24 mm – Drag coefficient vs ventilated pocket depth

Figure 5-24 presents what may, most likely, be a curve running through the results where the aspect ratio is equal to 32 and 40. From the final points of the L/D = 32 and 40 data series, it was observed that the data asymptotes towards a C_D of 0.6 – 0.65. The outliers in the data shown are for L/D = 2 (yellow) and 4 (green), where the results plotted are for the low velocity tests in which low ventilation occurs. It can be seen that in the partially ventilated, low velocity results that the drag coefficient is consistent throughout the change in aspect ratio.

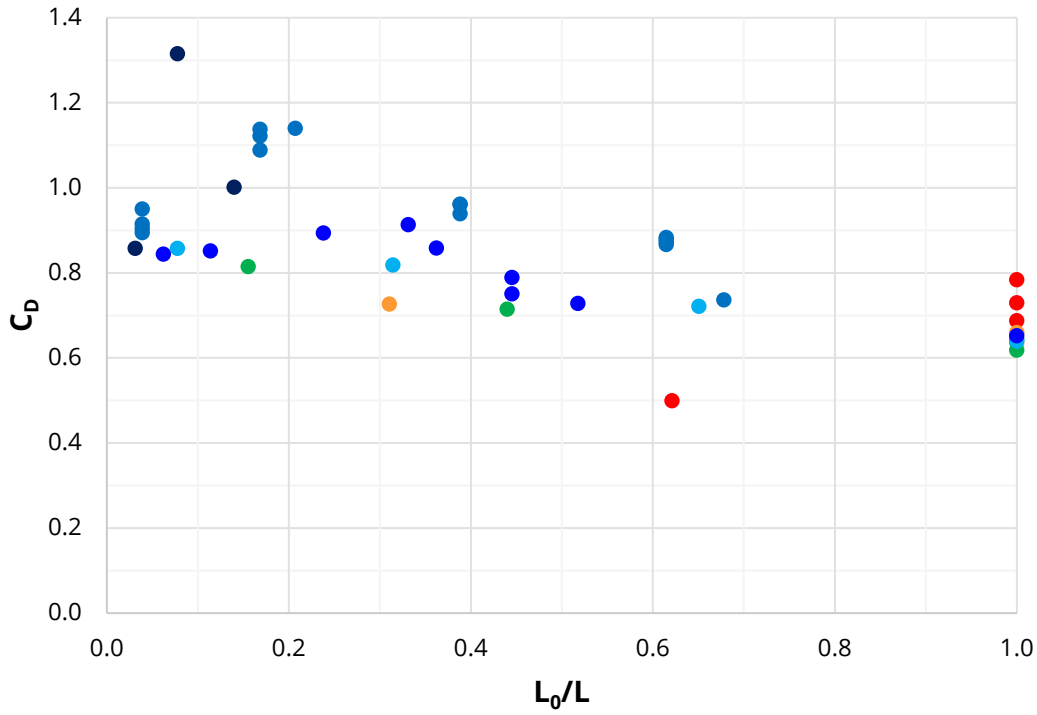

Figure 5-25: 48.3 mm – Closed – Drag coefficient vs ventilated pocket depth

The trend for *L*/*D* = 16 and 20 shown in Figure 5-25, Figure E-11 and Figure E-12 are similar to that of the 24 mm rod for the same aspect ratios. The similarity in the trend implies that the effect on the drag coefficient of the ventilated pocket depth is not driven by a change in the model's diameter.

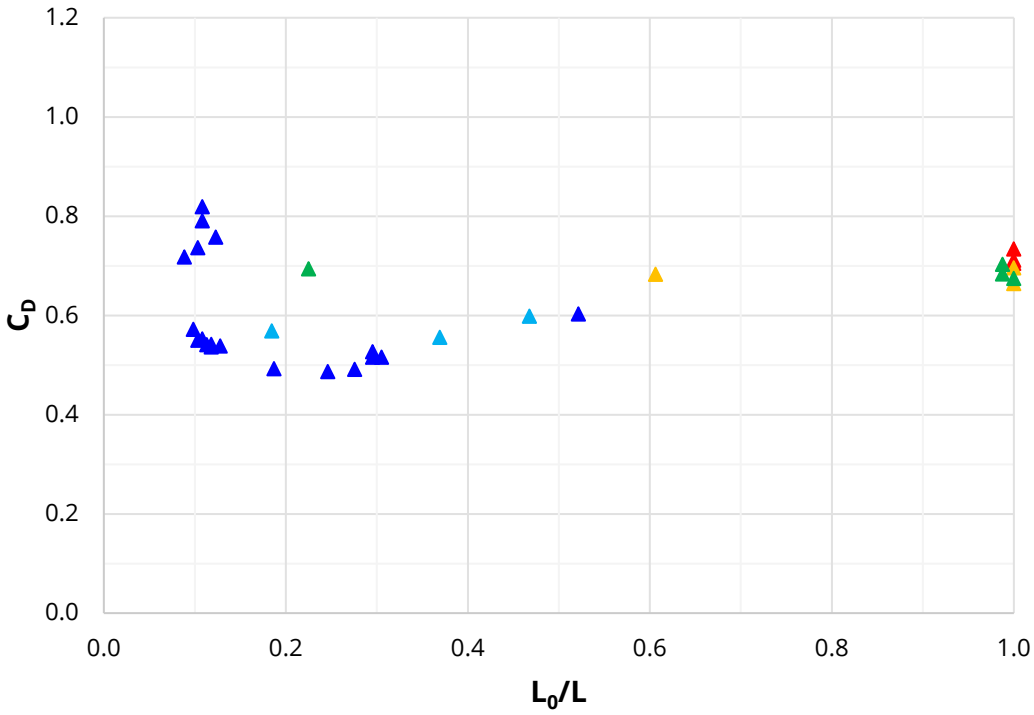

Figure 5-26: 101.6 mm – Drag coefficient vs ventilated pocket depth

The effect of ventilation on the drag coefficient for the 101.6 mm cylinder is substantially different to the smaller cylinder results. The C_D commences around 0.8 then reduces to just below 0.5 (Figure 5-26). This difference, in the effect of the ventilated flow, is due to the different Reynolds regime, and because the 101.6 mm cylinder goes through the drag crisis.

5.7 SUMMARY OF FINDINGS

The following insights and findings were derived from the test programme undertaken as part of this investigation to measure the hydrodynamics of a surface-piercing cylinder:

1. The results show a distinct relationship between the drag coefficient and the ventilated pocket depth, in concordance with the literature review.
2. The Bernoulli formula for inviscid flow, although it does not match the test results, does present as a limiting line, where one's results should not go above the line. This is useful in providing an initial predictive slope that closely correlates with the results.
3. To formulate a relationship to analytically determine D_1, it appears that both velocity and diameter must be considered. Keough attempted to account for the cylinder diameter with a dimensional diameter-dependent parameter. However, it appears that when non-dimensionalised, the resulting formula appears to be near identical to the Bernoulli equation for inviscid flow.
4. As with the bow wave height, there is a distinct relationship between the ventilated pocket depth and Froude number. This relationship most likely slightly differs from the proposed Chaplin and Teigen line based on the different test series results.
5. As would have been expected, the magnitude of the crossflow and inline oscillations are insignificant in comparison to a flexible cantilever or an elastically mounted cylinder. This is primarily due to the rigid mounting of the models, as well as the stiffness of the cylinders. Despite these conditions, even with minimal oscillations, the cylinders did indeed present with VIV lock-in for a range of aspect ratios. The 48.3 mm cylinder presents some very good examples of VIV lock-in for both crossflow and inline oscillations.
6. The drag coefficient asymptotes towards ≈ 0.6 – 0.65 for high aspect ratios as the Reynolds number increases, and to larger values for smaller aspect ratios.

Chapter 6 DISCUSSION

This chapter will analyse and discuss the results which were presented in the previous chapters.

Section 6.1 discusses the ventilated pocket depth in terms of the Froude number. The determination of a correlative relationship was found to be similar to the relationship developed by Chaplin and Teigen (2003).

Section 6.2 discusses the bow wave height for the closed cylinder conditions in comparison to the Bernoulli formula for inviscid flow.

Section 6.3 presents and discusses the drag coefficient as a function of the Reynolds number, ventilated pocket depth, aspect ratio, and the end condition effect. Each of the cylinder diameters have been presented separately to show the effect of diameter.

Section 6.4 discusses the effect that Vortex-Induced Vibrations have on the drag coefficient, as well as a comparison to the DNV GL recommended response curves.

Table 5-1 is still implemented herein as the legend for all of the plots, except where an explicit legend is provided. A fold-out version of Table 5-1 may be found on the very last page of this thesis.

6.1 VENTILATED POCKET DEPTH

Figure 6-1 presents a plot of L_0/D vs Fr^2 for all closed-ended cylinder test data, as a comparison to the Hay data presented in Figure 2-43. An orange line for L_0/D where $L_0 < L$ (i.e. not fully ventilated) corresponding to Equation 19 is also plotted, which Chaplin and Teigen (2003) derived from the Hay data for open-ended cylinders. It is apparent that the closed-ended cylinder results, though similar to the open-ended Hay results, have a steeper gradient than shown in Equation 20. Equation 31 describes the solid black line in the figure which better agrees with the closed-ended cylinder test data for L_0/D where $L_0 < L$.

$$\frac{L_0}{D} = 0.31 Fr_D^2 \qquad \text{Equation 31}$$

Of note in Figure 6-1 is the single point for $L/D = 16$ which sits well above the line, where it exhibited significant VIV excitation giving rise to an increased ventilated pocket depth for that given Froude number.

When considering the physics of the problem, it is evident that the ventilated flow depth is a function of both the velocity and the diameter. To then non-dimensionalise this problem and compare to various other results, Froude number was the obvious choice. By using Froude number, the ventilated flow must then also become non-dimensional to develop an entirely non-dimensional relationship.

The relationship described in Equation 31 is not dissimilar to the proposed relationship in Equation 19. While both formulae present a Froude squared relationship, it is the multiplier which varies, where the difference between 0.286 and 0.31 may be due to be experimental spread from both the Hay testing and the author's testing. A nominal multiplier of 0.3 may be implemented instead of the experimentally derived values.

Figure 6-2 presents the same data as in Figure 6-1, but is on a log-log scale, which allows for a direct visual comparison to the Hay results in Figure 3-4.

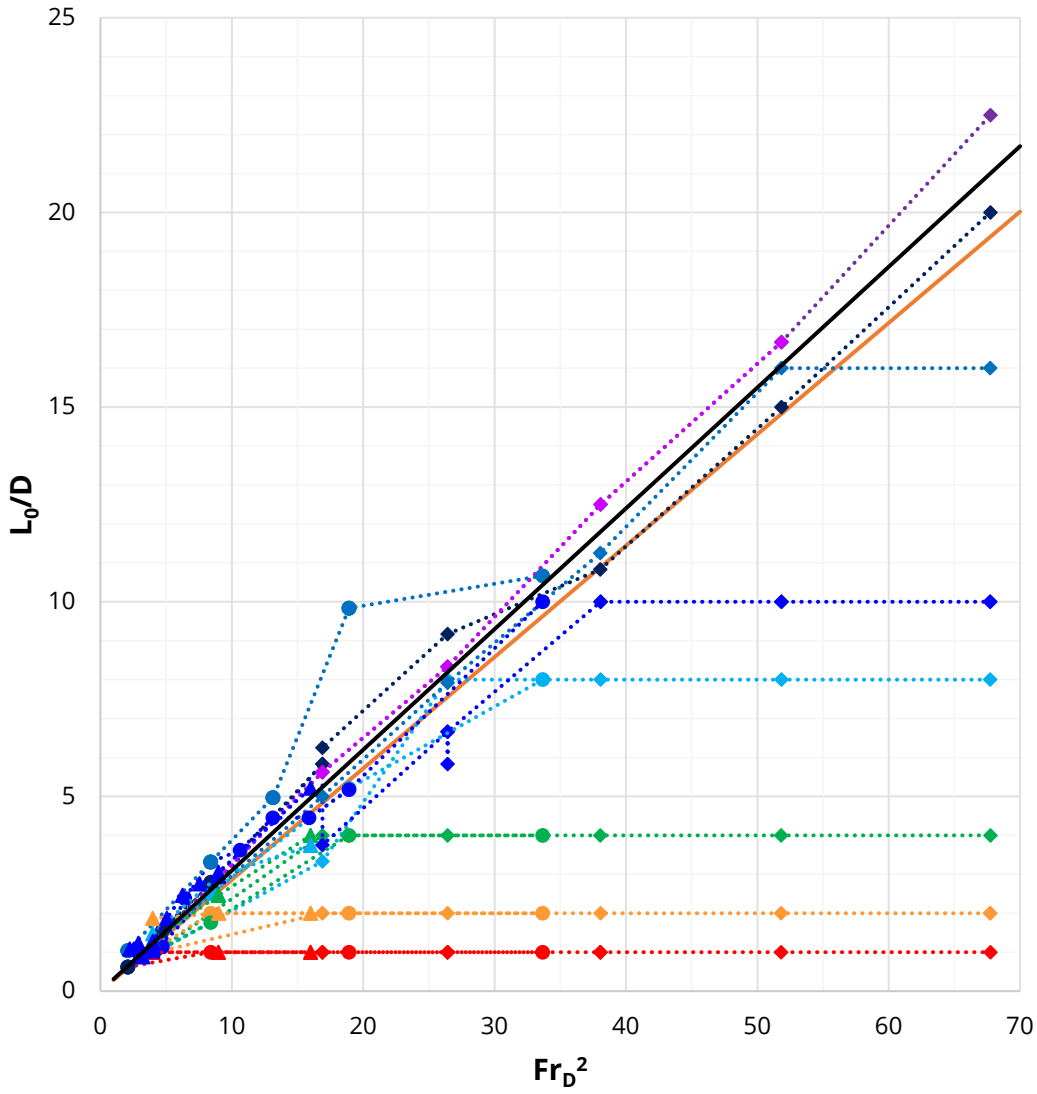

Figure 6-1: Test data for ventilated pocket depth as a function of Froude number, lin-lin plot

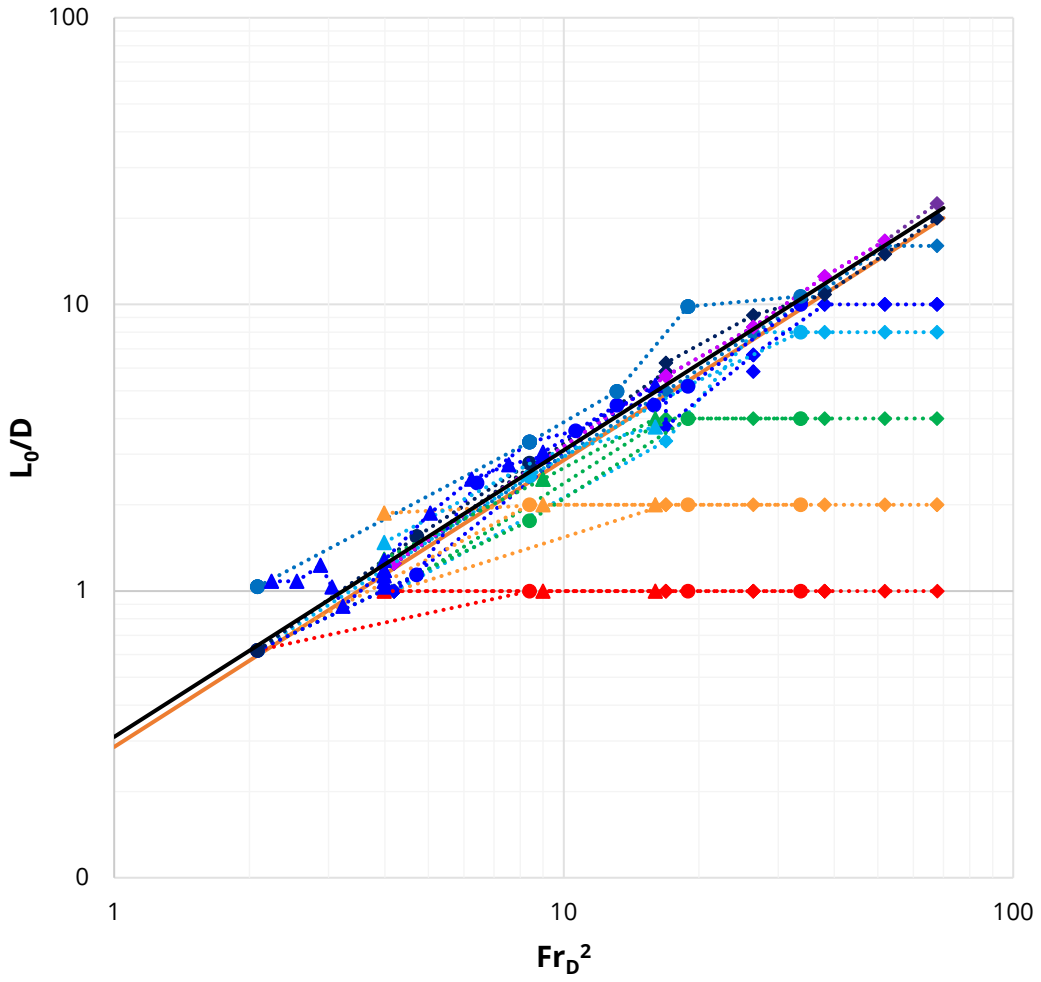

Figure 6-2: Test data for ventilated pocket depth as a function of Froude number, log-log plot

6.2 Bow Wave Height

Figure 6-3 presents the non-dimensionalised bow wave height (D_1/D) plotted against Fr^2 for all the closed cylinder test data series and compared against the Bernoulli Equation (black line). As with Hay's data in Figure 3-14 the bow wave height diverges markedly from the Bernoulli Equation and reaches an upper bound value of D_1/D = 10 – 12. A non-linear growth regression has been fitted through the test data, shown as a dashed line, which was developed using the Curve Fitting Toolbox in MATLAB and is described by Equation 32.

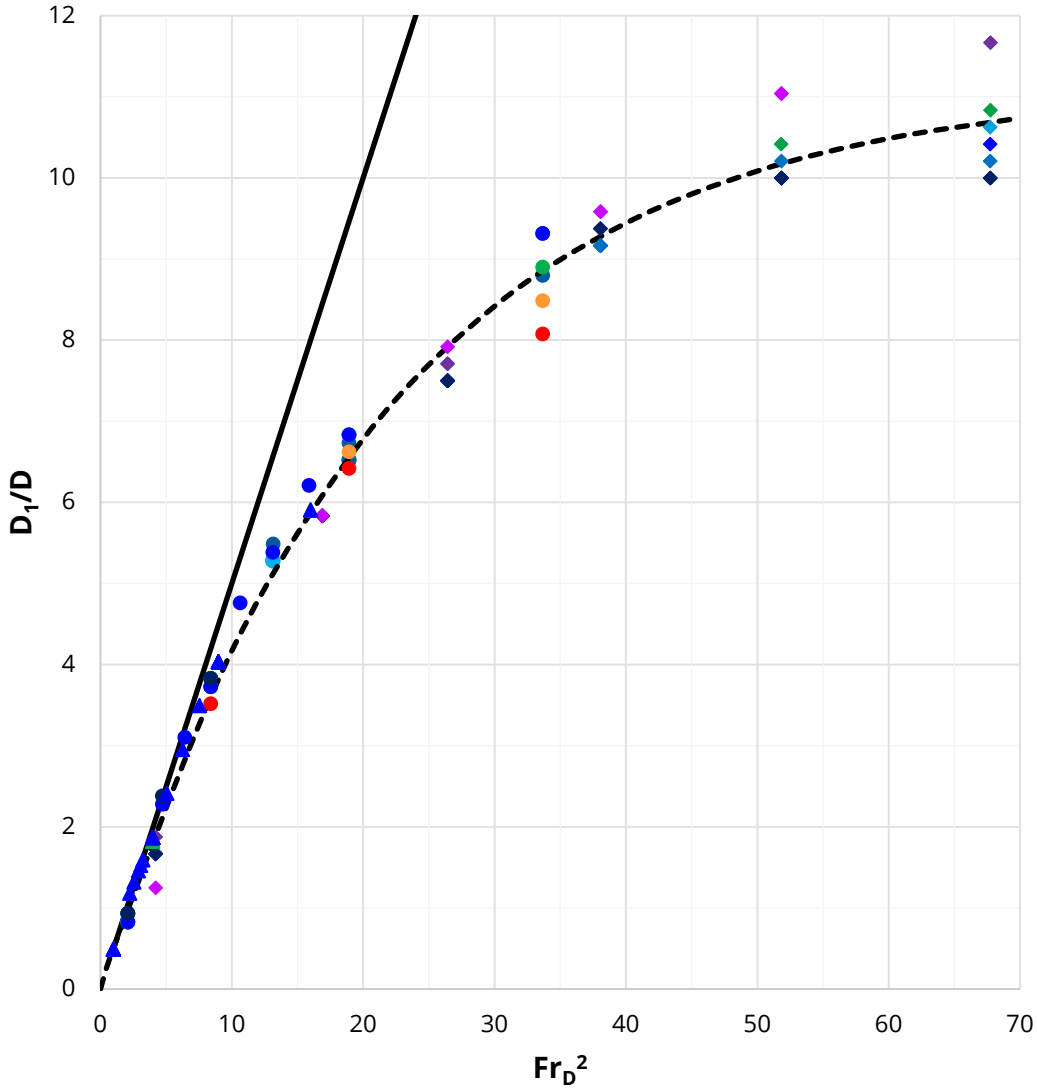

Figure 6-3: Non-dimensionalised bow wave height vs Froude number for all closed cylinder test cases, lin-lin plot

Figure 6-4 is a log-log plot of the data presented in Figure 6-3, which allows for direct visual comparison to Hay (Figure 3-14).

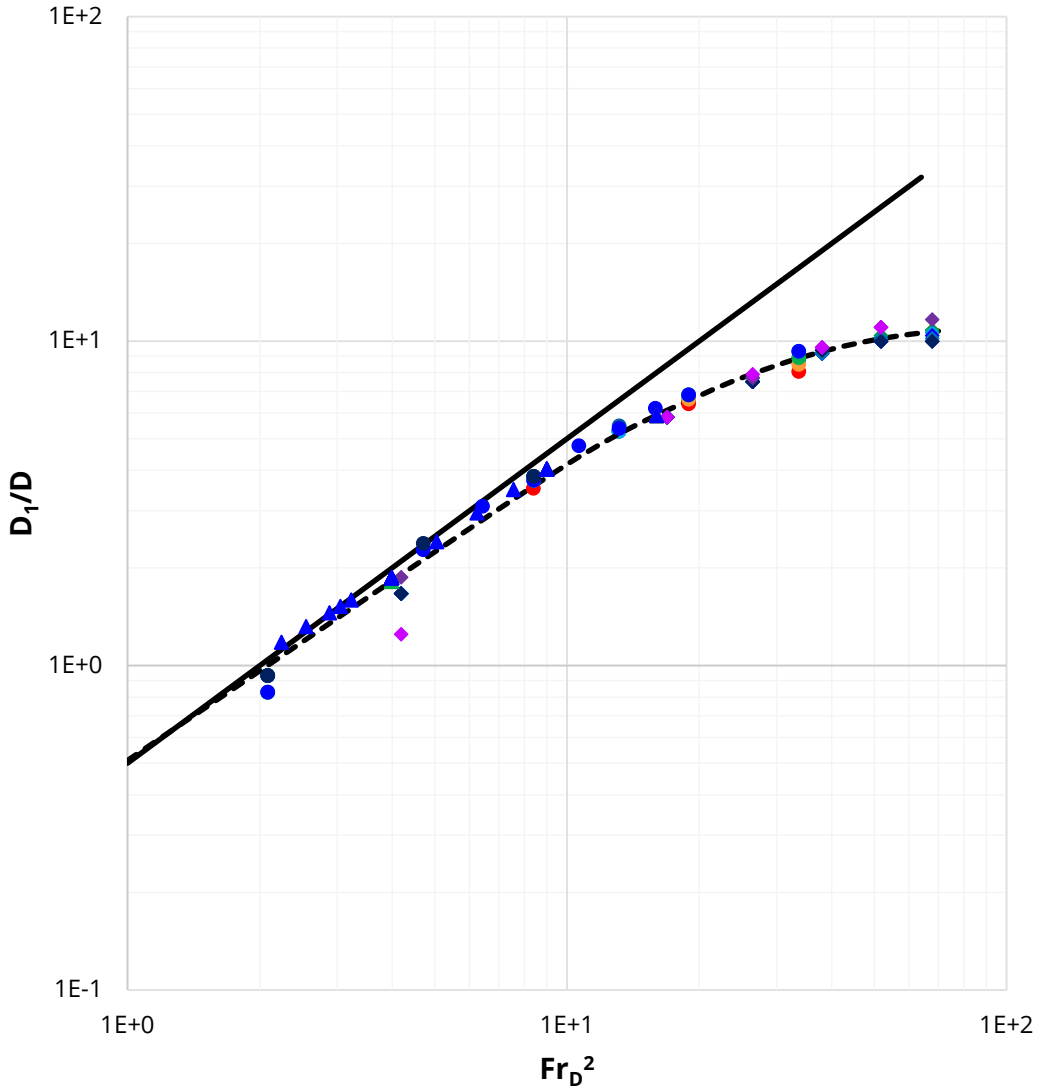

Figure 6-4: Non-dimensionalised bow wave height vs Froude number for all closed cylinder test cases, log-log plot

The exponential growth regression fit is described by Equation 32:

$$\frac{D_1}{D} = a\left(1 - e^{-bFr_D^2}\right) \qquad \text{Equation 32}$$

The parameters associated with Equation 32 are as follows:

a = 11.0685

b = 0.04678

The vast majority of the data presented in Figure 6-3 and Figure 6-4 falls within a 95% confidence band of the regression fit.

To further describe the physical phenomenon occurring, there is some disparity between the Bernoulli line and the authors developed LoBF from experimental model testing, as is evident in both Figure 6-3 and Figure 6-4. The difference between these lines may be attributed to viscous effects, which in turn result in a loss of head. Equation 34 defines the non-dimensional head loss:

$$\frac{\mathrm{D}_1}{\mathrm{D}_{\mathrm{Loss}}} = 0.5\mathrm{Fr}_{\mathrm{D}}^2 - a\left(1 - e^{-bFr_D^2}\right) \qquad \text{Equation 33}$$

Figure 6-5 presents the non-dimensional bow wave height with respect to Froude number squared for; the Bernoulli inviscid flow line, the authors developed LoBF and the head loss in order to visualise the change in the head loss as Froude number increases. It may be observed that the head loss becomes linearly parallel to Bernoulli at a Froude squared value of 50, this is due to the authors LoBF reaching the limiting asymptotic value.

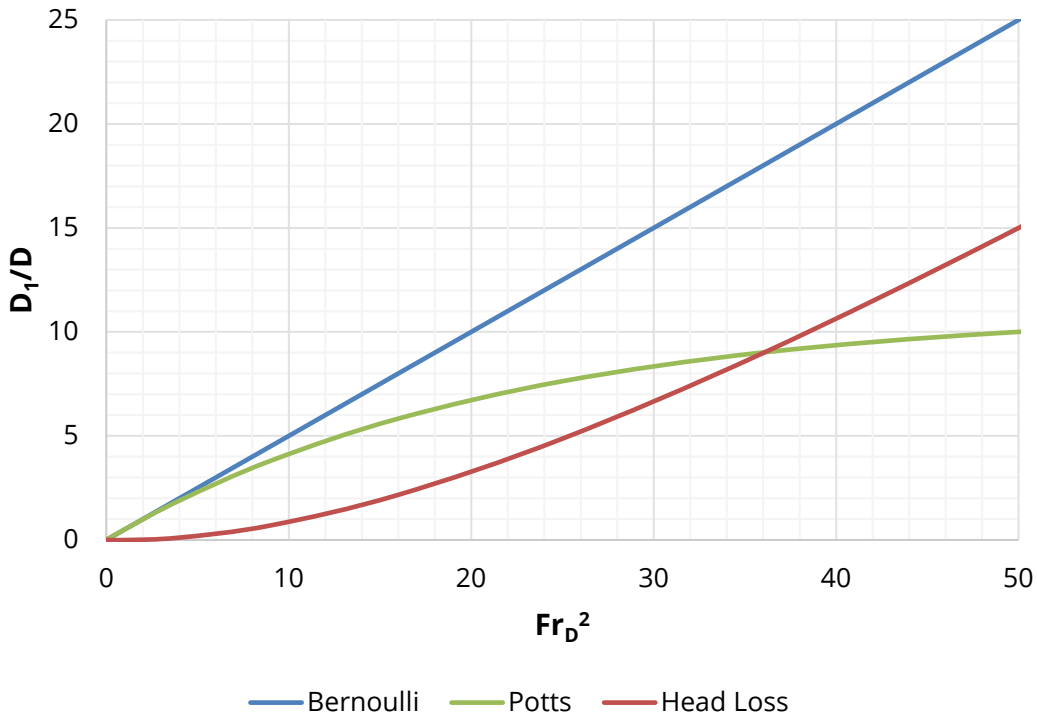

Figure 6-5: Non-dimensionalised bow wave height vs Froude number squared, highlighting the head loss phenomenon between the authors LoBF and the Bernoulli inviscid flow theory

6.3 Drag Coefficient

In order to understand the effect of a change in cylinder diameter, a comparison at one selected velocity has been studied. Figure 6-6 presents all of the models at a towing velocity of 1 m/s. Each of the diameters falls onto a distinct vertical spread (*Re* is constant for each different diameter). There is a visible separation in the C_D due to the aspect ratio: with the small ratios have a low drag coefficient, and the large aspect ratios have higher drag coefficients. The ordering of the aspect ratios seems to not apply in the case of the largest diameter cylinder. It is these aspect ratio-derived separations that are instrumental in the determination of an infinite *L*/*D* for vertical surface-piercing cylinders.

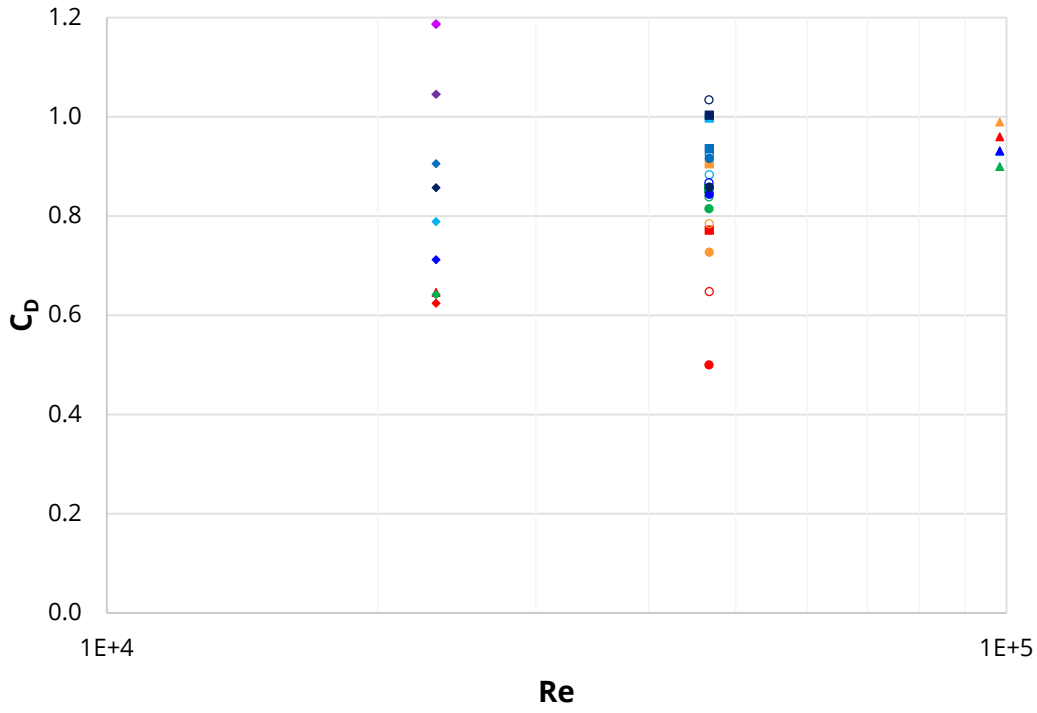

Figure 6-6: Drag coefficient vs Reynolds number for V = 1 m/s

Figure 6-7 presents only the closed-ended cylinder tests data at $V = 1$ m/s with averaged C_D in the upper plot and L_0/L in the lower plot, both with respect to the aspect ratio (L/D). It is apparent that the 101.6 mm cylinder has a virtually constant C_D, consistent with a near zero L_0/L. The 24 mm and 48.3 mm cylinders both exhibit significantly greater ventilated pocket formation with much larger L_0/L values, and concomitant reduction in the spanwise average C_D.

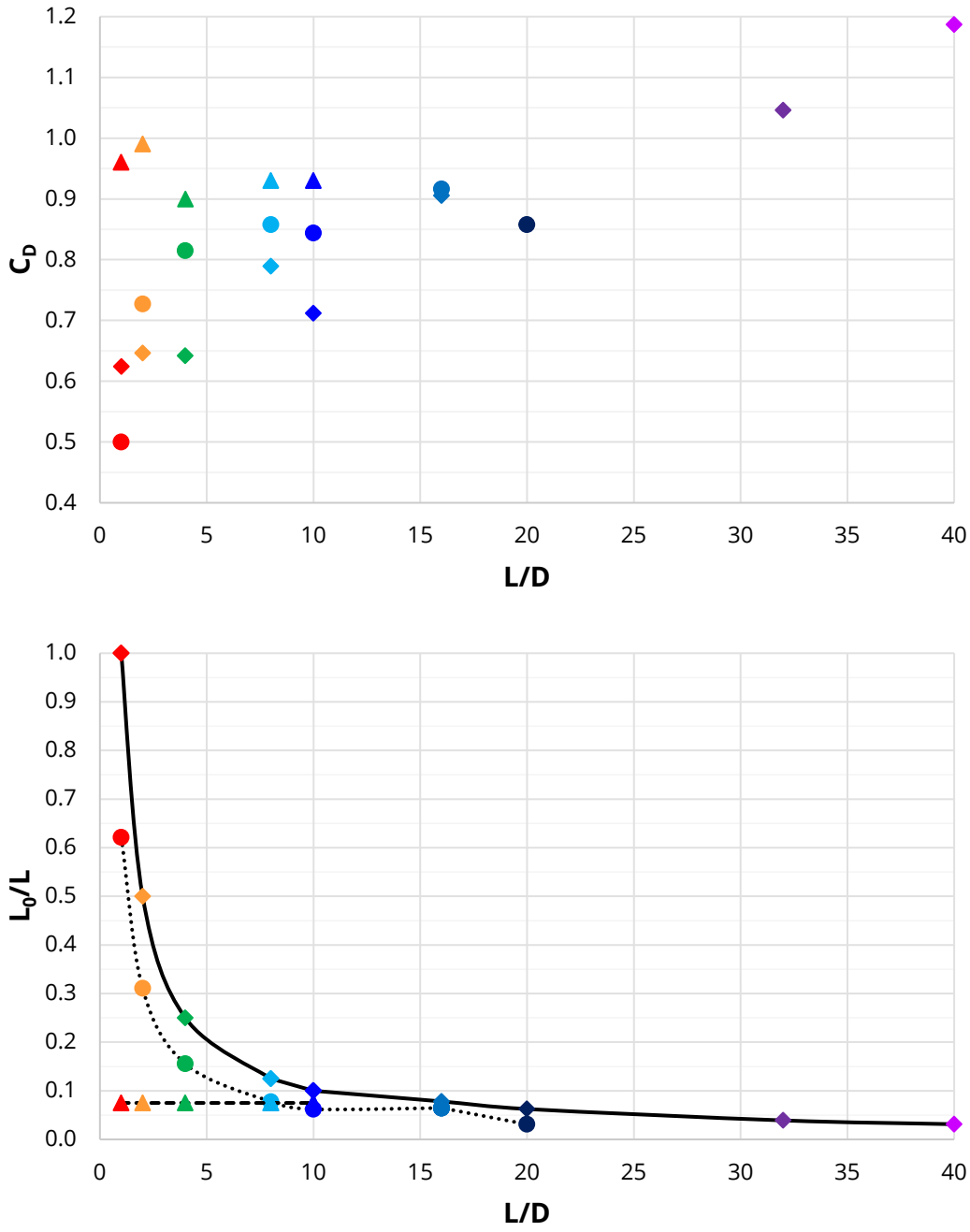

Figure 6-7: Closed cylinder C_D (averaged) and associated L_0/L vs L/D at V = 1 m/s for all test series

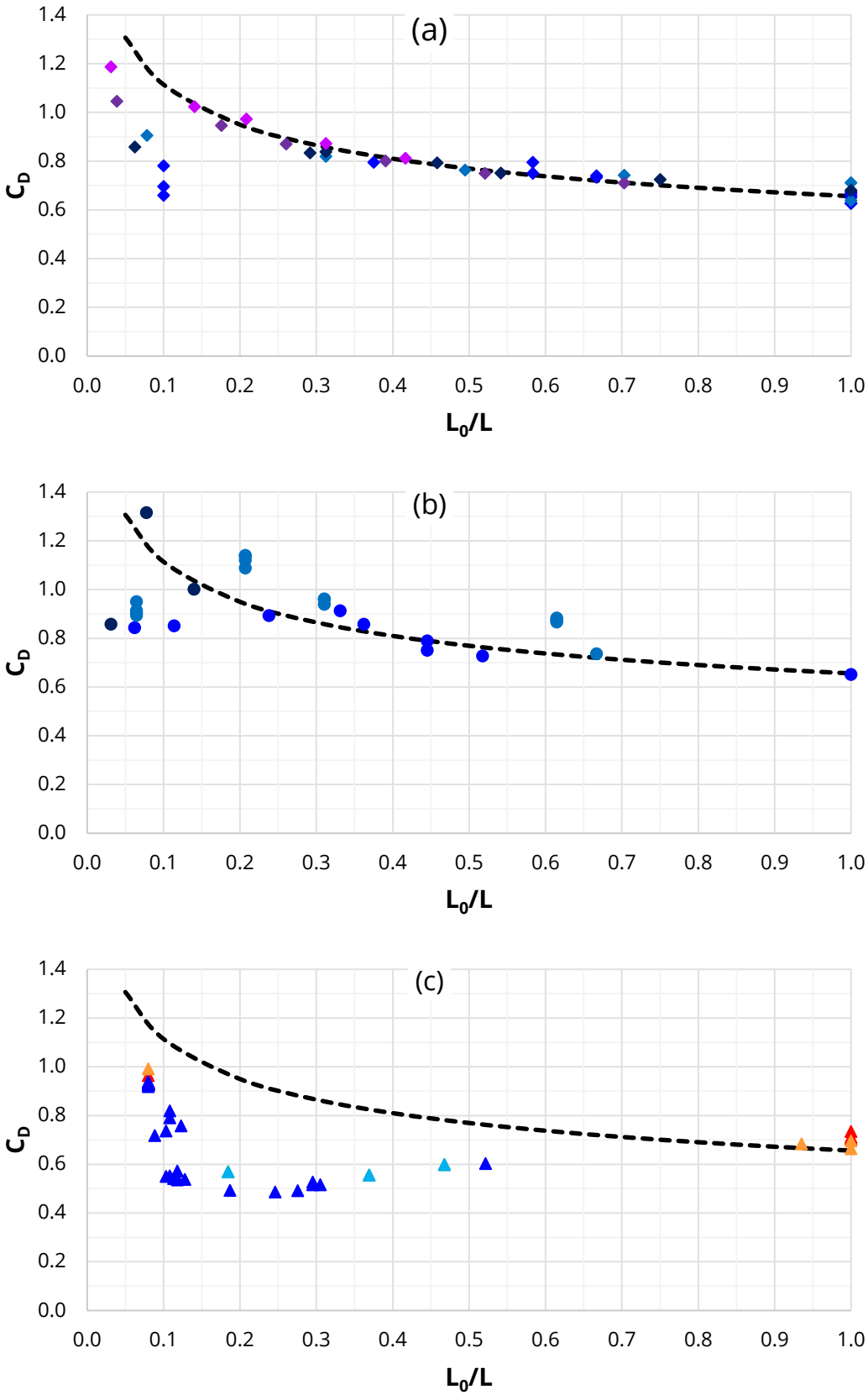

Figure 6-8: Closed cylinder C_D vs L_0/L for 24- 48- and 101- mm test series, (a), (b), and (c) respectively

Figure 6-8 presents plots of C_D vs L_0/L for each of the three-cylinder diameters closed ended datasets for aspect ratios $L/D \geq 10$. For $L_0/L > 0.1$ all the 24 mm cylinder data closely conform to a single curve, as described by Equation 34.

$$C_D = 0.656\left(\frac{L_0}{L}\right)^{-0.23} \qquad \text{Equation 34}$$

The 48.3 mm data also largely conforms with the curve, consistent with VIV associated drag amplification being experienced during this particular test series. The 101.6 mm test series exhibits a substantial divergence from the curve which is associated with the cylinder being within the drag crisis Reynolds regime.

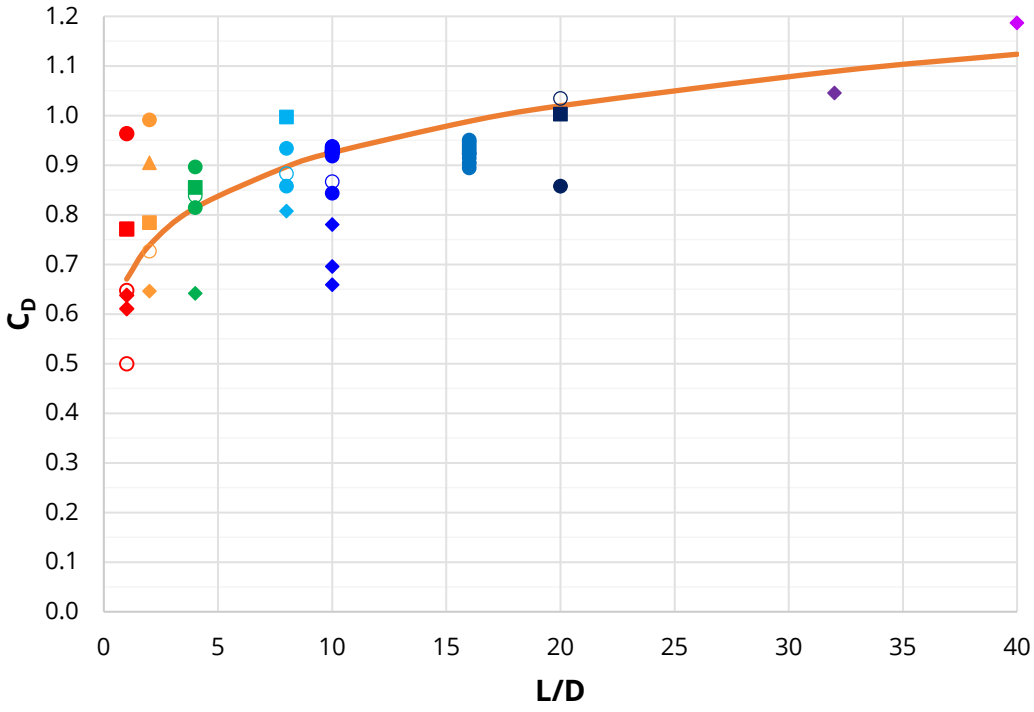

Figure 6-9: Drag coefficient vs aspect ratio at V = 1 m/s for all test series

Figure 6-9 plots the drag coefficient against the aspect ratio for only the low speed steady state velocity tests (V = 1 m/s) for all test series. The orange curve is a proposed relationship of C_D as a function of L/D for cantilevers in uniform sub-critical flow as presented in Potts et al. (2019a), described here as Equation 35.

$$C_D = \kappa * C_{D\infty}$$

$$\kappa = 0.583\left(\frac{L}{D}\right)^{0.14}$$

Equation 35

Figure 6-10 presents the drag reduction factor (κ) with respect to the aspect ratio (L/D) of the still water immersed length of the test cylinder for the 48 mm cylinder tests comparing the impact of the three end conditions. In all instances the cylinder with the end-plate disc exhibited the least reduction (or no reduction) in C_D, where it was most pronounced at very small aspect ratios of $L/D < 4$, where TAV associated drag has a significant contribution. However, the end-plates did not entirely suppress the effects of the short aspect ratio. The open-ended cylinder exhibited higher drag than the closed-ended cylinder at very small aspect ratios of $L/D < 4$, but thereafter they were largely the same. The relationship presented by Equation 35 has been plotted as the orange curve.

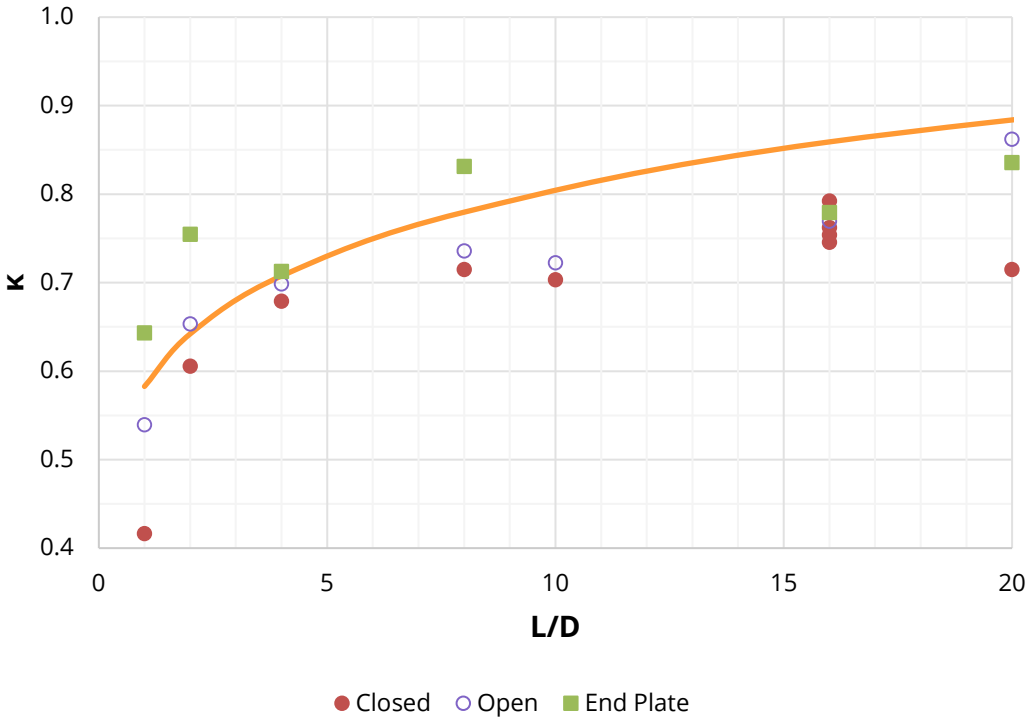

Figure 6-10: 48.3 mm cylinder end condition effects on drag modification factor, with respect to the aspect ratio

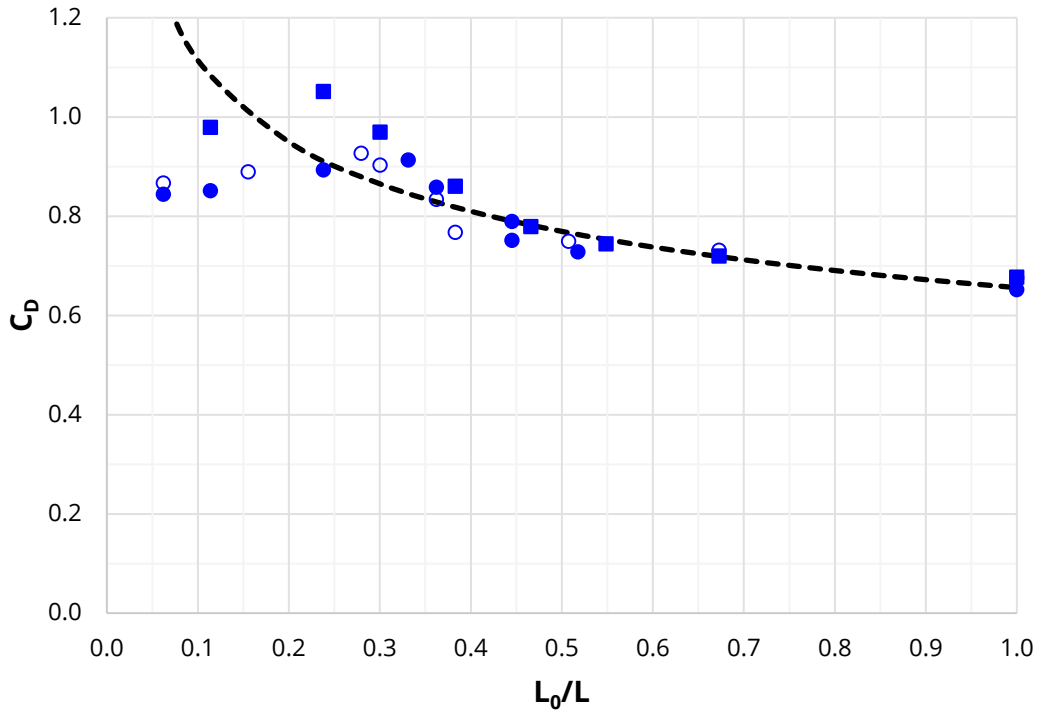

Figure 6-11: Alternate end condition effect on the drag coefficient for the 48.3 mm cylinder with respect to L_0/L

Figure 6-11 presents the L/D = 10 for the 48.3 mm diameter C_D vs L_0/L data for the three different end conditions tested, including closed end (as presented in Figure 6-8), open ended (comparable to Hay), and a disc end-plate of D_{EP}/D = 3.0. For L/D > 0.4 there is little discernible difference between the end conditions. For L/D < 0.4, the cylinder with the end-plate consistently exhibits a higher drag coefficient that the open or closed cylinders with the same degree of ventilated (L_0/L). The open-ended cylinder has either fractionally larger or comparable C_D to that of the close ended cylinder.

6.4 VORTEX-INDUCED VIBRATIONS

Both the crossflow and inline VIV are affected by the change in the end condition. The peak maximum oscillation amplitude varies amongst the aspect ratios by a maximum value of 25%. The reduced velocities at which the maximum oscillations occur do change, but they change due to the natural frequency of the model being altered. The change in natural frequency occurs as a function of the submerged length, the skin friction acting on the end disc, and the hydrofoil-like properties of the disc. The increase in the natural frequency translates to an increase in the reduced velocity up to 2.5 times greater than what is expected from the DNV GL response curve.

6.5 SUMMARY OF FINDINGS

The following findings and insights were derived from the discussion of the results as set out in this chapter:

1. A relationship regarding the ventilated pocket depth as a function of the velocity and the diameter has been empirically determined as per Equation 31. The derived empirical fit differs from the fit from Chaplin and Teigen (2003) (Equation 20). The difference between the two formulas is a function of the experimental scatter, and as such either of these formulas may be utilised when determining an estimate of the partially ventilated flow.
2. The relationship between the non-dimensional bow wave height and the Froude number may be described as an Exponential Growth regression fit, which has been defined in Equation 32.
3. In order to understand the change in drag coefficient with respect to the aspect ratio and the end conditions, the results from the V = 1 m/s tests were used.
    - Initially the difference within each diameter cylinder was that the lowest aspect ratios had the lowest drag coefficients, and the largest aspect ratios had the highest drag coefficients (Figure 6-7).
    - When considering the ventilated pocket depth, a relationship may be developed as a function of the drag coefficient as per Equation 34. This relationship, depicted in Figure 6-8, visually shows that as the ventilated pocket depth increases the drag coefficient decreases towards an asymptote of 0.6 – 0.65. The same formula was used when comparing the three end conditions as shown in Figure 6-11, where there are differences in the drag when $L_0/L < 0.4$, but for $L_0/L > 0.4$ the differences were found to be negligible.
    - The effect of the aspect ratio on the drag coefficient (drag reduction factor) was found to conform to the empirical fit defined as Equation 35 and represented in Figure 6-9 and Figure 6-10.

4. The vortex-induced vibrations were affected by the change in the end condition, where the peak maximum oscillations varied throughout the range of aspect ratios tested. The natural frequencies and mode shapes change as a function of the submerged length, skin friction, and hydrofoil-like properties of the end-plate.

Chapter 7 CONCLUSIONS

This investigation set out to determine the hydrodynamic characteristics of a vertical surface-piercing cylinder. Several aims, and objectives were developed, which provided the scope for which an extensive literature review was conducted, along with the reanalysis of the seminal paper on this topic. Since the inception of this field, the Hay (1947) reference has been cited by the majority of papers relating to vertical surface-piercing cylinders. A test programme was conducted to compare comprehensive data to historical data sets allowing novel discussion and conclusions to be drawn. In these regards this investigation determined the following conclusions:

7.1 INITIAL FINDINGS

The following findings are in direct response to the aims and objectives of this investigation:

1. **How do the end conditions of a vertical surface-piercing cylinder affect the VIV, near field wake and drag coefficient?**
    - The end conditions tested do not influence the bow wave height, nor the ventilated pocket depth significantly.
    - Although the results show some experimental scatter, this does not constitute the end condition significantly affecting the measured near field wake values.
    - The difference in the end conditions affects the peak end-tip amplitudes of oscillation (A/D) by an approximate value of 25%, which is further influenced by the prevalence of the cylinder entering into the VIV lock-in range (i.e. a larger cylinder with an end-plate will not be affected as much when compared to a smaller cylinder).
    - When considering the effect that the end conditions have on the drag coefficient, it has been shown that there is some disparity between the open, closed and end-plate conditions tested. The end-plate exhibited the highest drag coefficient of the conditions tested.

2. **What is the relationship of the depth of ventilated flow behind a vertical surface-piercing cylinder with respect to velocity and Froude number?**
    - Using the test data from Hay (1947), Chaplin and Teigen (2003) developed the following empirical relationship:

$$\frac{L_0}{D} = 0.286 Fr_D^2$$

This equation encompasses 80% of Hay's data within one standard deviation.

- From the test programme conducted during this investigation, the following empirical relationship was determined:

$$\frac{L_0}{D} = 0.31 Fr_D^2$$

When comparing the two formulae, it may be observed that the difference between them is most likely due to experimental variance, whereby a nominal value of 0.3 may be implemented instead of the two empirically fitted values as shown:

$$\frac{L_0}{D} = 0.3 Fr_D^2$$

3. **What is the near field hydrodynamic wake topology for a vertical surface-piercing cylinder?**
    - The metric by which the wake topology was defined was by the bow wave height (D_1).
    - From the test programme conducted during this investigation, the following relationship between D_1/D and Fr_D^2 was determined:

$$\frac{D_1}{D} = 11.0685\left(1 - e^{-0.04678 Fr_D^2}\right)$$

4. **At what aspect ratio (L/D) does the drag coefficient (C_D) become equal to that of a typically fully submerged infinite cylinder (i.e. C_D, at a Reynolds number range of 1E4 – 1E5) for a cylinder with an unventilated flow (i.e. $L_0 > L$)?**
    - From the literature, a fully submerged cylinder may be considered to be infinitely long with an aspect ratio ≥ 40 (Wieselsberger (1921)). From the perspective of a surface-piercing cantilevered cylinder in the sub-critical flow regime with an unventilated flow, the aspect ratio from this research has resulted in the following relationship:

$$\kappa = 0.583\left(\frac{L}{D}\right)^{0.14}$$

$$C_D = \kappa * C_{D\infty}$$

From the above defined relationship, the aspect ratio at which a cantilevered cylinder may be considered infinite can then be calculated to be slightly greater than 47. However, this number is less than one quarter of the current suggestion from DNV GL-RP-C205 regarding an infinite aspect ratio of L/D = 200 for a cantilevered cylinder.

7.2 ADDITIONAL FINDINGS

The following additional findings were made during this investigation:

- The end-plate diameter must have a minimum value of $D_{EP}/D \geq 3$ in order to greatly reduce the end-tip effects.
- The boundary layer thickness (δ) from the bottom of the tank has a significant effect on the drag coefficient (reduction factor). This effect must be accounted for when the boundary layer is present within a testing programme, as the drag coefficient is larger when affected by the boundary layer.
- Although the effect of compressible flow was not investigated, from the literature it was found to change the drag coefficient as a function of the aspect ratio, whereby in order to achieve $C_D = 1.2$, an aspect ratio of eight is required for a fully submerged cylinder.
- The use of an end-plate or splitter plate increases the drag coefficient within one diameter for both compressible and non-compressible flows.

7.3 WAY FORWARD

While this thesis has addressed the aims and objectives, as well as solving various other problems, several more questions have been posed and are yet to be answered. The following list highlights points which should be investigated going forward in order to further the knowledge in this field:

- What causes the bow wave to deviate from the Bernoulli formula for inviscid flow? (see Figure 6-3)
    - What are the physical processes for energy dissipation and diffusion?
        - Surface tension?
        - Stagnation point?
        - Angle of spray?
        - Flow fields?
- When measuring the drag coefficient along the length of a cylinder (either fully or partially submerged), is there a universal location for the infinite measurement of the drag coefficient?
    - This would be conducted by measuring the pressure around a cylinder as described in section 2.2.3.
    - At what distance from the end-plate does the drag coefficient alter?
- What is the minimum/optimal size and geometry of an end-plate in order to have no boundary layer effects, or end-tip effects?
- What is the effect of the Mach number in the development of the drag coefficient?
- What are the VIV characteristics of a rigidly mounted vertical surface-piercing cylinder?
- How will a change in stiffness alter the VIV characteristics of a rigidly mounted vertical surface-piercing cylinder?
- Does bottom mounting effect the results or can the problem be suitably addressed with top mounting?

Chapter 8 REFERENCES

A Rahman, M.A., (2015). *Vortex-Induced Vibration of Cylindrical Structure with Different Aspect Ratios* (Doctoral Thesis). The University of Western Australia, Perth, WA, Australia.

Achenbach, E., (1971). *Influence of Surface Roughness on the Cross-Flow Around a Circular Cylinder*. J. Fluid Mech. 46, 321–335. https://doi.org/10.1017/S0022112071000569

Allen, H.J., Vincenti, W.G., (1944). *Wall Interference in a Two-Dimensional-Flow Wind Tunnel, with Consideration of the Effect of Compressibility* (Technical Report No. NACA-TR-782). National Advisory Committee for Aeronautics (NACA), Moffet Field, CA, USA.

Apelt, C.J., Fox, T.A., (1992). *Fluctuating Loads on Cantilevered Cylinders in Uniform Flow*. Presented at the 11th Australasian Fluid Mechanics Conference, University of Tasmania, Hobart, AUS, pp. 523–526.

Ashworth Briggs, A., Fleming, A., Duffy, J., Binns, J.R., (2018). *Tracking the Vortex Core from a Surface-Piercing Flat Plate by Particle Image Velocimetry and Numerical Simulation*. Proc. IMechE. Part M: J. Engineering for the Maritime Environment 1–16. https://doi.org/10.1177/1475090218776202

Barltrop, N.D.P., Adams, A.J., (1991). *Dynamics of Fixed Marine Structures*, 3rd ed. Butterworth-Heinemann, Jordan Hill, OX, England.

Blevins, R.D., (1979). *Formulas for Natural Frequency and Mode Shape*. Van Nostrand Reinhold Company, Malabar, FL, USA.

Bruschi, G., Tsang, K., Nishioka, T., Wang, R., (2003). *A Comparison of Analytical Methods: Drag Coefficient of a Cylinder* (No. MAE 171A).

BSI, (1972). *Code of Basic Data for the Design of Buildings Chapter V. Loading Part 2. Wind Loads*, CP 3: Chapter V: Part 2: 1972. British Standards Institution, London, England.

Cathcart, S., (2014). *Experimental and Numerical Analysis of Flow around Semi-Submerged Circular Cylinders* (Final Year Project). University of Tasmania, Australian Maritime College, Launceston, TAS, Australia.

Chaplin, J.R., Teigen, P.S., (2003). *Steady Flow Past a Vertical Surface-Piercing Circular Cylinder*. J. Fluid Struc. 18, 271–285. https://doi.org/10.1016/j.jfluidstructs.2003.07.009

Conway, A.S.T., Binns, J.R., Ranmuthugala, D., Renilson, M., (2015). *Experimental and Numerical Analysis of Submarine Mast Surface Wakes*, in: PACIFIC 2015. Presented at the Pacific International Maritime Conference, Maritime Australia Limited, Sydney, NSW, Australia, p. 12.

Craig, I., (2016). *Review of Bonded Rubber Flexible Hose Design Codes and Guidelines in Relation to Sea Water Intake Risers on FPSO Vessels*. Presented at the Offshore Technology Conference Asia, Society of Petroleum Engineers, Kuala Lumpur, Malaysia. https://doi.org/10.4043/26648-MS

DNV GL, (2017a). *Free Spanning Pipelines* (Recommended Practice No. DNVGL-RP-F105). Det Norkse Veritas Germanischer Lloyd.

DNV GL, (2017b). *Environmental Conditions and Environmental Loads* (Recommended Practice No. DNVGL-RP-C205). Det Norkse Veritas Germanischer Lloyd.

Eisner, F., (1929). *Widerstandsmessungen an Umströmten Zylindern Von Kreis- Und Brückenpfeilerquerschnitt*. Springer, Vienna. https://doi.org/10.1007/978-3-7091-5394-9

Etzold, F., Fiedler, H., (1976). *The Near-Wake Structure of a Cantilevered Cylinder in a Cross-Flow*. Z. Flugwiss. 24, 77–82.

Finn, R.K., (1953). *Determination of the Drag on a Cylinder at Low Reynolds Numbers*. Journal of Applied Physics 24, 771–773. https://doi.org/10.1063/1.1721373

Fox, T.A., Apelt, C.J., (1993). *Fluid-Induced Loading of Cantilevered Circular Cylinders in a Low-Turbulence Uniform Flow. Part 3: Fluctuating Loads with Aspect Ratios 4 to 25*. J. Fluid Struc. 7, 375–386. https://doi.org/10.1006/jfls.1993.1022

Fox, T.A., West, G.S., (1993a). *Fluid-Induced Loading of Cantilevered Circular Cylinders in a Low-Turbulence Uniform Flow. Part 1: Mean Loading with Aspect Ratios in the Range 4 to 30*. J. Fluid Struc. 7, 1–14. https://doi.org/10.1006/jfls.1993.1001

Fox, T.A., West, G.S., (1993b). *Fluid-Induced Loading of Cantilevered Circular Cylinders in a Low-Turbulence Uniform Flow. Part 2: Fluctuating Loads on a Cantilever of Aspect Ratio 30*. J. Fluid Struc. 7, 15–28. https://doi.org/10.1006/jfls.1993.1002

Fox, T.A., West, G.S., (1990). *On the use of End Plates with Circular Cylinders*. Exp. Fluids 9, 237–239. https://doi.org/10.1007/BF00190426

Fujarra, A.L.C., Pesce, C.P., Flemming, F., Williamson, C.H.K., (2001). *Vortex-Induced Vibration of a Flexible Cantilever*. J. Fluids & Struc. 15, 651–658. https://doi.org/10.1006/jfls.2000.0368

Gowda, B.H.L., (1974). *Some Measurements on the Phenomenon of Vortex Shedding and Induced Vibrations of Circular Cylinders* (Report No. RN 437 (75-01)). Berlin Technical University, Berlin, Germany.

Gowen, F.E., Perkins, E.W., (1953). *Drag of Circular Cylinders for a Wide Range of Reynolds Numbers and Mach Numbers* (Technical Note No. NACA-TN-2960). National Advisory Committee for Aeronautics (NACA), Moffet Field, CA, USA.

Griffin, O.M., Ramberg, S.E., (1982). *Some Recent Studies of Vortex Shedding with Application to Marine Tubulars and Risers*. J. Energy Resourc. Technol. 104, 2–13. https://doi.org/10.1115/1.3230377

Hay, A.D., (1947). *Flow about Semi-Submerged Cylinders of Finite Length* (Technical Report No. NObs-34006). Princeton University, Princeton, NJ, USA.

Hay, A.D., (1941). *Various Communications*.

Hoerner, S.F., (1965). *Fluid-Dynamic Drag: Practical Information on Aerodynamic Drag and Hydrodynamic Resistance*, 2nd ed. Dr. Sighard F. Hoerner.

Hogben, N., (1974). *Wave Resistance of Surface Piercing Vertical Cylinders in Uniform Currents*. National Physical Laboratory.

Hsieh, T., (1964). *Resistance of Cylindrical Piers in Open-Channel Flow*. J. Hydraulics Div. 90, 161–173.

Huang, S., (2011). *VIV Suppression of a Two-Degree-of-Freedom Circular Cylinder and Drag Reduction of a Fixed Circular Cylinder by the use of Helical Grooves*. J. Fluid Struc. 27, 1124–1133. https://doi.org/10.1016/j.jfluidstructs.2011.07.005

Huang, S., (2010). *Cylinder Drag Reduction by the use of Helical Grooves*, in: HYDRALAB III. Presented at the Proceedings of the HYDRALAB III Joint User Meeting, Hannover.

Huang, S., (2006). *Preliminary Tank Testing of VIV Suppression of Helical Grooves*, in: OMAE2006. Presented at the 25th OMAE Conference, American Society of Mechanical Engineers (ASME), Hamburg, Germany, pp. 469–473. https://doi.org/10.1115/OMAE2006-92002

Institution of Naval Architects, (1955). *The Papers of William Froude*. Institution of Naval Architects, London.

ITTC, (2017). *Resistance Test* (Recommended Procedures and Guidelines No. 7.5-02-02–01). International Towing Tank Conference.

Jones Jr, G.W., Cincotta, J.J., Walker, R.W., (1969). *Aerodynamic Forces on a Stationary and Oscillating Circular Cylinder at High Reynolds Numbers* (Technical Report No. NASA-TR-R-300). National Aeronautics and Space Administration (NASA), Hampton, VA, USA.

Kawamura, T., Hiwada, M., Hibino, T., Mabuchi, I., Kumada, M., (1984). *Flow around a Finite Circular Cylinder on a Flat Plate: Cylinder Height Greater than Turbulent Boundary Layer Thickness*. Bulletin of JSME 27, 2142–2151. https://doi.org/10.1299/jsme1958.27.2142

Keough, S.J., Kermonde, I.L., Amiet, A., Philip, J., Ooi, A., Monty, J.P., Anderson, B., (2016). *Time Resolved Measurements of Wake Characteristics from Vertical Surface-Piercing Circular Cylinders*, in: 20 AFMC. Presented at the 20th Australasian Fluid Mechanics Conference, Perth, WA, Australia, p. 4.

Kilner, A.A., Kurts, P., Potts, D., Johnstone, D., Potts, A.E., Marcollo, H., (2018). *The Efficacy of Inverted Helical Strakes*. Presented at the 23rd Offshore Symposium, The Society of Naval Architects and Marine Engineers (SNAME), Houston, TX, USA, p. 17.

Kitagawa, T., Fujino, Y., Kimura, K., (1999). *Effects of Free-End Condition on End-Cell-Induced Vibration*. J. Fluids & Struc. 13, 499–518. https://doi.org/10.1006/jfls.1999.0214

Kitagawa, T., Fujino, Y., Kimura, K., Mizuno, Y., (2002). *Wind Pressures Measurement on End-Cell-Induced Vibration of a Cantilevered Circular Cylinder*. J. Wind Eng. Ind. Aerodyn. 90, 395–405. https://doi.org/10.1016/S0167-6105(01)00200-8

Kitagawa, T., Fujino, Y., Kimura, K., Mizuno, Y., (2001). *Wind Pressures on End-Cell-Induced Vibration of Circular Tower*. J. Eng. Mech. 127, 1135–1143. https://doi.org/10.1061/(ASCE)0733-9399(2001)127:11(1135)

Lamb, H., (1895). *Hydrodynamics*. Cambridge University Press, Cambridge University.

Lienhard, John.H., (1966). *Synopsis of Lift, Drag, and Vortex Frequency Data for Rigid Circular Cylinders* (Bulletin No. 300). Technical Extension Service, Washington State University, Pullman, WA, USA.

Nayyar, M.L. (Ed.), (2000). *Piping Handbook*, 7th ed, McGraw-Hill Handbooks. McGraw-Hill, New York.

Nestegård, A., (2018). *DNV-RP-C205 - External Customer Query*.

Norberg, C., (1994). *An Experimental Investigation of the Flow around a Circular Cylinder: Influence of Aspect Ratio*. J. Fluid Mech. 258, 287–316. https://doi.org/10.1017/S0022112094003332

Okajima, A., Nakamura, A., Kosugi, T., Uchida, H., Tamaki, R., (2004). *Flow-Induced In-Line Oscillation of a Circular Cylinder*. Eur. J. Mech. B/Fluids 23, 115–125. https://doi.org/10.1016/j.euromechflu.2003.09.009

Okamoto, S., Sunabashiri, Y., (1992). *Vortex Shedding from a Circular Cylinder of Finite Length Placed on a Ground Plane*. J. Fluids Eng. 114, 512. https://doi.org/10.1115/1.2910062

Okamoto, T., Yagita, M., (1973). *The Experimental Investigation on the Flow Past a Circular Cylinder of Finite Length Placed Normal to the Plane Surface in a Uniform Stream*. Bulletin of JSME 16, 805–814. https://doi.org/10.1299/jsme1958.16.805

Pechstein, W., (1942). *Wirkung des Natürlichen Windes auf einen Größeren Kreiszylinder*. VDI Zeitschrift 86, 220–222.

Perry, B., (1954). *Experiments on Struts Piercing the Water Surface* (Report No. E-55.1). California Institute of Technology, Pasadena, CA, USA.

Potts, A.E., Potts, D.A., Marcollo, H., Jayasinghe, K., (2018). *Strouhal Number for VIV Excitation of Long Slender Structures*, in: OMAE2018. Presented at the 37th OMAE Conference, American Society of Mechanical Engineers (ASME), Madrid, Spain, p. 18. https://doi.org/10.1115/OMAE2018-77433

Potts, D.A., (2018). *An Investigation of Structural Damping of Helically Laid Cables* (Honours Thesis). Victoria University, Melbourne, VIC, Australia.

Potts, D.A., Binns, J.R., Marcollo, H., Potts, A.E., (2019a). *Hydrodynamics of Towed Vertical Surface-Piercing Cylinders*, in: OMAE2019. Presented at the 38th OMAE Conference, American Society of Mechanical Engineers (ASME), Glasgow, Scotland, p. 15.

Potts, D.A., Binns, J.R., Potts, A.E., Marcollo, H., (2019b). *The Effect of Aspect Ratio on the Drag of Bare Cylinders*, in: OMAE2019. Presented at the 38th OMAE Conference, American Society of Mechanical Engineers (ASME), Glasgow, Scotland, p. 18.

Relf, E.F., (1914). *Discussion of the Results of Measurements of the Resistance of Wires, with Some Additional Tests on the Resistance of Wires of Small Diameter* (Reports and Memoranda No. R & M 102). Aeronautical Research Committee (ARC).

Relf, E.F., Simmons, L.F.G., (1925). *LIII. On the Frequency of the Eddies Generated by the Motion of Circular Cylinders through a Fluid*. Philosophical Magazine, 1901-1925 49, 509–511. https://doi.org/10.1080/14786442508634628

Reynolds, O., (1883). *XXIX: An Experimental Investigation of the Circumstances Which Determine Whether the Motion of Water Shall Be Direct or Sinuous, and of the Law of Resistance in Parallel Channels*. Philosophical Transactions of the Royal Society of London 174, 935–982. https://doi.org/10.1098/rstl.1883.0029

Roshko, A., (1961). *Experiments on the Flow Past a Circular Cylinder at Very High Reynolds Number*. J. Fluid Mech. 10, 345–356. https://doi.org/10.1017/S0022112061000950

Roshko, A., (1955). *On the Wake and Drag of Bluff Bodies*. Journal of the Aeronautical Sciences 22, 124–132. https://doi.org/10.2514/8.3286

Rostamy, N., Sumner, D., Bergstrom, D.J., Bugg, J.D., (2012). *Local Flow Field of a Surface-Mounted Finite Circular Cylinder*. J. Fluids & Struc. 34, 105–122. https://doi.org/10.1016/j.jfluidstructs.2012.04.014

Schiller, L., Linke, W., (1933). *Pressure and Frictional Resistance of a Cylinder at Reynolds Numbers 5,000 to 40,000* (Technical Memorandum No. NACA-TM-715). National Advisory Committee for Aeronautics (NACA), Washington D.C., VA, USA.

Schlichting, H., Gersten, K., (2017). *Boundary-Layer Theory*, 9th ed. Springer, Berlin Heidelberg.

Standards Australia, Standards New Zealand, (2016). *Cold-Formed Structural Steel Hollow Sections*, (AS/NZS 1163-2016+A1). SAI Global.

Stansby, P.K., (1974). *The Effects of End Plates on the Base Pressure Coefficient of a Circular Cylinder*. The Aeronautical Journal 78, 36–37. https://doi.org/10.1017/S0001924000036319

Strouhal, V., (1878). *Ueber eine besondere Art der Tonerregung*. Ann. Phys. 241, 216–251. https://doi.org/10.1002/andp.18782411005

Sumer, B.M., Fredsoe, J., (2006). *Hydrodynamics Around Cylindrical Structures*, 2nd ed, Advanced Series on Ocean Engineering. World Scientific, Denmark.

Sumner, D., (2013). *Flow Above the Free End of a Surface-Mounted Finite-Height Circular Cylinder: A Review*. J. Fluids & Struc. 43, 41–63. https://doi.org/10.1016/j.jfluidstructs.2013.08.007

Szepessy, S., Bearman, P.W., (1992). *Aspect Ratio and End Plate Effects on Vortex Shedding from a Circular Cylinder*. J. Fluid Mech. 234, 191–217. https://doi.org/10.1017/S0022112092000752

Tanaka, S., Murata, S., (1999). *An Investigation of the Wake Structure and Aerodynamic Characteristics of a Finite Circular Cylinder. Time-Averaged Wake Structures behind Circular Cylinders with Various Aspect Ratios.* JSME International Journal Series B 42, 178–187. https://doi.org/10.1299/jsmeb.42.178

Tanida, Y., Okajima, A., Watanabe, Y., (1973). *Stability of a Circular Cylinder Oscillating in Uniform Flow or in a Wake*. J. Fluid Mech. 61, 769–784. https://doi.org/10.1017/S0022112073000935

Taniguchi, S., Sakamoto, H., Arie, M., (1981). *Flow around Circular Cylinders of Finite Height Placed Vertically in Turbulent Boundary Layers*. Bulletin of JSME 24, 37–44. https://doi.org/10.1299/jsme1958.24.37

Thomsen, P., (1963). *Cavity Shape and Drag in Ventilated Flow; Theory and Experiment* (Scientific Report No. TRG-156-SR-2). Technical Research Group, Syosset, NY, USA. https://doi.org/10.21236/AD0401925

Thomson, S.W., (1880). *XVI: On Gravitational Oscillations of Rotating Water*. The London, Edinburgh, and Dublin Philosophical Magazine and Journal of Science 10, 109–116. https://doi.org/10.1080/14786448008626897

Tritton, D.J., (1959). *Experiments on the Flow Past a Circular Cylinder at Low Reynolds Numbers*. J. Fluid Mech. 6, 547. https://doi.org/10.1017/S0022112059000829

Uematsu, Y., Yamada, M., Ishii, K., (1990). *Some Effects of Free-Stream Turbulence on the Flow Past a Cantilevered Circular Cylinder*. J. Wind Eng. Ind. Aerodyn. 33, 43–52. https://doi.org/10.1016/0167-6105(90)90019-9

Vandiver, J.K., (2012). *Damping Parameters for Flow-Induced Vibration*. J. Fluid Struc. 35, 105–119. https://doi.org/10.1016/j.jfluidstructs.2012.07.002

Vandiver, J.K., (1983). *Drag Coefficients of Long Flexible Cylinders*, in: Offshore Technology Conference. Presented at the 15th Annual Offshore Technology Conference, Society of Petroleum Engineers, Houston, TX, USA. https://doi.org/10.4043/4490-MS

Welsh, C.J., (1953). *The Drag of Finite-Length Cylinders Determined from Flight Tests at High Reynolds Numbers for a Mach Number Range from 0.5 to 1.3* (Technical Note No. NACA-TN-2941). National Advisory Committee for Aeronautics (NACA), Langley Field, VA, USA.

White, C.M., (1946). *The Drag of Cylinders in Fluids at Slow Speeds*. Proc. R. Soc. Lond. A Math. Phys. Sci. 186, 472–479. https://doi.org/10.1098/rspa.1946.0059

Wieselsberger, C., (1922). *New Data on the Laws of Fluid Resistance* (Technical Note No. NACA-TN-84). National Advisory Committee for Aeronautics (NACA).

Wieselsberger, C., (1921). *Neure Festellungen uber die Gesetze des Flussigkeits- und Luftwiderstands*. Phys. Z. 321–328.

Zdravkovich, M.M., (2003). *Flow Around Circular Cylinders: Volume II: Applications*, Flow Around Circular Cylinders: A Comprehensive Guide Through Flow Phenomena, Experiments, Applications, Mathematical Models, and Computer Simulations. Oxford University Press Inc., New York, NY, USA.

Zdravkovich, M.M., (1997). *Flow Around Circular Cylinders: Volume I: Fundamentals*, Flow Around Circular Cylinders: A Comprehensive Guide Through Flow Phenomena, Experiments, Applications, Mathematical Models, and Computer Simulations. Oxford University Press Inc., New York, NY, USA.

Zdravkovich, M.M., (1981). *Review and Classification of Various Aerodynamic and Hydrodynamic Means for Suppressing Vortex Shedding*. J. Wind Eng. Ind. Aerodyn. 7, 145–189. https://doi.org/10.1016/0167-6105(81)90036-2

Chapter 9 BIBLIOGRAPHY

A Rahman, M.A., (2015). *Vortex-Induced Vibration of Cylindrical Structure with Different Aspect Ratios* (Doctoral Thesis). The University of Western Australia, Perth, WA, Australia.

A Rahman, M.A., Krish, T., (2013). *Vortex-Induced Vibration of Cylindrical Structure with Different Aspect Ratio*. Presented at the Twenty-Third International Offshore and Polar Engineering Conference, International Society of Offshore and Polar Engineers, Anchorage, AL, USA, p. 7.

Achenbach, E., (1971). *Influence of Surface Roughness on the Cross-Flow Around a Circular Cylinder*. J. Fluid Mech. 46, 321–335. https://doi.org/10.1017/S0022112071000569

Allen, H.J., Vincenti, W.G., (1944). *Wall Interference in a Two-Dimensional-Flow Wind Tunnel, with Consideration of the Effect of Compressibility* (Technical Report No. NACA-TR-782). NACA, Moffet Field, CA, USA.

Anagnostopoulos, E., Gerrard, J.H., (1976). *A Towing Tank with Minimal Background Motion*. J. Phys. E 9, 951–954. https://doi.org/10.1088/0022-3735/9/11/020

Ashworth Briggs, A., Fleming, A., Duffy, J., Binns, J.R., (2018). *Tracking the Vortex Core from a Surface-Piercing Flat Plate by Particle Image Velocimetry and Numerical Simulation*. Proc. IMechE. Part M: J. Engineering for the Maritime Environment 1–16. https://doi.org/10.1177/1475090218776202

Ayoub, A., Karamcheti, K., (1982). *An Experiment on the Flow Past a Finite Circular Cylinder at High Subcritical and Supercritical Reynolds Numbers*. J. Fluid Mech. 118, 1–26. https://doi.org/10.1017/S0022112082000937

Baban, F., So, R.M.C., (1991). *Aspect Ratio Effect on Flow-Induced Forces on Circular Cylinders in a Cross-Flow*. Exp. Fluids 10, 313–321. https://doi.org/10.1007/BF00190247

Barltrop, N.D.P., Adams, A.J., (1991). *Dynamics of Fixed Marine Structures*, 3rd ed. Butterworth-Heinemann, Jordan Hill, OX, England.

Bearman, P.W., Graham, J.M.R., (1980). *Vortex Shedding from Bluff Bodies in Oscillatory Flow: A Report on Euromech 119*. J Fluid Mech 99, 225–245. https://doi.org/10.1017/S0022112080000596

Benaroya, H., Wei, T.J. (Eds.), (2003). *IUTAM Symposium on Integrated Modeling of Fully Coupled Fluid Structure Interactions Using Analysis, Computations and Experiments*, 1st ed, Fluid Mechanics and Its Applications. Springer-Dordrecht, New Jersey, NY, USA.

Blevins, R.D., (1979). *Formulas for Natural Frequency and Mode Shape*. Van Nostrand Reinhold Company, Malabar, FL, USA.

Bouché, H. (Ed.), (1920). *L'Aéronautique*, in: L'Aéronautique. Gauthier-Villars, Paris, France, pp. 331–552.

Bruschi, G., Tsang, K., Nishioka, T., Wang, R., (2003). *A Comparison of Analytical Methods: Drag Coefficient of a Cylinder* (No. MAE 171A).

BSI, (1972). *Code of Basic Data for the Design of Buildings Chapter V. Loading Part 2. Wind Loads*, CP 3: Chapter V: Part 2: 1972. British Standards Institution, London, England.

Budair, M., Ayoub, A., Karamcheti, K., (1981). *An Experimental Investigation of the Flow Past a Finite Circular Cylinder at Low Subcritical Reynolds Number* (Technical Report No. NASA-CR-168661). Stanford University; Joint Institute for Aeronautics and Acoustics, Stanford, CA, USA.

Burcharth, H.F., Frigaard, P., (1989). *Wave Load on Cylinders*, in: CEEC COMMETT. Presented at the Seminar on Wave and Ice Forces on Offshore Structures, Salford, UK, p. 45.

Cambridge Philosophical Society, (1849). *Transactions of the Cambridge Philosophical Society*. Cambridge University Press, Cambridge, MA, USA.

Cathcart, S., (2014). *Experimental and Numerical Analysis of Flow around Semi-Submerged Circular Cylinders* (Final Year Project). University of Tasmania, Australian Maritime College, Launceston, TAS, Australia.

Cebeci, T., (1970). *Laminar and Turbulent Incompressible Boundary Layers on Slender Bodies of Revolution in Axial Flow*. Journal of Basic Engineering 92, 545. https://doi.org/10.1115/1.3425060

Chaplin, J.R., Teigen, P.S., (2003). *Steady Flow Past a Vertical Surface-Piercing Circular Cylinder*. J. Fluid Struc. 18, 271–285. https://doi.org/10.1016/j.jfluidstructs.2003.07.009

Coder, D.W., (1971). *Location of Separation on a Circular Cylinder in Crossflow as a Function of Reynolds Number* (Report No. 3647). David Taylor Model Basin, Bethesda, ML, USA.

Cohen, E., (1960). *Wind Load on Towers*, in: Topics in Engineering Meteorology, Meteorological Monographs. American Meteorological Society, Boston, MA, USA, pp. 25–42. https://doi.org/10.1007/978-1-940033-39-6_6

Conway, A.S.T., (2017). *Investigation into Wakes Generated by Surface Piercing Periscopes* (Doctoral Thesis). University of Tasmania, Australian Maritime College, Launceston, TAS, Australia.

Conway, A.S.T., Binns, J.R., Ranmuthugala, D., Renilson, M., (2015). *Experimental and Numerical Analysis of Submarine Mast Surface Wakes*, in: PACIFIC 2015. Presented at the Pacific International Maritime Conference, Maritime Australia Limited, Sydney, NSW, Australia, p. 12.

Conway, A.S.T., Ranmuthugala, D., Binns, J.R., (2013). *Predicting Surface Wakes using LES and RANS-SST Analysis*. Presented at the Second Submarine Science and Technology Conference, Submarine Institute of Australia, Adelaide, SA, Victoria, p. 7.

Coyote Steel & Co., n.d. *No. 1 Handbook for Steel Sizes and Weights*.

Craig, I., (2016). *Review of Bonded Rubber Flexible Hose Design Codes and Guidelines in Relation to Sea Water Intake Risers on FPSO Vessels*. Presented at the Offshore Technology Conference Asia, Society of Petroleum Engineers, Kuala Lumpur, Malaysia. https://doi.org/10.4043/26648-MS

Crowther, A., Gargano, S., Rickard, K., (2017). *Professional Engineers Employment and Remuneration Report 2017* (Remuneration Report No. PEERP 2017). The Association of Professional Engineers Australia, Melbourne, VIC, Australia.

Dalton, C., (2016). *Fundamentals of Vortex-Induced Vibration*.

Diehl, W.S., (1986). *Engineering Aerodynamics*, 2nd ed. David W. Taylor Naval Ship Research and Development Centre, Bethesda, ML, USA.

DNV GL, (2017a). *Free Spanning Pipelines* (Recommended Practice No. DNVGL-RP-F105). Det Norkse Veritas Germanischer Lloyd.

DNV GL, (2017b). *Environmental Conditions and Environmental Loads* (Recommended Practice No. DNVGL-RP-C205). Det Norkse Veritas Germanischer Lloyd.

Drawn Metal Tube, n.d. Brass, Copper & Nickel-Silver Tubing Sizes | Drawn Metal Tube | [WWW Document]. URL https://drawnmetal.com/size-ranges/ (accessed 8.16.18).

Dryden, H.L., Heald, R.H., (1926). *Investigation of Turbulence in Wind Tunnels by a Study of the Flow About Cylinders* (Technical Report No. NACA-TR-231). National Bureau of Standards, Washington D.C., VA, USA.

Dryden, H.L., Hill, G.C., (1930). *Wind Pressure on Circular Cylinders and Chimneys*. Journal of Research of the National Bureau of Standards 5, 653.

Ducrocq, T., Cassan, L., Chorda, J., Roux, H., (2017). *Flow and Drag Force around a Free Surface Piercing Cylinder for Environmental Applications*. Environ Fluid Mech 17, 629–645. https://doi.org/10.1007/s10652-016-9505-9

Eames, I., Jonsson, C., Johnson, P.B., (2011). *The Growth of a Cylinder Wake in Turbulent Flow*. Journal of Turbulence 12, N39. https://doi.org/10.1080/14685248.2011.619985

Eiffel, G., (1910). *La Résistance de l'Air et l'Aviation: Expériences Effectuées au Laboratoire du Champ-de-Mars*. ETH-Bibliotek Zürich, Paris, France.

Eisner, F., (1929). *Widerstandsmessungen an umströmten Zylindern von Kreis- und Brückenpfeilerquerschnitt*. Springer, Vienna. https://doi.org/10.1007/978-3-7091-5394-9

Etzold, F., Fiedler, H., (1976). *The Near-Wake Structure of a Cantilevered Cylinder in a Cross-Flow*. Z. Flugwiss. 24, 77–82.

Farell, C., (1981). *Flow around Fixed Circular Cylinders: Fluctuating Loads*. Journal of the Engineering Mechanics Division 107, 565–588.

Fariver, D.J., (1981). *Turbulent Uniform Flow around Cylinders of Finite Length*. AIAA J. 19, 275–281. https://doi.org/10.2514/3.7771

Fenton, J., (2008). *Obstacles in Streams and their Roles as Hydraulic Structures*. Presented at the 2nd International Junior Researcher and Engineer Workshop on Hydraulic Structures, Pisa, Italy, pp. 15–22.

Finn, R.K., (1953). *Determination of the Drag on a Cylinder at Low Reynolds Numbers*. Journal of Applied Physics 24, 771–773. https://doi.org/10.1063/1.1721373

Flachsbart, O., (1930). *Winddruck auf Bauwerke*. Die Naturwissenschaften 18, 475–479. https://doi.org/10.1007/BF01492667

Fox, T.A., Apelt, C.J., (1993). *Fluid-Induced Loading of Cantilevered Circular Cylinders in a Low-Turbulence Uniform Flow. Part 3: Fluctuating Loads with Aspect Ratios 4 to 25*. J. Fluid Struc. 7, 375–386. https://doi.org/10.1006/jfls.1993.1022

Fox, T.A., Apelt, C.J., West, G.S., (1993). *The Aerodynamic Disturbance Caused by the Free-Ends of a Circular Cylinder Immersed in a Uniform Flow*. J. Wind Eng. Ind. Aerodyn. 49, 389–399. https://doi.org/10.1016/0167-6105(93)90033-K

Fox, T.A., West, G.S., (1993a). *Fluid-Induced Loading of Cantilevered Circular Cylinders in a Low-Turbulence Uniform Flow. Part 1: Mean Loading with Aspect Ratios in the Range 4 to 30*. J. Fluid Struc. 7, 1–14. https://doi.org/10.1006/jfls.1993.1001

Fox, T.A., West, G.S., (1993b). *Fluid-Induced Loading of Cantilevered Circular Cylinders in a Low-Turbulence Uniform Flow. Part 2: Fluctuating Loads on a Cantilever of Aspect Ratio 30*. J. Fluid Struc. 7, 15–28. https://doi.org/10.1006/jfls.1993.1002

Fox, T.A., West, G.S., (1991a). *Experiments on Smooth Cantilevered Circular Cylinders in Low-Turbulence Uniform Flow. Part 1: Mean Loading with Aspect Ratios in the Range of 4 to 30* (Research Report No. CE130). University of Queensland, Brisbane, QLD, AUS.

Fox, T.A., West, G.S., (1991b). *Experiments on Smooth Cantilevered Circular Cylinders in Low-Turbulence Uniform Flow. Part 2: Fluctuating Loads on a Cantilever of Aspect Ratio 30* (Research Report No. CE131). University of Queensland, Brisbane, QLD, AUS.

Fox, T.A., West, G.S., (1990). *On the use of End Plates with Circular Cylinders*. Exp. Fluids 9, 237–239. https://doi.org/10.1007/BF00190426

Fujarra, A.L.C., Pesce, C.P., Flemming, F., Williamson, C.H.K., (2001). *Vortex-Induced Vibration of a Flexible Cantilever*. J. Fluids & Struc. 15, 651–658. https://doi.org/10.1006/jfls.2000.0368

Genstil, S.M., (1969). *The Oscillatory Forces on a Semi-Submerged Circular Cylinder in Water and in Dilute Aqueous Solution of Poly (Ethylene Oxide).* (Masters Thesis). Naval Postgraduate School, Monterey, CA, USA.

Gerrard, J.H., (1978). *The Wakes of Cylindrical Bluff Bodies at Low Reynolds Number*. Phil. Trans. Roy. Soc. Lond., Mathematical, Physical and Engineering Sciences 288, 351–382. https://doi.org/10.1098/rsta.1978.0020

Gerrard, J.H., (1966). *The Mechanics of the Formation Region of Vortices Behind Bluff Bodies*. J. Fluid Mech. 25, 401–413. https://doi.org/10.1017/S0022112066001721

Glauert, H., (1934). *Heavy Flexible Cable for Towing a Heavy Body Below an Aeroplane* (Reports and Memoranda No. R & M 1592). Aeronautical Research Committee (ARC).

Glauert, H., (1930). *The Stability of a Body Towed by a Light Wire* (Reports and Memoranda No. R & M 1312). Aeronautical Research Committee (ARC).

Gonçalves, R.T., Franzini, G.R., Rosetti, G.F., Meneghini, J.R., Fujarra, A.L.C., (2015). *Flow Around Circular Cylinders with Very Low Aspect Ratio*. J. Fluids & Struc. 54, 122–141. https://doi.org/10.1016/j.jfluidstructs.2014.11.003

Gonçalves, R.T., Rosetti, G.F., Franzini, G.R., Meneghini, J.R., Fujarra, A.L.C., (2013). *Two-Degree-of-Freedom Vortex-Induced Vibration of Circular Cylinders with very Low Aspect Ratio and Small Mass Ratio*. J. Fluids & Struc. 39, 237–257. https://doi.org/10.1016/j.jfluidstructs.2013.02.004

Gorman, D.J., (1974). *Free Lateral Vibration Analysis of Double-Span Uniform Beams*. Int. J. Mech. Sci. 16, 345–351. https://doi.org/10.1016/0020-7403(74)90008-3

Gould, R.W.F., Raymer, W.G., Ponsford, P.J., (1968). *Wind Tunnel Tests on Chimneys of Circular Section at High Reynolds Numbers*. Presented at the Symposium on Wind Effect on Buildings and Structures, Loughborough, UK, pp. 10.1-10.17.

Gowda, B.H.L., (1974). *Some Measurements on the Phenomenon of Vortex Shedding and Induced Vibrations of Circular Cylinders* (Report No. RN 437 (75-01)). Berlin Technical University, Berlin, Germany.

Gowen, F.E., Perkins, E.W., (1953). *Drag of Circular Cylinders for a Wide Range of Reynolds Numbers and Mach Numbers* (Technical Note No. NACA-TN-2960). NACA, Moffet Field, CA, USA.

Griffin, O.M., (1985). *Vortex Shedding from Bluff Bodies in a Shear Flow: A Review*. J. Fluids Eng. 107, 298. https://doi.org/10.1115/1.3242481

Griffin, O.M., Ramberg, S.E., (1982). *Some Recent Studies of Vortex Shedding with Application to Marine Tubulars and Risers*. J. Energy Resourc. Technol. 104, 2–13. https://doi.org/10.1115/1.3230377

Haritos, N., (1992). *Morison Force Coefficient for Vertical Bottom-Mounted Cylinders*. Presented at the Second International Offshore and Polar Engineering Conference, International Society of Offshore and Polar Engineers (ISOPE), San Francisco, CA, USA, p. 8.

Hay, A.D., (1947). *Flow about Semi-Submerged Cylinders of Finite Length* (Technical Report No. NObs-34006). Princeton University, Princeton, NJ, USA.

Hay, A.D., (1945). *Job Order No.1 under Princeton contract DTMB-1(2026)46; N0bs-34006; HAS: LMS*.

Hay, A.D., (1941). *Various Communications*.

Heidari, M., Balachandar, R., Roussinova, V., Barron, R.M., (2017). *Characteristics of Flow Past a Slender, Emergent Cylinder in Shallow Open Channels*. Phys. Fluids 29, 15. https://doi.org/10.1063

Heseltine, J.L., (2003). *Flow Around a Cylinder with a Free End* (Masters Thesis). University of Saskatchewan, Saskatoon, SK, Canada.

Hoerner, S.F., (1965). *Fluid-Dynamic Drag: Practical Information on Aerodynamic Drag and Hydrodynamic Resistance*, 2nd ed. Dr. Sighard F. Hoerner.

Hoerner, S.F., Borst, H.V., (1985). *Fluid-Dynamic Lift: Practical Information on Aerodynamic Lift and Hydrodynamic Resistance*, 2nd ed. Mrs. Liselotte A. Hoerner.

Hogben, N., (1974). *Wave Resistance of Surface Piercing Vertical Cylinders in Uniform Currents*. National Physical Laboratory.

Hsieh, T., (1964). *Resistance of Cylindrical Piers in Open-Channel Flow*. J. Hydraulics Div. 90, 161–173.

Huang, S., (2011). *VIV Suppression of a Two-Degree-of-Freedom Circular Cylinder and Drag Reduction of a Fixed Circular Cylinder by the use of Helical Grooves*. J. Fluid Struc. 27, 1124–1133. https://doi.org/10.1016/j.jfluidstructs.2011.07.005

Huang, S., (2010). *Cylinder Drag Reduction by the use of Helical Grooves*, in: HYDRALAB III. Presented at the Proceedings of the HYDRALAB III Joint User Meeting, Hannover.

Huang, S., (2006). *Preliminary Tank Testing of VIV Suppression of Helical Grooves*, in: OMAE2006. Presented at the 25th OMAE Conference, American Society of Mechanical Engineers (ASME), Hamburg, Germany, pp. 469–473. https://doi.org/10.1115/OMAE2006-92002

Inoue, M., Baba, N., Himeno, Y., (1993). *Experimental and Numerical Study of Viscous Flow Field around an Advancing Vertical Circular Cylinder Piercing a Free-Surface*. J. Kansai Soc. Naval Arch. 220, 57–64.

Institution of Naval Architects, (1955). *The Papers of William Froude*. Institution of Naval Architects, London.

ITTC, (2017). *Resistance Test* (Recommended Procedures and Guidelines No. 7.5-02-02–01). International Towing Tank Conference.

Jiang, L., Shao, W., Zhu, D.Z., Sun, Z., (2014). *Forces on Surface-Piercing Vertical Circular Cylinder Groups on Flooding Staircase*. J. Fluid Struc. 46, 17–28. https://doi.org/10.1016/j.jfluidstructs.2013.12.011

Jones Jr, G.W., Cincotta, J.J., Walker, R.W., (1969). *Aerodynamic Forces on a Stationary and Oscillating Circular Cylinder at High Reynolds Numbers* (Technical Report No. NASA-TR-R-300). NASA, Hampton, VA, USA.

Kawamura, T., Hiwada, M., Hibino, T., Mabuchi, I., Kumada, M., (1984). *Flow around a Finite Circular Cylinder on a Flat Plate: Cylinder Height Greater than Turbulent Boundary Layer Thickness*. Bulletin of JSME 27, 2142–2151. https://doi.org/10.1299/jsme1958.27.2142

Kawamura, T., Mayer, S., Garapon, A., Sørensen, L., (2002). *Large Eddy Simulation of a Flow Past a Free Surface Piercing Circular Cylinder*. J. Fluids Eng. 124, 91–101. https://doi.org/10.1115/1.1431545

Keough, S.J., Kermonde, I.L., Amiet, A., Philip, J., Ooi, A., Monty, J.P., Anderson, B., (2016). *Time Resolved Measurements of Wake Characteristics from Vertical Surface-Piercing Circular Cylinders*, in: 20 AFMC. Presented at the 20th Australasian Fluid Mechanics Conference, Perth, WA, Australia, p. 4.

Keulegan, G.H., Carpenter, L.H., (1958). *Forces on Cylinder and Plates in an Oscillating Fluid*. J. Res. Natl. Bur. Stand. 60, 423–440.

Khalak, A., (1996). *Experimental Investigation of Vortex-Induced Vibration of a Circular Cylinder* (Masters Thesis). Cornell University, Ithaca, NY, USA.

Kilner, A.A., Kurts, P., Potts, D., Johnstone, D., Potts, A.E., Marcollo, H., (2018). *The Efficacy of Inverted Helical Strakes*. Presented at the 23rd Offshore Symposium, The Society of Naval Architects and Marine Engineers (SNAME), Houston, TX, USA, p. 17.

King, R., (1974). *Vortex Excited Structural Oscillations of a Circular Cylinder in Steady Currents*, in: Offshore Technology Conference. Presented at the Sixth Annual Offshore Technology Conference, Houston, TX, USA, p. 12. https://doi.org/10.4043/1948-MS

King, R., Prosser, M.J., Johns, D.J., (1973). *On Vortex Excitation of Model Piles in Water*. Journal of Sound and Vibration 29, 169–188. https://doi.org/10.1016/S0022-460X(73)80133-6

Kitagawa, T., Fujino, Y., Kimura, K., (1999). *Effects of Free-End Condition on End-Cell-Induced Vibration*. J. Fluids & Struc. 13, 499–518. https://doi.org/10.1006/jfls.1999.0214

Kitagawa, T., Fujino, Y., Kimura, K., Mizuno, Y., (2002). *Wind Pressures Measurement on End-Cell-Induced Vibration of a Cantilevered Circular Cylinder*. J. Wind Eng. Ind. Aerodyn. 90, 395–405. https://doi.org/10.1016/S0167-6105(01)00200-8

Kitagawa, T., Fujino, Y., Kimura, K., Mizuno, Y., (2001). *Wind Pressures on End-Cell-Induced Vibration of Circular Tower*. J. Eng. Mech. 127, 1135–1143. https://doi.org/10.1061/(ASCE)0733-9399(2001)127:11(1135)

Kitagawa, T., Wakahara, T., Fujino, Y., Kimura, K., (1997). *An Experimental Study on Vortex-Induced Vibration of a Circular Cylinder Tower at a High Wind Speed*. J. Wind Eng. Ind. Aerodyn. 69–71, 731–744. https://doi.org/10.1016/S0167-6105(97)00201-8

Koo, B., Yang, J., Yeon, S.M., Stern, F., (2014). *Reynolds and Froude Number Effect on the Flow Past an Interface-Piercing Circular Cylinder*. Int. J. Nav. Archit. Ocean Eng. 6, 529–561. https://doi.org/10.2478/IJNAOE-2013-0197

Korotkin, A.I., (1976). *The Three Dimensionality of the Flow Transverse to a Circular Cylinder*. Fluid Mech. Sov. Res. 5, 96–103.

Koterayama, W., Nakamura, M., (1992a). *Drag and Inertia Force Coefficients Derived from Fields Tests*. Presented at the Second International Offshore and Polar Engineering Conference, International Society of Offshore and Polar Engineers (ISOPE), San Francisco, CA, USA, p. 8.

Koterayama, W., Nakamura, M., (1992b). *Drag and Inertia Force Coefficients Derived from Fields Tests*. ISOPE 2, 7.

Lamb, H., (1911). *XV. On the Uniform Motion of a Sphere Through a Viscous Fluid*. Philosophical Magazine 21, 112–121. https://doi.org/10.1080/14786440108637012

Lamb, H., (1895). *Hydrodynamics*. Cambridge University Press, Cambridge University.

Lienhard, J.H., (1966). *Synopsis of Lift, Drag, and Vortex Frequency Data for Rigid Circular Cylinders* (Bulletin No. 300). Technical Extension Service, Washington State University, Pullman, WA, USA.

Lin, C., (1980). *Fluid Forces on Smooth and Rough Circular Cylinders* (Doctoral Thesis). Oregon State University, Corvallis, OR, USA.

Lindsey, W.F., (1938). *Drag of Cylinders of Simple Shapes* (Technical Report No. NACA-TR-619). NACA, Langley Field, VA, USA.

Luxton, R.E., Bull, M.K., Rajagopalan, S., (1984). *The Thick Turbulent Boundary Layer on a Long Fine Cylinder in Axial Flow*. The Aeronautical Journal 88, 186–199. https://doi.org/10.1017/S0001924000020480

Maull, D.J., Young, R.A., (1973). *Vortex Shedding from Bluff Bodies in a Shear Flow*. J. Fluid Mech. 60, 401. https://doi.org/10.1017/S0022112073000236

Mayes, C., Schlichting, H., Krause, E., Oertel, H.J., Gersten, K., (2003). *Boundary-Layer Theory*, Physic and Astronomy. Springer Berlin Heidelberg.

Meijer, M.C., (1964). *An Experiment Concerning Partly Closed Cavities Behind a Surface-Piercing Rod* (Report No. E-110.1). California Institute of Technology, Pasadena, CA, USA.

Metcalf, B., Longo, J., Ghosh, S., Stern, F., (2006). *Unsteady Free-Surface Wave-Induced Boundary-Layer Separation for a Surface-Piercing NACA 0024 Foil: Towing Tank Experiments*. Journal of Fluids and Structures 22, 77–98. https://doi.org/10.1016/j.jfluidstructs.2005.09.004

Nasif, G., Balachandar, R., Barron, R.M., (2015). *Characteristics of Flow Structures in the Wake of a Bed-Mounted Bluff Body in Shallow Open Channels*. J. Fluids Eng. 137, 101207. https://doi.org/10.1115/1.4030537

Nayyar, M.L. (Ed.), (2000). *Piping Handbook*, 7th ed, McGraw-Hill Handbooks. McGraw-Hill, New York.

Nestegård, A., (2018). *DNV-RP-C205 - External Customer Query*.

Norberg, C., (1994). *An Experimental Investigation of the Flow around a Circular Cylinder: Influence of Aspect Ratio*. J. Fluid Mech. 258, 287–316. https://doi.org/10.1017/S0022112094003332

Okajima, A., Kosugi, T., Nakamura, A., (2002). *Flow-Induced In-Line Oscillation of a Circular Cylinder in a Water Tunnel*. J. Pressure Vessel Technol. 124, 89. https://doi.org/10.1115/1.1430670

Okamoto, S., (1988). *Flow Past Circular Cylinder of Finite Length Placed on Ground Plane*. J. Jap. Soc. Aeronaut. 36, 343–350. https://doi.org/10.2322/jjsass1969.36.343

Okamoto, T., Yagita, M., (1973). *The Experimental Investigation on the Flow Past a Circular Cylinder of Finite Length Placed Normal to the Plane Surface in a Uniform Stream*. Bulletin of JSME 16, 805–814. https://doi.org/10.1299/jsme1958.16.805

Park, C.W., Lee, S.J., (2004). *Effects of Free-End Corner Shape on Flow Structure around a Finite Cylinder*. J. Fluids & Struc. 19, 141–158. https://doi.org/10.1016/j.jfluidstructs.2003.12.001

Park, C.W., Lee, S.J., (2002). *Flow Structure around a Finite Circular Cylinder Embedded in Various Atmospheric Boundary Layers*. Fluid Dyn. Res. 197–215. https://doi-org.ezproxy.lib.monash.edu.au/10.1016/S0169-5983(02)00037-0

Park, C.-W., Lee, S.-J., (2000). *Free End Effects on the Near Wake Flow Structure behind a Finite Circular Cylinder*. J. Wind Eng. Ind. Aerodyn. 88, 231–246. https://doi.org/10.1016/S0167-6105(00)00051-9

Patel, V.C., Landweber, L., Tang, C.J., (1984). *Free-Surface Boundary Layer and the Origin of Bow Vortices:* (Technical Report No. IIHR 284). Iowa Institute of Hydraulic Research, Iowa City, IA, USA. https://doi.org/10.21236/ADA147427

Pechstein, W., (1942). *Wirkung des Natürlichen Windes auf einen Größeren Kreiszylinder*. VDI Zeitschrift 86, 220–222.

Perry, B., (1954). *Experiments on Struts Piercing the Water Surface* (Report No. E-55.1). California Institute of Technology, Pasadena, CA, USA.

Pesce, C.P., Fujarra, A.L.C., (2000). *Vortex-Induced Vibrations and Jump Phenomenon: Experiments with a Clamped Flexible Cylinder in Water*. ISOPE 10, 26–33.

Polhamus, E.C., (1958). *Effect of Flow Incidence and Reynolds Number on Low-Speed Aerodynamic Characteristics of Several Noncircular Cylinders with Applications to Directional Stability and Spinning* (Technical Note No. NACA-TN-4176). NACA, Langley Field, VA, USA.

Porteous, R., Moreau, D.J., Doolan, C.J., Prime, Z., (2014). *Wake Dynamics of Circular Finite Wall-Mounted Cylinders in Different Boundary Layers*, in: 19 AFMC. Presented at the 19th Australasian Fluid Mechanics Conference, Australasian Fluid Mechanics Society, Melbourne, VIC, Australia, p. 4.

Potts, A.E., Potts, D.A., Marcollo, H., Jayasinghe, K., (2018). *Strouhal Number for VIV Excitation of Long Slender Structures*, in: OMAE2018. Presented at the 37th OMAE Conference, American Society of Mechanical Engineers (ASME), Madrid, Spain, p. 18. https://doi.org/10.1115/OMAE2018-77433

Potts, D.A., (2018). *An Investigation of Structural Damping of Helically Laid Cables* (Honours Thesis). Victoria University, Melbourne, VIC, Australia.

Potts, D.A., Binns, J.R., Marcollo, H., Potts, A.E., (2019a). *Hydrodynamics of Towed Vertical Surface-Piercing Cylinders*, in: OMAE2019. Presented at the 38th OMAE Conference, American Society of Mechanical Engineers (ASME), Glasgow, Scotland, p. 15.

Potts, D.A., Binns, J.R., Potts, A.E., Marcollo, H., (2019b). *The Effect of Aspect Ratio on the Drag of Bare Cylinders*, in: OMAE2019. Presented at the 38th OMAE Conference, American Society of Mechanical Engineers (ASME), Glasgow, Scotland, p. 18.

Prandtl, L., Wieselsberger, C., Betz, A. (Eds.), (2009). *Ergebnisse der Aerodynamischen Versuchsanstalt zu Göttingen - II. Lieferung*, Göttinger Klassiker der Strömungmechanik. Göttingen University Press, Göttingen. https://doi.org/10.17875/gup2009-101

Raheja, L., (2001). *On Submerged Stagnation Points and Bow Vortices Generation*, in: Symposium on Naval Hydrodynamics. Presented at the Twenty-Third Symposium on Naval Hydrodynamics, National Academies Press, Val de Reuil, France, pp. 540–552.

Relf, E.F., (1914). *Discussion of the Results of Measurements of the Resistance of Wires, with Some Additional Tests on the Resistance of Wires of Small Diameter* (Reports and Memoranda No. R & M 102). Aeronautical Research Committee (ARC).

Relf, E.F., Simmons, L.F.G., (1925). *LIII. On the Frequency of the Eddies Generated by the Motion of Circular Cylinders through a Fluid*. Philosophical Magazine, 1901-1925 49, 509–511. https://doi.org/10.1080/14786442508634628

Reynolds, O., (1883). *XXIX: An Experimental Investigation of the Circumstances Which Determine Whether the Motion of Water Shall Be Direct or Sinuous, and of the Law of Resistance in Parallel Channels*. Philosophical Transactions of the Royal Society of London 174, 935–982. https://doi.org/10.1098/rstl.1883.0029

Roh, S., Park, S., (2003). *Vortical Flow over the Free End Surface of a Finite Circular Cylinder Mounted on a Flat Plate*. Exp. Fluids 34, 63–67. https://doi.org/10.1007/s00348-002-0532-6

Roshko, A., (1961). *Experiments on the Flow Past a Circular Cylinder at Very High Reynolds Number*. J. Fluid Mech. 10, 345–356. https://doi.org/10.1017/S0022112061000950

Roshko, A., (1955). *On the Wake and Drag of Bluff Bodies*. Journal of the Aeronautical Sciences 22, 124–132. https://doi.org/10.2514/8.3286

Rostamy, N., Sumner, D., Bergstrom, D.J., Bugg, J.D., (2012). *Local Flow Field of a Surface-Mounted Finite Circular Cylinder*. J. Fluids & Struc. 34, 105–122. https://doi.org/10.1016/j.jfluidstructs.2012.04.014

Sakamoto, H., Arie, M., (1983). *Vortex Shedding from a Rectangular Prism and a Circular Cylinder placed Vertically in a Turbulent Boundary Layer*. J. Fluid Mech. 126, 147–165. https://doi.org/10.1017/S0022112083000087

Sakamoto, H., Oiwake, S., (1984). *Fluctuating Forces on a Rectangular Prism and a Circular Cylinder Placed Vertically in a Turbulent Boundary Layer*. J. Fluids Eng. 106, 160. https://doi.org/10.1115/1.3243093

Sarpkaya, T., (2004). *A Critical Review of the Intrinsic Nature of Vortex-Induced Vibrations*. J. Fluid Struc. 19, 389–447. https://doi.org/10.1016/j.jfluidstructs.2004.02.005

Schiller, L., Linke, W., (1933). *Pressure and Frictional Resistance of a Cylinder at Reynolds Numbers 5,000 to 40,000* (Technical Memorandum No. NACA-TM-715). NACA, Washington D.C., VA, USA.

Schmidt, L.V., (1965). *Measurements of Fluctuating Air Loads on a Circular Cylinder*. J. Aircraft 2, 49–55. https://doi.org/10.2514/3.43618

Shangshang Desheng Group, n.d. Definition and Advantages of Thin-Wall Stainless Steel Tube [WWW Document]. URL http://sssshangshang.com/Industry/Advantages-of-Thin-wall-Stainless-Steel-Tube.shtml (accessed 8.6.18).

Slaouti, A., Gerrard, J.H., (1981). *An Experimental Investigation of the End Effects on the Wake of a Circular Cylinder Towed through Water at Low Reynolds Numbers*. Journal of Fluid Mechanics 112, 297. https://doi.org/10.1017/S0022112081000414

Spray System Co., n.d. Roughness of Pipes [WWW Document]. SF Pressure Drop Online-Calculator. URL https://www.spray.com/calculators/Pressure_Drop_Calc/rauh.html (accessed 4.10.19).

Stack, J., (1941). *Compressibility Effects in Aeronautical Engineering* (Technical Report No. NACA-ACR-207, NACA-SR-207). NACA, Langley Field, VA, USA.

Standards Australia, Standards New Zealand, (2016). *Cold-Formed Structural Steel Hollow Sections*, (AS/NZS 1163-2016+A1). SAI Global.

Stansby, P.K., (1974). *The Effects of End Plates on the Base Pressure Coefficient of a Circular Cylinder*. The Aeronautical Journal 78, 36–37. https://doi.org/10.1017/S0001924000036319

Stappenbelt, B., Lalji, F., Tan, G., (2007). *Low Mass Ratio Vortex-Induced Motion*, in: 16 AFMC. Presented at the 16th Australasian Conference on Hydraulics and Fluid Mechanics, Australasian Fluid Mechanics Society, Gold Coast, QLD, Australia, pp. 1491–1947.

Suh, J., Yang, J., Stern, F., (2011). *The Effect of Air–Water Interface on the Vortex Shedding from a Vertical Circular Cylinder*. J. Fluids & Struc. 27, 1–22. https://doi.org/10.1016/j.jfluidstructs.2010.09.001

Sumer, B.M., Fredsoe, J., (2006). *Hydrodynamics Around Cylindrical Structures*, 2nd ed, Advanced Series on Ocean Engineering. World Scientific, Denmark.

Sumner, D., (2013). *Flow Above the Free End of a Surface-Mounted Finite-Height Circular Cylinder: A Review*. J. Fluids & Struc. 43, 41–63. https://doi.org/10.1016/j.jfluidstructs.2013.08.007

Sumner, D., (2010). *Two Circular Cylinders in Cross-Flow: A Review*. J. Fluids & Struc. 26, 849–899. https://doi.org/10.1016/j.jfluidstructs.2010.07.001

Sumner, D., (1999). *Circular Cylinders in Cross-Flow* (Doctoral Thesis). McGill University, Montreal, QC, Canada.

Sumner, D., Heseltine, J.L., Dansereau, O.J.P., (2004). *Wake Structure of a Finite Circular Cylinder of Small Aspect Ratio*. Experiments in Fluids 37, 720–730. https://doi.org/10.1007/s00348-004-0862-7

Sykes, D.M., (1962). *The Supersonic and Low-Speed Flows Past Circular Cylinders of Finite Length Supported at One End*. J. Fluid Mech. 12, 367. https://doi.org/10.1017/S0022112062000270

Szepessy, S., Bearman, P.W., (1992). *Aspect Ratio and End Plate Effects on Vortex Shedding from a Circular Cylinder*. J. Fluid Mech. 234, 191–217. https://doi.org/10.1017/S0022112092000752

Tanaka, S., Murata, S., (1999). *An Investigation of the Wake Structure and Aerodynamic Characteristics of a Finite Circular Cylinder. Time-Averaged Wake Structures behind Circular Cylinders with Various Aspect Ratios.* JSME International Journal Series B 42, 178–187. https://doi.org/10.1299/jsmeb.42.178

Tanida, Y., Okajima, A., Watanabe, Y., (1973). *Stability of a Circular Cylinder Oscillating in Uniform Flow or in a Wake*. J. Fluid Mech. 61, 769–784. https://doi.org/10.1017/S0022112073000935

Taniguchi, S., Sakamoto, H., Arie, M., (1981). *Flow around Circular Cylinders of Finite Height Placed Vertically in Turbulent Boundary Layers*. Bulletin of JSME 24, 37–44. https://doi.org/10.1299/jsme1958.24.37

The Editors of Encyclopaedia Britannica, (2018). William Froude | British engineer [WWW Document]. Encyclopedia Britannica. URL https://www.britannica.com/biography/William-Froude (accessed 6.8.18).

Thomsen, P., (1963). *Cavity Shape and Drag in Ventilated Flow; Theory and Experiment* (Scientific Report No. TRG-156-SR-2). Technical Research Group, Syosset, NY, USA. https://doi.org/10.21236/AD0401925

Thomson, S.W., (1880). *XVI: On Gravitational Oscillations of Rotating Water*. The London, Edinburgh, and Dublin Philosophical Magazine and Journal of Science 10, 109–116. https://doi.org/10.1080/14786448008626897

Toebes, G.H., (1969). *The Unsteady Flow and Wake Near an Oscillating Cylinder*. J. Basic Eng. 91, 493–502. https://doi.org/10.1115/1.3571165

Tørum Alf, (1989). *Wave Forces on Pile in Surface Zone*. J. Waterw. Port. Coast. Ocean Eng. 115, 547–565. https://doi.org/10.1061/(ASCE)0733-950X(1989)115:4(547)

Tritton, D.J., (1959). *Experiments on the Flow Past a Circular Cylinder at Low Reynolds Numbers*. J. Fluid Mech. 6, 547. https://doi.org/10.1017/S0022112059000829

Uematsu, Y., Yamada, M., Ishii, K., (1990). *Some Effects of Free-Stream Turbulence on the Flow Past a Cantilevered Circular Cylinder*. J. Wind Eng. Ind. Aerodyn. 33, 43–52. https://doi.org/10.1016/0167-6105(90)90019-9

Vandiver, J.K., (2012). *Damping Parameters for Flow-Induced Vibration*. J. Fluid Struc. 35, 105–119. https://doi.org/10.1016/j.jfluidstructs.2012.07.002

Vandiver, J.K., (1983). *Drag Coefficients of Long Flexible Cylinders*, in: Offshore Technology Conference. Presented at the 15th Annual Offshore Technology Conference, Society of Petroleum Engineers, Houston, TX, USA. https://doi.org/10.4043/4490-MS

Weller, R., (1947). *The Optical Investigation of Fluid Flow*. J. App. Mech. 14, A103–A107.

Welsh, C.J., (1953). *The Drag of Finite-Length Cylinders Determined from Flight Tests at High Reynolds Numbers for a Mach Number Range from 0.5 to 1.3* (Technical Note No. NACA-TN-2941). NACA, Langley Field, VA, USA.

White, C.M., (1946). *The Drag of Cylinders in Fluids at Slow Speeds*. Proceedings of the Royal Society A: Mathematical, Physical and Engineering Sciences 186, 472–479. https://doi.org/10.1098/rspa.1946.0059

Wieselsberger, C., (1922). *New Data on the Laws of Fluid Resistance* (Technical Note No. NACA-TN-84).

Wieselsberger, C., (1921). *Neure Festellungen uber die Gesetze des Flussigkeits- und Luftwiderstands*. Phys. Z. 321–328.

Williamson, C.H.K., Govardhan, R., (2004). *Vortex-Induced Vibrations*. Annu. Rev. Fluid Mech. 36, 413–455. https://doi.org/10.1146/annurev.fluid.36.050802.122128

Woodward-Clyde Consultants, (1980). *Assessment of the Morison Equation* (Final Report No. CR-80.022). Woodward-Clyde Consultants, Houston, TX, USA.

Yean, S.M., (2014). *Large-Eddy Simulation of Sub-, Critical and Super-Critical Reynolds Number Flow Past a Circular Cylinder* (Doctoral Thesis). The University of Iowa, Iowa City, IA, USA.

Yu, G., Avital, E.J., Williams, J.J.R., (2008). *Large Eddy Simulation of Flow Past Free Surface Piercing Circular Cylinders*. J. Fluids Eng. 130, 9. https://doi.org/10.1115/1.2969462

Zahm, A.F., (1927). *Flow and Drag Formulas for Simple Quadrics* (Report No. NACA-TR-253). NACA, Washington DC, VA, USA.

Zahm, A.F., Smith, R.H., Louden, F.A., (1929). *Forces on Elliptic Cylinders in Uniform Air Stream* (Technical Report No. NACA-TR-289). Bureau of Construction and Repair (Navy), Washington D.C., VA, USA.

Zdravkovich, M.M., (1997). *Flow Around Circular Cylinders: Volume I: Fundamentals*, Flow Around Circular Cylinders: A Comprehensive Guide Through Flow Phenomena, Experiments, Applications, Mathematical Models, and Computer Simulations. Oxford University Press Inc., New York, NY, USA.

Zdravkovich, M.M., (1981). *Review and Classification of Various Aerodynamic and Hydrodynamic Means for Suppressing Vortex Shedding*. J. Wind Eng. Ind. Aerodyn. 7, 145–189. https://doi.org/10.1016/0167-6105(81)90036-2

Appendix A Anticipated Dynamic Frequencies

Table A-1: 101.6 mm First Natural Frequencies

	L/D = 1		L/D = 2		L/D = 4		L/D = 8		L/D = 10	
Velocity (m/s)	**f_n**	**Vr**	**f_n**	**Vr**	**f_n**	**Vr**	**f_n**	**Vr**	**f_n**	**Vr**
0.25	51.9	0.0	39.5	0.1	24.8	0.1	12.1	0.2	9	0.3
0.50		0.1		0.1		0.2		0.4		0.5
0.75		0.1		0.2		0.3		0.6		0.8
1.00		0.2		0.2		0.4		0.8		1.1
1.25		0.2		0.3		0.5		1.0		1.4
1.50		0.3		0.4		0.6		1.2		1.6
1.75		0.3		0.4		0.7		1.4		1.9
2.00		0.4		0.5		0.8		1.6		2.2
2.25		0.4		0.6		0.9		1.8		2.5
2.50		0.5		0.6		1.0		2.0		2.7
2.75		0.5		0.7		1.1		2.2		3.0
3.00		0.6		0.7		1.2		2.4		3.3
3.25		0.6		0.8		1.3		2.6		3.5
3.50		0.7		0.9		1.4		2.8		3.8
3.75		0.7		0.9		1.5		3.1		4.1
4.00		0.8		1.0		1.6		3.3		4.4

Table A-2: 101.6 mm Second Natural Frequencies

	L/D = 1		L/D = 2		L/D = 4		L/D = 8		L/D = 10	
Velocity (m/s)	**f_n**	**Vr**	**f_n**	**Vr**	**f_n**	**Vr**	**f_n**	**Vr**	**f_n**	**Vr**
0.25		0.0		0.0		0.0		0.0		0.0
0.50		0.0		0.0		0.0		0.0		0.0
0.75		0.0		0.0		0.0		0.0		0.1
1.00		0.0		0.0		0.0		0.1		0.1
1.25		0.0		0.0		0.0		0.1		0.1
1.50		0.0		0.0		0.1		0.1		0.1
1.75		0.0		0.1		0.1		0.1		0.2
2.00	385	0.1	339	0.1	261	0.1	148	0.1	112	0.2
2.25		0.1		0.1		0.1		0.1		0.2
2.50		0.1		0.1		0.1		0.2		0.2
2.75		0.1		0.1		0.1		0.2		0.2
3.00		0.1		0.1		0.1		0.2		0.3
3.25		0.1		0.1		0.1		0.2		0.3
3.50		0.1		0.1		0.1		0.2		0.3
3.75		0.1		0.1		0.1		0.2		0.3
4.00		0.1		0.1		0.2		0.3		0.4

Table A-3: 48.3 mm First Natural Frequencies

	L/D = 1		L/D = 2		L/D = 4		L/D = 8		L/D = 10		L/D = 16		L/D = 20	
Velocity (m/s)	**f_n**	**Vr**	**f_n**	**Vr**	**f_n**	**Vr**	**f_n**	**Vr**	**f_n**	**Vr**	**f_n**	**Vr**	**f_n**	**Vr**
0.25		0.2		0.2		0.3		0.4		0.5		0.8		1.0
0.50		0.4		0.4		0.5		0.8		1.0		1.6		2.1
0.75		0.5		0.6		0.8		1.2		1.5		2.4		3.1
1.00		0.7		0.8		1.1		1.6		1.9		3.2		4.2
1.25		0.9		1.0		1.3		2.0		2.4		4.0		5.2
1.50		1.1		1.2		1.6		2.4		2.9		4.7		6.3
1.75		1.3		1.4		1.8		2.8		3.4		5.5		7.3
2.00	28.6	1.4	25	1.7	19.6	2.1	12.8	3.2	10.6	3.9	6.5	6.3	4.9	8.4
2.25		1.6		1.9		2.4		3.6		4.4		7.1		9.4
2.50		1.8		2.1		2.6		4.0		4.9		7.9		10.5
2.75		2.0		2.3		2.9		4.4		5.3		8.7		11.5
3.00		2.2		2.5		3.2		4.8		5.8		9.5		12.5
3.25		2.4		2.7		3.4		5.2		6.3		10.3		13.6
3.50		2.5		2.9		3.7		5.6		6.8		11.1		14.6
3.75		2.7		3.1		4.0		6.1		7.3		11.9		15.7
4.00		2.9		3.3		4.2		6.5		7.8		12.7		16.7

Notes:
1: Red highlighted cells are within the lock-in range

Table A-4: 48.3 mm Second Natural Frequencies

	L/D = 1		L/D = 2		L/D = 4		L/D = 8		L/D = 10		L/D = 16		L/D = 20	
Velocity (m/s)	**f_n**	**Vr**	**f_n**	**Vr**	**f_n**	**Vr**	**f_n**	**Vr**	**f_n**	**Vr**	**f_n**	**Vr**	**f_n**	**Vr**
0.25		0.0		0.0		0.0		0.0		0.0		0.1		0.1
0.50		0.1		0.1		0.1		0.1		0.1		0.1		0.2
0.75		0.1		0.1		0.1		0.1		0.1		0.2		0.3
1.00		0.1		0.1		0.1		0.2		0.2		0.3		0.3
1.25		0.1		0.1		0.2		0.2		0.2		0.3		0.4
1.50		0.2		0.2		0.2		0.2		0.3		0.4		0.5
1.75		0.2		0.2		0.2		0.3		0.3		0.5		0.6
2.00	193	0.2	184	0.2	166	0.2	133	0.3	118	0.4	80	0.5	61	0.7
2.25		0.2		0.3		0.3		0.4		0.4		0.6		0.8
2.50		0.3		0.3		0.3		0.4		0.4		0.6		0.8
2.75		0.3		0.3		0.3		0.4		0.5		0.7		0.9
3.00		0.3		0.3		0.4		0.5		0.5		0.8		1.0
3.25		0.3		0.4		0.4		0.5		0.6		0.8		1.1
3.50		0.4		0.4		0.4		0.5		0.6		0.9		1.2
3.75		0.4		0.4		0.5		0.6		0.7		1.0		1.3
4.00		0.4		0.5		0.5		0.6		0.7		1.0		1.4

Table A-5: 24 mm First Natural Frequencies

	L/D = 1		L/D = 2		L/D = 4		L/D = 8		L/D = 10		L/D = 16		L/D = 20		L/D = 32		L/D = 40	
Velocity (m/s)	**f_n**	**Vr**	**f_n**	**Vr**	**f_n**	**Vr**	**f_n**	**Vr**	**f_n**	**Vr**	**f_n**	**Vr**	**f_n**	**Vr**	**f_n**	**Vr**	**f_n**	**Vr**
0.25		0.9		1.0		1.1		1.4		1.5		2.0		2.4		3.8		2.4
0.50		1.9		2.0		2.2		2.8		3.1		4.1		4.8		7.5		4.9
0.75		2.8		3.0		3.4		4.2		4.6		6.1		7.2		11.3		7.3
1.00		3.8		4.0		4.5		5.6		6.1		8.1		9.6		15.1		9.8
1.25		4.7		5.0		5.6		6.9		7.7		10.1		12.0		18.8		12.2
1.50		5.7		6.0		6.7		8.3		9.2		12.2		14.4		22.6		14.6
1.75		6.6		7.0		7.8		9.7		10.7		14.2		16.8		26.4		17.1
2.00	11	7.5	10.4	8.0	9.3	9.0	7.5	11.1	6.8	12.3	5.1	16.2	4.3	19.2	2.8	30.2	4	19.5
2.25		8.5		9.0		10.1		12.5		13.8		18.3		21.6		33.9		22.0
2.50		9.4		10.0		11.2		13.9		15.3		20.3		24.0		37.7		24.4
2.75		10.4		11.0		12.3		15.3		16.9		22.3		26.4		41.5		26.8
3.00		11.3		12.0		13.5		16.7		18.4		24.3		28.8		45.2		29.3
3.25		12.3		13.0		14.6		18.0		20.0		26.4		31.3		49.0		31.7
3.50		13.2		14.0		15.7		19.4		21.5		28.4		33.7		52.8		34.2
3.75		14.1		15.0		16.8		20.8		23.0		30.4		36.1		56.5		36.6
4.00		15.1		16.0		17.9		22.2		24.6		32.5		38.5		60.3		39.0

Notes:
1: Red highlighted cells are within the lock-in range

Table A-6: 24 mm Second Natural Frequencies

	L/D = 1		L/D = 2		L/D = 4		L/D = 8		L/D = 10		L/D = 16		L/D = 20		L/D = 32		L/D = 40	
Velocity (m/s)	**f_n**	**Vr**	**f_n**	**Vr**	**f_n**	**Vr**	**f_n**	**Vr**	**f_n**	**Vr**	**f_n**	**Vr**	**f_n**	**Vr**	**f_n**	**Vr**	**f_n**	**Vr**
0.25		0.1		0.1		0.2		0.2		0.2		0.2		0.2		0.3		0.4
0.50		0.3		0.3		0.3		0.3		0.3		0.4		0.4		0.6		0.8
0.75		0.4		0.4		0.5		0.5		0.5		0.6		0.6		0.9		1.2
1.00		0.6		0.6		0.6		0.6		0.7		0.8		0.9		1.2		1.6
1.25		0.7		0.7		0.8		0.8		0.8		1.0		1.1		1.5		2.0
1.50		0.9		0.9		0.9		1.0		1.0		1.2		1.3		1.8		2.3
1.75		1.0		1.0		1.1		1.1		1.2		1.4		1.5		2.1		2.7
2.00	73	1.1	73	1.2	69	1.2	64	1.3	62	1.3	54	1.6	48	1.7	34	2.5	27	3.1
2.25		1.3		1.3		1.4		1.5		1.5		1.7		1.9		2.8		3.5
2.50		1.4		1.5		1.5		1.6		1.7		1.9		2.2		3.1		3.9
2.75		1.6		1.6		1.7		1.8		1.9		2.1		2.4		3.4		4.3
3.00		1.7		1.7		1.8		1.9		2.0		2.3		2.6		3.7		4.7
3.25		1.9		1.9		2.0		2.1		2.2		2.5		2.8		4.0		5.1
3.50		2.0		2.0		2.1		2.3		2.4		2.7		3.0		4.3		5.5
3.75		2.2		2.2		2.3		2.4		2.5		2.9		3.2		4.6		5.9
4.00		2.3		2.3		2.4		2.6		2.7		3.1		3.5		4.9		6.3

Notes:
1: Red highlighted cells are within the lock-in range

Appendix B Calibration Curves

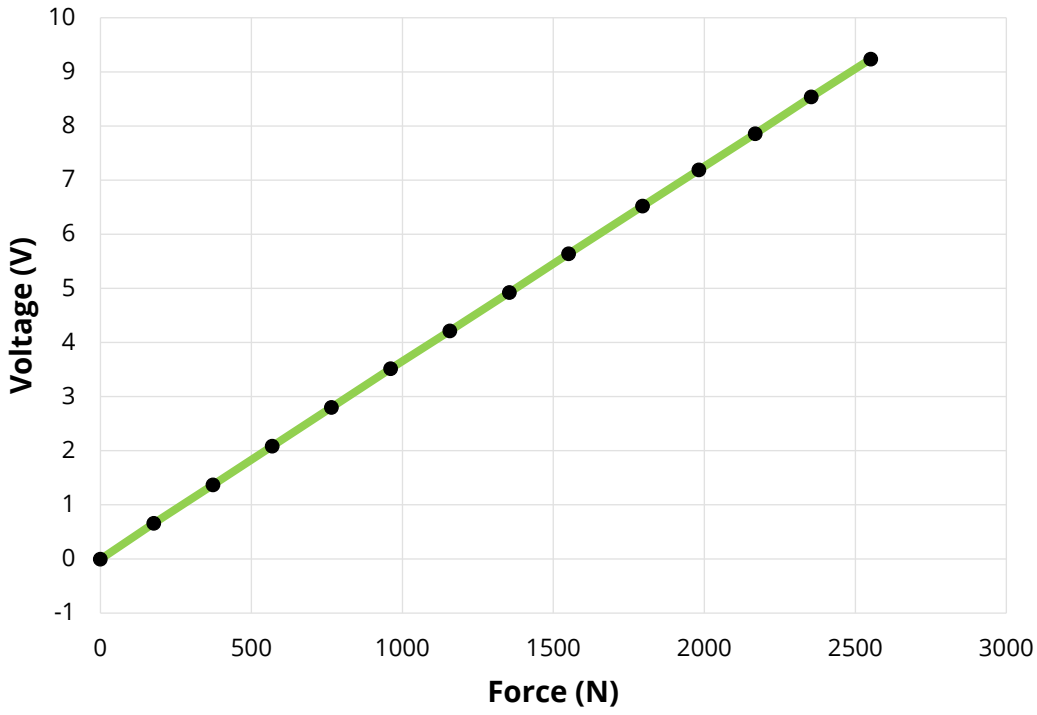

Figure B-1: 101.6 mm – Top Load Cell Calibration

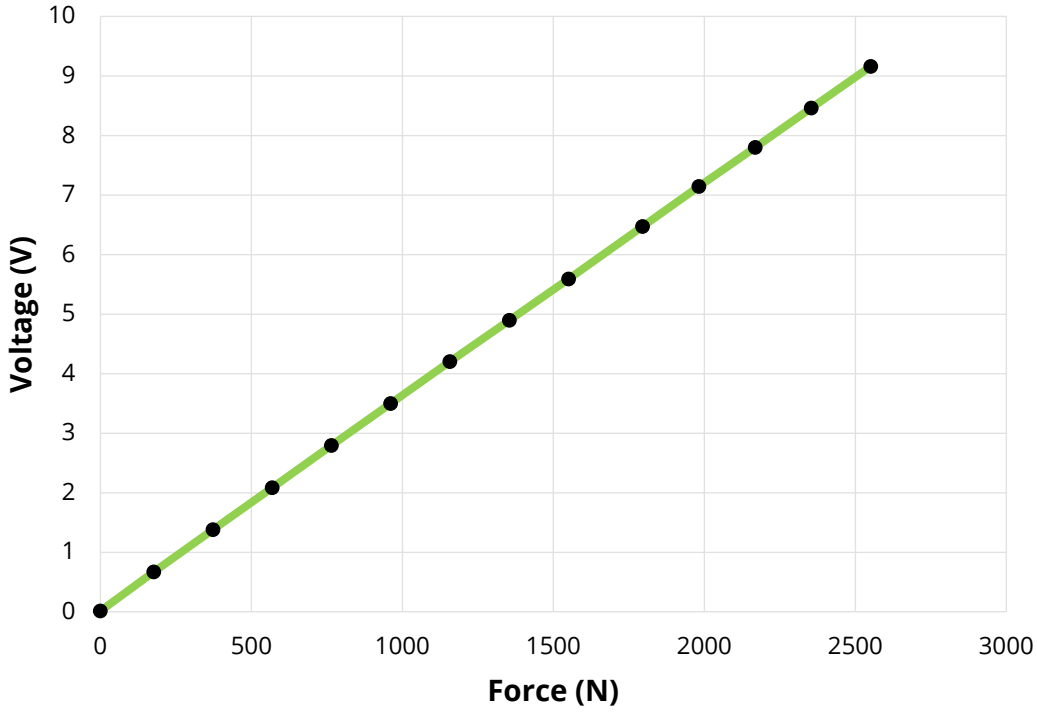

Figure B-2: 101.6 mm – Bottom Load Cell Calibration

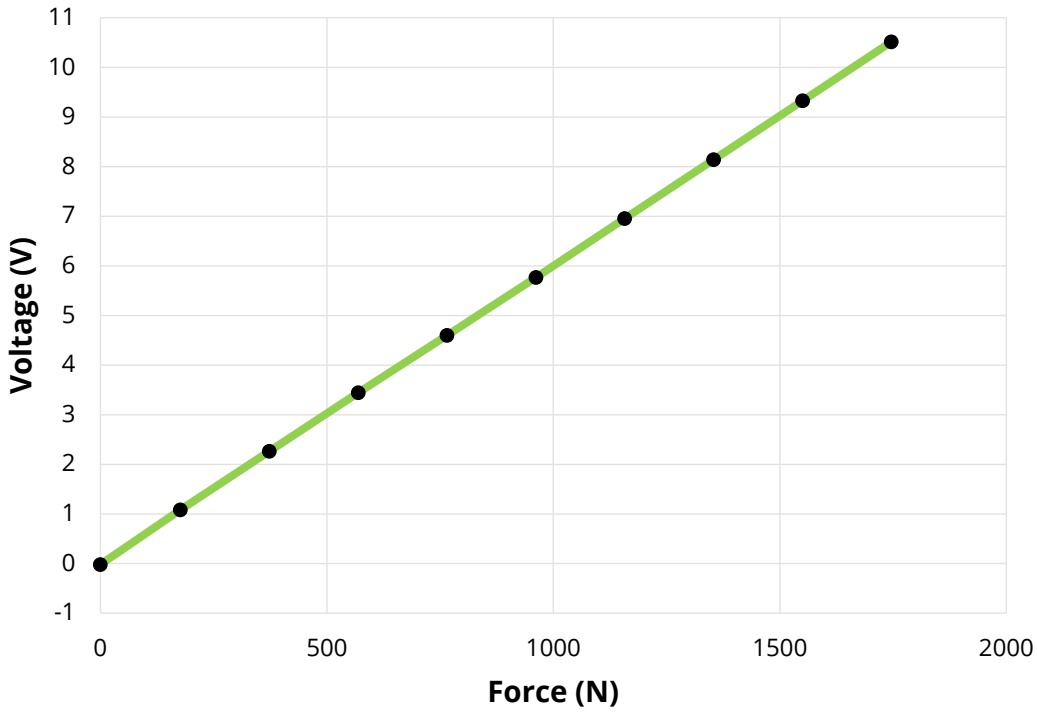

Figure B-3: 48.3 mm – Top Load Cell Calibration

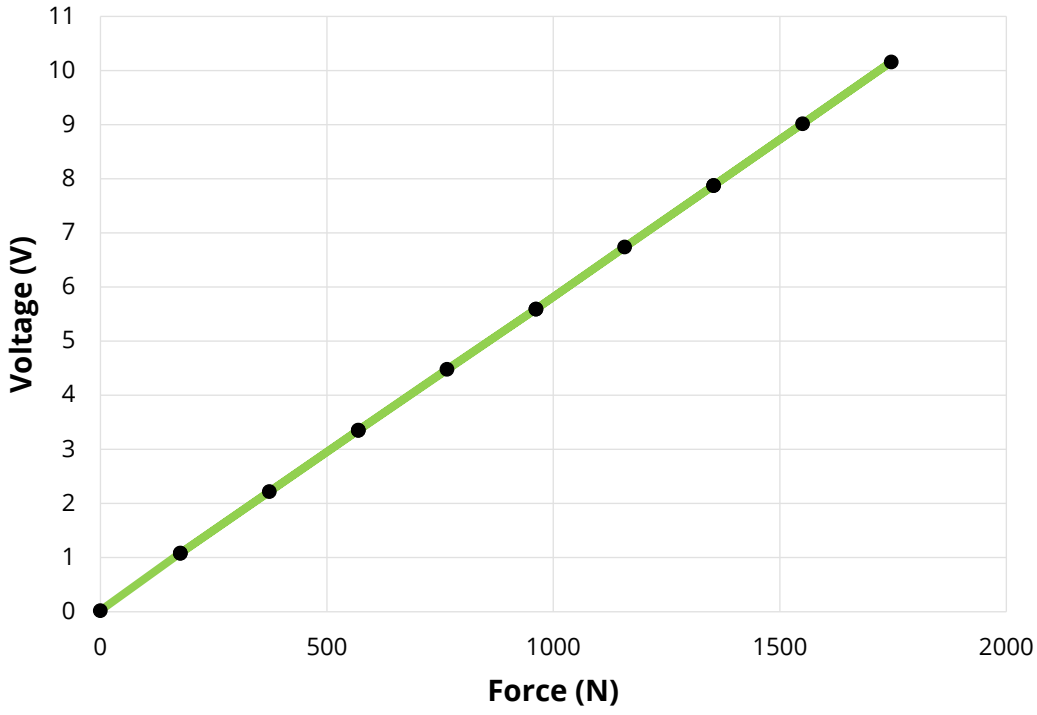

Figure B-4: 48.3 mm – Bottom Load Cell Calibration

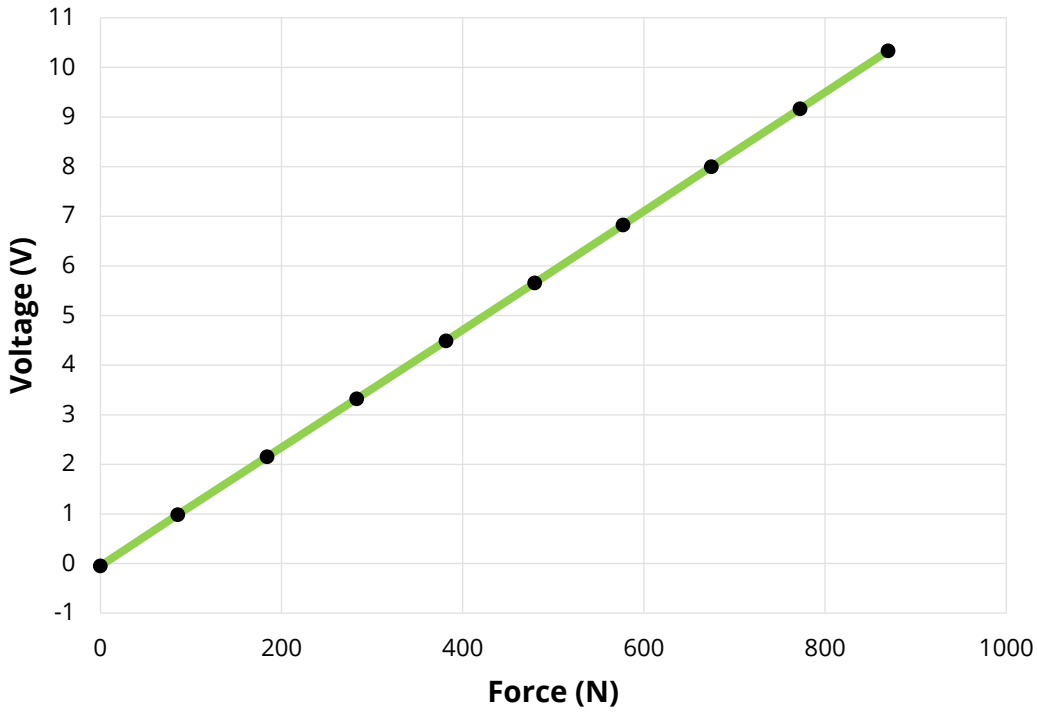

Figure B-5: 24 mm – Top Load Cell Calibration

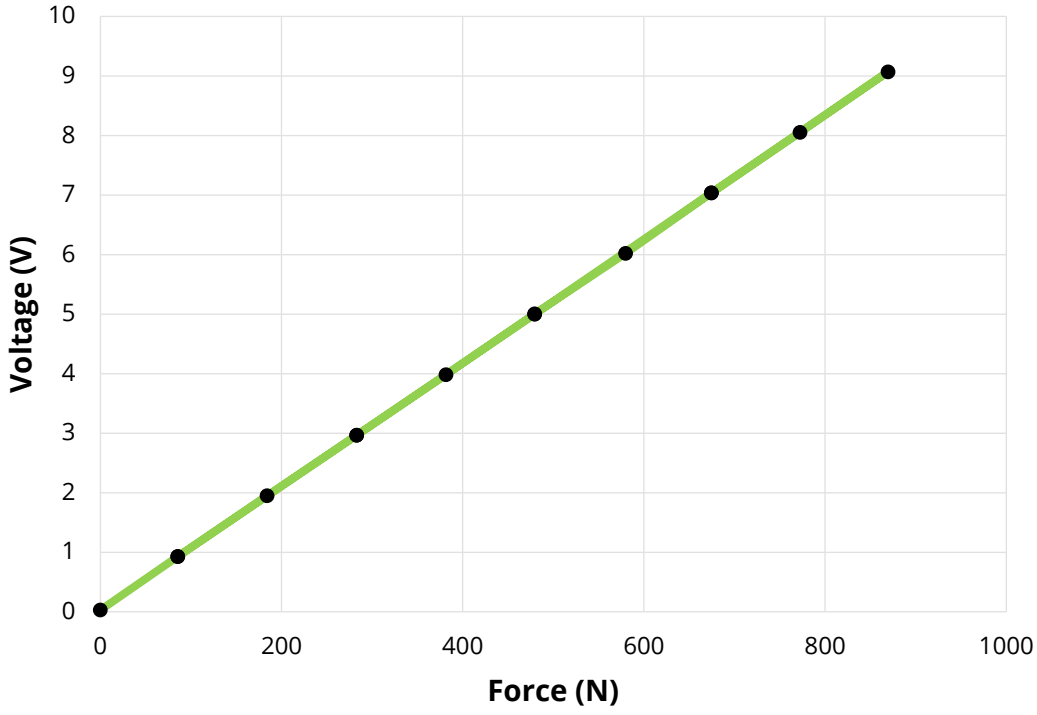

Figure B-6: 24 mm – Bottom Load Cell Calibration

Appendix C Testing Equipment Data Sheets

C.1 XTRAN LOAD CELL

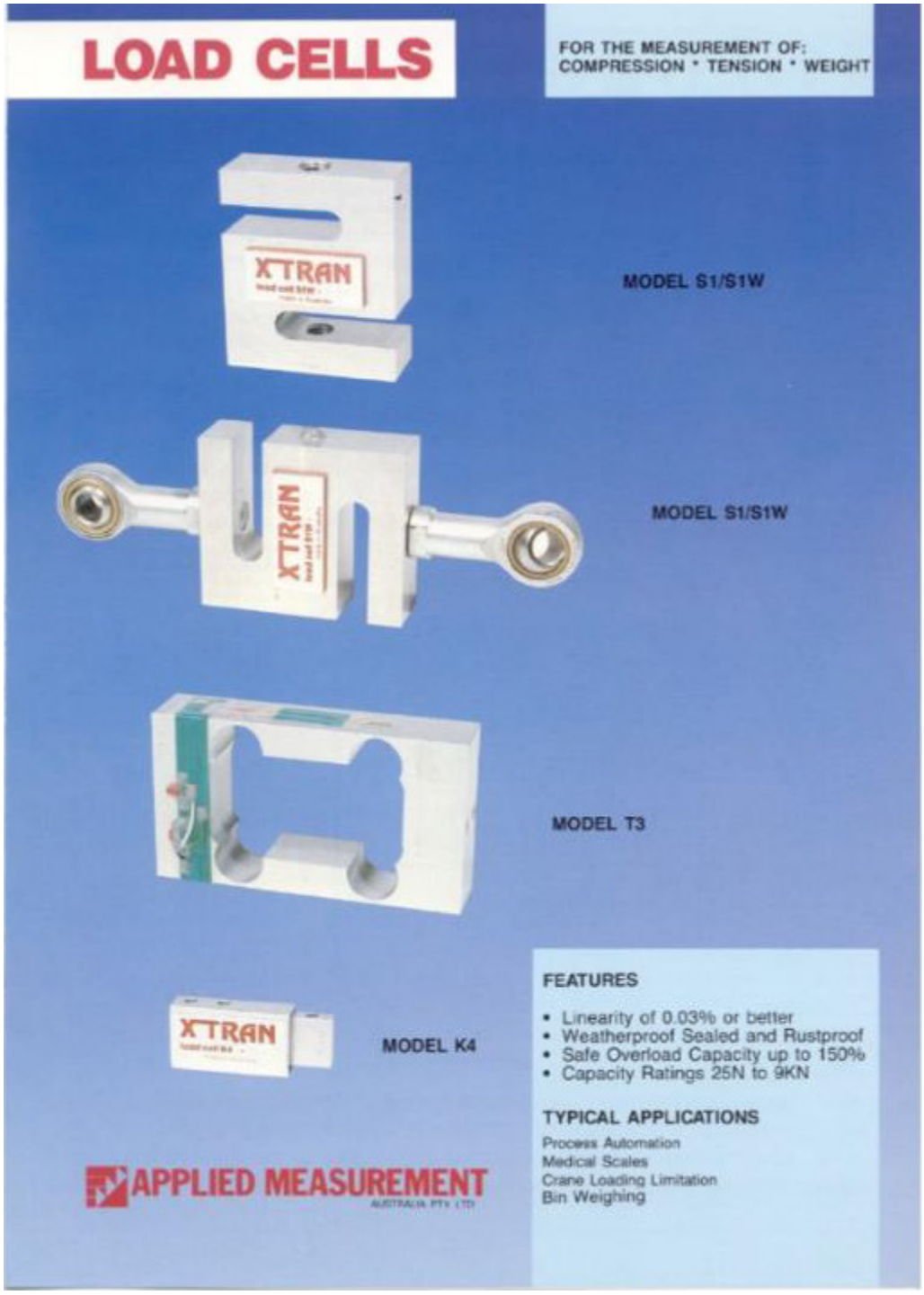

LOAD CELLS

	"S" BEAM LOAD CELLS		SHEARBEAM LOAD CELLS
Type	**S1**	**S1W**	**K2**
Protection Class	Sealed, splashproof	Sealed, submersible	Indoor, controlled temperature environment
Load Direction	**Tension &**		

						2	12	16	M12		
VF-5-G	750N, 1KN	47.6	34.9	19.1	25.4	7.9	8.7	11.1	M6	12.7	11.1
VF-10-G	7.5, 9KN	83.3	63.5	38.1	39.7	15.8	14.3	19.1	M12	25.4	22.2

reserve the right to amend specifications without notice

C.2 XSENS MTi ACCELEROMETER

MTi 10-series

The reliable industry standard for MEMS based IMU, VRU and AHRS

- ✔ Industry-proven, cost-effective MEMS based orientation sensor
- ✔ Full-featured sensor fusion algorithm with easy to use SDK
- ✔ 3 integration levels available: IMU, VRU and AHRS

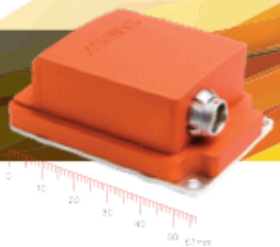

Proven Xsens sensor fusion algorithm

- Superior heading tracking using Active Heading Stabilization (AHS)
- In-run Compass Calibration (ICC)
- XKF3 sensor fusion algorithm trusted by high-profile customers
- Selectable filter profiles for range of applications

Easy software integration

- Extensive suite of configurable output formats, calculated onboard the MTi
- MT Software Suite with intuitive GUI
- Complete SDK for all operating systems
- Support for Robotic Operating System (ROS)
- Xsens Xbus protocol or ASCII (NMEA)
- Access to BASE (by Xsens), an extensive knowledge base and community forum

Excellent hardware design

- High quality industrial grade components
- Signal processing pipeline, optimized for industrial applications
- Low latency for real-time applications
- 10 kHz simultaneous sampling, 2 kHz SDI algorithm with coning/sculling compensation
- Wide array of synchronization options

Specification highlights

- Available as IP67 encased MTi or OEM board
- Choice of several interfaces and onboard USB
- All Xsens products are fully interchangeable
- Cost-effective system integrator solution

Product Overview

		MTi-10 IMU	MTi-20 VRU	MTi-30 AHRS
Calibrated Sensor Data		yes	yes	yes
Roll/pitch	Static	-	0.2°	0.2°
	Dynamic	-	0.5°	0.5°
Yaw	In homogenous magnetic field	-	Active Heading Stabilization (AHS)	1.0°

All above specifications based on typical application scenarios

WWW.XSENS.COM

Sensor specifications

	Gyroscopes	Accelerometers
Standard full range *	+/- 450 °/s	+/- 20 g
Initial bias error	0.2 °/s	5 mg
In-run bias stability	18 °/h	15 µg
Bandwidth (-3 dB)	415 Hz	375 Hz
Noise density	0.03 °/s/√Hz	60 µg/√Hz
g-sensitivity (calibrated)	0.006 °/s/g	N/A
Non-orthogonality	0.05 deg	0.05 deg
Non-linearity	0.03%	0.1%

	Magnetometer
Standard full range	+/- 8 G
Total RMS noise	0.5 mG
Non-linearity	0.2%
Resolution	0.25 mG

* Optional +/- 1000 °/s available on request.

System specifications

Input voltage	4.5 to 34V or 3V3	Interfaces	RS232/RS422/RS485/USB/ UART
Typical power consumption	550 mW @ 5V	Latency	<2 ms
IP-rating	IP67 (encased)	Sync options	SyncIn, SyncOut, Clock sync
Temperature (in use)	-40 to 85 °C	Interface protocol	Xbus or ASCII (NMEA)
Casing material	Anodized aluminum 6082	Mounting orientation	No restriction, full 360° in all axes
Sampling frequency	10 kHz/channel (60 kS/s)	Built-in self test (BIT)	Gyroscopes, accelerometers, magnetometer
Clock drift	10 ppm or external reference	MTBF	300,000 hours
Output frequency	Up to 2 kHz		

MTi 10-series
Development Kit:
MTi, software and cabling

MTi encased:
57x42x23.5 mm, 52g,
9-pins push-pull connector

MTi OEM:
37x33x12 mm, 11g,
16-pins header

WWW.XSENS.COM

Appendix D Test Matrix

Table D-1: Test Matrix

Cylinder Diameter (D)	Cylinder L/D Ratio	Cylinder Submergence (L)	Towing Velocity (V)	Max Velocity (V_{max})	End Conditions	VIV Excitation	Reynolds Number Range	Froude Number Range
101.6	1	101.6	1, 2, 3, 4, Ramp to max	4	Closed	No	1.01E+5 – 4.02E+5	1.00 – 4.01
	2	203.2	1, 2, 3, 4, Ramp to max	4	Closed			
	4	406.4	1, 2, 3, 4, Ramp to max	4	Closed			
	8	812.8	1, 2, 3, 4, Ramp to max	4	Closed			
	10	1016.0	1, 2, 3, 4, Ramp to max	4	Closed			
48.3	1	48.3	1, 2, 3, 4, Ramp to max	4	Open, Closed, End-plate	No	4.78E+4 – 1.91E+5	1.45 – 5.81
	2	96.6	1, 2, 3, 4, Ramp to max	4	Open, Closed, End-plate			
	4	193.2	1, 2, 3, 4, Ramp to max	4	Open, Closed, End-plate			
	8	386.4	1, 2, 3, 4, Ramp to max	4	Open, Closed, End-plate			
	10	483.0	1, 2, 3, 4, Ramp to max	4	Open, Closed, End-plate			
	16	772.8	1, 1.5, 2, 2.5, Ramp to max	2.5[1]	Open, Closed, End-plate	At high V		
	20	966.0	1, 1.5, 2, Ramp to max	2[1]	Open, Closed, End-plate			
24	1	24.0	1, 2, 2.5, 3, 4, Ramp to max	4	Closed	No	2.38E+4 – 9.50E+4	2.06 – 8.24
	2	48.0	1, 2, 2.5, 3, 4, Ramp to max	4	Closed			
	4	96.0	1, 2, 2.5, 3, 4, Ramp to max	4	Closed			
	8	192.0	1, 2, 2.5, 3, 4, Ramp to max	4	Closed			
	10	240.0	1, 2, 2.5, 3, 4, Ramp to max	4	Closed			
	16	384.0	1, 2, 2.5, 3, 4, Ramp to max	4	Closed	At high V		
	20	480.0	1, 2, 2.5, 3, 4, Ramp to max	4	Closed			
	32	768.0	1, 2, 2.5, 3, 4, Ramp to max	4	Closed	At full V range		
	40	960.0	1, 2, 2.5, 3, 4, Ramp to max	4	Closed			

Notes:
1: Large crossflow amplitudes (velocities greater than the max resulted in the carriage stopping)

Appendix E Additional Results

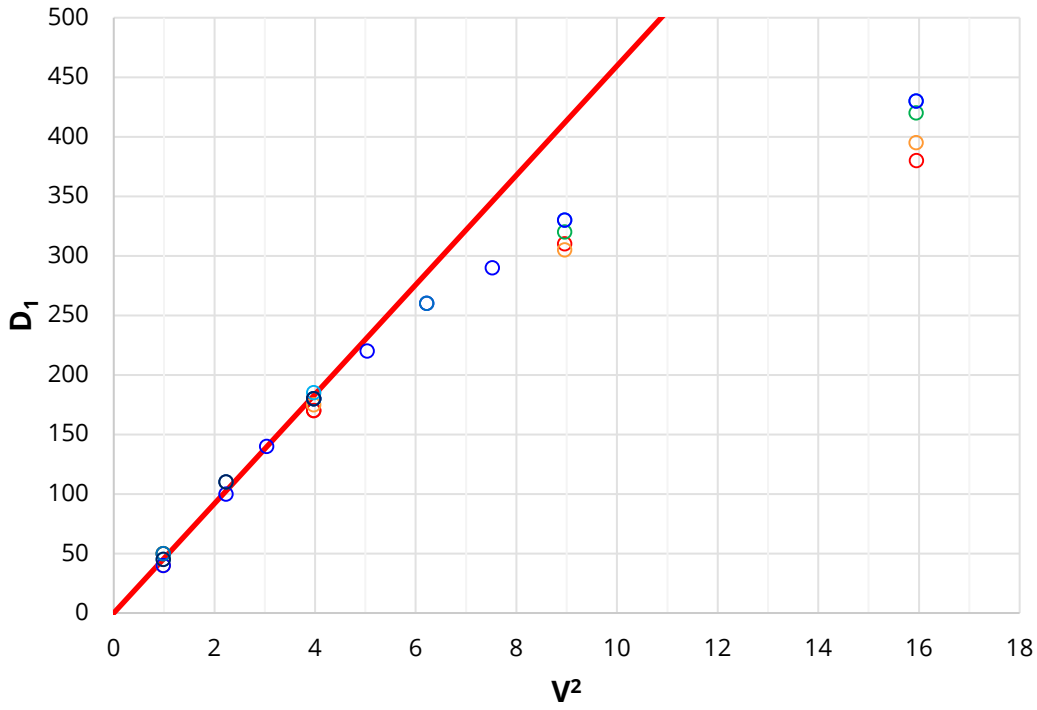

Figure E-1: 48.3 mm – Open – Bow wave height vs velocity squared

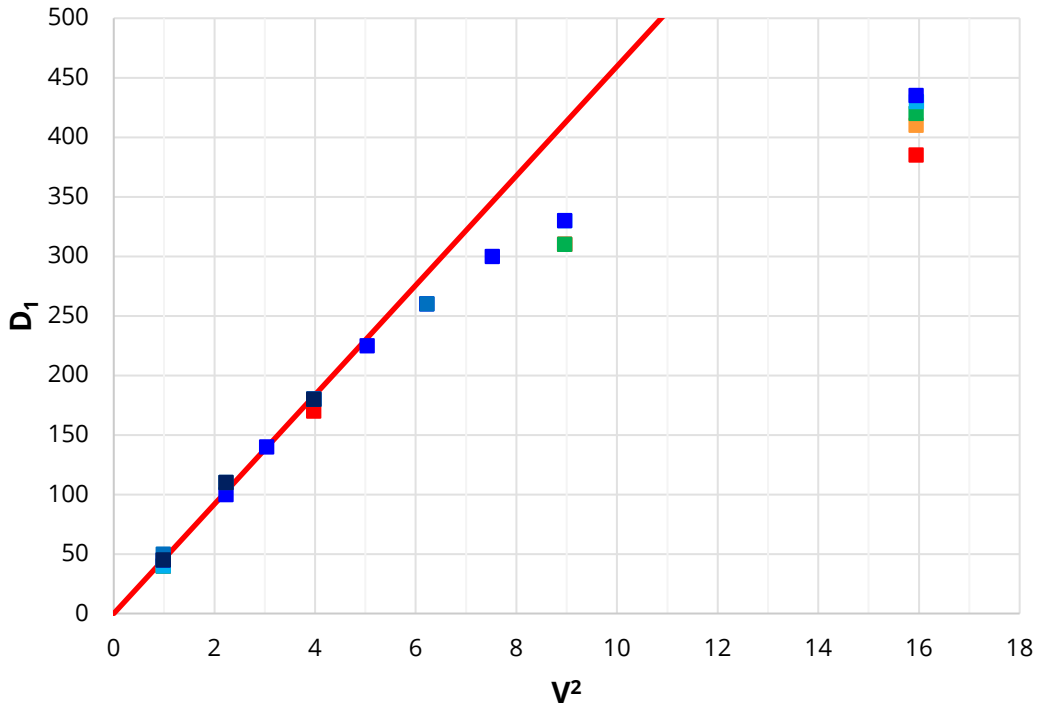

Figure E-2: 48.3 mm – End-plate – Bow wave height vs velocity squared

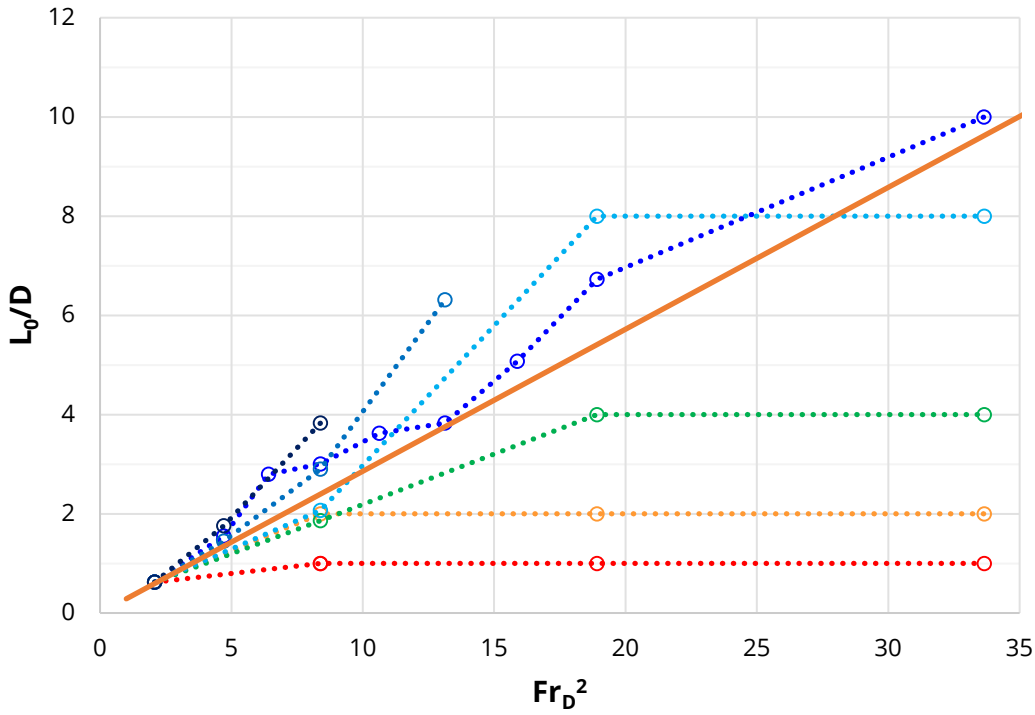

Figure E-3: 48.3 mm – Open – Ventilated pocket depth vs Froude squared

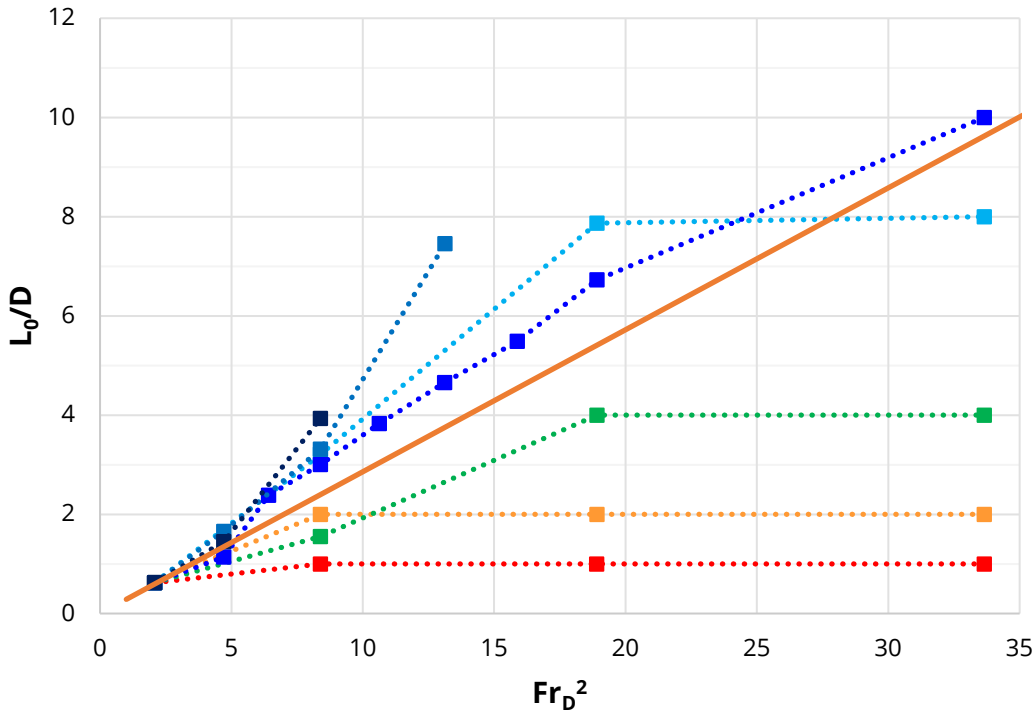

Figure E-4: 48.3 mm – End-plate – Ventilated pocket depth vs Froude squared

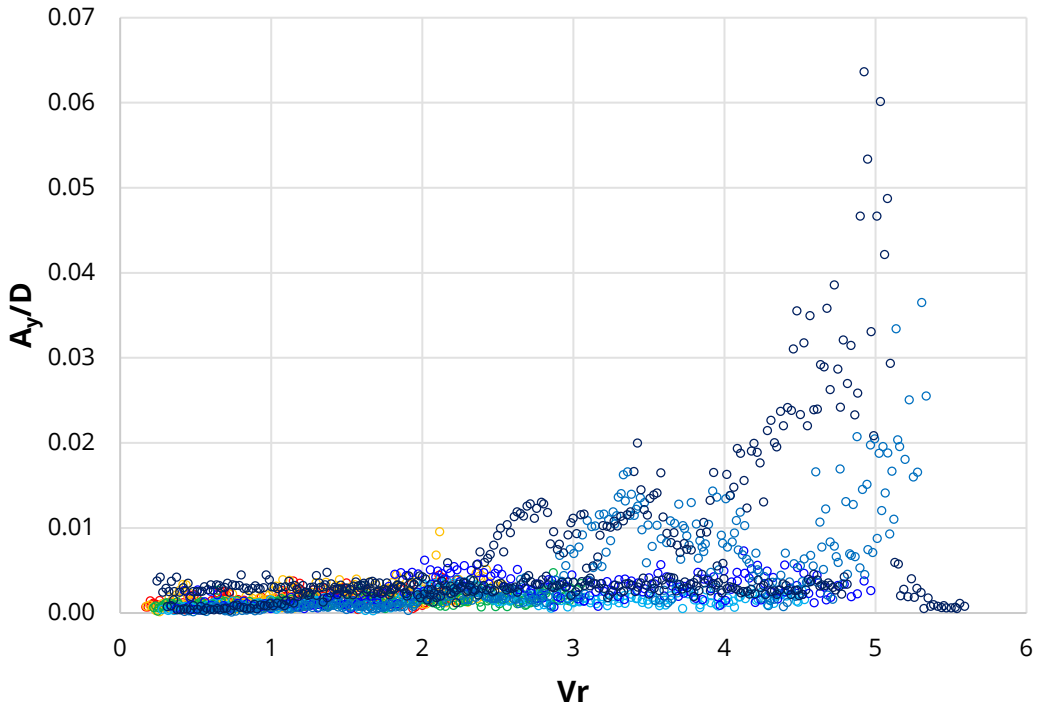

Figure E-5: 48.3 mm – Ramp – Open – Crossflow oscillation vs reduced velocity

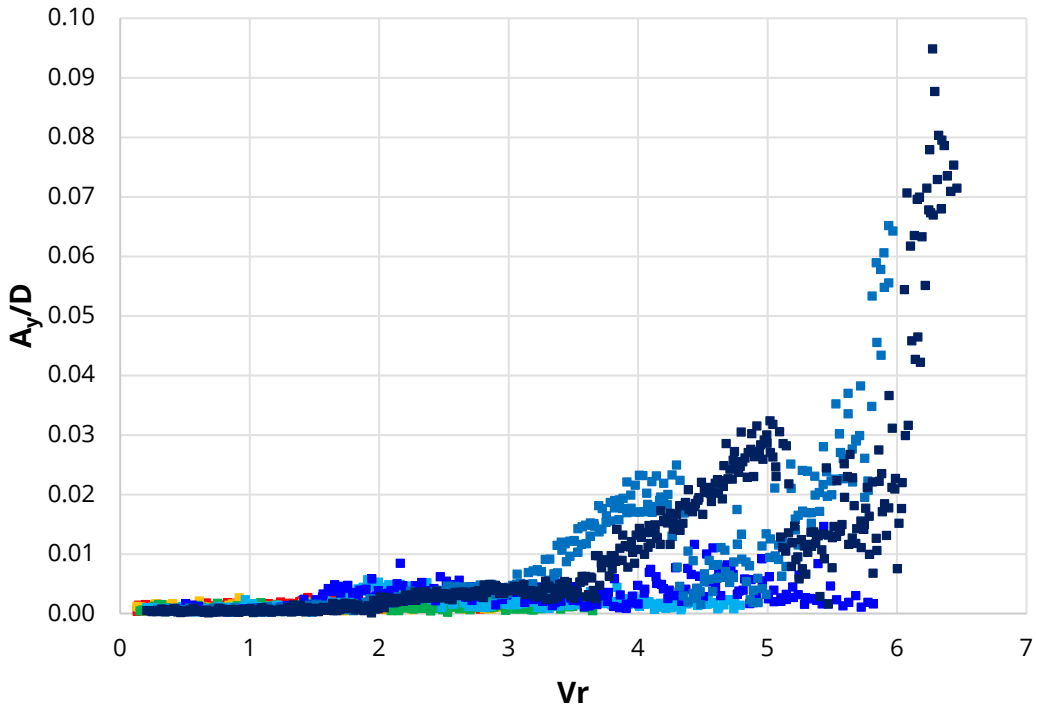

Figure E-6: 48.3 mm – Ramp – End-plate – Crossflow oscillation vs reduced velocity

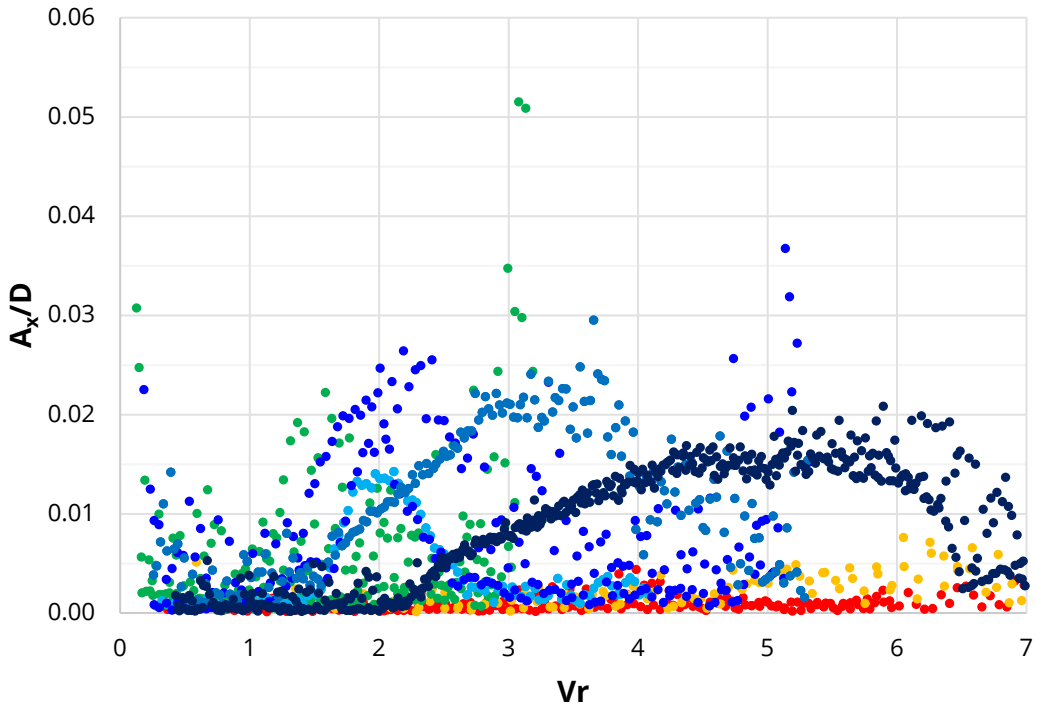

Figure E-7: 48.3 mm – Ramp – Closed – In-line oscillation vs reduced velocity

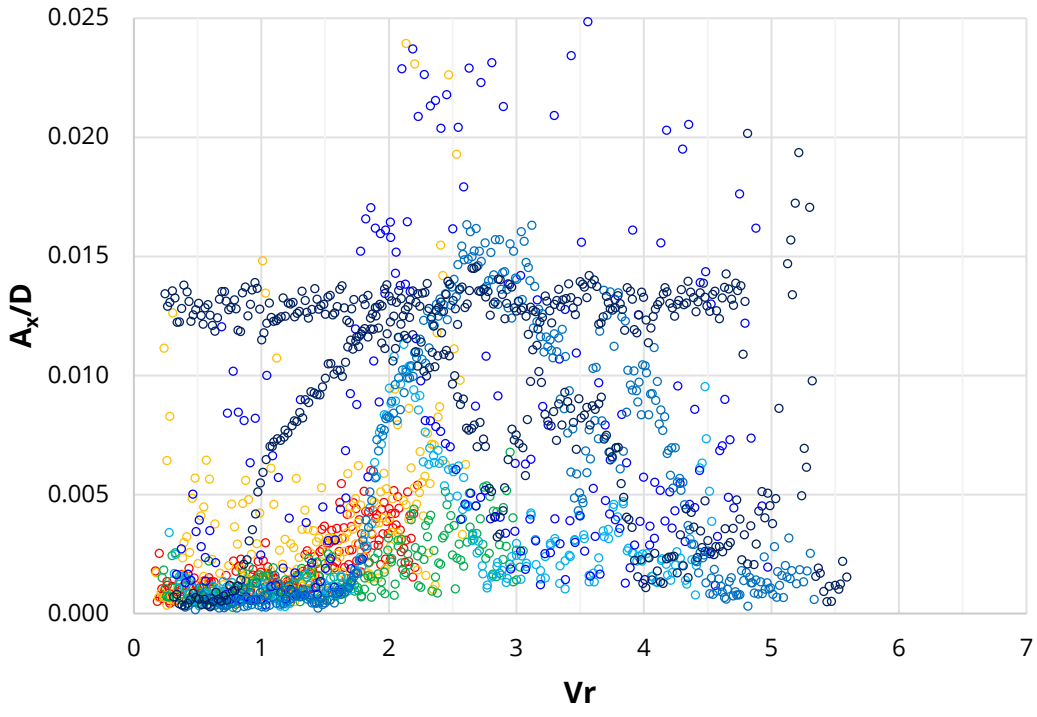

Figure E-8: 48.3 mm – Ramp – Open – In-line oscillation vs reduced velocity

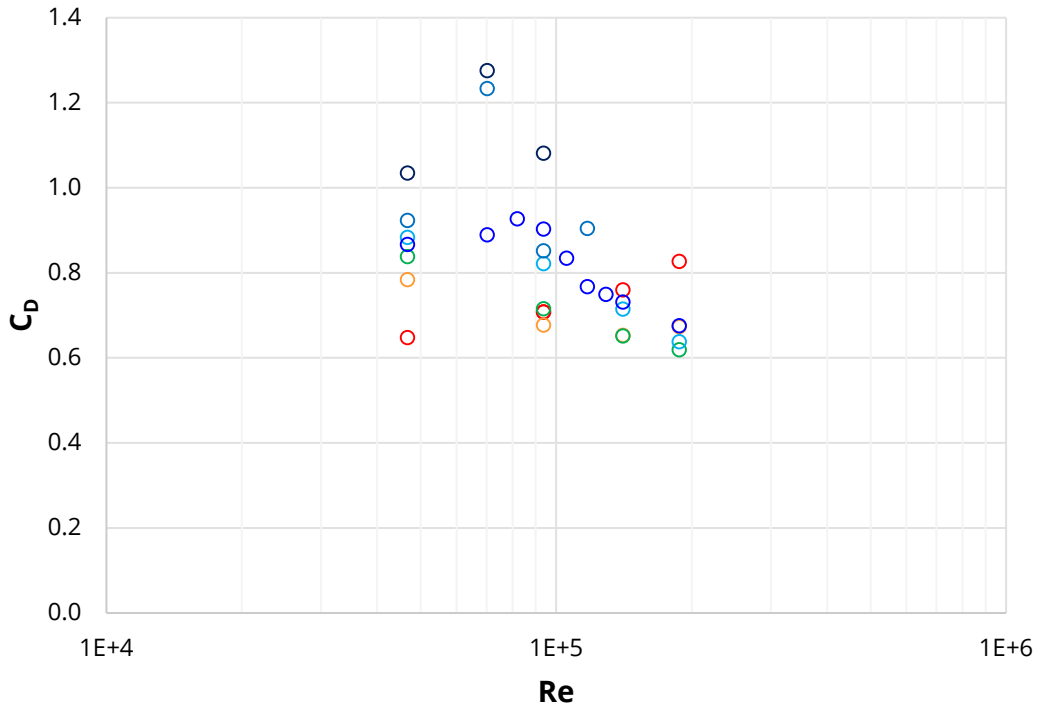

Figure E-9: 48.3 mm – Open – Drag coefficient vs Reynolds number

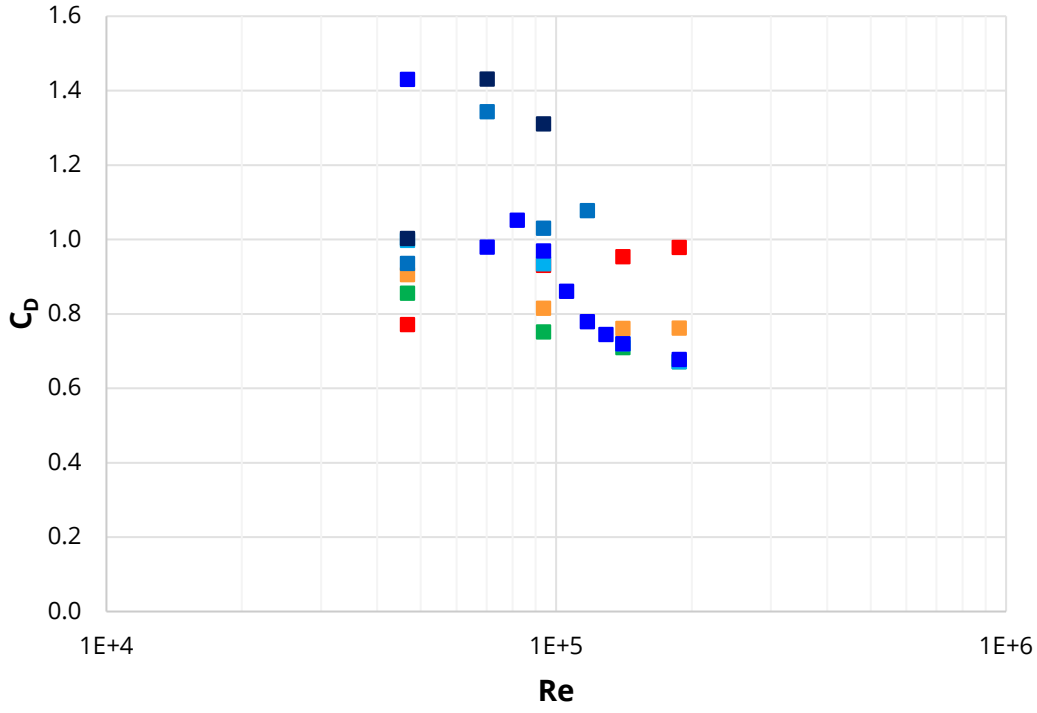

Figure E-10: 48.3 mm – End-plate – Drag coefficient vs Reynolds number

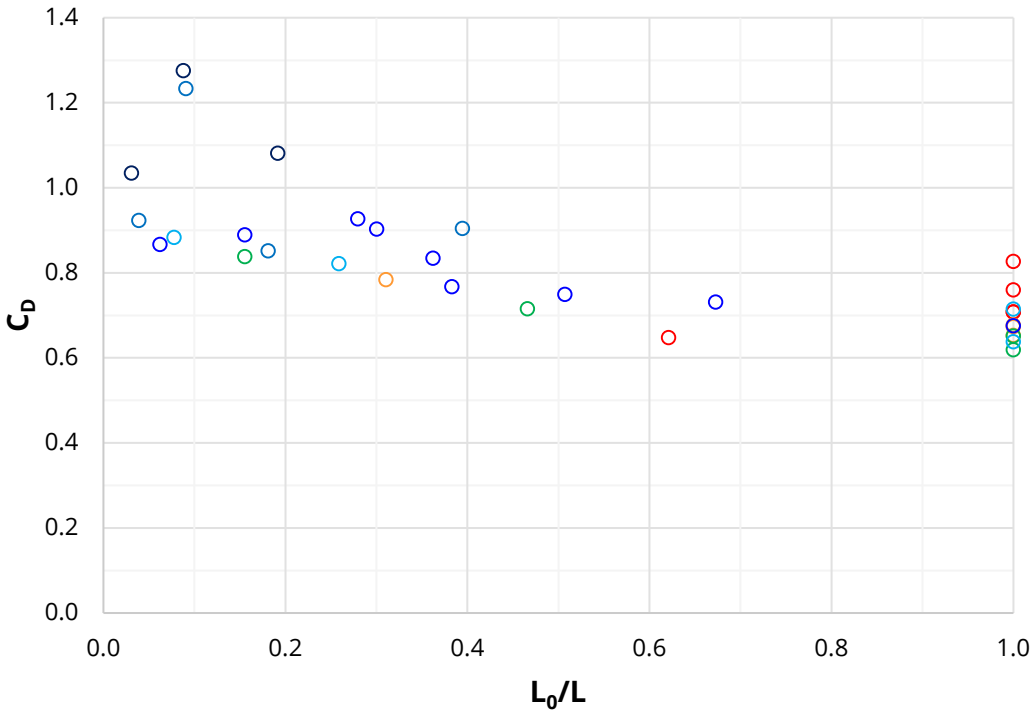

Figure E-11: 48.3 mm – Open – Drag coefficient vs ventilated pocket depth

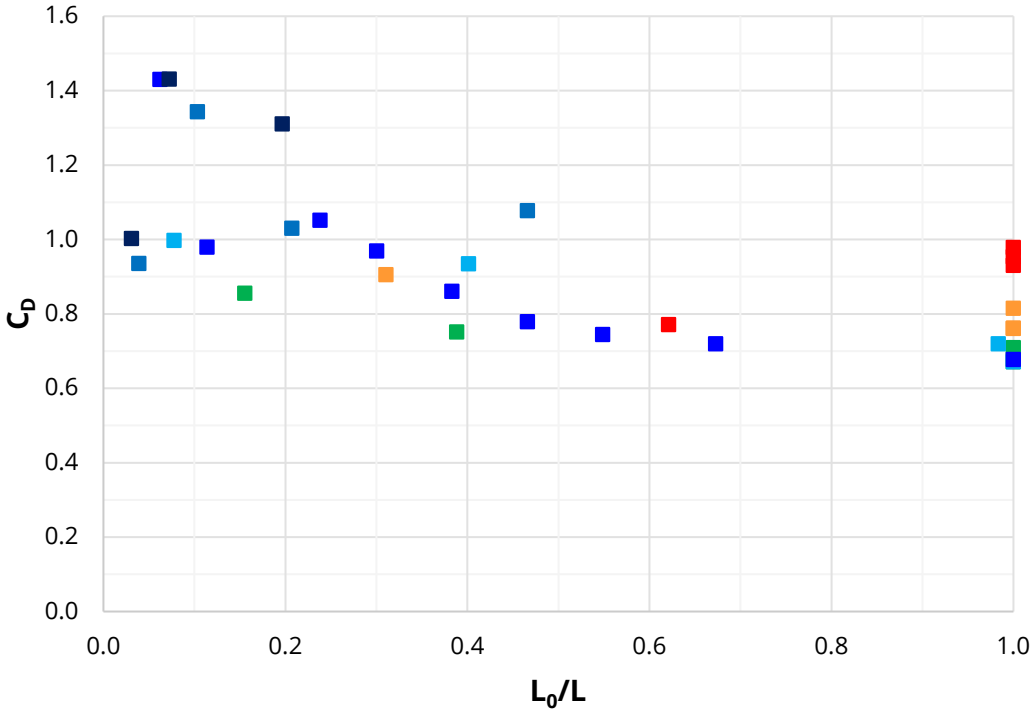

Figure E-12: 48.3 mm – End-plate – Drag coefficient vs ventilated pocket depth

Appendix F Foldout Legends

Chapter 3

Aspect Ratio	Colour
1	
2	
4	
8	
16	
32	

Model Cylinder	Symbol
1/8″	■
1/4"	◆
1/2″	▲
1″	●
2″	×
4″	✳
8″	+

Chapter 5 & 6

Aspect Ratio	Colour
1	
2	
4	
8	
10	
16	
20	
32	
40	

Model Cylinder	Symbol
24 mm Closed	◆
48.3 mm Closed	●
48.3 mm Open	○
48.3 mm End-plate	■
101.6 mm Closed	▲